INTERACTION NOTES

Note 233

January 1973

SPACE TIME INTEGRAL EQUATION APPROACH TO THE LARGE BODY SCATTERING PROBLEM

C. L. Bennett
A. M. Auckenthaler
R. S. Smith
J. D. DeLorenzo

Sperry Research Center

ABSTRACT

The space-time integral equation approach is extended to the solution of the large body problem for smooth convex targets. This is accomplished by the development of the impulse response augmentation technique that combines the smoothed impulse response, which is computed exactly with the space-time integral equation, and known features of the returns from the specular point, the join regions, and the creeping wave. This technique produces a total impulse response and the frequency response over the entire spectrum. Results are obtained for the sphere, the prolate spheroid, and the sphere-capped cylinder for axial incidence and are found to be in good agreement with available data. In addition, the polarization dependent effects on the leading edge of the impulse response are determined for the case of nonaxial incidence on smooth convex targets. Results are presented for the impulse response and frequency response of the prolate spheroid and the sphere-capped cylinder for nonaxial incidence with both polarizations.

An expression is developed for the minimum number of orientations at which the smoothed impulse response of a target must be measured or calculated for a given time sample rate or given bandwidth of the incident pulse. The results are in good agreement with measurements.

Smoothed impulse response measurements of nine targets taken on the time domain scattering range are presented and used as a basis of the design of various identification processors with OLPARS.

TABLE OF CONTENTS

TABLE OF CONTENTS (cont.)

LIST OF ILLUSTRATIONS

LIST OF ILLUSTRATIONS (cont.)

LIST OF ILLUSTRATIONS (cont.)

LIST OF ILLUSTRATIONS (cont.)

LIST OF ILLUSTRATIONS (cont.)

LIST OF ILLUSTRATIONS (cont.)

SECTION 1

INTRODUCTION

This document is submitted as the final report in response to the requirements set forth in Contract No. F30602-71-C-0162 between the Sperry Rand Research Center, Sudbury, Massachusetts, and the Air Force Systems Command, Rome Air Development Center, Griffiss Air Force Base, New York. The primary objective of this program, performed during the period 1971 March 9 through 1972 December 5, was to extend the applicability of the space-time integral equation approach to bodies of arbitrary size. Past attempts to apply frequency domain techniques to this problem have been, at best, only partially successful.

In Sec. 2.0 the extension of the space-time integral equation technique to the large body problem is considered. The impulse response augmentation technique is developed, described and applied to three smooth, convex targets: the sphere, the prolate spheroid and the sphere-capped cylinder. Both the case of axial incidence and the case of nonaxial incidence for the prolate spheroid and sphere-capped cylinder were treated. For the axial incidence case the leading edge portion of the impulse response was found to be polarization independent. However, for the nonaxial incidence case the leading edge of the impulse response was found to be polarization dependent, and, furthermore, the functional form of this dependence was found to be proportional to the difference between the principal curvatures at the specular point and the first derivative of the area function. This polarization dependence effect was incorporated into the impulse response augmentation technique and applied to the nonaxial incidence case. The results were in good agreement with other available data.

In Sec. 3.0 a relationship is developed which gives the minimum number of angular samples required in time domain calculations and measurements in order to adequately characterize the target response for a given time sample rate. The results of the theoretical study are compared and found to be in good agreement with time-domain scattering range measurements.

Section 4 describes additional time-domain scattering range measurements that were made during this contract to obtain smoothed impulse responses for additional target aspect angles and polarizations. These measurements, together with previous measurements, were used as a data base for OLPARS to design several different identification processors, which are described in Sec. 5. Conclusions are presented in Sec. 6.

SECTION 2

EXTENSION OF SPACE-TIME INTEGRAL EQUATION TECHNIQUE TO THE LARGE BODY PROBLEM

2.1 INTRODUCTION

The general scattering problem is depicted in Fig. 1. The incident electromagnetic field sets up currents on the body which in turn radiate and produce a scattered field. The problem is to compute the scattered field when the incident field and object shape are known. This scattering problem has been solved in the frequency domain by numerical solution of the frequency-domain integral equation for body sizes up to several wavelengths.[1,2] It has also been solved exactly in the time domain by numerical solution of the space-time integral equation for body sizes up to several pulse widths.[3,4] In addition, Fourier transformation of the time domain solutions yields the frequency response of the targets with results which are in good agreement with both frequency domain measurements and calculations up to body sizes of several wavelengths. While the inverse transformations of the numerical solutions in the frequency domain have the potential for yielding time domain results, this approach has not been demonstrated nor has its accuracy been evaluated. Hence, the time domain technique is the most versatile method of solving the scattering problem at the present time. In addition, it can also be used as the basis for large body solutions as discussed below.

The target responses to very large bodies can be computed with optics techniques such as geometric optics,[5] physical optics,[6] or Keller's geometric theory of diffraction.[7] In the time domain the singular portions of the response due to the specular return can be determined exactly by inspection of the space-time integral equation. In effect, it demonstrates that the physical optics currents are exact in the neighborhood of the specular point and produce a singular response. A simple technique for computing these values is by taking the second derivative of the target area function as described by Kennaugh and Cosgriff.[8] This yields the impulse response due to the physical optics approximation and is exact initially in time.

Unfortunately, practical radar systems operate in neither the optics region nor in the Rayleigh or low resonance region, but rather at an intermediate region. Moreover, in order to do a proper design of a target identification system it is necessary to know the target response over the entire frequency spectrum. This permits a valid trade off between the best identification from a theoretical viewpoint and the cost and practicability of implementing such a system. It allows the testing of a paper design at minimal expense compared with the best present approach available, viz., to build it and hope. Thus, since both the low frequency or long pulse response and the high frequency or short pulse response are known, it remains to bridge the wide gulf that now exists between them.

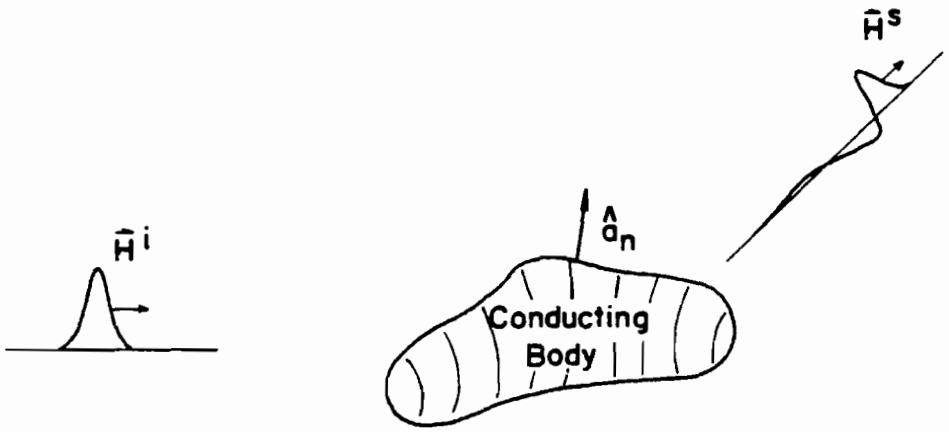

FIG. 1 General scattering problem.

There are several approaches to this problem. One approach would be to start at the optics limit and then attempt to extrapolate downward. First, Keller's geometric theory of diffraction[7] has met with success in considering simple shapes such as flat plates and right circular cylinders. The technique, however, is inherently scalar in nature, depends upon extrapolating the solution of a canonical problem (i.e., the wedge), and becomes very difficult to extend to more complex targets.

Another approach has been to start with the approximate impulse response computed using the physical optics approximation and then modify the response in some way so that the first two moment conditions were satisfied. This yields a better approximate impulse response,[8] but still contains a large uncertainty since the moment conditions give information about the integral of the response but not about its shape.

The only finite, three dimensional target for which there exists an "exact" frequency response, or "exact" impulse response over the entire spectrum is the sphere. The frequency response is given by the Mie series[9] and can be easily computed numerically from this series up to moderate body size. Senior and Goodrich[10] have passed the Mie series through a transform to obtain an expression which can be used for numerical computation at larger body sizes. Combining these two pieces yields the "exact" frequency response of the sphere over the entire spectrum. The "exact" impulse response of the sphere can then be obtained from the frequency response using a procedure outlined in Sec. 2.3.1 of this report.

A third technique for computing the impulse response or the frequency response has been developed for targets whose geometry can be obtained by deforming a sphere. In particular, this technique has been demonstrated in a prolate spheroid with axial incidence.[11] This technique consists of the following procedure. First the impulse response of the sphere is integrated twice to yield the ramp response of the sphere. Next, the ramp response of the sphere is "stretched" in the same way that the sphere would have to be stretched to form a prolate spheroid. This yields the approximate ramp response of the prolate spheroid. Next the ramp response is differentiated twice and then fitted with an exponential sum to yield the approximate impulse response of the prolate spheroid. Finally, the Fourier transform is carried out to obtain the approximate frequency response of the prolate spheroid. This result is in reasonable agreement with frequency domain measurements which have been performed. However, it is limited to target shapes which are close to a sphere and contains substantial uncertainty due to the approximations used.

There appear to be two basic approaches to the extension of the space-time integral equation approach to the large body problem. One approach would be to consider and try to determine the detailed behavior of the surface currents. Alternately, the far-field could be considered directly, which would greatly simplify the problem. This study deals with the second approach to the large body problem.

In this report a new technique for obtaining the impulse response and frequency response of an arbitrary target over the entire spectrum is described. The impulse response augmentation technique utilizes the proven computational procedure of determining the smoothed impulse response of an arbitrary target by numerical solution of the space-time integral equation and the known variation of the impulse response due to the specular return. These two results provide both low and high frequency information exactly and are combined in a natural and rigorous manner to yield the frequency response over the entire spectrum and total impulse response with a minimum of uncertainty.

2.2 IMPULSE RESPONSE AUGMENTATION TECHNIQUE

The space-time integral equation approach[3,4] solves the scattering problem directly in the time domain where the units of time are in light meters. (A light meter is defined as the time it takes an electromagnetic wave moving at the speed of light to travel one meter. It has the effect of normalizing time by the speed of light and is computed by multiplying time in seconds by the speed of light in meters/second). The space-time integral equation is valid for any excitation. The impulse response of a target, if known, could be used to compute the response of the target due to any excitation by a simple convolution procedure, and thus an impulse excitation would yield the universal solution for a particular target. However, present-day computer limitations preclude the direct numerical solution of the space-time integral equation for the impulse excitation. The most useful excitation has been found to be a regularized (or smoothed) impulse of the form

$$H^i(t/a) = \frac{n}{\sqrt{\pi}} e^{-(na)^2(t/a)^2} \tag{1}$$

where $H^i(t/a)$ is the incident magnetic field at the origin of the coordinate system

a is the characteristic linear dimension of the target

n is the parameter which controls the width of the smoothed impulse e(t) and is chosen such that the product (na) is a constant

which is the standard Gaussian regularization of an impulse in the theory of distributions.

The response $r_0 H^s(t_f/a)$ due to this excitation is thus a regularized (or smoothed) impulse response and can be computed exactly with the space-time integral equation. The smoothed impulse response has been obtained for body sizes up to several pulse widths using this technique.[3,4] The smoothed impulse response can also be used to calculate the response of a target due to any excitation waveform whose frequency spectrum is contained within the frequency spectrum of the incident smoothed impulse. In particular, the frequency response of the target can be calculated by dividing the Fourier transform of the smoothed impulse response by the Fourier transform of the smoothed impulse excitation. The smoothed impulse response has been used to obtain the frequency response of targets ranging in size from zero to several wavelengths.[12]

In order to simplify the notation in this report the electromagnetic field variables are equated to their linear system counterparts as described below:

$H^i(t/a) \rightarrow e(t)$ = incident pulse

$r_o H^s(t_f/a) \rightarrow r(t)$ = smoothed impulse response

$h(t)$ = impulse response

$t/a \rightarrow t$ = time

$H^i(ka)/a \rightarrow E(\omega)$ = transform of $e(t)$

$r_o H^s(ka)/a \rightarrow R(\omega)$ = transform of $r(t)$

$H(\omega)$ = frequency response

$ka \rightarrow \omega$ = frequency

where

H^i = incident magnetic field intensity

H^s = far scattered magnetic field intensity

r_o = distance of far field observer from origin

t/a = normalized time

ka = normalized frequency

a = characteristic linear dimension of target.

The scaling and normalization that is indicated above yields curves which are independent of target size, as described in Sec. 8.1.

The impulse response augmentation technique, first suggested in 1968[3], deals directly with the smoothed impulse response of targets in the far field. As described earlier, the smoothed impulse response is computed using the space-time integral equation approach and has yielded good results up to body sizes of several pulse widths or, equivalently, up to body sizes of several wavelengths. The regions of slow variation in the smoothed impulse response remain the same in the exact impulse response; thus it is only necessary to determine the structure of the singular regions and any other regions of fast variation. But the singular portions of the exact impulse response that result from scattering by specular points on smooth convex targets can be computed exactly and hence do not need to be computed by solving the space-time integral equation. The impulse response augmentation technique combines the smoothed impulse response, the known singular contribution to the impulse response, and the theory of Fourier transforms to produce the total impulse response and the frequency response (system function) of the target at all frequencies.

The impulse response augmentation technique is most easily understood by considering the most basic approach to the deconvolution (or system identification) problem. Figure 2 shows the functional diagram of a linear system (in this case electromagnetic scattering by a target) that is characterized by its impulse response h(t) or, equivalently, its system function (or frequency

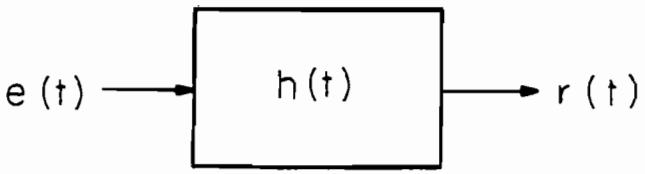

FIG. 2 Linear system.

response) $H(\omega)$. Of course,

$$h(t) \leftrightarrow H(\omega) \tag{2}$$

where $\leftrightarrow$ denotes Fourier transform. The excitation $e(t)$ of the linear system in this case is the regularized (or smoothed) impulse

$$e(t) = \frac{n}{\sqrt{\pi}} e^{-(nt)^2} \tag{3}$$

which produces the regularized (or smoothed) impulse response $r(t)$ of the system. This response is given by

$$r(t) = e(t) * h(t) \tag{4}$$

where * represents a convolution. In the problem being considered here, $e(t)$ is specified analytically and $r(t)$ is computed by solving the space-time integral equation. It is desired to find $h(t)$ and/or $H(\omega)$. This is the system identification or deconvolution problem.

One way to solve this problem, at least in principle, is to transform Eq. (4) and rearrange to obtain

$$H(\omega) = \frac{R(\omega)}{E(\omega)}$$

$$h(t) = F^{-1}\{H(\omega)\} \tag{5}$$

where

$$E(\omega) \leftrightarrow e(t)$$

$$R(\omega) \leftrightarrow r(t)$$

$F^{-1}\{\ \}$ is the inverse Fourier transform.

However, the estimate of the system response $\hat{r}(t)$ that is computed contains some uncertainty or noise. Thus, the transform of the computed or measured smoothed impulse response $R(\omega)$ also contains noise $N(\omega)$ and may be written as

$$\hat{R}(\omega) = R(\omega) + N(\omega) \ . \tag{6}$$

Substitution of Eq. (6) and the transform of e(t) into Eq. (5) yields the estimate of the system function $\hat{H}(\omega)$ as

$$\hat{H}(\omega) = H(\omega) + e^{(\omega/2n)^2} N(\omega) \tag{7}$$

and it is clear that the noise at high frequencies in the estimate of the system function increases exponentially. Physically this occurs because the interrogating signal is a smoothed impulse and its transform decays exponentially with frequency. The resulting response r(t) will contain negligible high frequency information. Thus, this approach by itself will not yield the system function at all frequencies, and since the impulse response is the inverse transform of the system function, then it will not yield the exact impulse response.

The impulse response augmentation technique is displayed in block diagram form in Fig. 3. This technique first augments the smoothed impulse response to remove the contribution from singular portions of the impulse response that are known exactly. This produces the augmented smoothed impulse response $r_a(t)$ that is given by

$$r_a(t) = r(t) - e(t) * f_a(t) \tag{8}$$

where $f_a(t)$ is a suitable augmentation function that contains the known singular portions of the impulse response.

Next, the transform of the augmented smoothed impulse response, $R_a(\omega)$, is computed and divided by the transform of the incident pulse to yield the augmented frequency response, $H'_a(\omega)$. This function contains noise which increases exponentially at frequencies above some value. However, it is known that the augmented frequency response must go to zero with increasing frequency. Thus, an estimate of the high frequency behavior of the augmented frequency response $\hat{H}_a(\omega)$, is of the form

$$\hat{H}_a(\omega) = \begin{cases} H'_a(\omega); & \omega \le \omega_c \\ F(\omega); & \omega \ge \omega_c \end{cases} \tag{9}$$

where ω_c is the boundary point and $F(\omega)$ is the high frequency estimate of $H_a(\omega)$. The inverse Fourier transform of $\hat{H}_a(\omega)$ then yields the estimate of the augmented impulse response, $\hat{h}_a(t)$.

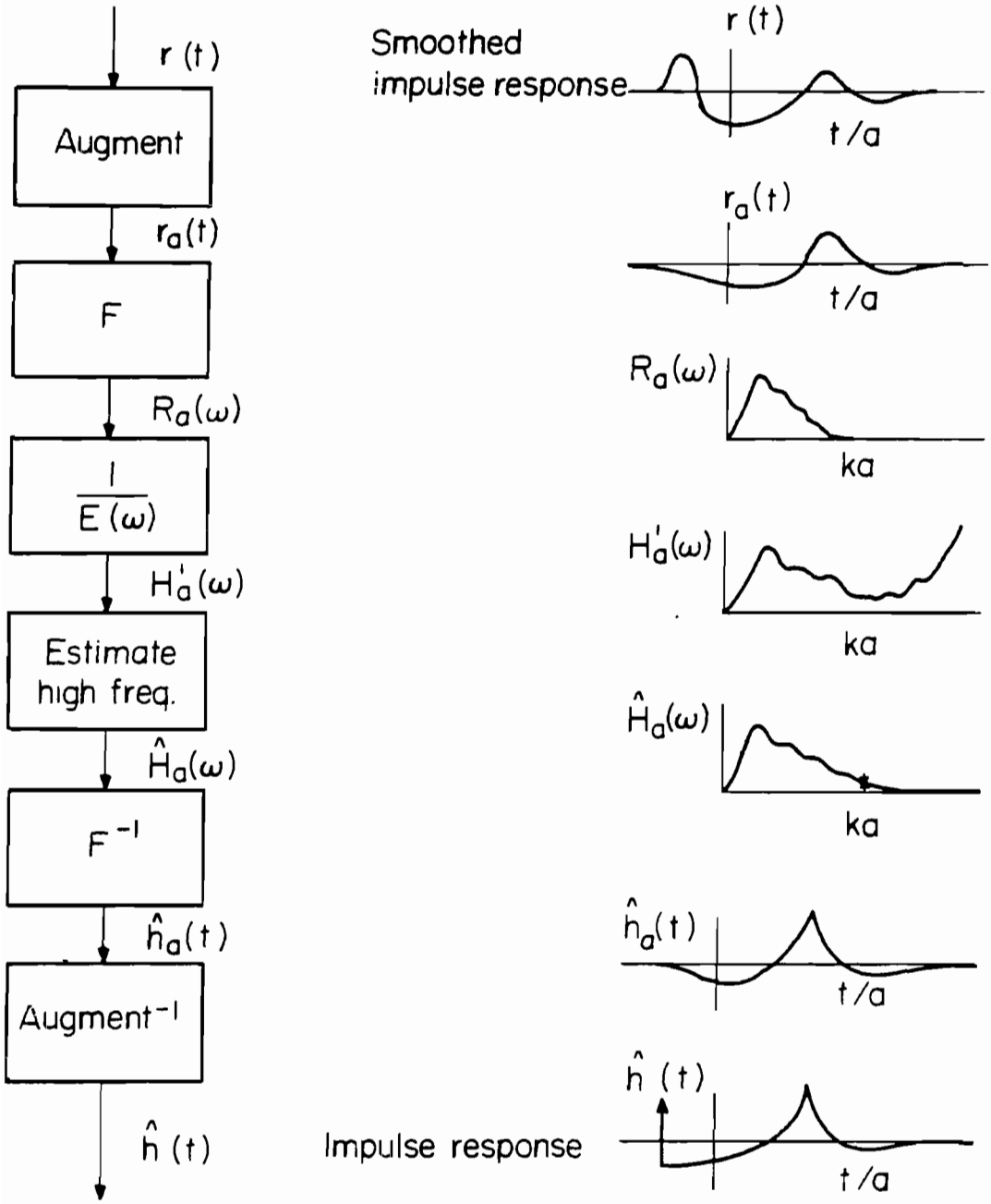

FIG. 3 Impulse response augmentation technique.

Finally, the inverse of the augmentation procedure is performed on $\hat{h}_a(t)$, which yields the estimate of the impulse response, $\hat{h}(t)$. Moreover, an estimate of the system function $\hat{H}(\omega)$, is obtained by applying the inverse of the augmentation procedure in the frequency domain to $H_a(\omega)$.

The augmentation function represents the contributions of the singular portions of the impulse response which are known exactly from optics considerations. These singular portions may contribute to not only the high frequency behavior but also to the low frequency behavior of the response, as in the case of an impulse. These contributions are removed by subtracting the effect of the augmentation function $f_a(t)$ from the response to yield the augmented response as given in Eq. (8), which is repeated here for convenience:

$$r_a(t) = r(t) - e(t) * f_a(t) \tag{8}$$

or

$$h_a(t) = h(t) - f_a(t) \ .$$

Since the effect of the optics or high frequency contributions have been removed, then it remains to estimate the manner in which the lower frequency components approach zero with increasing frequency. Various augmentation functions are now presented and discussed.

The first augmentation function considered is the impulse response predicted by geometric optics, which for smooth convex targets is simply an impulse of the form

$$f_a(t) = \frac{1}{2}\delta\left(t/\sqrt{R_1R_2} + 2r_o/\sqrt{R_1R_2}\right) \tag{10}$$

where R_1 and R_2 are the principal radii of curvature of the target at the specular point and r_o is the distance of the specular point from the origin.

This augmentation function can be improved by using the physical optics approximation for the surface currents to obtain an approximate impulse response for the target. In the physical optics approximation the surface currents are taken to be

$$\vec{J}(\vec{r},t) = \begin{cases} 2\hat{a}_n \times \vec{H}^i(\vec{r},t); & \text{illuminated side} \\ 0 \leftarrow \qquad\quad ; & \text{shadow side} \end{cases}$$

where

$\vec{J}(\vec{r},t)$ is the surface current

$\vec{H}^i(\vec{r},t)$ is the incident magnetic field intensity

$\hat{a}_n$ is the unit normal to the surface

(r,t) is the coordinate position in space time.

It has been shown[8] that the impulse response resulting from the physical optics approximation is given by

$$r_o H^s(\vec{r},t) = \frac{1}{2\pi} \frac{\partial^2 S(t_s)}{\partial t^2} \tag{11}$$

where

$S(t_s)$ is the silhouette area of the scatterer as delineated by the incident impulse assumed to be moving over the scatterer at one half the free space velocity

$t = t_s + r_o$

r_o = distance of far field observer from the origin.

The response for the case of a sphere of radius a is

$$f_a(t) = \frac{1}{2}\,\delta(t/a + 2) + \frac{1}{4}\,[u(t/a + 2) - u(t/a)]$$

and is displayed in Fig. 4(a). The physical optics approximation yields an approximate impulse response which is exact at $t/a = -2$ and satisfies the zero order moment condition, but at the same time introduces a second step function at $t/a = 0$ that is not present in the theoretical impulse response. This second step will add high frequency components to the augmented response, and thus, the physical optics approximation is not a suitable augmentation function.

This difficulty with the physical optics approximation can be easily circumvented by using a triangular pulse for the case of the sphere, as shown in Fig. 4(b). The triangular portion of the augmentation function is adjusted so that the amplitude of the negative step at $t/a = 2$ maintains the physical optics value and the area of the triangle is equal to the area of the impulse. This second constraint preserves the zero order moment of the response wave-fomr. For the case of a sphere with radius a this augmentation function is

$$f_{a1} = \frac{1}{2}\,\delta(t/a + 2) + w_1(t) \tag{12}$$

where

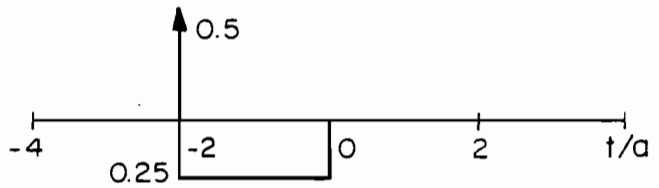

(a) Physical optics $f_a(t/a)$

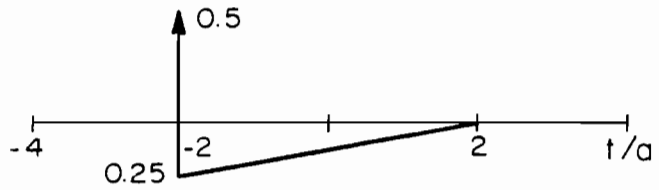

(b) Continuous $f_{a_1}(t/a)$

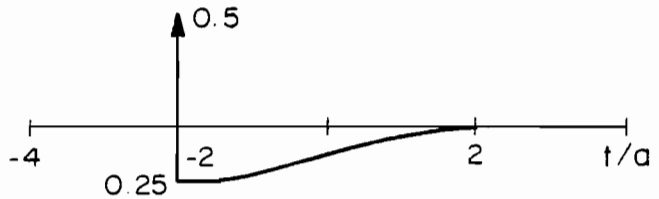

(c) Smooth $f_{a_2}(t/a)$

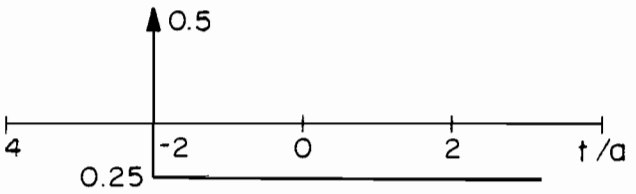

(d) Linear phase $f_{a_3}(t/a)$

FIG. 4 Augmentation functions for a sphere with radius a.

$$w_1(t) = \begin{cases} \frac{(t/a - 2)}{16} & ; \quad -2 < t/a < 2 \\ 0 & ; \quad \text{elsewhere} . \end{cases}$$

The augmentation function $f_{a1}(t)$ introduces a finite slope at $t/a = -2$ and also a discontinuity in the first derivative at $t/a = 2$. In the case of the sphere and other smooth convex targets the initial slope of the response is zero and smooth thereafter. One augmentation function which satisfies these two additional criteria by using a cosine pulse is for the case of a sphere with radius a:

$$f_{a2} = \frac{1}{2}\delta(t/a + 2) + w_2(t) \tag{13}$$

where

$$w_2(t) = \begin{cases} -\frac{1}{8}[1+\cos\frac{\pi}{2}(t/a + 2)] ; & -2 \le t/a \le 2 \\ 0 ; & \text{elsewhere} \end{cases}$$

a = sphere radius

The cosine pulse was specified such that the initial value of $w_2(t)$ corresponds to the exact results and the total function $f_{a2}(t)$ satisfies the zero moment condition. This augmentation function $f_{a2}(t)$ is displayed in Fig. 4(c) and is the function which is used together with the finite Fourier transform (FFT) to numerically obtain the frequency response from the impulse response and vice versa.

This augmentation function introduces a nonlinear phase term into the augmented frequency response, however, and thus increases the difficulty in estimating the high frequency variation of the augmented frequency response. To obviate this difficulty, an augmentation function which contains only an impulse and step at $t/a = -2$ is used. For the case of a sphere with radius a this is given by

$$f_{a3}(t) = \frac{1}{2}\,\delta(t/a + 2) - \frac{1}{4}u(t/a + 2) \tag{14}$$

and is displayed in Fig. 4(d). This augmentation function adds only a linear phase term, is exact at $t/a = -2$, and varies smoothly beyond that point. This function has been used to obtain the augmented responses discussed and displayed in this report.

2.3 SCATTERING BY A SPHERE

2.3.1 Theoretical Impulse Response of the Sphere

In this section the method of obtaining the theoretical response of the sphere which is used as a comparison standard for testing the effectiveness of the impulse response augmentation technique is presented. The classic solution to the problem of scattering by a perfectly conducting sphere with a plane electromagnetic wave incident is given by the Mie series.[9] In principle, this yields the solution at all frequencies; however, in practice it is convenient to use for numerical computations at the lower end of the frequency spectrum only. In order to extend the frequency range of the exact numerical results, the formulas derived by Senior and Goodrich[10] were used. These formulas were obtained by applying a Watson transform to the Mie series. This work not only provided a form of the far scattered field suitable for numerical computation at high frequencies, but also expressed the far scattered field as the sum of optics and creeping wave terms, which provided both insight and guidance into developing the impulse response augmentation technique. In this study the exact far field of the sphere was obtained by using the Mie series for a range of ka from 0 to 20 and the Senior-Goodrich expression for a ka greater than 20. In particular, for a sphere of radius a the far scattered magnetic field $r_o H^s(ka)$,

$$r_o H^s(ka) = \begin{cases} \text{Mie series} \; ; & 0 \le ka \le 20 \\ H_{CE}(ka) + H_{CM}(ka) + \left[\frac{a}{2} - \frac{0.25}{jk}\right] \exp(j2ka) \; ; & 20 \le ka \end{cases} \tag{15}$$

where

$$H_{CE}(ka) = + j\frac{\tau^4}{k} \exp(-j\pi ka + j\pi/6) \left\{ \frac{1}{\beta_1 A_1^2} \left[1 + \frac{1}{2}(1-j\sqrt{3}) \frac{8\beta_1}{15\tau^2} \left(1 + \frac{9}{32\beta_1^3} \right) \right. \right.$$

$$\left. \left. \cdot \exp\left[-\frac{1}{2}(\sqrt{3}+j)\beta_1 \tau\pi - \frac{1}{2}(\sqrt{3}-j) \frac{\beta_1^2 \pi}{60\tau} \left(1 - \frac{9}{\beta_1^3} \right) \right] \right\}$$

$$H_{CM}(ka) = - j\frac{\tau^4}{k} \exp(-j\pi ka + j\pi/6) \left\{ \frac{1}{A_2^2} \left[1 + \frac{1}{2}(1 - j\sqrt{3}) \frac{8\alpha_1}{15\tau^2} \right] \right.$$

$$\left. \cdot \exp\left[-\frac{1}{2}(\sqrt{3} + j)\alpha_1 \tau\pi - \frac{1}{2}(\sqrt{3}-j) \frac{\alpha_1^2 \pi}{60\tau} \right] \right\}$$

$$\beta_1 = 1.01879297$$
$$\alpha_1 = 2.33810741$$
$$A_1 = .53565666$$
$$A_2 = .70121082$$
$$\tau = \left(\frac{ka}{2}\right)^{1/3}$$

It should be noted that in Eq. (15) only the first order creeping wave terms in $H_{CE}(ka)$ and $H_{CM}(ka)$ have been retained and to this extent the expression is approximate. The third term in Eq. (15) is the optics term, which contains the impulse and negative step which occur at $t/a = -2$ in the impulse response. Contributions of $O(1/ka^3)$ in the optics term have not been retained.

Figure 5 displays the amplitude of theoretical frequency response computed with this procedure and Fig. 6 displays the theoretical radar cross section.

In theory, in order to obtain the impulse response, one just takes the inverse Fourier transform of $H(\omega)$. In practice, however, it is not possible to do this directly with an FFT due to the presence of singularities (impulse and step) in the impulse response. The transformation is accomplished by using the impulse response augmentation technique on the frequency response data. In particular, the contribution of the impulse and step are removed from the frequency response by subtracting the transform of the augmentation function $W_2(\omega)$ from the frequency response to obtain the augmented frequency response to obtain the augmented frequency response, $H_a(\omega)$; i.e.,

$$H_a(\omega) = H(\omega) - D(\omega) - W_2(\omega) \tag{16}$$

where

$$D(\omega) \leftrightarrow \frac{1}{2}\,\delta(t/a + 2)$$

$$W_2(\omega) \leftrightarrow w_2(t)$$

$$w_2(t) = \begin{cases} -\frac{1}{8}\left[1 + \cos\frac{\pi}{4}(t/a + 2)\right] ; & -2 \le t/a \le 2 \\ 0 ; & \text{elsewhere .} \end{cases}$$

The augmented impulse response, $h_a(t)$, is the transform of the augmented frequency response. The total impulse response is then found by adding the augmented impulse response to the augmentation function,

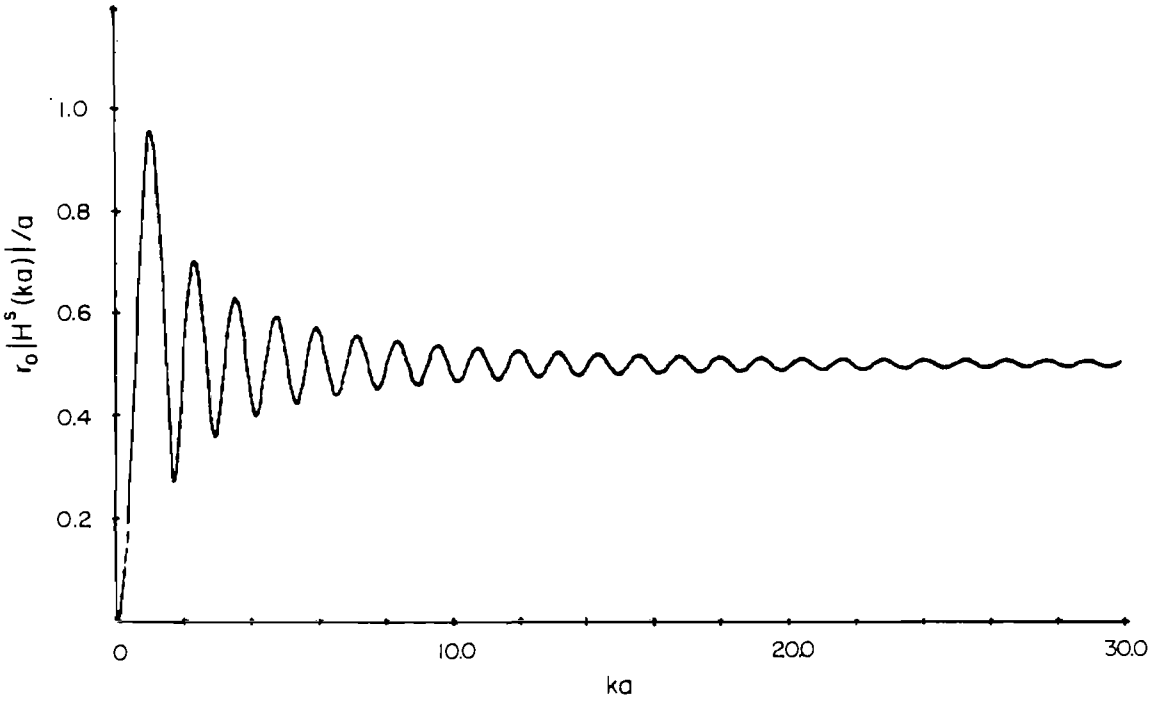

FIG. 5 Theoretical frequency response of sphere with radius a.

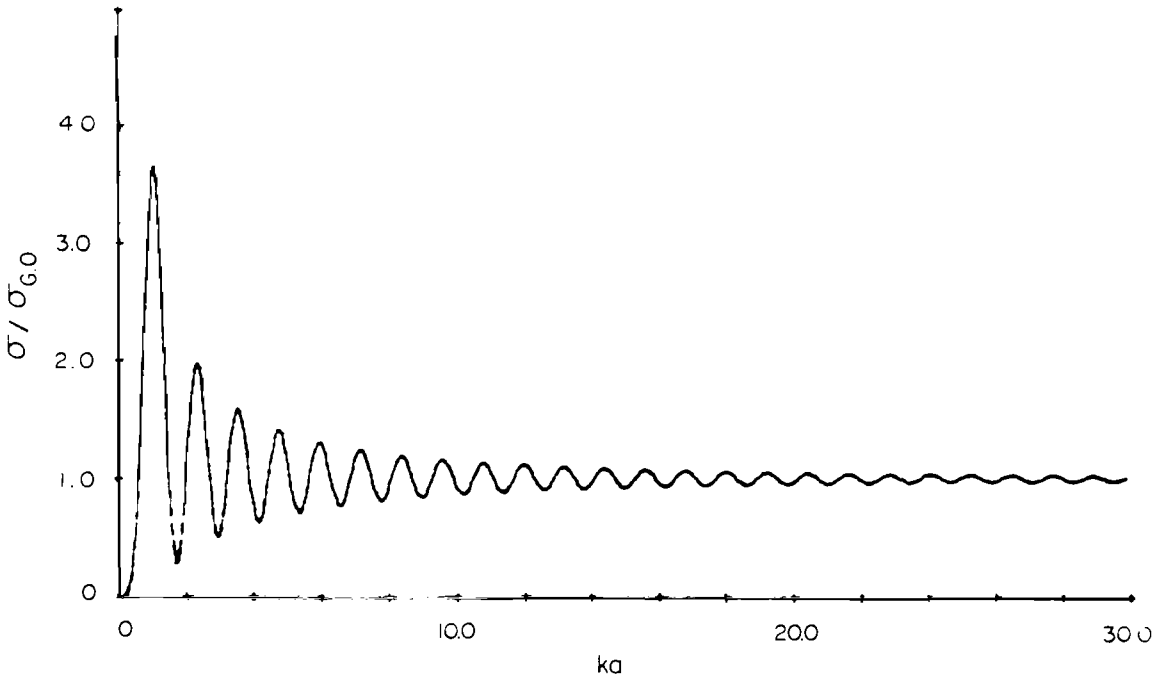

FIG. 6 Theoretical radar cross section of sphere with radius a.

$$h(t) = h_a(t) + \frac{1}{2}\,\delta(t/a + 2) + w_2(t)\ 1 \qquad (17)$$

This result, plotted in Fig. 7, shows the impulse and step at t/a = 2 due to the specular reflection or optics term. Subsequently, there is a second positive peak in the response at t/a = 3.20 due to the creeping wave.

2.3.2 Wiener-Lee Filter for High Frequency Estimate of Augmented Frequency Response

This technique is a variation on the impulse response augmentation technique described in Sec. 2.2. In this technique the theory of optimum linear filters is used to find the augmented impulse response instead of trying to fit the asymptotic behavior of the augmented frequency response.

Figure 2 shows the functional diagram of a linear system (in this case electromagnetic scattering by a target) that is characterized by its impulse response, h(t), or its system function, H(ω) The excitation e(t) of the linear system in this case is a regularized impulse

$$e(t) = \frac{n}{\sqrt{\pi}}\, e^{-(nt)^2} \qquad (18)$$

and produces the response r(t) which is the regularized impulse response of the system. The response is given by

$$r(t) = e(t) * h(t) \qquad (19)$$

where * represents convolution.

In the problem considered here, e(t) is specified analytically and r(t) is computed by solving the space-time integral equation. It is desired to find h(t) or H(ω).

Since r(t) is found through numerical calculations in solving the space-time integral equation, the actual data from which the impulse response must be calculated contains noise. That is, the smoothed impulse response $\hat{r}(t)$ that is actually computed may be represented by

$$\hat{r}(t) = r(t) + n(t)$$

where r(t) is the actual smoothed impulse response and n(t) is the noise or numerical error introduced by the computational process. Hence, the problem can be restated as a problem in recovering a distorted signal (the impulse response) from noise. One way this can be done is through the use of linear

filters.

Figure 8 shows a functional diagram of the identification system. The function $h_{opt}(t)$ is the impulse response of a linear filter whose output, $\hat{h}(t)$, is a least mean squares estimate of h(t): i.e., $h_{opt}(t)$ minimizes the functional

$$\int_{-\infty}^{\infty} |h(t) - \hat{h}(t)|^2 \, dt \, . \tag{20}$$

Note that in the diagram the incident pulse, e(t), is treated as the impulse response of a linear system and that the impulse response of the scatterer, h(t) , is treated as a signal. This is a valid representation, since the convolution operation is symmetric in its operands.

The optimum filter for the system in Fig. 8 has been found[13] to be

$$H_{opt}(\omega) = \frac{1}{E(\omega)} \frac{1}{1 + \dfrac{\varphi_{nn}(\omega)}{|H(\omega)|^2 |E(\omega)|^2}} \tag{21}$$

where

$H_{opt}(\omega)$ is the transform of $h_{opt}(t)$

$E(\omega)$ is the transform of e(t)

$H(\omega)$ is the transform of h(t)

$\varphi_{nn}(\omega)$ is the power density spectrum of n(t)

The estimate of the system function will then be

$$\hat{H}(\omega) = \frac{\hat{R}(\omega)}{E(\omega)} \frac{1}{1 + \dfrac{\varphi_{nn}(\omega)}{|H(\omega)|^2 |E(\omega)|^2}} \tag{22}$$

where $\hat{R}(\omega)$ is the transform of $\hat{r}(t)$.

Note that in the presence of no noise [$\varphi_{nn}(\omega) = 0$], the estimate $\hat{H}(\omega)$ is simply the ratio of the output spectrum to the input spectrum, and in the presence of noise the ratio is weighted by a function of the signal-to-noise ratio.

In order to understand one inadequacy of this method, let us substitute the spectrum of e(t) into Eq. (22), which yields

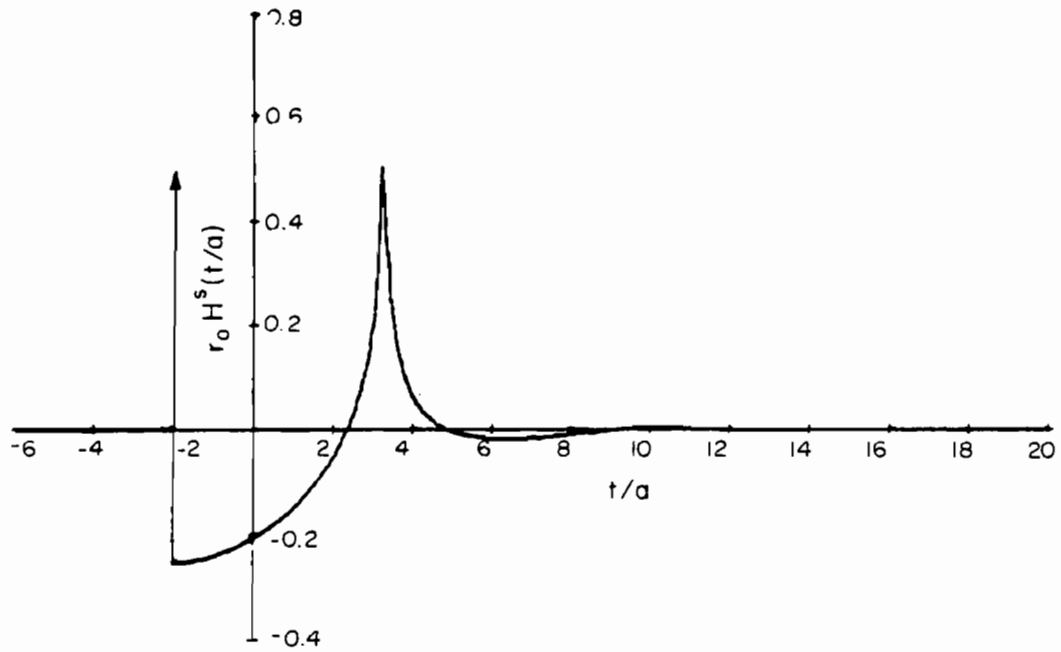

FIG. 7 Theoretical impulse response of sphere with radius a.

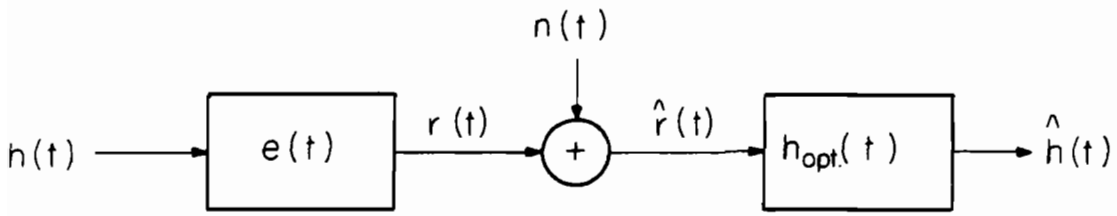

FIG. 8 Optimum identification system.

$$\hat{H}(\omega) = \left[H(\omega) + e^{(\frac{\omega}{2n})^2} N(\omega)\right] \frac{1}{1 + e^{2(\frac{\omega}{2n})^2} \frac{\varphi_{nn}(\omega)}{|H(\omega)|^2}} \tag{23}$$

where $N(\omega)$ is the transform of $n(t)$. For typical spectra the estimate $\hat{H}(\omega)$ indicated by Eq. (23) will fall off exponentially to zero at high frequencies. This will yield a very poor estimate of the system function at high frequencies, since in most cases the magnitude of the system function approaches a finite constant.

In order to improve the estimate of the system function, the technique is used to estimate the spectrum of the augmented impulse response, which does approach zero at high frequencies. In this case the spectrum of the augmented impulse response becomes

$$\hat{H}_a(\omega) = \frac{\hat{R}_a(\omega)}{E(\omega)} \frac{1}{1 + \frac{\varphi_{nn}(\omega)}{|H_a(\omega)|^2 |E(\omega)|^2}} \tag{24}$$

where

$\hat{H}_a(\omega)$ is spectrum of the estimate of the augmented impulse response

$\hat{R}_a(\omega)$ is the spectrum of the noisy smoothed augmented impulse response.

This technique has been applied to the scattering from a sphere with radius a. Equation (24) requires an estimate of the noise power density present in the smoothed augmented impulse response and an estimate of the magnitude of the augmented impulse response spectrum. No estimate of the phase is required.

The estimate of $|H_a(\omega)|$ used was

$$|H_a(\omega)| = \begin{cases} \dfrac{\hat{R}_a(\omega)}{E(\omega)} ; & \omega \leq \omega_c \\ \dfrac{H_a(\omega_c)(\omega_c)}{\omega} ; & \omega > \omega_c \end{cases} \tag{25}$$

where $\omega_c = 3.43/a$.

The noise waveform was estimated by taking the difference between the theoretical smoothed impulse response as obtained from the Mie series[9] and the one obtained from the space-time integral equation. Figure 9 displays the smoothed impulse response of the sphere obtained with the space-time integral equation using a rather large space-time mesh sample size. Also displayed in Fig. 9 is the difference between this result and the theoretical smoothed impulse response. This difference may be considered to be the noise n(t) that corrupts the true smoothed impulse response. Figure 10 shows the Fourier transform of the noise waveform, and it should be noted that the noise doesn't go to zero with increasing frequency. Based on Fig. 10, three different estimates of the noise power density spectrum $\varphi_{nn}(\omega)$ were made.

The first estimate of $\varphi_{nn}(\omega)$ was

$$\varphi_{nn}(\omega) = \left[K\omega e^{\left(\frac{\omega}{2n}\right)^2}\right]^2 \tag{26}$$

where $k = 5 \times 10^{-3}$ and $n = 2$.

This estimate was an attempt to have an approximate fit to the envelope of the noise spectrum, which was simply related to the spectrum of the input pulse. This estimate proved to be inadequate because the actual noise spectrum did not approach zero at high frequencies as the estimate assumed.

The second estimate of the noise spectrum was an attempt to correct for the defect in the first estimate and was of the form

$$\varphi_{nn}(\omega) = \left[K\omega e^{-\left(\frac{\omega}{2n}\right)^2} + A\right]^2 \tag{27}$$

where $A = .2 \times 10^{-3}$.

The third estimate of noise spectrum was an attempt to determine the best that could be done when the noise spectrum was known exactly. In this case $\varphi_{nn}(\omega)$ is given by

$$\varphi_{nn}(\omega) = |N(\omega)|^2 \tag{28}$$

where $N(\omega)$ is the transform of the noise waveform.

Figure 11 displays the estimate of the frequency response $\hat{H}(\omega)$ that was obtained using the second and third estimates of the noise spectrum along with the theoretical frequency response. The result of the second estimate indicate that the noise response was not filtered enough. The result of the third estimate, which may be considered as the best result that could be obtained with this approach, is still far inferior to results which will be presented in a later section.

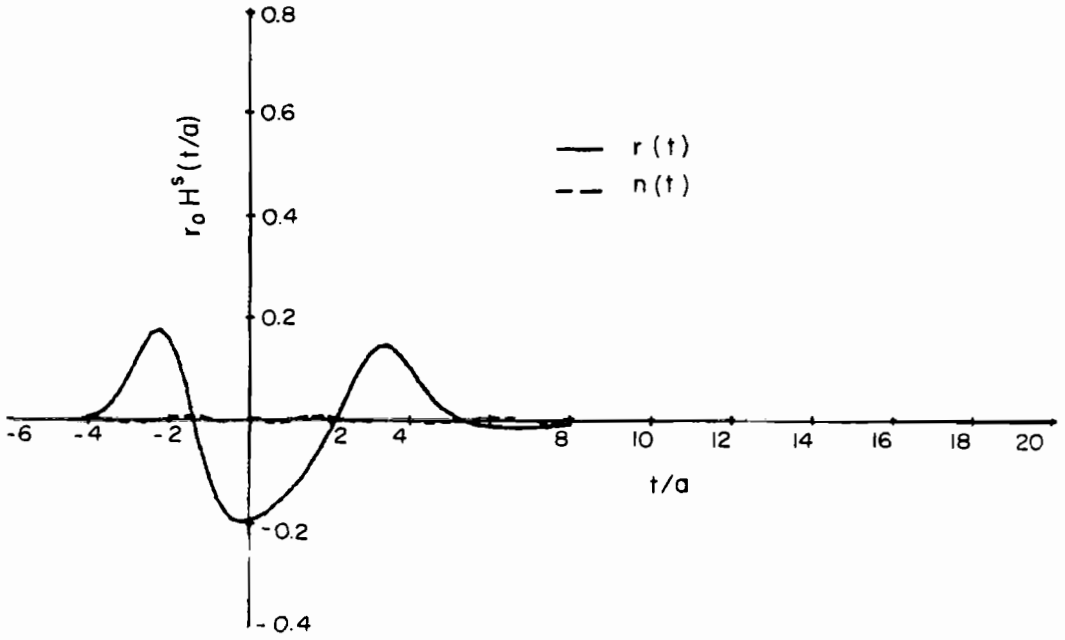

FIG. 9 Smoothed impulse response of sphere with radius a.

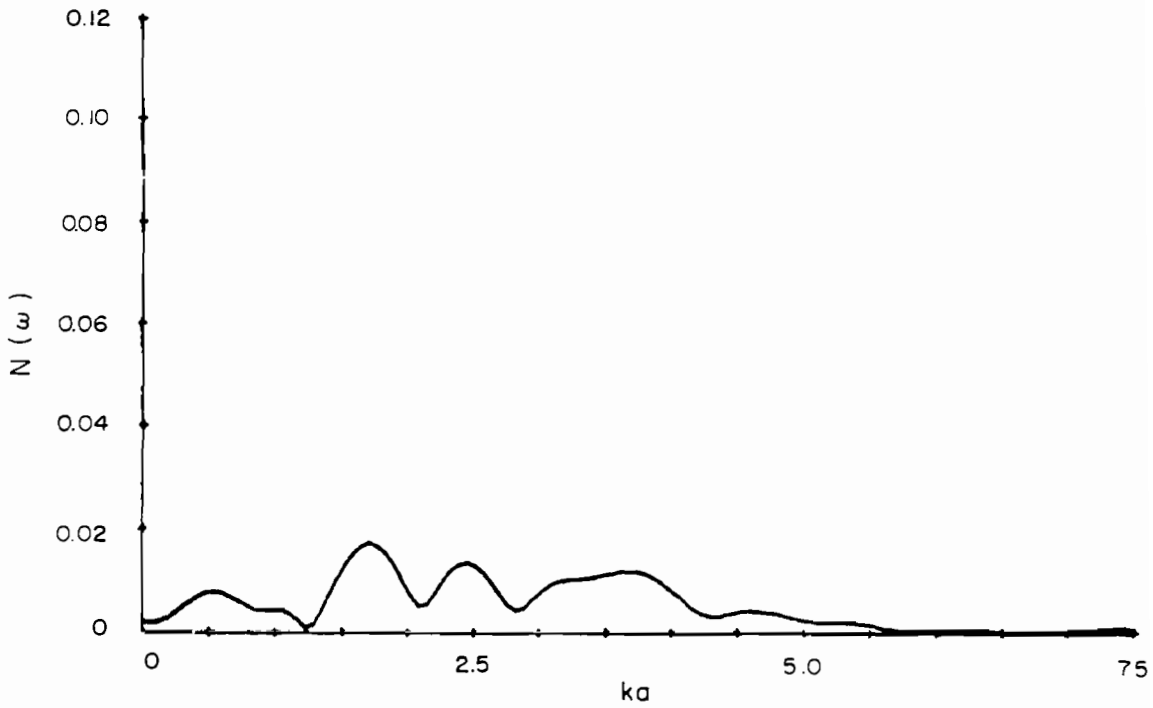

FIG. 10 Fourier transform of noise waveform.

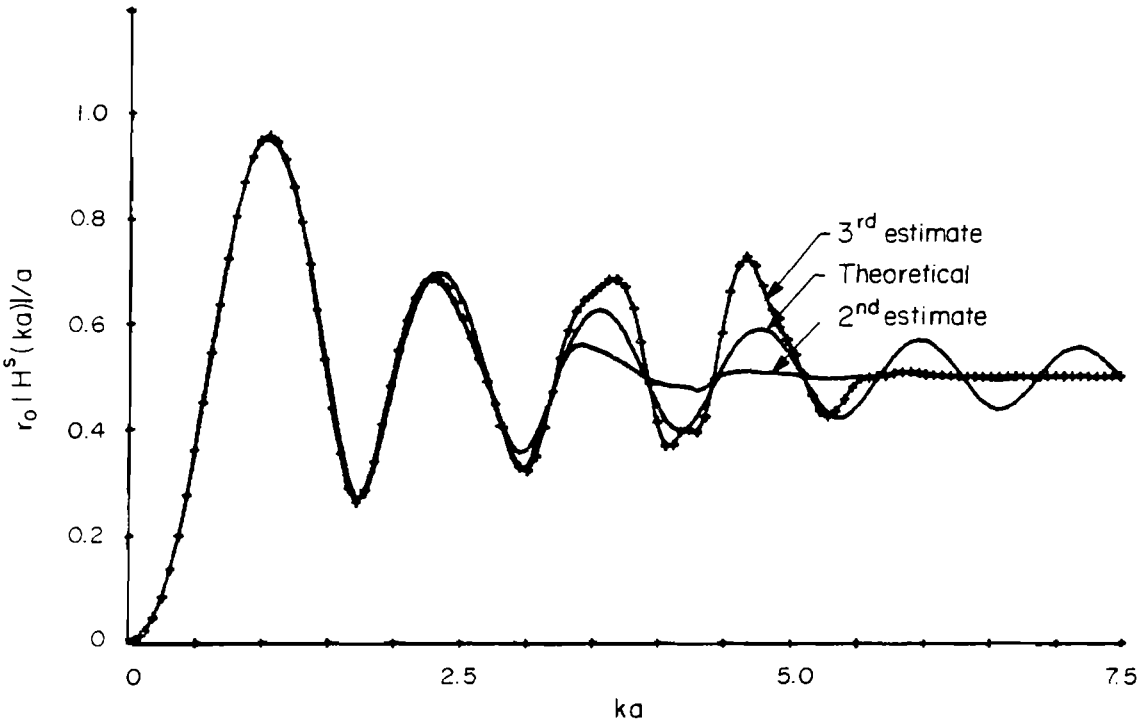

FIG. 11 Frequency response of sphere with radius a estimated using a Wiener-Lee filter.

Figure 12 displays the estimate of the impulse response, $\hat{h}(t)$, that this approach yields for the second two noise estimates. Note that both waveforms possess a substantial precursor and thus violate the causality requirement. Moreover, both waveforms possess a ripple structure which is also in error. As a result of this study, it is clear that the best results which can be hoped for using Wiener-Lee filtering are not adequate.

2.3.3 Inverse Power Law for High Frequency Estimate of Augmented Frequency Response

For this case, a sphere of radius a centered at the origin was illuminated with the incident wave traveling in the negative z direction and given by

$$e(z,t) = \frac{n}{\sqrt{\pi}} e^{-(na)^2(t/a + z/a)^2} \tag{29}$$

where na = 1.

The incident pulse is obtained by setting z equal to zero. This yields an incident pulse width of two sphere diameters, as shown in Fig. 13.

The smoothed impulse response that results from solution of this problem with the space-time integral equation is displayed in Fig. 14. In this figure the normalized far scattered magnetic field intensity $r_0 H^s(t/a)$ is plotted as a function of the normalized far field time t/a, as described in Sec. 8.1. The far field time is given by

$$t = t_s - r$$

where

r = the distance of the far field observer from the origin.

t_s = the surface current time.

The frequency response may be obtained by dividing the transform of the smoothed impulse response by the transform of the incident pulse, i.e.,

$$H(\omega) = \frac{R(\omega)}{E(\omega)}$$

where

$$E(\omega) = e^{-\left(\frac{ka}{2n}\right)^2}$$

and the result is displayed in Fig. 15 along with the theoretical sphere response. There is good agreement up to a ka of approximately 3 or up to a frequency at which the width of the incident pulse is two wavelengths. This is also the point at which $E(\omega)$ is approximately 10% of its maximum value,

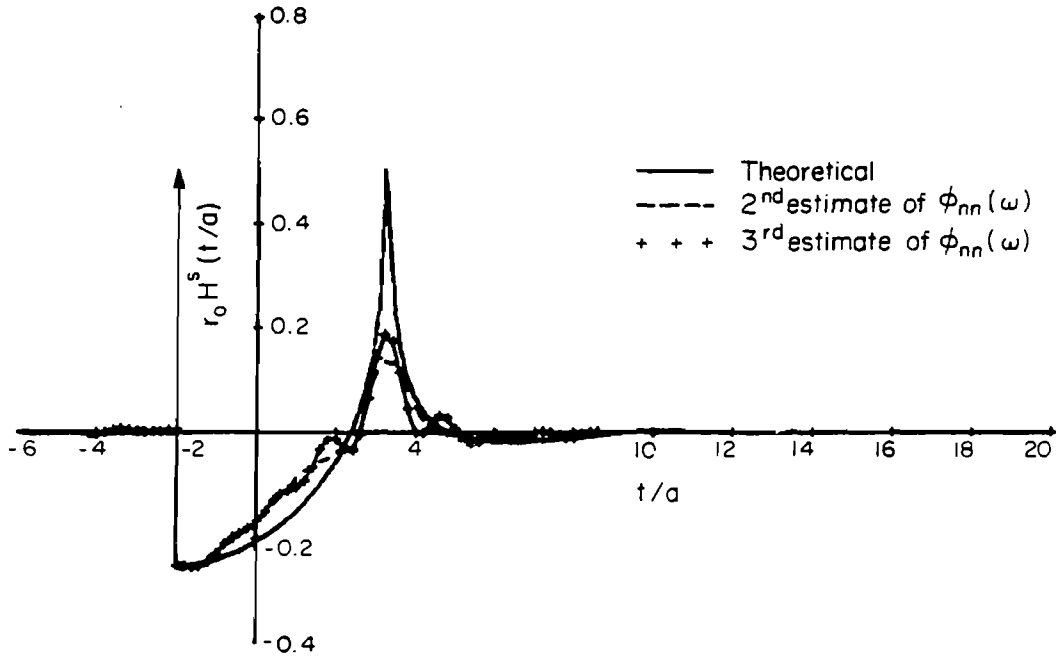

FIG. 12 Impulse response of sphere estimated using Wiener-Lee filter.

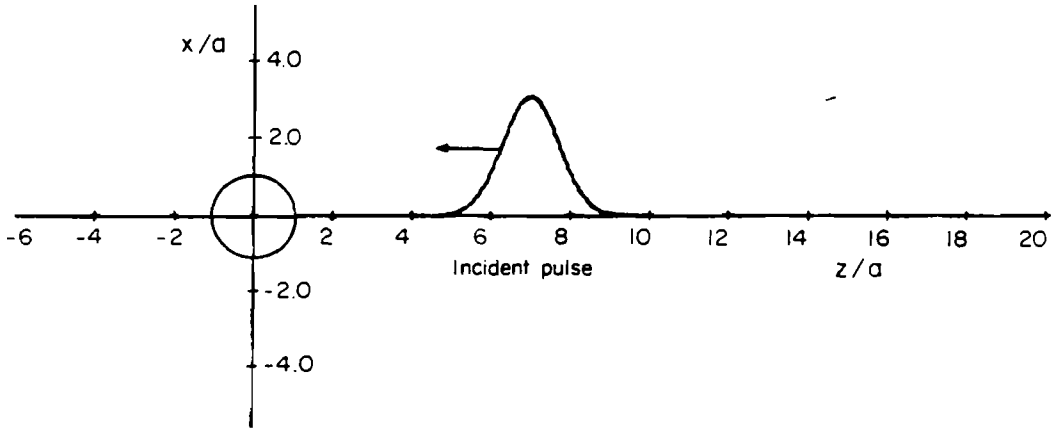

FIG. 13 Incident pulse and sphere with radius a.

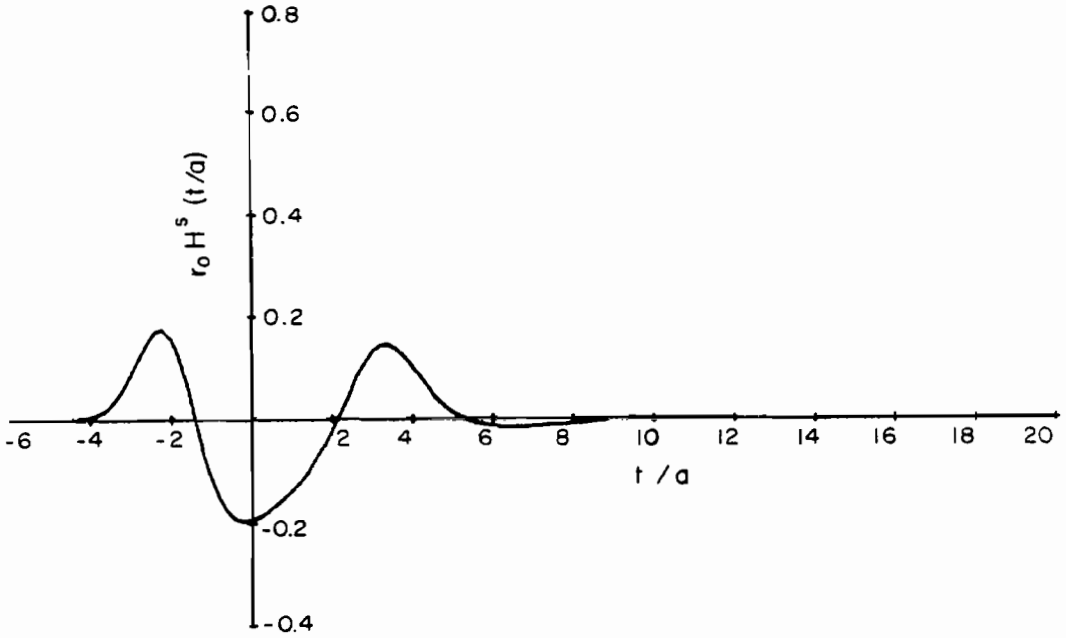

FIG. 14 Smoothed impulse response of sphere with radius a.

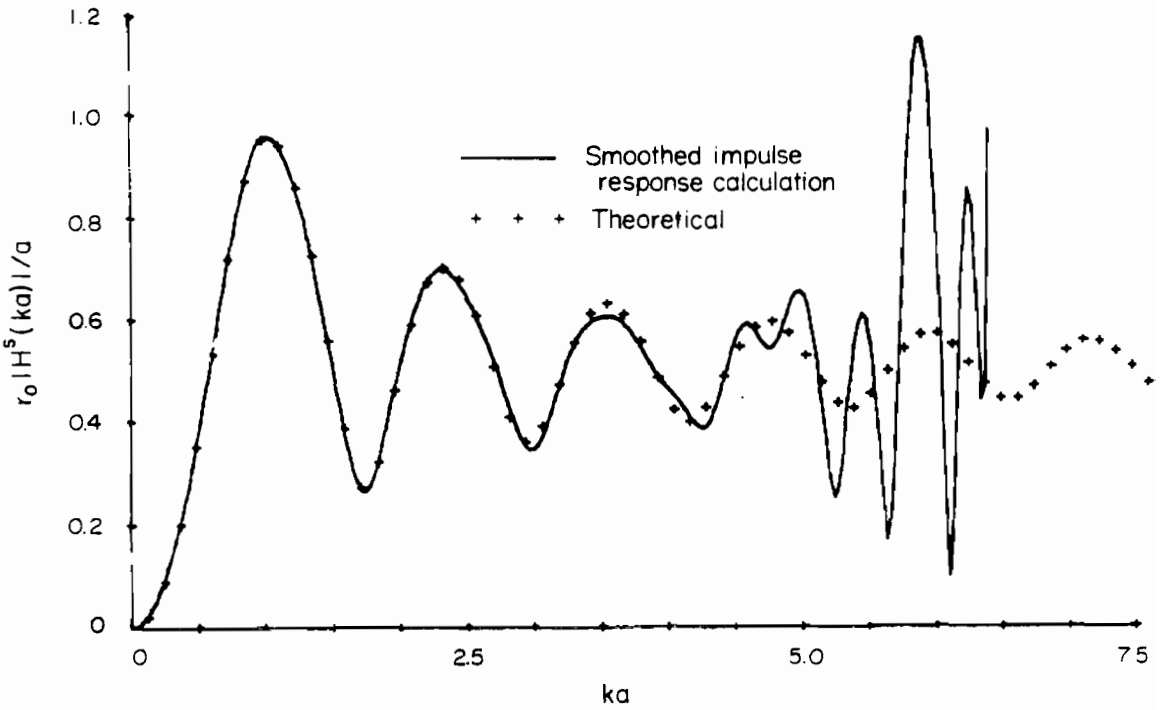

FIG. 15 Frequency response of sphere with radius a.

and beyond this point in frequency there are negligible components in the interrogating signal and thus negligible components in the smoothed impulse response.

The augmented frequency response is obtained by subtracting the transform of the augmentation function from the frequency response. As noted earlier in Sec. 2.2.2, the most appropriate augmentation function to use contains only the singularity functions which are known exactly. For the case of a sphere of radius a this is given by

$$f_a(t) = \frac{1}{2}\,\delta(t/a + 2) + \frac{1}{4}\,u\,(t/a + 2)\ . \tag{30}$$

This augmentation function is infinitely smooth for $t/a > -2$ and upon transformation yields linear phase. Both of these features simplify the high frequency estimation procedure for the augmented frequency response, since now the augmentation function introduces no new discontinuities in any derivatives and introduces no nonlinear phase terms. The augmented frequency response is given by

$$H_a'(\omega) = \frac{R(\omega)}{E(\omega)} - F_a(\omega) \tag{31}$$

where $R(\omega) \leftrightarrow r(t)$

$E(\omega) \leftrightarrow e(t)$

$F_a(\omega) \leftrightarrow f_a(t)$

$$F_a(\omega) = \left(\frac{a}{2} - \frac{1}{4}\,\frac{1}{j\omega}\right)e^{j\omega(2a)} \tag{32}$$

The magnitude is displayed in Fig. 16(a) and the phase is displayed in Fig. 16(b). The effect of computation noise is clearly evident as the exponential increase of the augmented frequency response magnitude above a ka of approximately 5. The next step is to replace the exponential increase by a suitable estimate of the high frequency behavior of the augmented frequency response.

In estimating the high frequency behavior of the augmented frequency response, both the amplitude and phase must be considered. It should be noted here that since the augmented impulse response is causal, then care must be taken so that the estimate of phase and amplitude is consistent with the causality requirement. A more detailed discussion of the causality condition is presented in Sec. 8.2. Both the theoretical augmented frequency response of the sphere and the computed augmented frequency responses at lower frequencies indicate a linear phase variation. Hence, in this work a linear phase variation of the augmented frequency response is assumed at high frequencies. This estimate is of the form

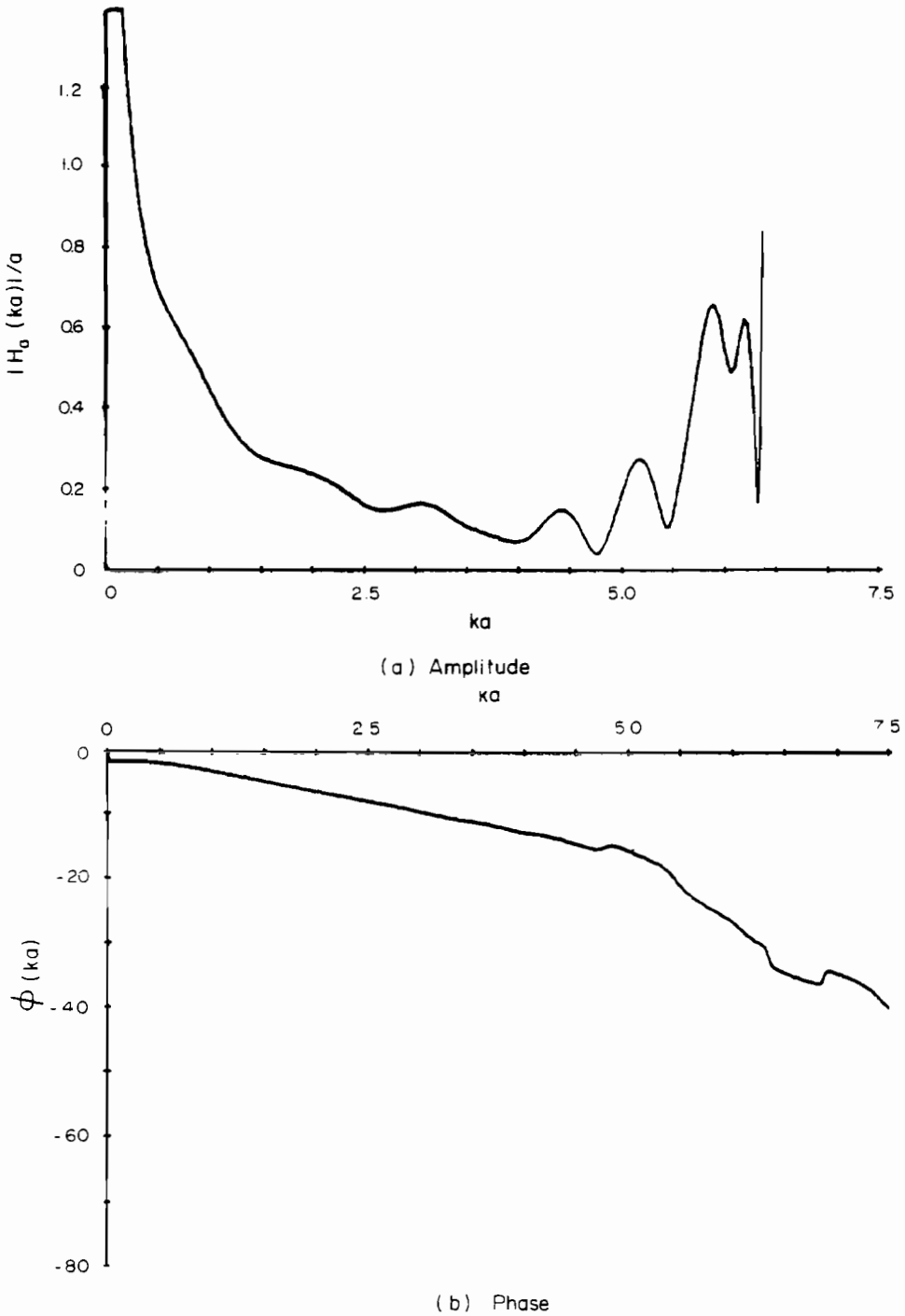

FIG. 16 Augmented frequency response of sphere with radius a computed from smoothed impulse response data.

$$\varphi(\omega) = m\omega + b \qquad \omega > \omega_c \tag{33}$$

where m is chosen such that the phase is continuous at the fit point, ω_c, and b is zero. A discontinuous phase response may yield ripples in the time domain together with a noncausal time response. The parameter m yields the point in time where the high frequency portion of the augmented impulse response occurs. The parameter b controls the symmetry of the response about this time point. A symmetric response is obtained for b = 0 and an anti-symmetric response is obtained for b = $\pi/2$. It was found that the theoretical sphere response yielded a value for b of nearly zero. In addition, the high frequency portion of the augmented frequency response corresponds to the creeping wave contribution, which has a nearly symmetric appearance in the time domain. For these reasons the parameter b was taken to be zero in this work.

The estimate of the amplitude of the response is more difficult. The frequency response cannot be simply set to zero above a certain frequency because this will cause ripples in the time response due to truncation error and yield a noncausal time response. It is necessary to use an estimate which approaches zero asymptotically as ω approaches infinity. To get an idea of what to use as an estimate, consider the bounds on the high frequency portion of the augmented frequency response.

The augmented impulse response contains one region of fast variation which is due to the creeping wave. It seems to be a reasonable assumption that the augmented impulse response is absolutely continuous (continuous functions of interest are also absolutely continuous) and of finite duration. With these two conditions satisfied, the theory of Fourier analysis indicates the augmented frequency response will be bounded by a function of the form

$$B(\omega) = \frac{\delta}{\omega} \tag{34}$$

where δ is an arbitrarily small positive constant. This bound suggests using an estimate of the form

$$F(\omega) = \frac{A}{\omega^{1+\epsilon}} \tag{35}$$

where ϵ is an arbitrarily non-negative constant.

If it is also assumed that the first derivative of the augmented impulse response is absolutely continuous (i.e., the slope of $h_a(t)$ is absolutely continuous), then the appropriate bound is of the form

$$B(\omega) = \frac{\delta}{\omega^2} \tag{36}$$

where δ is an arbitrarily small positive constant.

The resulting estimate should be of the form

$$F(\omega) = \frac{H}{\omega^{2+\epsilon}} \tag{37}$$

where $\epsilon \geq 0$.

In summary, the estimate of the augmented frequency response, $\hat{H}_a(\omega)$, is given by

$$\hat{H}_a(\omega) = \begin{cases} H_a'(\omega) & ; \quad \omega < \omega_c \\ F(\omega)\, e^{j\varphi(\omega)} & ; \quad \omega > \omega_c \end{cases} \tag{38}$$

where ω_c is the boundary point
$F(\omega_c)\, e^{j\varphi(\omega_c)} = H_a'(\omega_c)$.

For the case of the sphere, the inverse power law for high frequency estimates of the augmented frequency response of the form

$$F_1(\omega) = A/\omega$$

and

$$F_2(\omega) = \frac{B}{\omega^2}$$

was examined. Figure 17(a) displays the magnitude of the augmented frequency response with both estimates of the high frequency variation. The estimate of the high frequency phase variation is displayed in Fig. 17(b). For these estimates the following parameters were used:

$\omega_c = 1.4726$
$m = -3.21984$
$b = 0.0$
$A = 0.41692$
$B = 0.61395$.

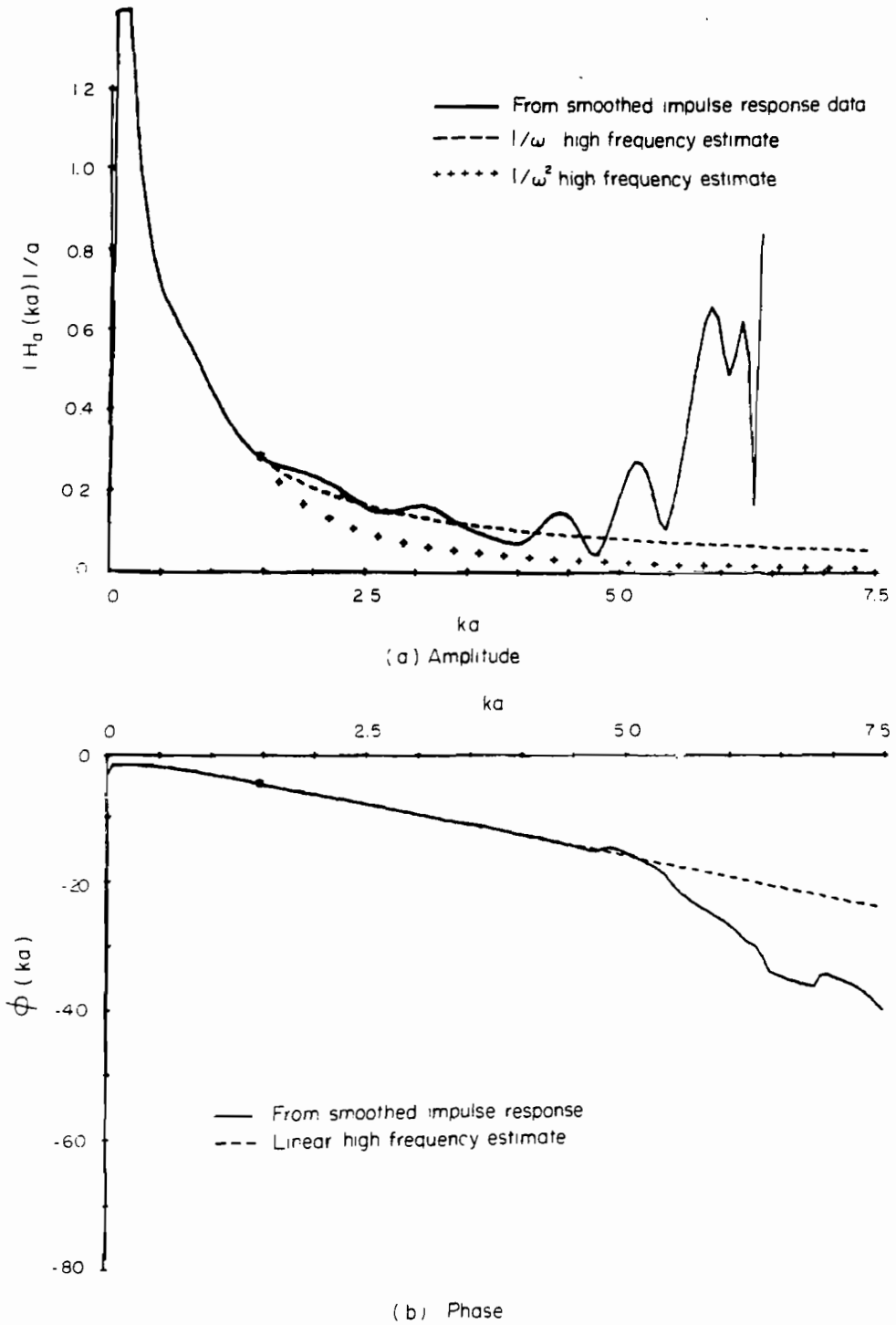

FIG. 17 Augmented frequency response of sphere with radius a.

Note that the boundary point ω_c was chosen to be substantially below the value at which the effect of noise becomes clearly evident in the augmented frequency response.

The impulse response that was obtained with these inverse power law estimates is displayed in Fig. 18 for the A/ω variation and in Fig. 19 for the B/ω^2 variation. Note that both results agree well with the theoretical sphere response in all regions except in the neighborhood of the creeping wave return at $t/a = 3.2$. The $1/\omega$ estimate yields a better result than the $1/\omega^2$ estimate when compared to the theoretical sphere results.

The frequency response for the $1/\omega$ estimate is shown in Fig. 20 and for the $1/\omega^2$ estimate is shown in Fig. 21. Note that the $1/\omega$ estimate yields a response that damps out less rapidly than the theoretical result, whereas the $1/\omega^2$ estimate yields a response that damps out more rapidly than the theoretical result. At this point it would seem logical to examine an estimate of the form A/ω^α, where $1 < \alpha < 2$. Carrying this logic forward, the exact augmented sphere response was plotted on log-log paper in order to obtain the appropriate value of α. Figure 22 displays this result, and it is clear that the high frequency portion of the augmented frequency response does not obey an inverse power law. However, the $1/\omega$ estimate does appear to provide an upper bound.

2.3.4 Exponential High Frequency Estimate of Augmented Frequency Response

In the previous section it was found that neither a $1/\omega$ nor a $1/\omega^2$ estimate of the high frequency variation of the augmented frequency response was adequate, although the $1/\omega$ estimate did appear to provide an upper bound. Moreover, on examination of the exact augmented frequency response the exponential nature of its variation became apparent. The Senior-Goodrich expression[10] for the far scattered magnetic field of a sphere given in Eq. (15) for large ka is repeated here for convenience:

$$r_o H^s(ka) = H_{CE}(ka) + H_{CM}(ka) + \left[\left(\frac{a}{2} - \frac{0.25}{jk}\right) \exp(j2ka)\right] \qquad (39)$$

where $H_{CE}(ka)$ and $H_{CM}(ka)$ are given in Eq. (15).

This expression is valid for high frequencies and was used to obtain the theoretical sphere response for $ka > 20$. The total response in Eq. (39) is divided into two parts. The second part in the square brackets represents the impulse and step contribution to the impulse response of the sphere and is simply the augmentation function now being used in this work. Thus, the augmented far scattered field is given by

$$r_o H_a^s(ka) = H_{CE}(ka) + H_{CM}(ka) \ . \qquad (40)$$

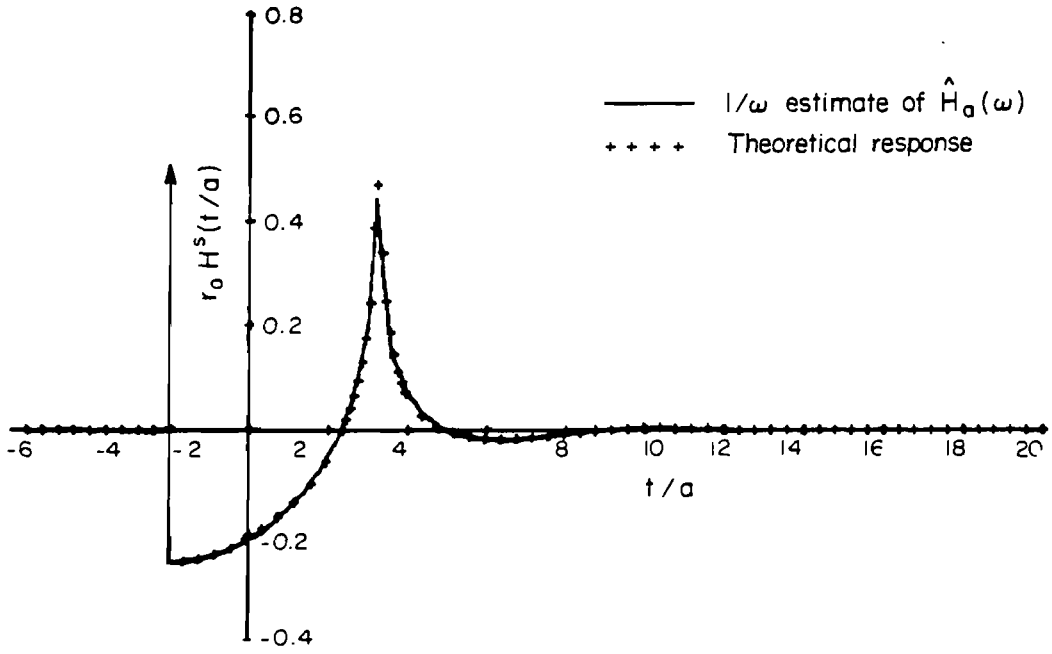

FIG. 18 Impulse response of sphere with radius a using $1/\omega$ high frequency estimate for the augmented frequency response.

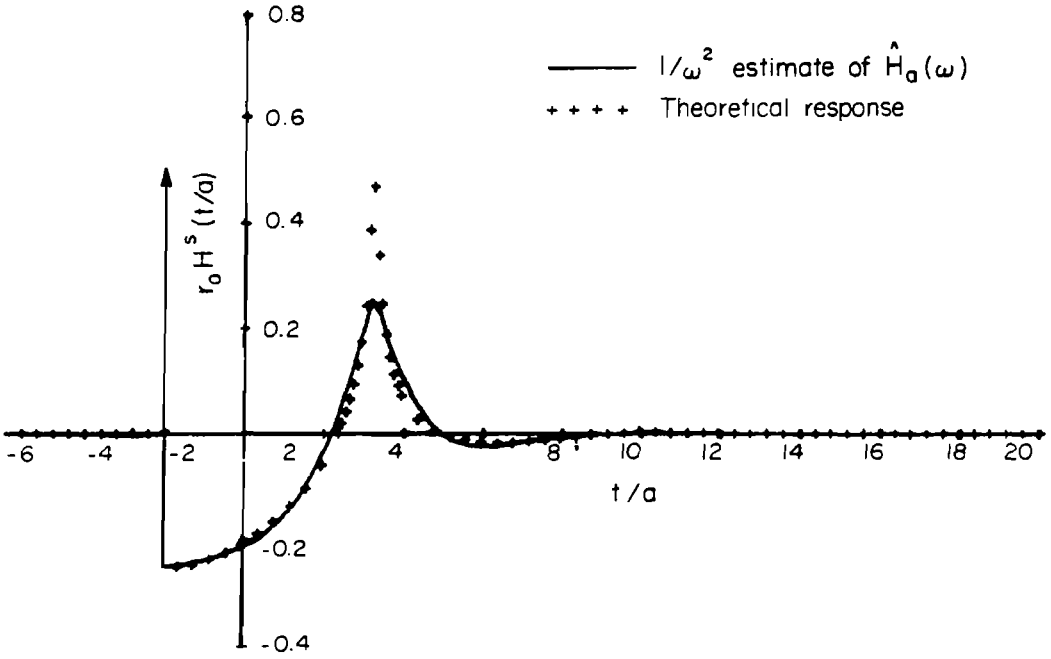

FIG. 19 Impulse response of sphere with radius a using $1/\omega^2$ high frequency estimate for the augmented frequency response.

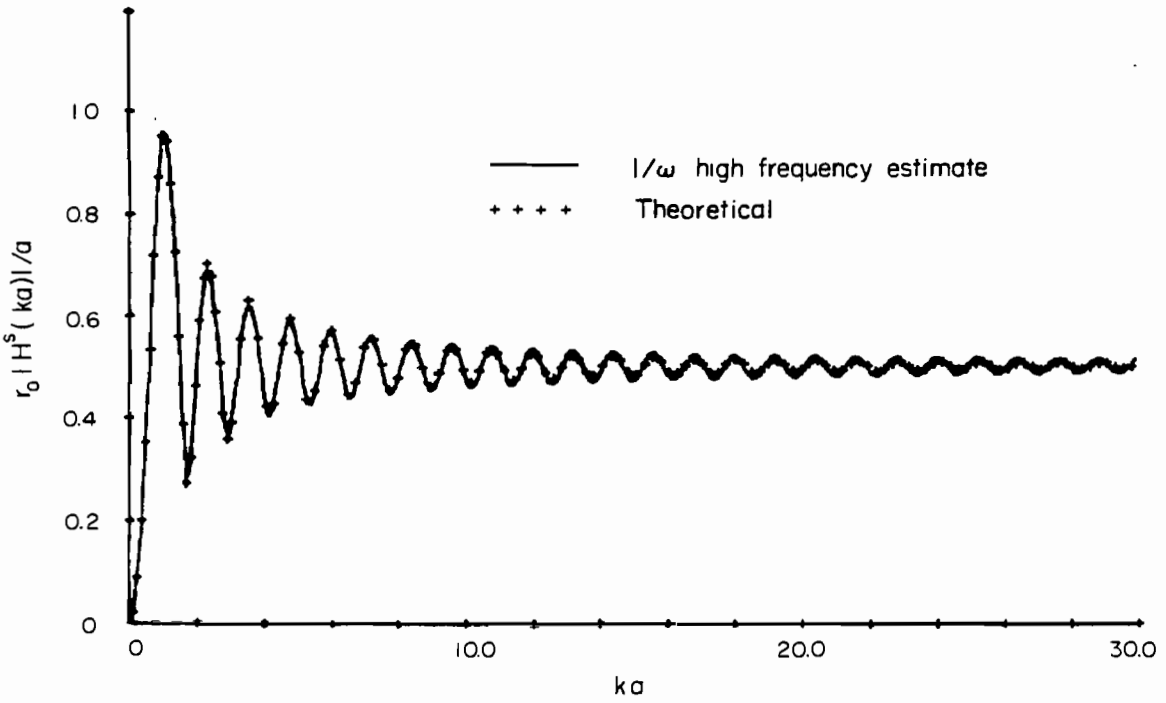

FIG. 20 Frequency response of sphere with radius a for $1/\omega$ high frequency estimate of augmented frequency response.

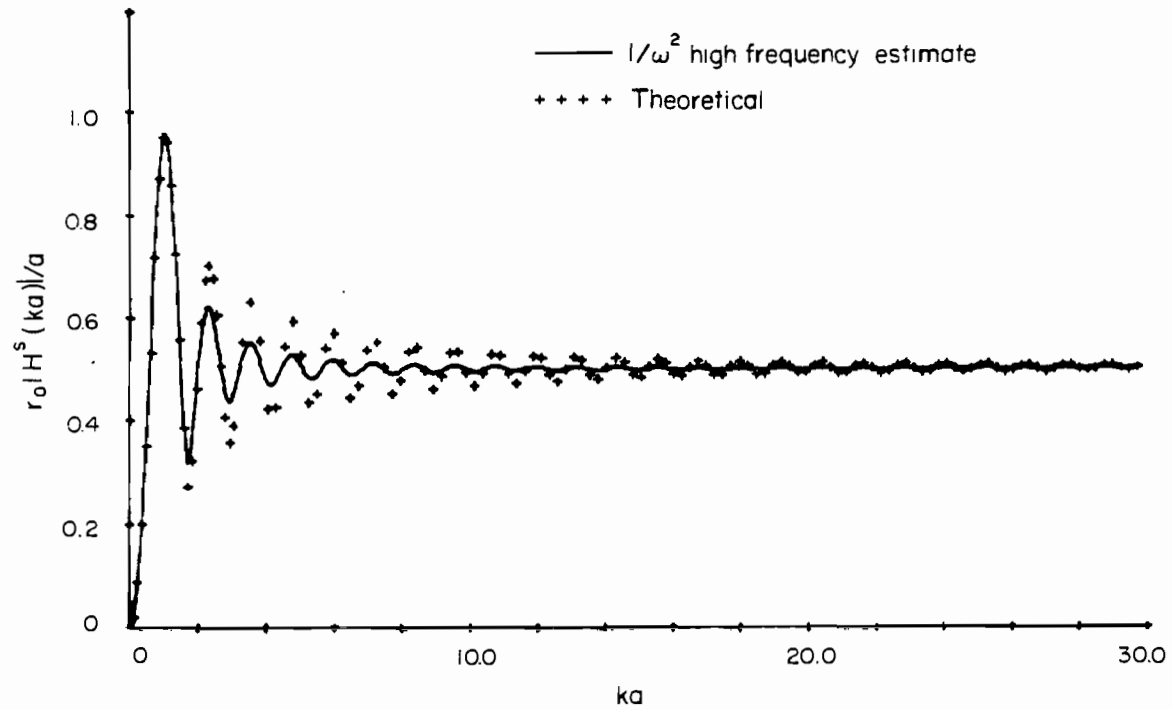

FIG. 21 Frequency response of sphere with radius a for $1/\omega^2$ estimate of augmented frequency response.

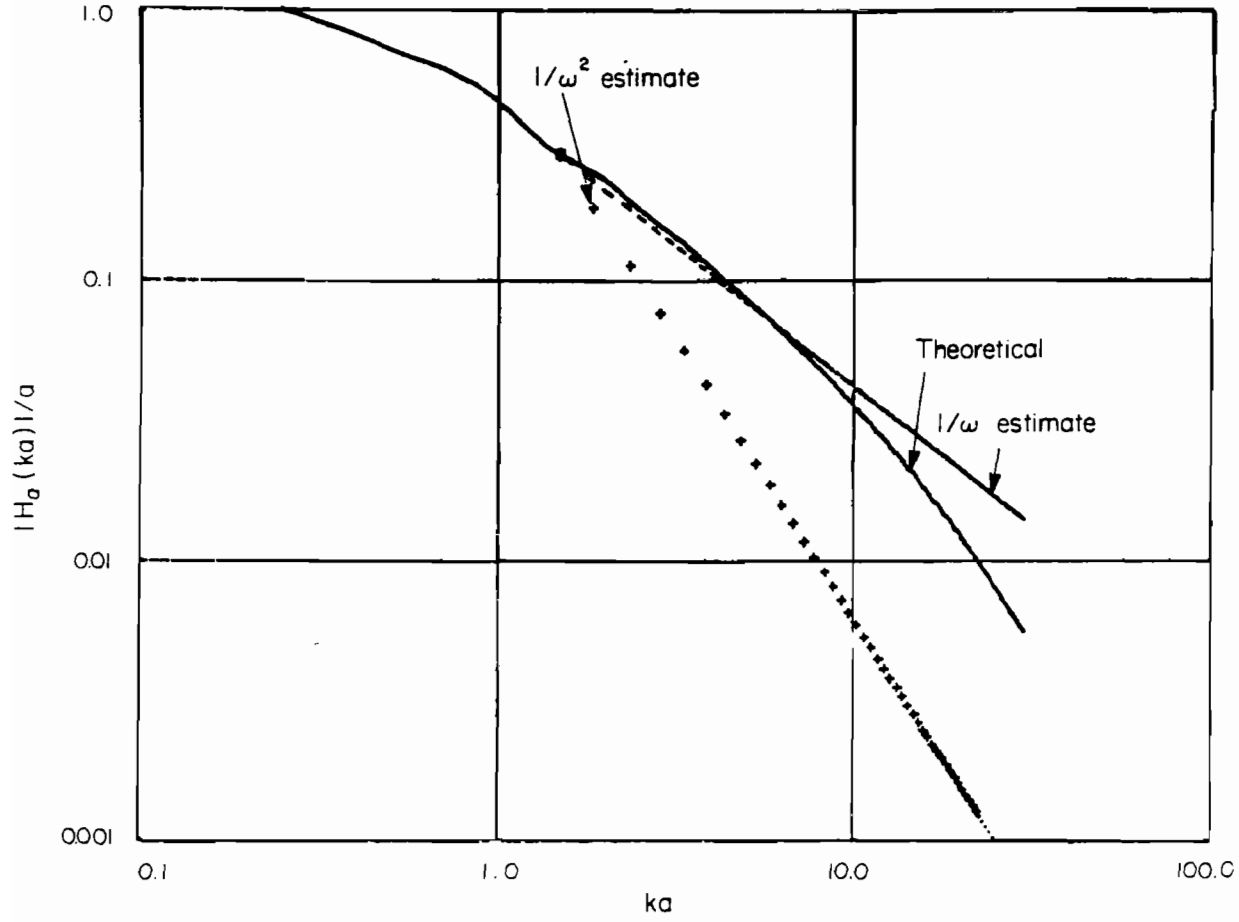

FIG. 22 Amplitude of augmented frequency response on log-log plot.

These two terms are the creeping wave response. The high frequency asymptote of the creeping wave response obtained from Eq. (15) is of the form

$$r_o H_c^s(ka) = A(ka)^{1/3} \exp\left[-B(ka)^{1/3}\right] \exp\left[-j(mka + b)\right] \tag{41}$$

where A, B, m and b are constants. Moreover, on plotting the natural log of the amplitude of the theoretical creeping wave response given in Eq. (40) against the cube root of ka, a curve well represented by a straight line was obtained. This suggests a simpler representation for the high frequency estimate of the augmented frequency response is of the form

$$\hat{H}_a(\omega) = A \exp\left[-B(\omega)^{1/3}\right] \exp\left[-j(m\omega + b)\right] \tag{42}$$

where the linear system parameter ω has been substituted for ka. The constants A and B are obtained from the low frequency portion of the augmented frequency response using two fit points, ω_1 and ω_2, where $\omega_1 = \omega_c$. The phase is likewise obtained from the low frequency portion, where m is chosen such that the phase is continuous at ω_c and b is set to zero. Applying this procedure to the theoretical augmented frequency response yields

$$\begin{aligned} \omega_c = \omega_1 &= 1.4726 \\ \omega_2 &= 2.8839 \\ m &= -3.21984 \\ b &= 0.0 \\ A &= 2.85224 \\ B &= 2.03041 \end{aligned}$$

This high frequency estimate is compared with the theoretical result for the case of a sphere in Fig. 23. The good agreement for both the amplitude and the phase displayed in Fig. 23 demonstrates the validity of the high frequency estimate given in Eq. (47). Moreover, since this estimate of the augmented frequency response is directly attributable to the creeping wave, the form of this estimate should remain the same for the creeping wave response of any smooth convex body.

The augmented frequency response for a sphere with radius a which was obtained via solution of the space time integral equation is displayed in Fig. 16. Applying the high frequency estimate of Eq. (42) to this response yields

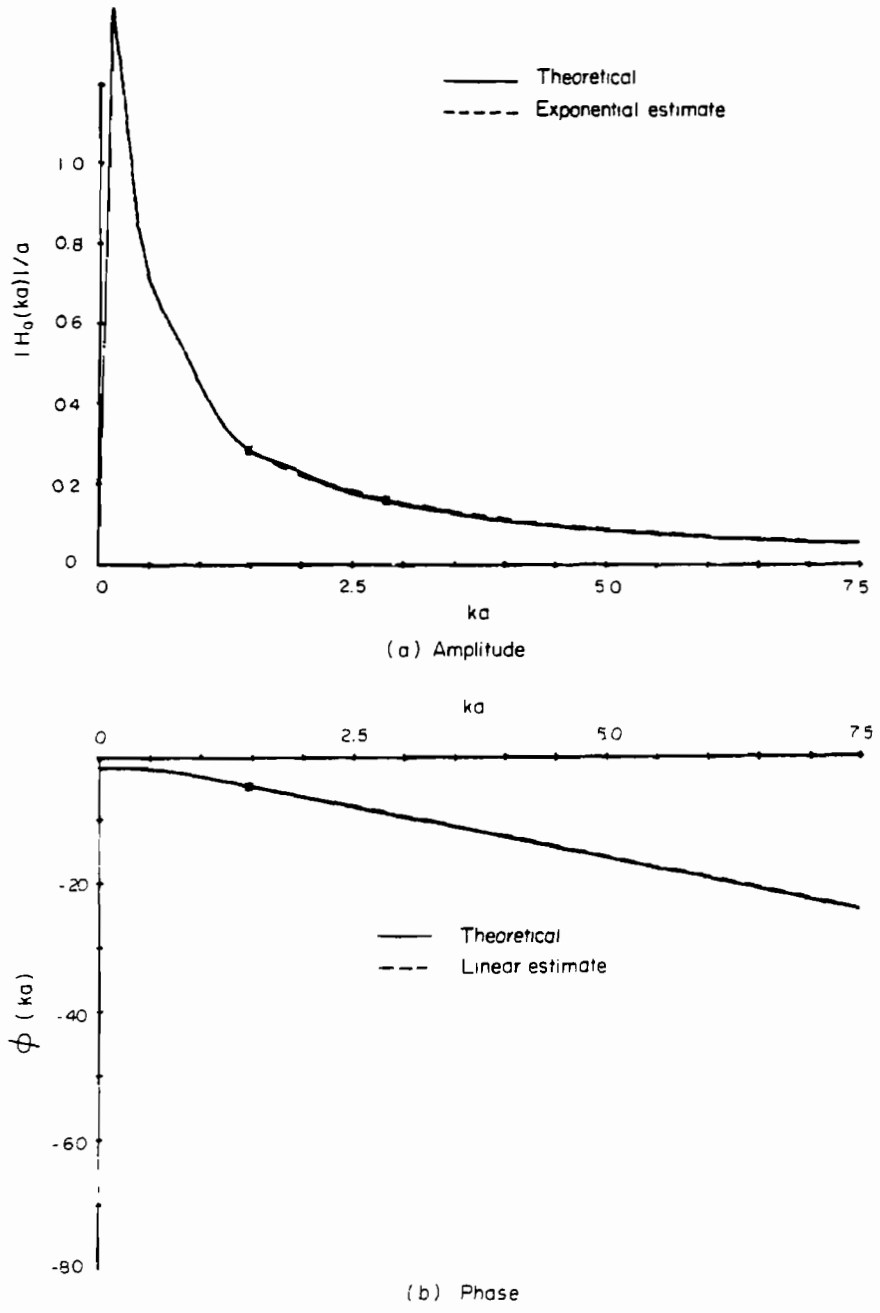

FIG. 23 Theoretical augmented frequency response of sphere with radius a.

$$\omega_c = \omega_1 = 1.4726$$
$$\omega_2 = 2.8839$$
$$m = -3.22914$$
$$b = 0.0$$
$$A = 2.90426$$
$$B = 2.05085$$

The amplitude result is displayed in Fig. 24 and the phase estimate remains the same as that obtained in the previous section and displayed in Fig. 17(b).

The impulse response obtained using the exponential estimate is displayed in Fig. 25 along with the theoretical result. From this figure the agreement is seen to be excellent, including the neighborhood of the creeping wave response.

The frequency response for the exponential estimate is shown in Fig. 26 and the radar cross section is shown in Fig. 27 along with the companion theoretical results. Again, the agreement is excellent.

2.4 SCATTERING BY A PROLATE SPHEROID - AXIAL INCIDENCE

The space-time integral equation technique yields the smoothed impulse response of arbitrarily shaped targets which may in turn be used to compute the frequency response well into the resonance region. The accuracy of this technique for computing the slow variation of the impulse response and the lower portion of frequency response has been verified for numerous target shapes by comparison with measured data.

At the other end of the spectrum the physical optics approximation yields exact results for the specular return in the case of the impulse response and for the very high frequency region in the case of the frequency response.

In the previous two sections, a technique has been developed which combines the space-time integral equation results with the physical optics results to yield the response over the remainder of the spectrum. The impulse response augmentation technique was demonstrated on the sphere and gave results in excellent agreement with theoretical responses.

For comparison, theoretical impulse and frequency responses are available only for the case of the sphere ; however, approximate results (which agree well with measurements) do exist for the case of the prolate spheroid.[11] It is the purpose of this section to demonstrate the impulse response augmentation technique for the case of the prolate spheroid with axial incidence.

Figure 28 displays the incident pulse and the cross section of the prolate spheroid with an axial ratio of 2:1 and with a minor axis radius of a. The target is centered at the origin such that its major axis coincides with the z-axis. The width of the incident pulse is equal to the length of the

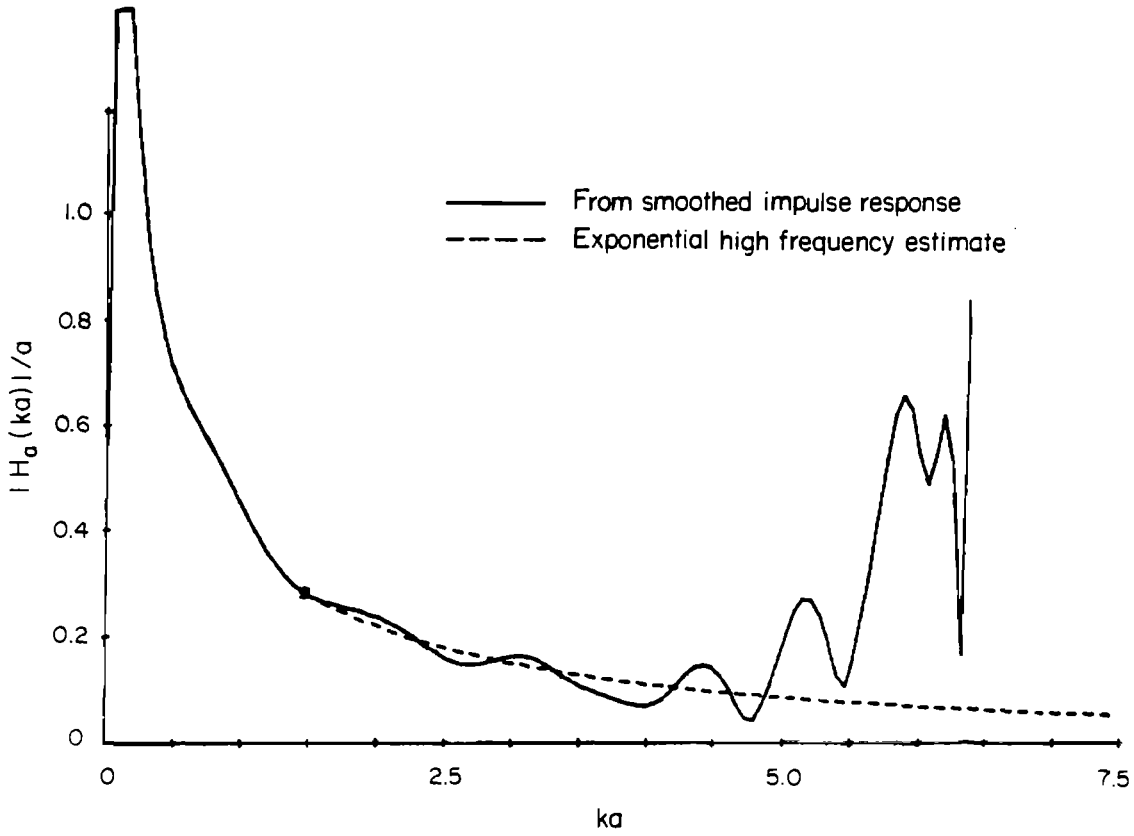

FIG. 24 Augmented frequency response of sphere with radius a.

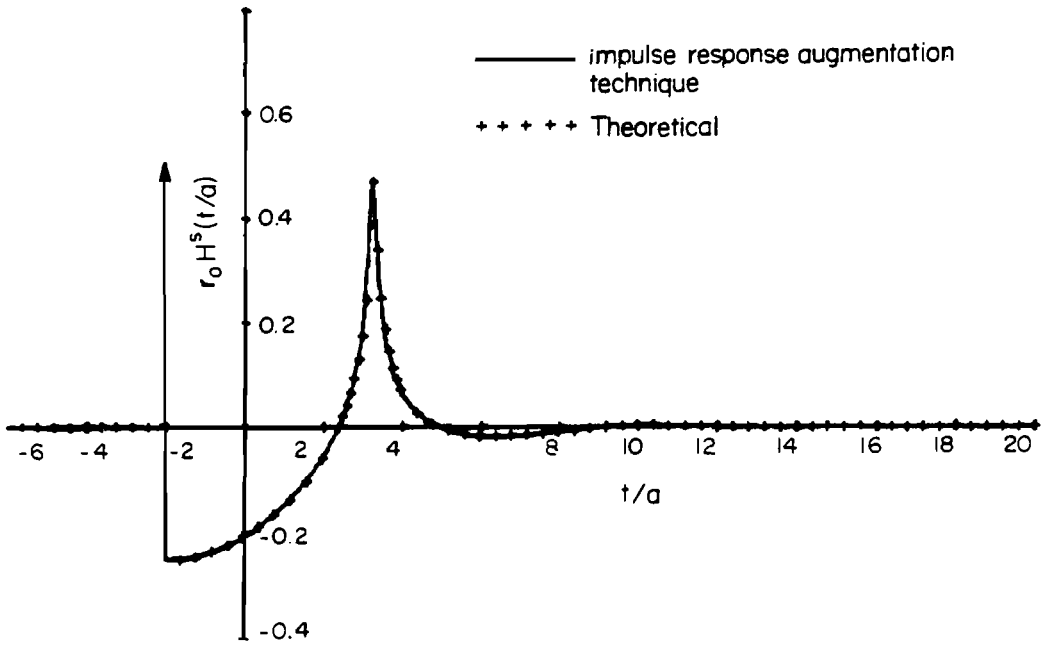

FIG. 25 Impulse response of sphere with radius a.

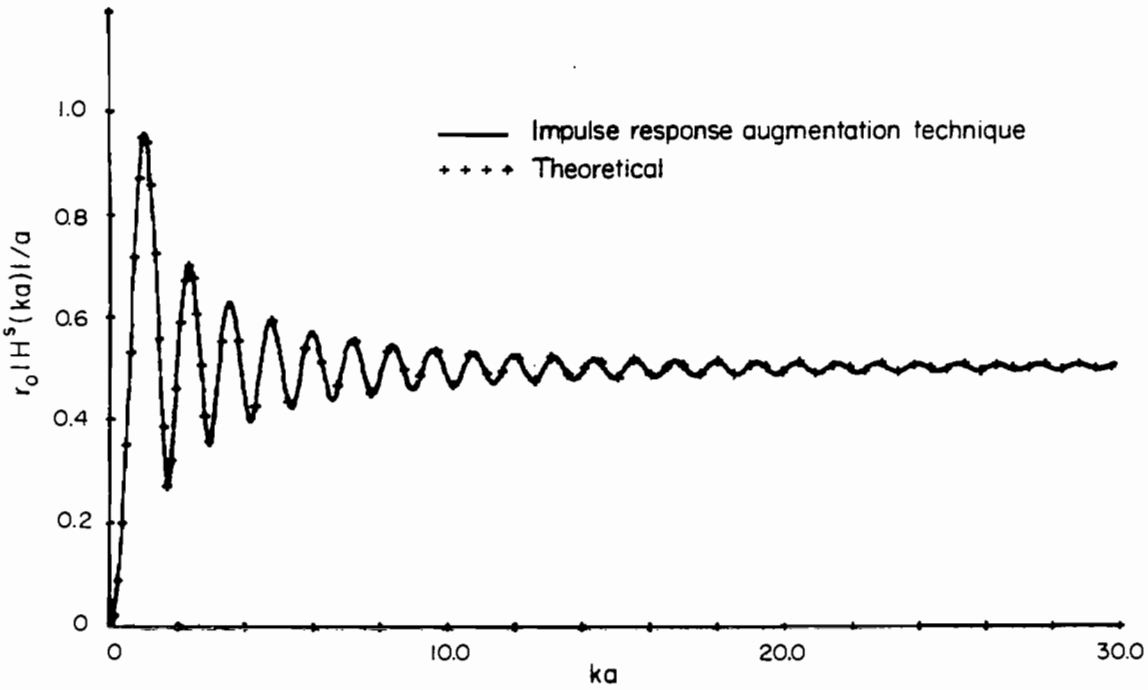

FIG. 26 Frequency response of sphere with radius a.

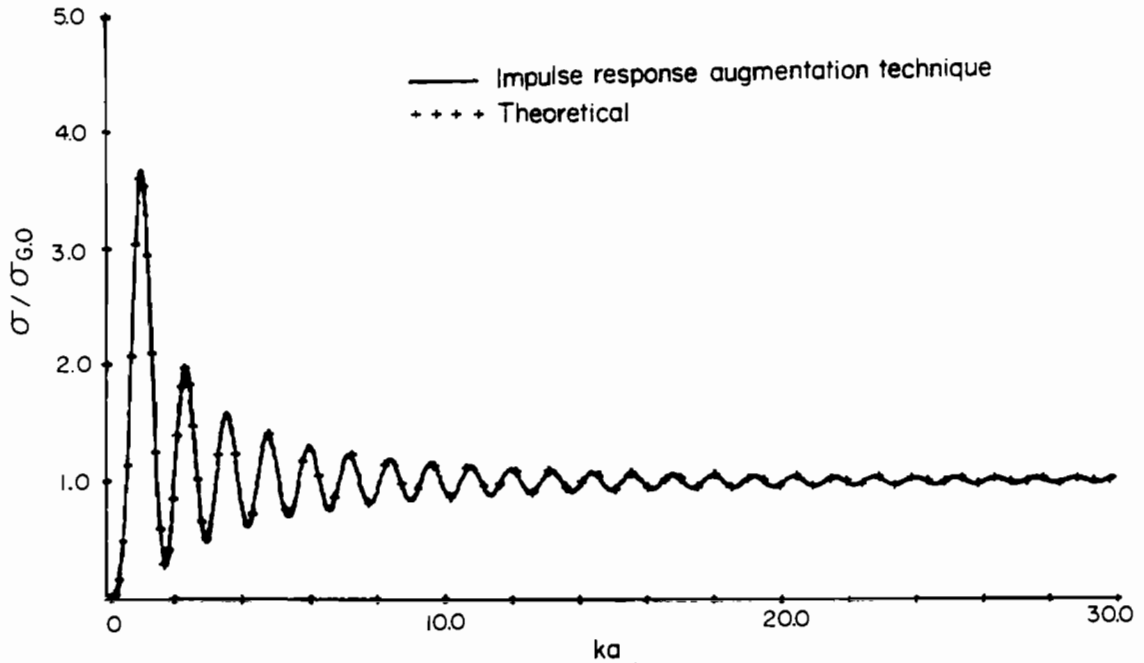

FIG. 27 Radar cross-section of sphere with radius a.

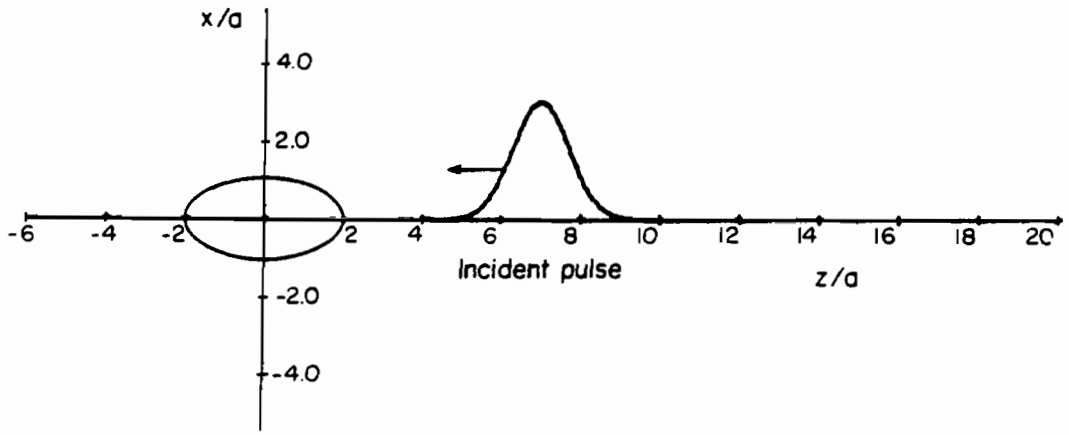

FIG. 28 Incident pulse and prolate spheroid of minor radius a and axial ratio 2.

prolate spheroid: i.e.,

$$e(t) = \frac{n}{\sqrt{\pi}} e^{-(na)^2(t/a)^2} \tag{43}$$

where $na = 1$.

The smoothed impulse response that was computed using the space-time integral equation is displayed in Fig. 29. Note the spectral return at $t/a = -4$, the subsequent nearly constant negative value of 0.0625, and finally the creeping wave return at approximately $t/a = 4.6$.

The frequency response obtained from dividing the transform of the smoothed impulse response by the transform of the incident pulse is shown in Fig. 30 along with results measured by Moffatt and Kennaugh.[11] The agreement is good in most cases, and at points where measured values fall off the computed curve the difference is less than the expected measurement accuracy, as indicated by the spread of the measured data.

From the physical optics approximation the approximate augmentation function for this prolate spheroid is

$$f_a(t) = \frac{1}{4} \delta(t/a + 4) - \frac{1}{16} u(t/a + 4) \tag{44}$$

where a is the semi-minor axis of the body. Figure 31 displays the augmented frequency response of the prolate spheroid obtained using this augmentation function. To this is applied the exponential estimate of the high frequency variation given in Eq. (42) which yields the following parameters:

$$\begin{aligned} \omega_c = \omega_1 &= 2.14755 \\ \omega_2 &= 3.80425 \\ m &= -4.87750 \\ b &= 0 \\ A &= 2.18519 \\ B &= 1.77802 \end{aligned}$$

This estimate is also plotted in Fig. 31.

The impulse response of the prolate spheroid obtained with this technique is displayed in Fig. 32 along with the Moffatt-Kennaugh exponential sum approximation[11] for easy reference. Both results agree well in all areas except in the region of creeping wave return, and it should be noted that it is precisely this region where the greatest liberty is taken in fitting the "stretched" sphere response with the exponential sum.

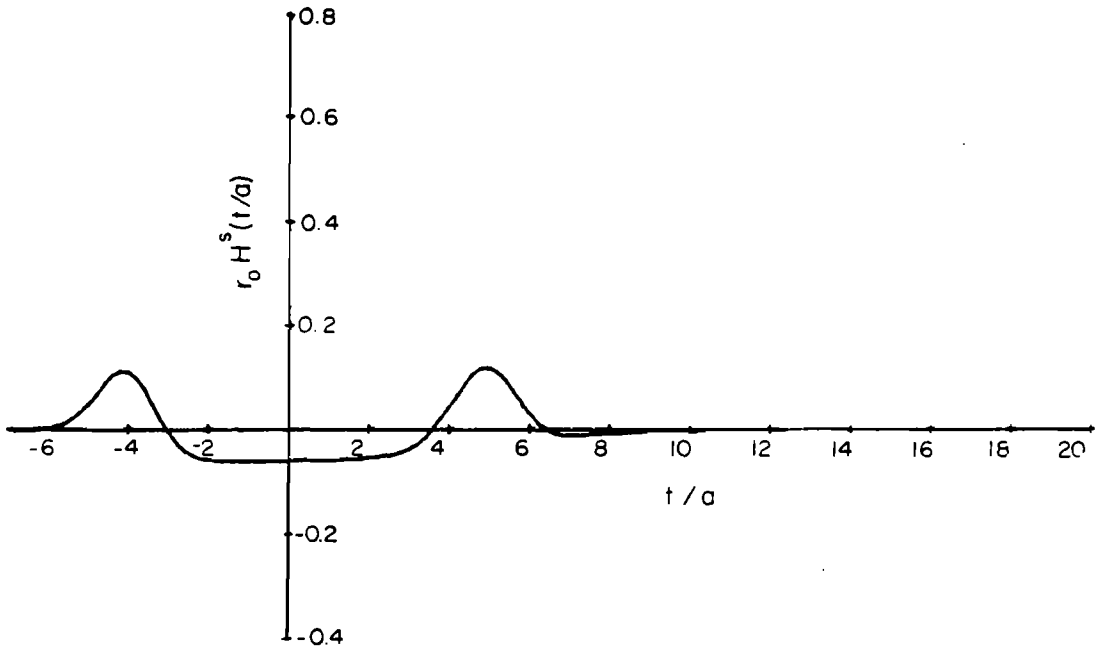

FIG. 29 Smoothed impulse response of prolate spheroid with minor radius a and axial ratio 2 for axial incidence.

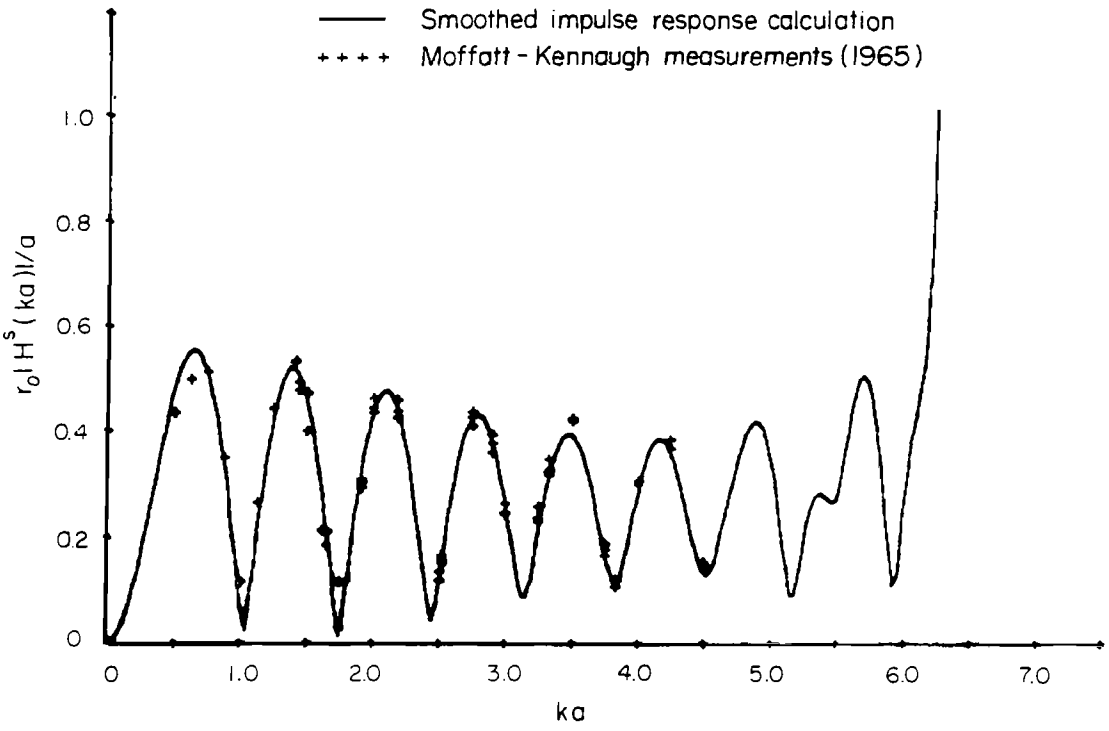

FIG. 30 Frequency response of prolate spheroid with minor radius a and axial ratio of 2 for axial incidence.

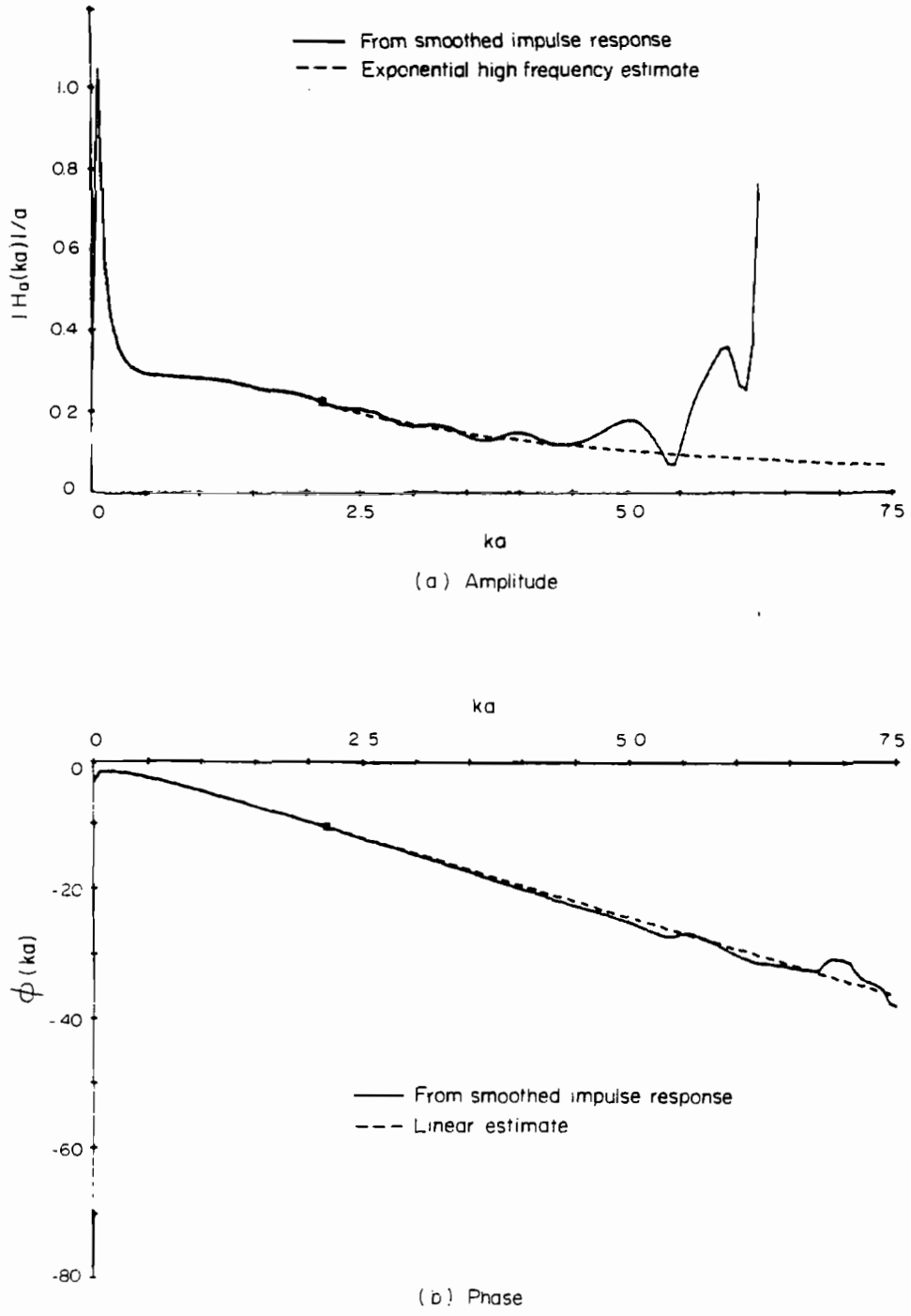

FIG. 31 Augmented frequency response of prolate spheroid.

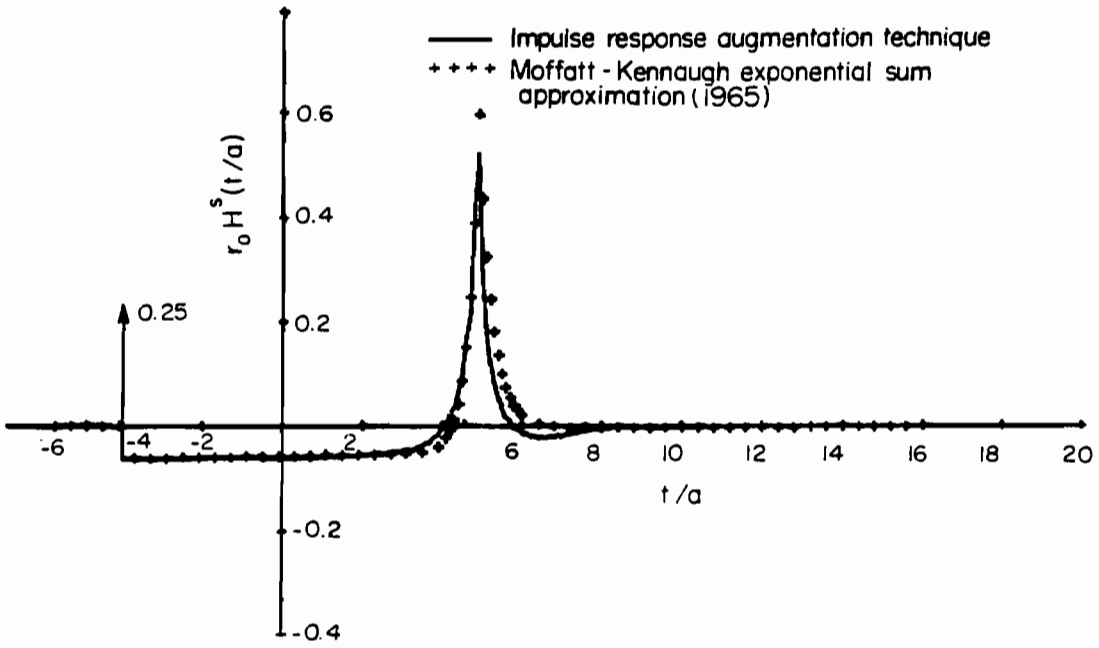

FIG. 32 Impulse response of prolate spheroid with minor radius a and axial ratio 2 for axial incidence.

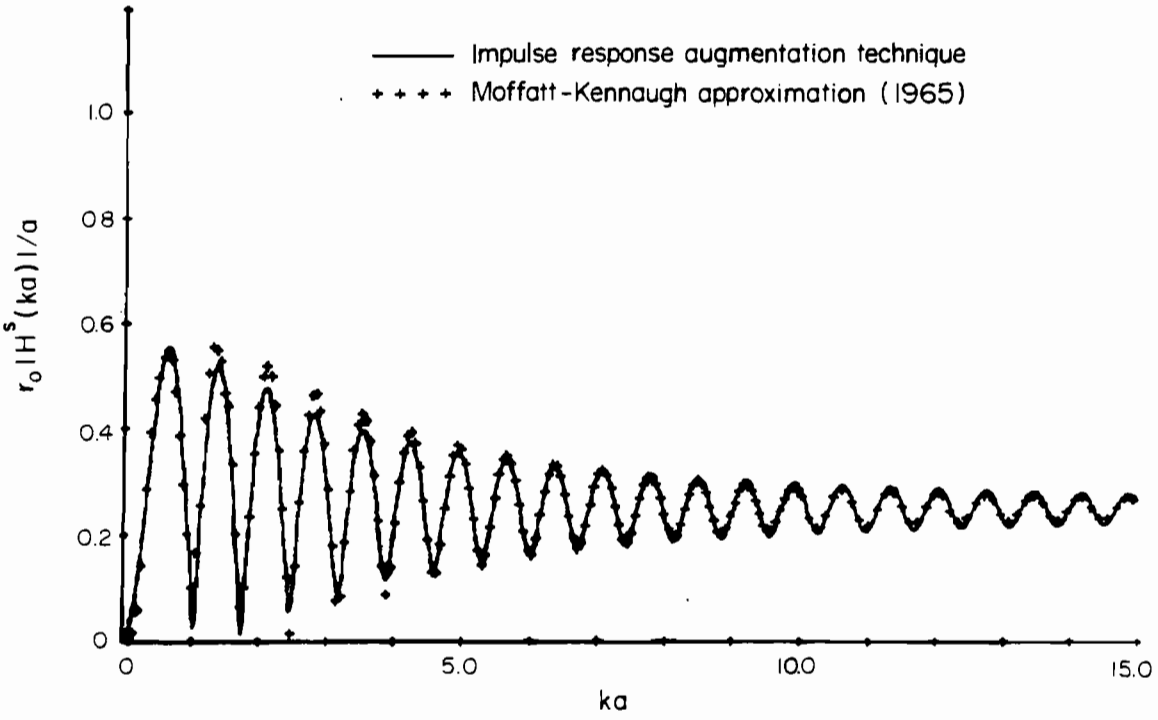

FIG. 33 Frequency response of prolate spheroid with minor radius a and axial ratio 2 for axial incidence.

The frequency response of the prolate spheroid computed with this technique is displayed in Fig. 33 along with the result from the Moffatt-Kennaugh approximation. Note the good agreement for ka less than 1, where Moffatt and Kennaugh integrated the "stretched" sphere impulse response directly. Between ka of 1 and 6 the Moffatt-Kennaugh result is larger than the impulse response augmentation technique result. It is over this region that the exponential sum approximation seems to lead to the largest error. Beyond a ka of 6 the agreement between the two results again becomes quite good. Finally, for completeness, both the frequency response and the radar cross section of a prolate spheroid with a 2:1 axial ratio were computed with the impulse response augmentation technique and are displayed in Figs. 34 and 35, respectively, for a range of ka from 0 to 30.

2.5 SCATTERING BY A SPHERE-CAPPED CYLINDER - AXIAL INCIDENCE

The third target on which the impulse response augmentation technique was demonstrated is a circular cylinder of radius a with spherical end caps and a length-to-diameter ratio of 3:1. The cylinder is positioned such that the center of the illuminated end cap coincides with the origin and the cylinder axis coincides with the z axis, as shown in Fig. 36. This target is illuminated with an incident wave given by

$$e(z,t) = \frac{n}{\sqrt{\pi}} e^{-(na)^2(t/a+z/a)^2} \tag{45}$$

where $na = 1$

a = radius of cylinder.

This yields an incident pulse width equal to two-thirds the length of the sphere-capped cylinder, as shown in Fig. 36.

The smoothed impulse response that was computed by the space-time integral equation technique is displayed in Fig. 37. The effect of the impulse from the specular point is apparent at $t/a = -2$, and is then followed by the effect of the negative step. Between $t/a = -2$ and $t/a = 6$ the response is near zero, indicating a negligible return from the sides of the cylinder. Next, at approximately $t/a = 8.7$ a negative pulse occurs that may be attributed to the region of the join between the cylinder and rear sphere cap. This is followed by a positive pulse at approximately $t/a = 11$ which is due to the creeping wave that travels around the rear of the cylinder.

The frequency response was computed by dividing the transform of the smoothed impulse response shown in Fig. 37 with the transform of the incident pulse. This response is shown in Fig. 38 and indicates results which are stable up to a ka of approximately 5. The interference between the returns from the specular point and the rear of the cylinder is evident in the form of ripples in the response.

The augmentation function used for the sphere-capped cylinder is the same as was used for the sphere in Eq. (30) and is repeated here for convenience:

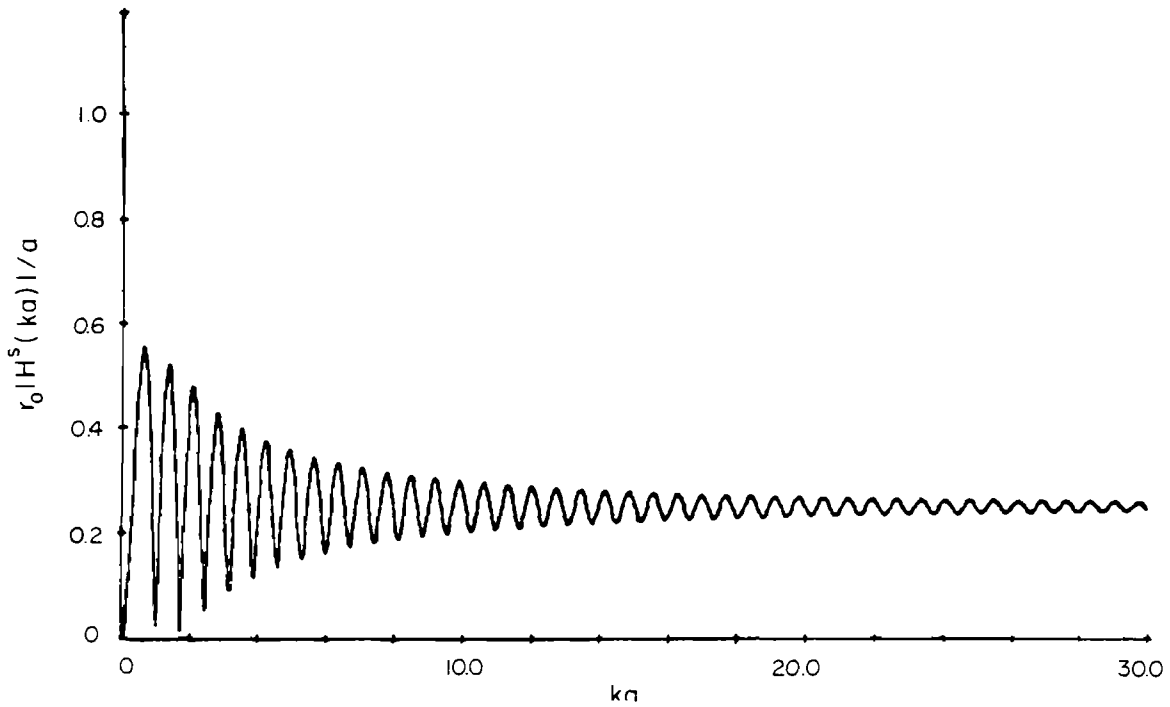

FIG. 34 Frequency response of prolate spheroid with minor radius a .

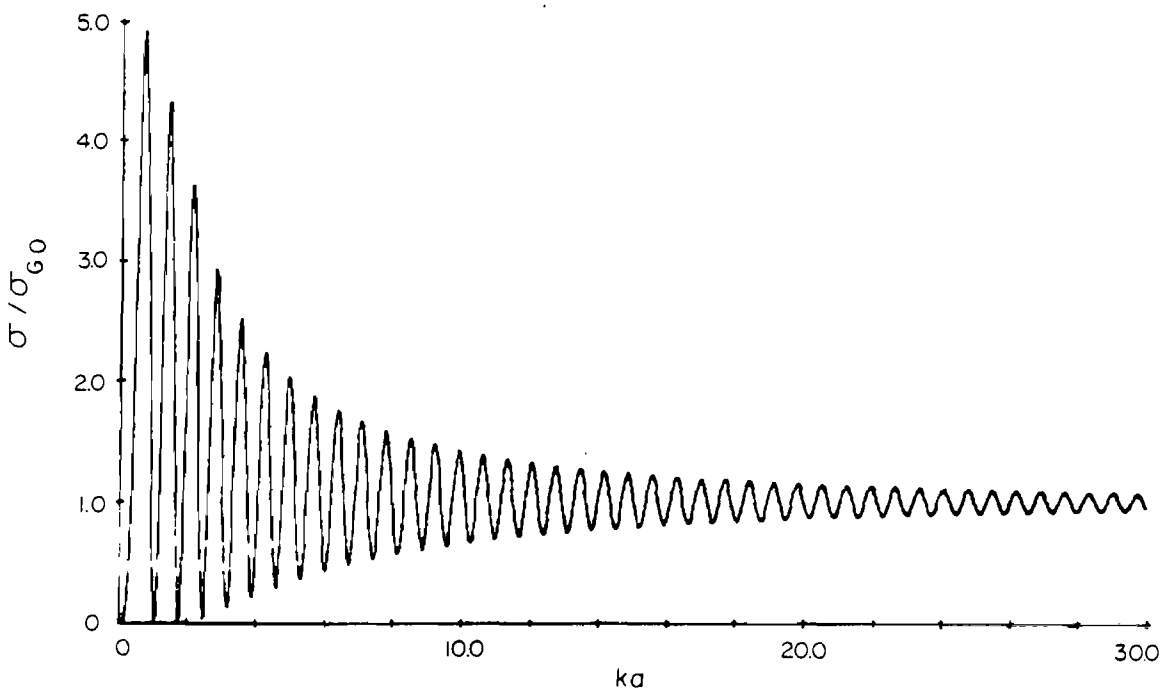

FIG. 35 Radar cross section of prolate spheroid with minor radius a.

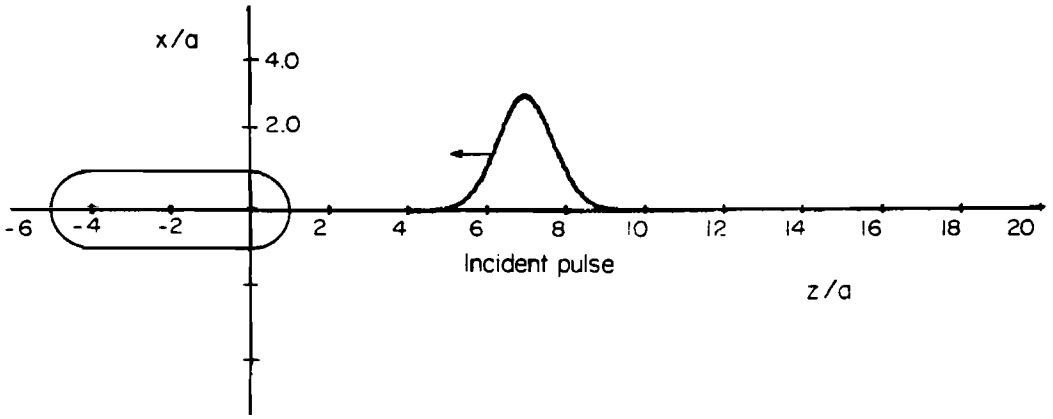

FIG. 36 Incident pulse and sphere-capped cylinder with radius a and length-to-diameter ratio 3.

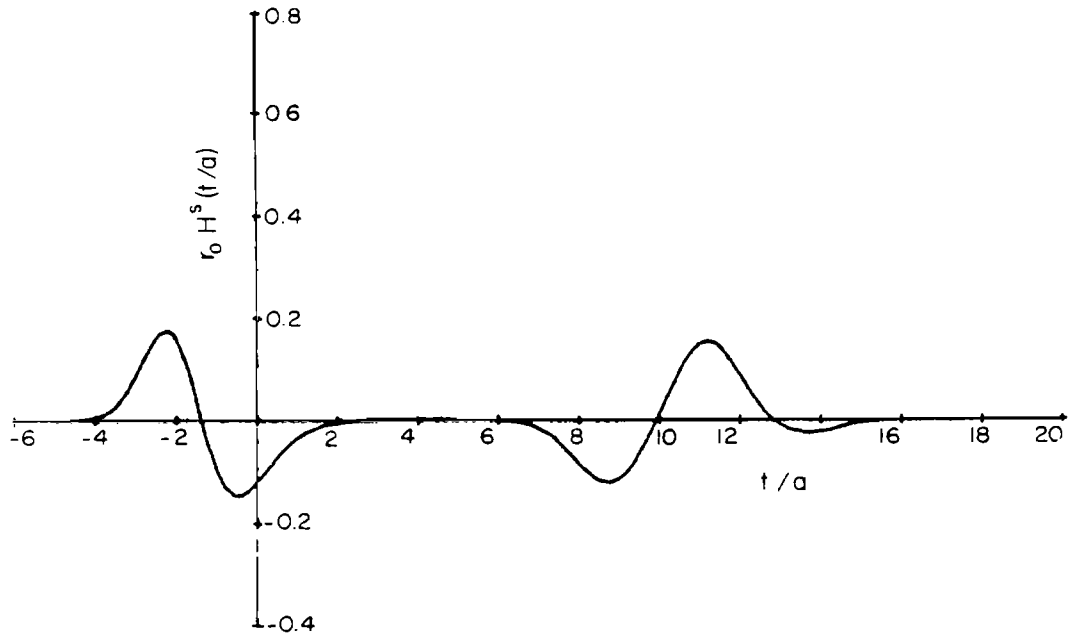

FIG. 37 Smoothed impulse response of sphere-capped cylinder with radius a and L/D - 3 for axial incidence.

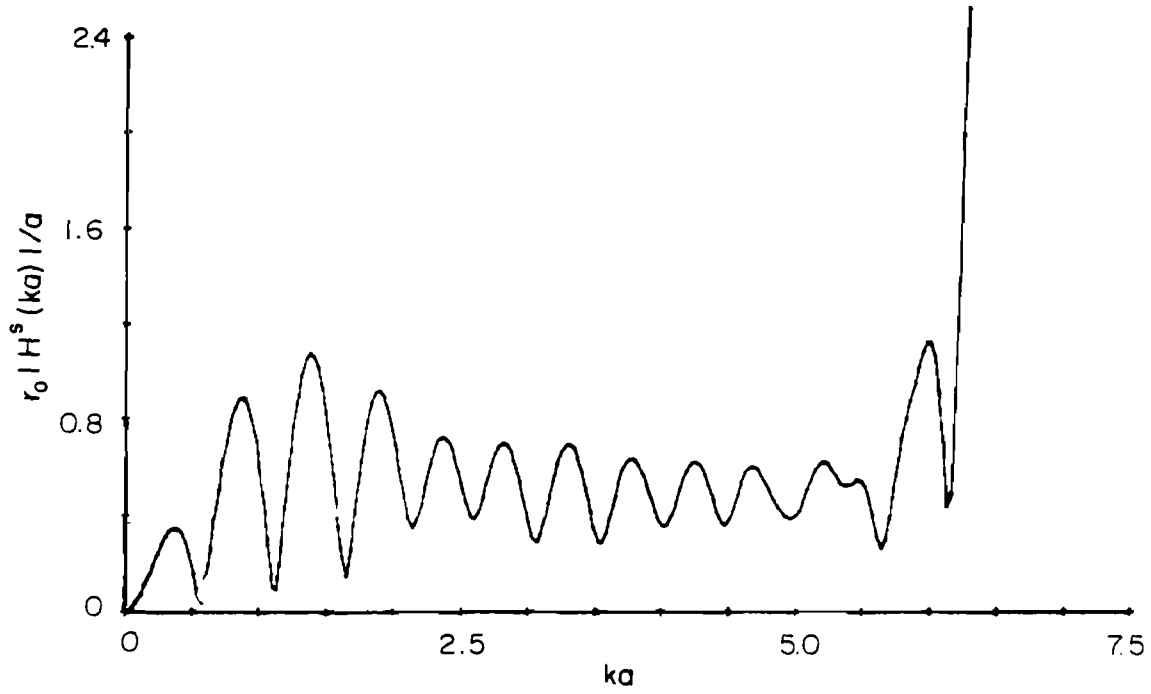

FIG. 38 Magnitude of frequency response of sphere-capped cylinder with axial incidence.

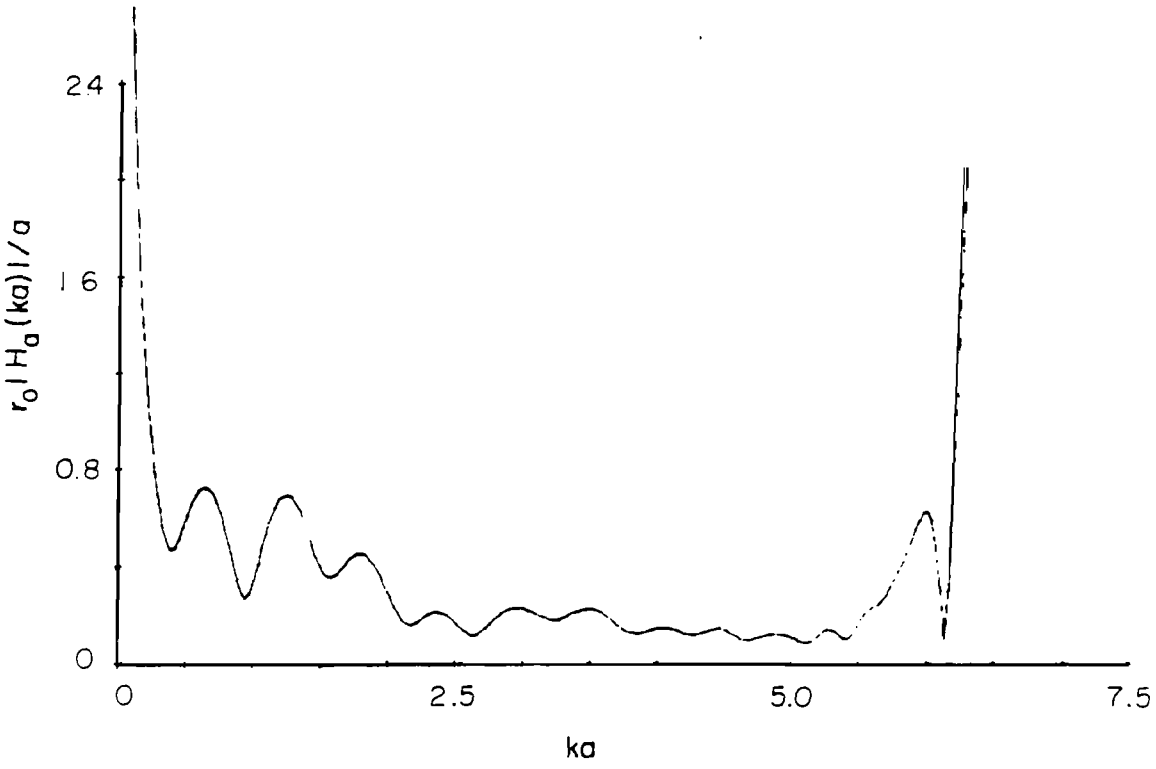

FIG. 39 Augmented frequency response of sphere-capped cylinder.

$$f_a(t) = \frac{1}{2}\,\delta(t/a + 2) - \frac{1}{4}\,u(t/a + 2)\ . \qquad (46)$$

Applying this function yields the augmented frequency response shown in Fig. 39. The response for this target is more complicated than it was for the case of either the sphere or the prolate spheroid, and in particular it does not seem appropriate to estimate the high frequency variation simply with the exponential used for the previous two targets. The period of the fine ripples indicates an interference between two returns which possess a time separation of approximately $\Delta\ t/a = 12$, or the approximate time separation between the return from the front of the cylinder and the return from the rear of the cylinder. Moreover, it is obvious from the smoothed impulse response shown in Fig. 37 that the returns from these two regions can easily be separated in time. Thus, to facilitate the estimation of the high frequency portion of the augmented frequency response, the smoothed impulse response of the sphere-capped cylinder, r(t), was divided into two parts and each section was considered separately.

The smoothed impulse response from the front part of the sphere-capped cylinder is shown in Fig. 40. The frequency response that results from this portion of the smoothed impulse response, shown in Fig. 41, is notable for its absence of ripples. Using the augmentation function given by Eq. (46) yields the augmented frequency response due to the front part of the sphere-capped cylinder shown in Fig. 42. Note that the amplitude in Fig. 42(a) decreases very rapidly and the the phase in Fig. 42(b) is nearly constant. The phase response indicates the high frequency portion of the response occurs in time at $t/a = 0$, or from the region of the join between the cylinder and the front sphere cap. The amplitude was assumed to possess a $1/2^{3/2}$ variation and the phase was assumed to be constant. Thus, the high frequency portion of the augmented frequency response was given by

$$\hat{H}_{a1}(\omega) = \frac{A_0}{\omega^{\frac{3}{2}}}\ \exp(jb_o) \qquad \omega > \omega_c \qquad (47)$$

where

$$\omega_c = 2.000$$
$$b_o = -1.619$$
$$A_0 = 0.213$$

and the resulting high frequency estimate is shown in Fig. 42.

The impulse response $\hat{h}_1(t)$ due to this portion of the return is displayed in Fig. 43 and the companion frequency response $\hat{H}_1(\omega)$ is displayed in Fig. 44. Note that the impulse response is time limited and has a negligible precursor, which increases confidence in these results. The frequency response exhibits very little resonant character.

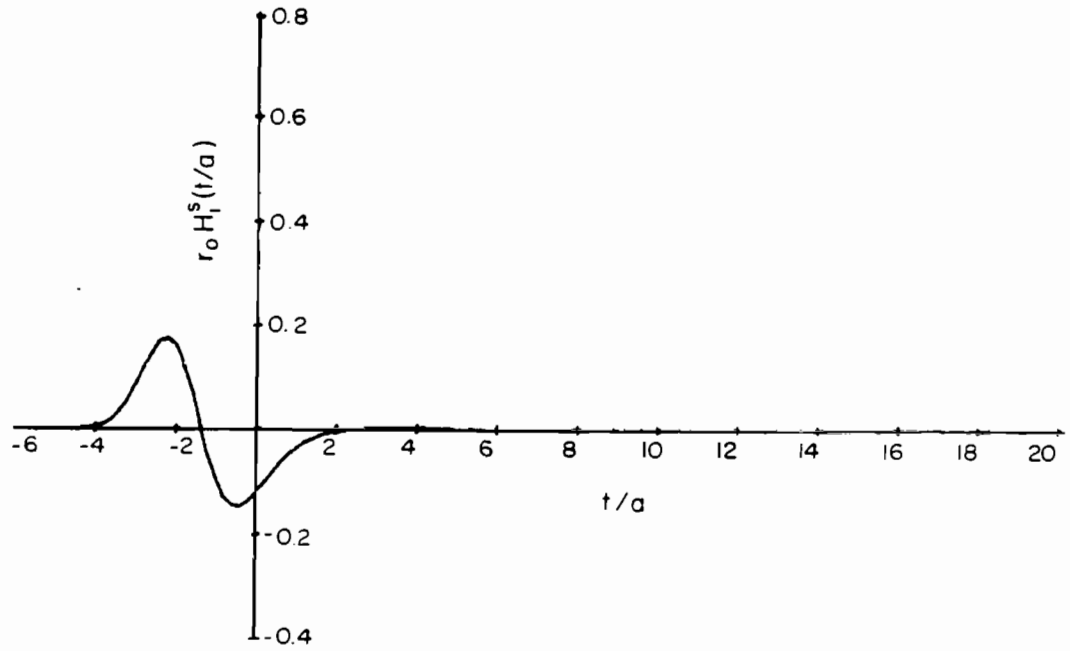

FIG. 40 Smoothed impulse response from front of sphere-capped cylinder.

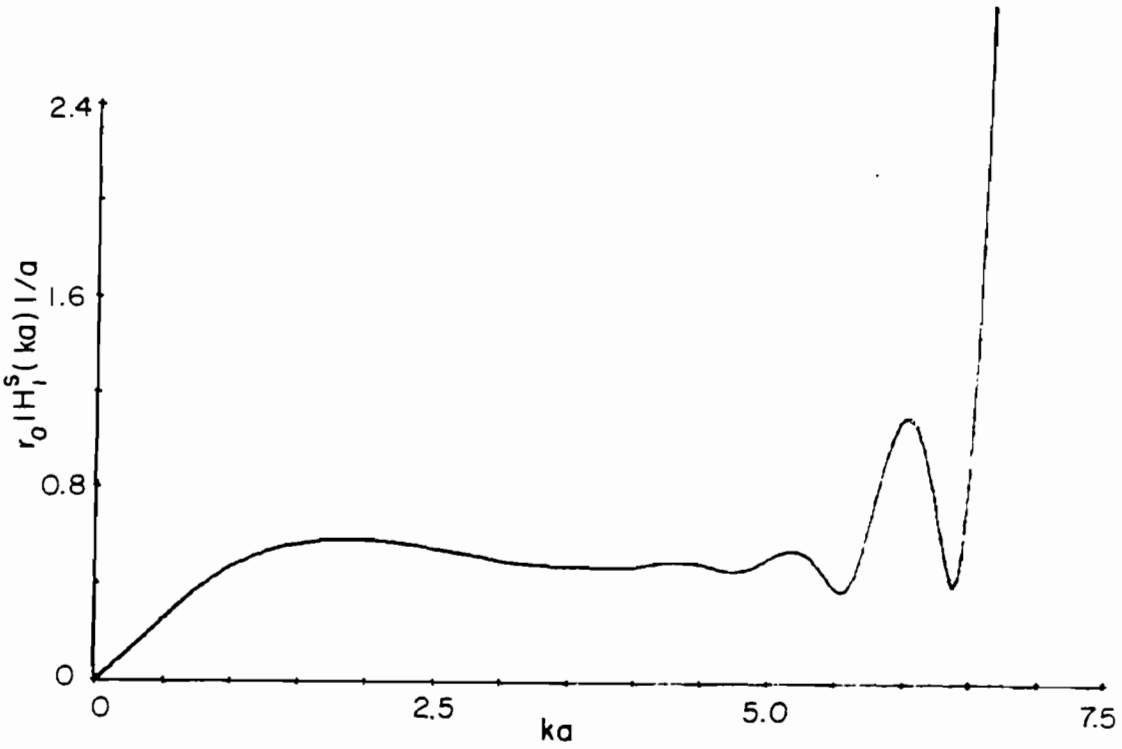

FIG. 41 Frequency response due to the front part of the sphere-capped cylinder.

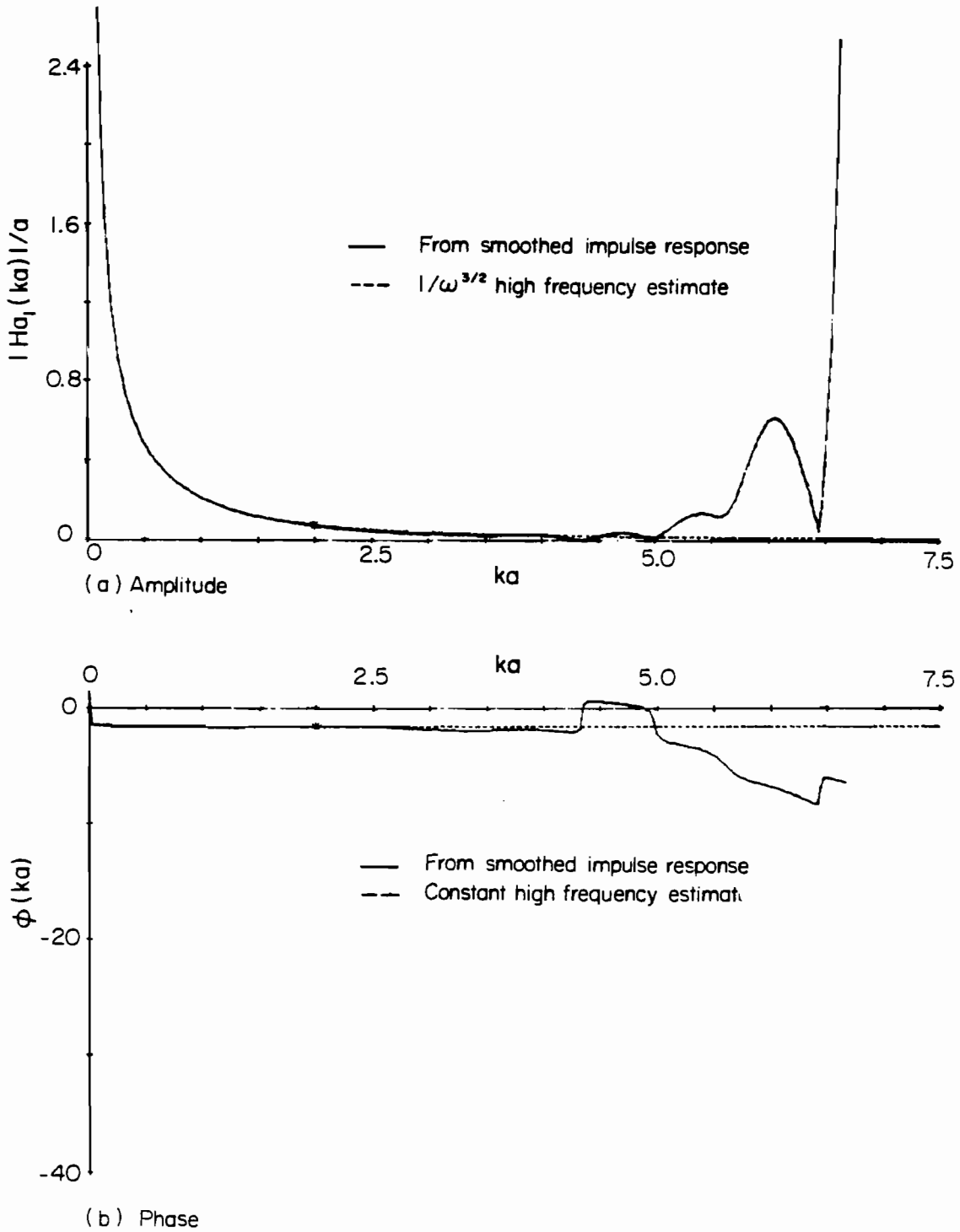

FIG. 42 Augmented frequency response of return due to front part of sphere-capped cylinder.

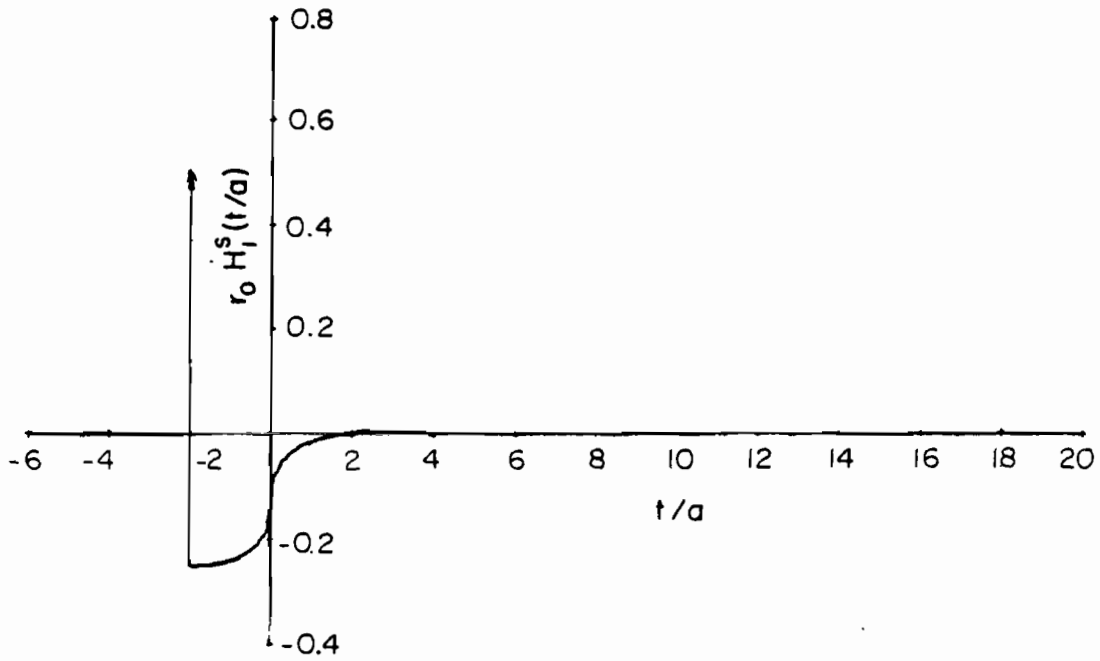

FIG. 43 Impulse response from near end of sphere-capped cylinder.

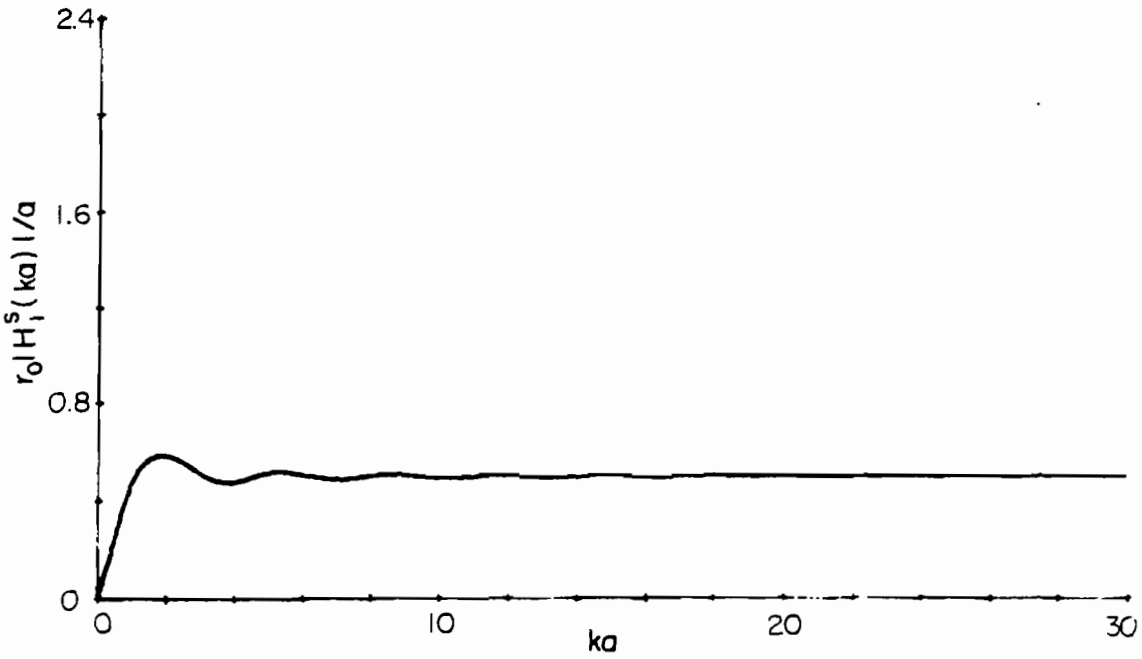

FIG. 44 Frequency response from near end of sphere-capped cylinder.

The portion of the smoothed impulse response due to the far end of the cylinder, $r_2(t)$, is shown in Fig. 45. Since no specular points contribute to this portion of the response, the appropriate augmentation function is zero, and thus the frequency response due to this portion corresponds to the augmented frequency response. Both the amplitude and phase of the augmented frequency response are displayed in Fig. 46. The phase response in Fig. 46(b) possesses a linear phase term with a slope of approximately -11, which indicates a response in the time domain at approximately t/a = 11, and can be attributed to the creeping wave. The phase also deviates from linearity with the same period as the variation in amplitude, or a Δ ka of approximately 2.6. This corresponds to the effect of a second, lower level response which occurs at Δt/a of 2.4 before the creeping wave return and could be attributed to a return from the join between the cylinder and the rear sphere cap. It is assumed that the amplitude of the creeping wave return has the exponential form used for the sphere and prolate spheroid and the amplitude of the join return has a $1/\omega^{3/2}$ form. Both are assumed to possess a linear phase variation. Thus, the form of the high frequency estimate used for the second portion of the sphere-capped cylinder augmented frequency response is

$$\hat{H}_{a2}(\omega) = A_1 \exp(-B_1\omega^{1/3})\exp(j\omega m_1 + jb_1) + \frac{A_2}{\omega^{3/2}} \exp(j\omega m_2 + jb_2) \qquad \omega > \omega_c \tag{48}$$

The parameters in Eq. (48) were chosen in the following manner:

ω_1 = the approximate value of frequency at which the first maximum in the amplitude response occurs; this was chosen

φ_1 = the phase at ω_1

$m_1 = \varphi_1/\omega_1$
This is the slope of the linear phase in $\hat{H}_{a2}(\omega)$

$b_1 = 0$

ω_2 = the exact point in frequency at which the phase of $H_{a2}(\omega)$ exp $(-jm_1\omega + jb_1)$ is zero, corresponding to the first minimum of $H_{a2}(\omega)$

t_{j2} = the time at which the second join return would first appear; this was specified

$m_2 = t_{j2}$

$\omega_3 = \omega_2 + \pi/(m_2 - m_1)$

$b_2 = \pi - m_2\omega_2$

B_1 = the value obtained from the sphere with radius a was used for this parameter

A_1 & A_2 = these two parameters are chosen such that

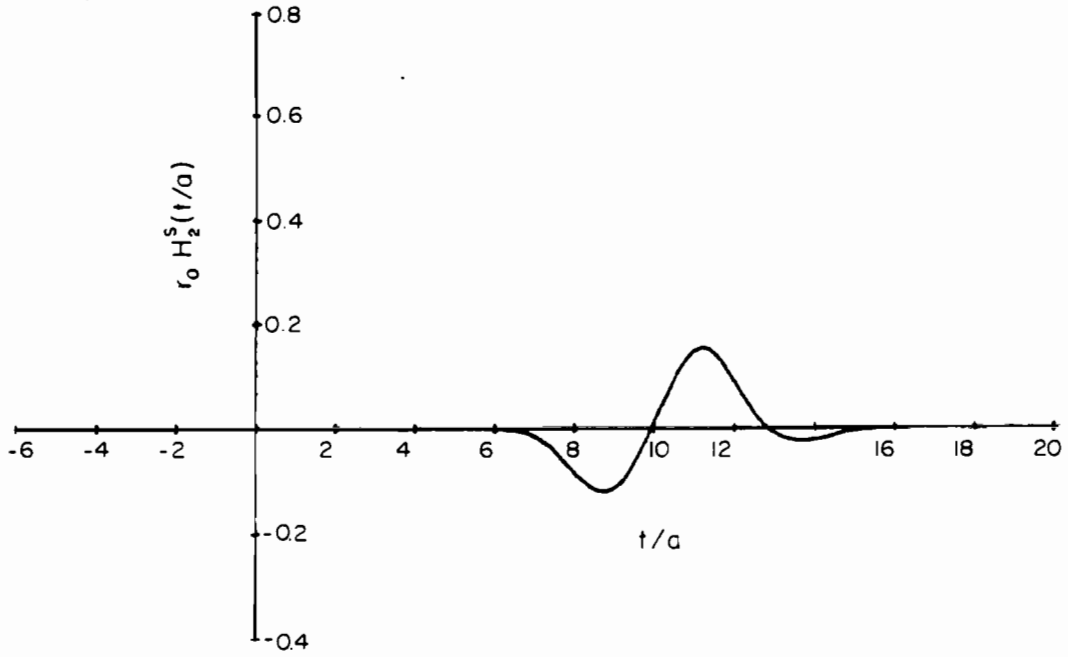

FIG. 45 Smoothed impulse response from far end of sphere-capped cylinder.

$$\hat{H}_{a2}(\omega_2) = H_{a2}(\omega_2)$$

$$\hat{H}_{a2}(\omega_3) = 0.2095$$

Carrying out the above procedure yields the following values for these parameters:

$\omega_1 = 1.48855$
$m_1 = -11.192$
$b_1 = 0.0$
$\omega_2 = 2.486$

$\omega_3 = 3.470$
$m_2 = -8.00$
$b_2 = -4.795$
$B = 2.05085$
$A_1 = 3.676$
$A_2 = 0.289$

Substituting these values into Eq. (48) yields the estimate of the high frequency portion of the augmented frequency response shown by the broken line in Fig. 46. Since the augmentation function is zero in this case, this is also the frequency response which is shown in Fig. 47 for the larger frequency window.

The impulse response for the second part of the return from the sphere-capped cylinder is displayed in Fig. 48 where it is noted that the creeping wave peak occurs at $t/a = 11.19$, which is slightly later than the $t/a = 11.14$ that a wave traveling at the speed of light would appear. This is consistent with the result obtained for the case of the sphere. The return due to the region of the join between the cylinder and the rear sphere cap causes a sharp negative swing in the response at $t/a = 8.00$ although there is a small precursor immediately prior to this time which should not be there.

Finally, the two portions of the impulse response are combined and the resulting total impulse response of the sphere-capped cylinder is displayed in Fig. 49. The total frequency response and radar cross section are shown in Figs. 50 and 51, respectively. In Fig. 50 the fast variation in the response corresponds to an interference between the return from the nose of the cylinder and the return from the far end of the cylinder. The interference between the creeping wave return and the rear join return is also evident in the form of an amplitude modulation of the fast ripples.

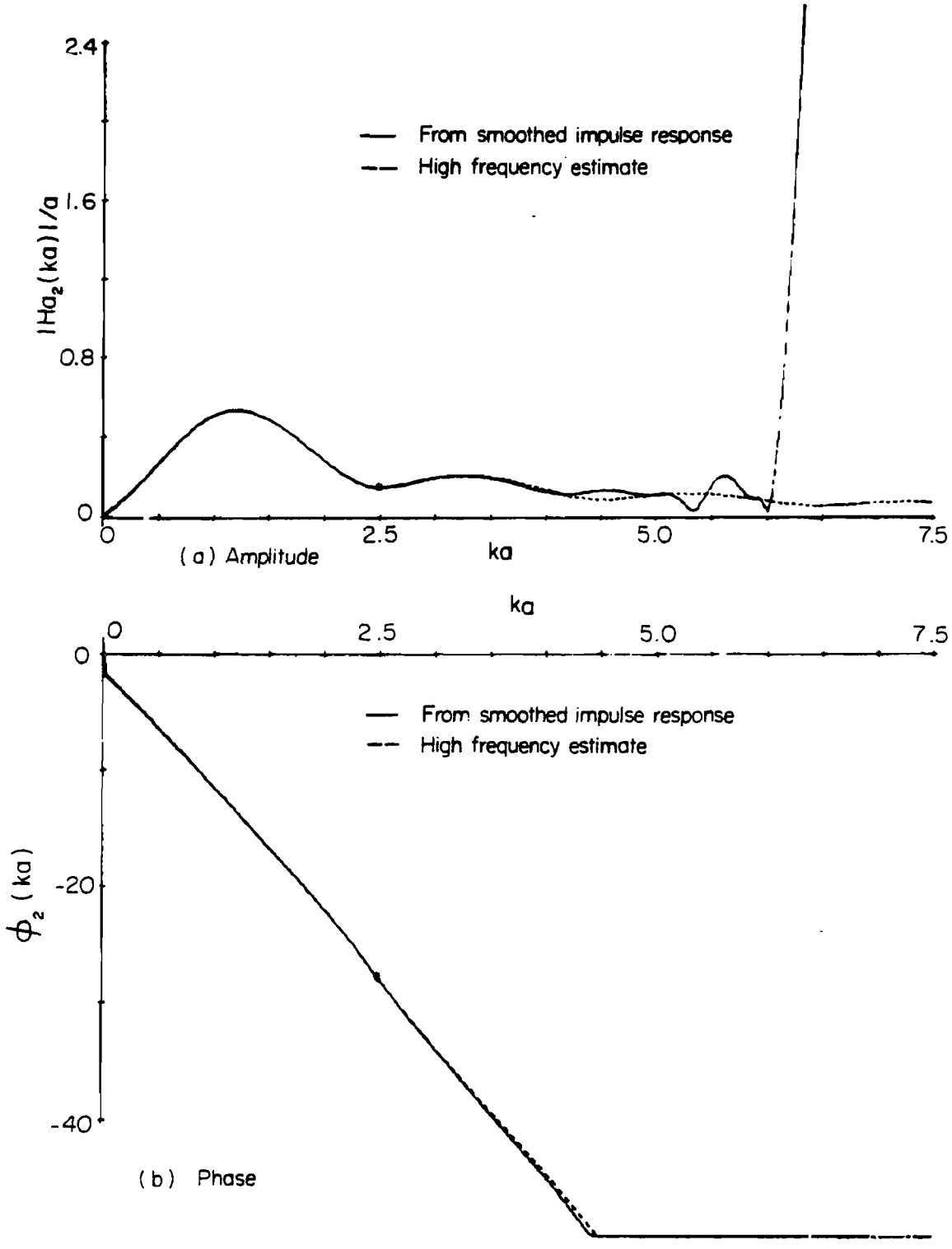

FIG. 46 Augmented frequency response of return due to far part of sphere-capped cylinder.

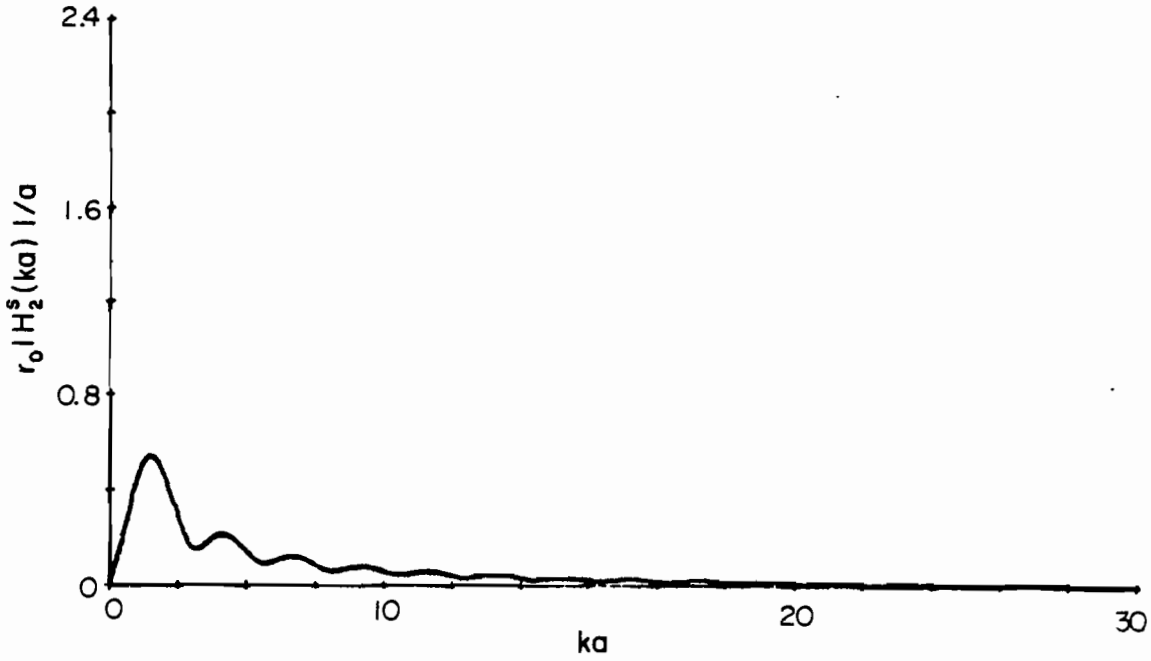

FIG. 47 Frequency response of return due to far part of sphere-capped cylinder.

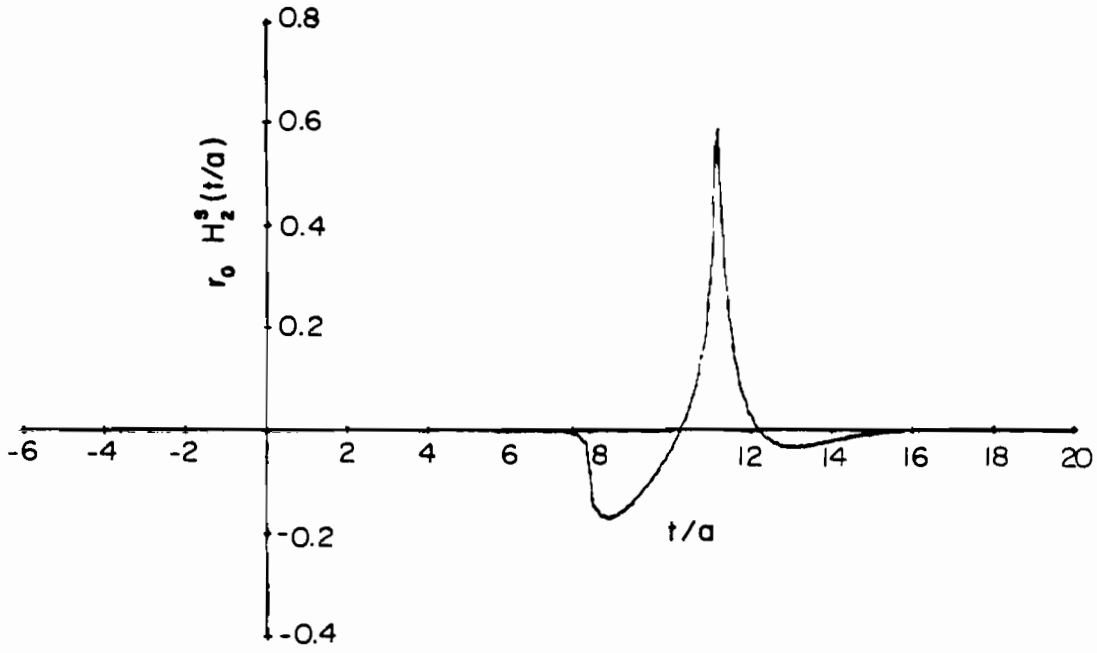

FIG. 48 Impulse response due to return from far end of sphere-capped cylinder.

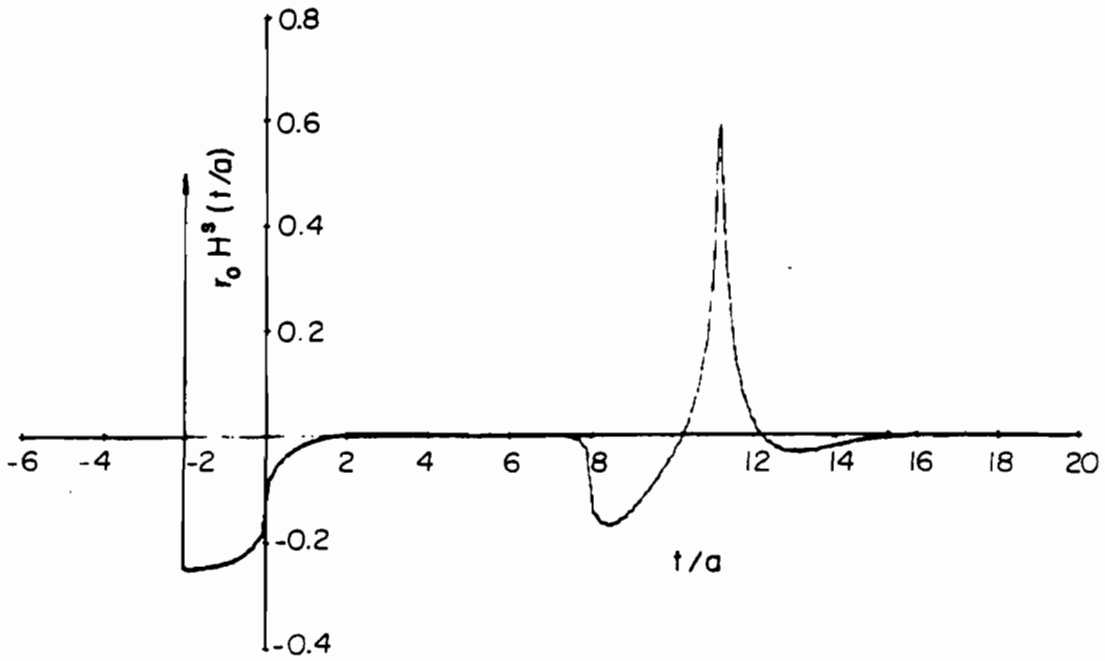

FIG. 49 Impulse response of sphere-capped cylinder with radius a and length-to-diameter ratio 3:1.

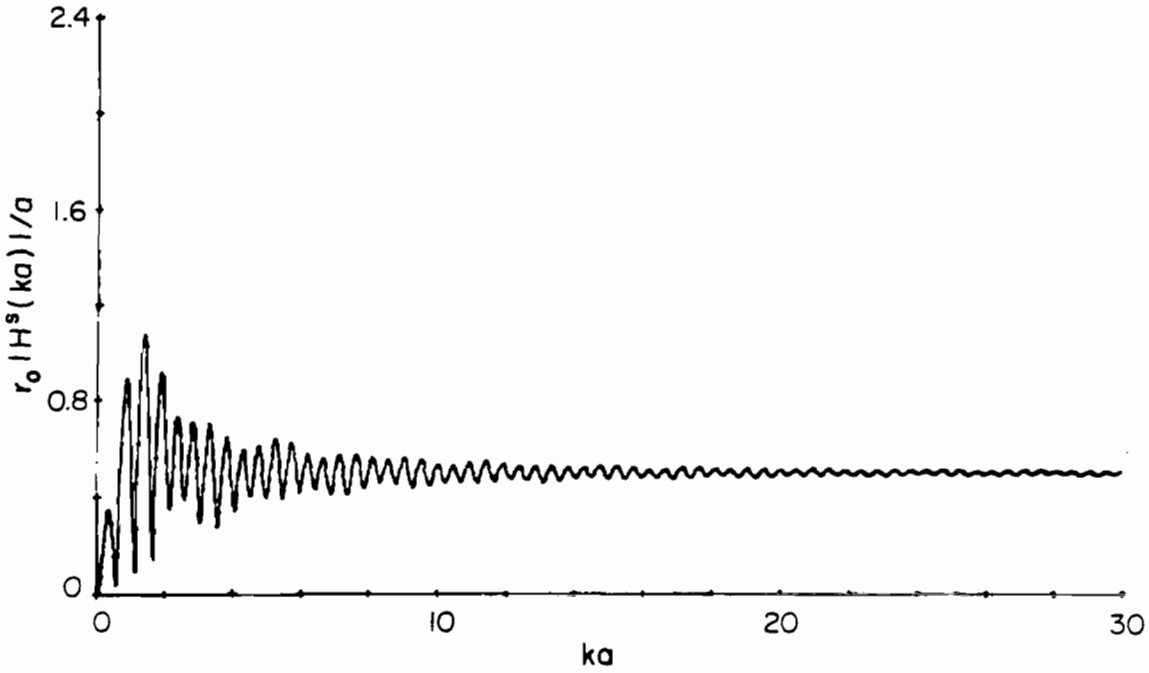

FIG. 50 Frequency response of sphere-capped cylinder with radius a.

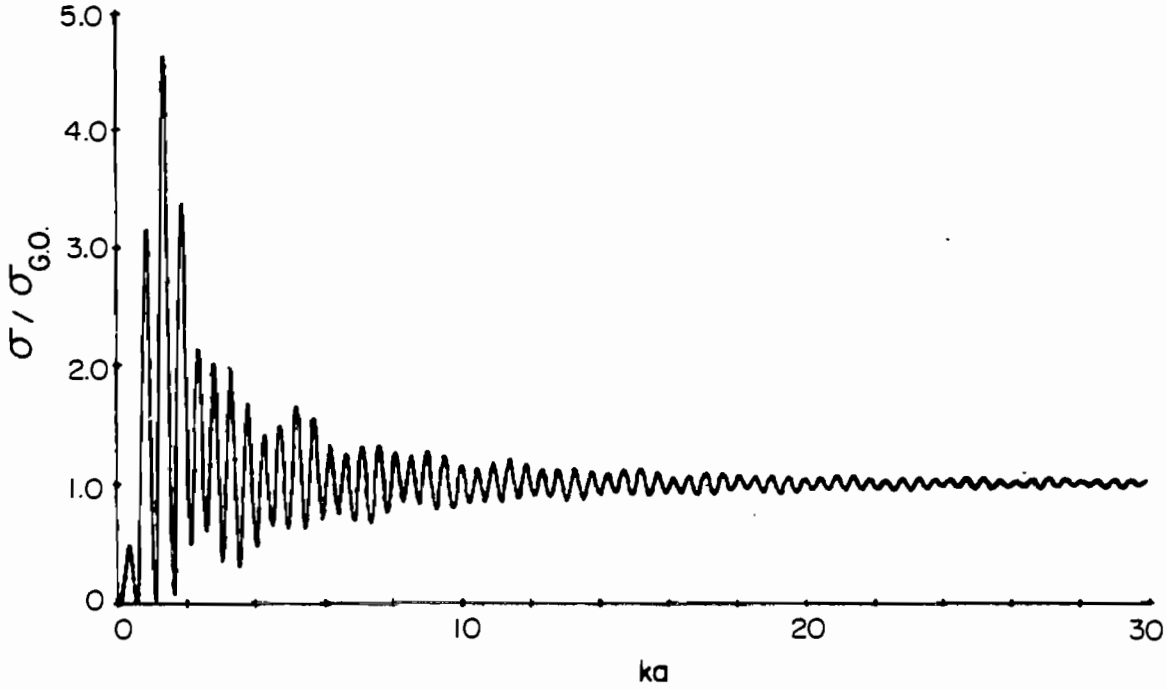

FIG. 51 Radar cross section of sphere-capped cylinder with radius a.

2.6 POLARIZATION DEPENDENT EFFECTS FOR NONAXIAL INCIDENCE

In the preceding sections, scattering from rotationally symmetric targets with axial incidence has been considered. The back-scattered far field in this rotationally symmetric scattering problem is polarization independent; however, as the direction of incidence deviates from the axial case, the back-scattered far field no longer remains polarization independent. In order to obtain an estimate of the leading edge (or equivalently, the high frequency) response of the target, the physical optics currents have been assumed. This assumption leads to polarization independence by virtue of the fact that the impulse response which results may be written as the second derivative of the target's projected area as given in Eq. (11). The question then arises as to whether or not the polarization dependent effects appear as singularity functions at the leading edge of the impulse response. It is the finding of this work that they indeed do and, to a first approximation for smooth convex bodies, are functions of the difference in the principal radii of curvature at the specular point and have the form of the first derivative of the projected area. Section 2.6.1 describes the self-term correction which is used in the numerical solution of the space-time integral equation and which provides the approximate expression for the first interaction currents on the targets. Section 2.6.2 applies this result to compute a crude approximation for the polarization dependent effects that appear at the leading edge of the impulse response.

2.6.1 Consideration of Self-Term Correction

The space-time integral equation for currents on the surface of a conducting body has been derived previously[3] and is given by

$$\vec{J}(\vec{r},\, t) = 2\hat{a}_n \times \vec{H}^i(\vec{r},\, t) + \frac{1}{2\pi} \int_S \hat{a}_n \times \left\{ \left[\frac{1}{R^2} + \frac{1}{R} \frac{\partial}{\partial \tau} \right] \vec{J}(\vec{r}\,',\, \tau) \times \hat{a}_R \right\} dS' \qquad \tau = t - R \qquad (49)$$

$\vec{r}$ = position vector to the observation point

$\vec{r}\,'$ = position vector to the integration point

$R = |\vec{r} - \vec{r}\,'|$

$\hat{a}_R = \dfrac{\vec{r} - \vec{r}\,'}{R}$

t = time in light meters

S = surface of the scattering body

$\hat{a}_n$ = unit normal vector at $\vec{r}$

$\vec{J}$ = surface current

$\vec{H}^i$ = incident magnetic field.

The integral equation in (49) may be solved exactly. Briefly, the numerical solution of the integral equation is carried out in the following manner. The vector integral equation (49) is written in terms of its components:

$$\vec{J}(\vec{r}, t) = \hat{a}_u (J_u^i + I_u) + \hat{a}_v (J_v^i + I_v) \tag{50}$$

where

$$\vec{J}^i = \hat{a}_u J_u^i + \hat{a}_v J_v^i$$

$$= 2\hat{a}_n \times \vec{H}^i$$

$$\vec{I} = \hat{a}_u I_u + \hat{a}_v I_v$$

$$= \frac{1}{2\pi} \int \hat{a}_n \times \left\{ \left[\frac{1}{R^2} + \frac{1}{R} \frac{\partial}{\partial \tau} \right] \vec{J}(\vec{r}, \tau) \times \hat{a}_R \right\}_{\tau = t-R} dS' \tag{51}$$

$\hat{a}_n$ = unit normal vector at $\vec{r}$

$\hat{a}_u$ = unit tangent vector to the line of curvature u = constant

$\hat{a}_v$ = unit tangent vector to the line of curvature v = constant.

Thus, the surface current J is written in terms of its components in the curvature directions. This yields the two coupled integral equations

$$\begin{aligned} J_u(\vec{r}, t) &= J_u^i(\vec{r}, t) + I_u(\vec{r}, t) \\ J_v(\vec{r}, t) &= J_v^i(\vec{r}, t) + I_v(\vec{r}, t) \end{aligned} \tag{52}$$

The solution of Eq. (51) is obtained by carrying out both the integration and differentiation numerically. First, the scattering surface is divided into curvilinear square patches of approximately equal area with a space sample point at the center of each patch. The spacing of these sample points (and thus, the size of the patches) on the surface is chosen small enough to give both a good representation of the scatterer and also a good

representation of the currents that exist on the scatterer. Next, the time increment Δt between the points in time at which the current is computed must be less than the time it takes a wave, moving at the speed of light, to travel between the closest space points. The space integration in Eq. (51) is carried out numerically and may be represented as

$$J_u(\vec{r}_i, t) = J_u^i(\vec{r}_i, t) + \rho_{ui}\, J_u(\vec{r}_i, t) + \sum_{k\neq i} f_{uik}\, \Delta S_k$$

$$J_v(\vec{r}_i, t) = J_v^i(\vec{r}_i, t) + \rho_{vi}\, J_v(\vec{r}_i, t) + \sum_{k\neq i} f_{vik}\, \Delta S_k \qquad (53)$$

where

ΔS_k = the area of the patch centered about $\vec{r}_k$

f_{uik}, f_{vik} = the functions of the currents J_u and J_v at other points on the scatterer and at times earlier than $t - \Delta t$ given in Eq. (51)

ρ_{ui}, ρ_{vi} = the self-term correction for r_i which represents the contribution due to the currents flowing in the patch on which the observer is located.

The expression for the self-term correction is derived in Appendix 8.3 and is given by

$$\rho_{ui} = \frac{1}{4}\sqrt{\frac{\Delta S_i}{\pi}}\,(\kappa_{ui} - \kappa_{vi})$$

$$\rho_{vi} = \frac{1}{4}\sqrt{\frac{\Delta S_i}{\pi}}\,(\kappa_{vi} - \kappa_{ui}) \qquad (54)$$

where

κ_{ui} = the curvature in the u direction (which is a principal curvature)

κ_{vi} = the curvature in the v direction (which is the other principal curvature).

Equation (54) shows that the self-term correction is proportional to the difference in the principal curvatures at the observation point and to the linear dimensions of the patch. Note that for the case where the target surface is locally spherical (i.e., $\kappa_u = \kappa_v$) the first order self-term correction is zero. It should also be pointed out that for the first order self-term correction the components are decoupled as shown in Eq. (53) for the case where the coordinate system coincides with the lines of curvature on the target surface. It is also interesting to observe that the self-term correction has the same magnitude but is of opposite sign for the two components. This effect will also manifest itself in the polarization dependence of the impulse response.

Finally, the terms in Eq. (53) may be rearranged to yield

$$J_u(\vec{r}_i, t) = \frac{j_u^i(\vec{r}_i, t) + \sum_{k \neq i} f_{uik} \Delta S_k}{1 - \rho_{ui}}$$

$$J_v(\vec{r}_i, t) = \frac{j_v^i(\vec{r}_i, t) + \sum_{k \neq i} f_{vik} \Delta S_k}{1 - \rho_{vi}} \qquad (55)$$

Equation (49) has been reduced to the recurrence relation in time given in Eq. (55), which is solved on a digital computer by simply marching on in time. The self-term correction factor ρ is included as part of the denominator and must be small (and thus, the patch size and curvature must be small or the solution will certainly be unstable.

This self-term correction has been incorporated into the computer programs and has yielded a substantial reduction in errors in the test case of a circular cylinder, for which a "classical solution" may be obtained for the initial portion of time before the end effects have reached the observer. The smoothed impulse responses that follow were calculated with this improved program.

2.6.2 Consideration of Polarization Effects in Leading Edge of Impulse Response

In the previous section, the effect of one interaction between currents has been incorporated into the numerical solution of the space-time integral equation to account for the self-term contribution. In this section, the same technique will be applied to the far-scattered field expression to obtain a crude estimate of the first order correction to the physical optics result.

The equation for the far field is given by

$$r_o \vec{H}^s(\vec{r}, t_f) = \frac{1}{4\pi} \int_S \left[\frac{\partial \vec{J}(\vec{r}, \tau)}{\partial \tau} \right]_{\tau = t-R} \times \hat{a}_r \, dS' \tag{56}$$

where

$\vec{H}^s$ = the far-scattered magnetic field at $\vec{r}$

$\vec{r}$ = the position vector to the observer

$\vec{r}'$ = the position vector to the integration point

$\hat{a}_r$ = the unit vector to the far field observer

t = the surface current time in light meters

$t_f = t - r_o$ (the far field time)

$r_o = |\vec{r}|$.

The physical optics currents

$$\vec{J}_{po} = \begin{cases} 2\hat{a}_n \times \vec{H}^i ; & \text{illuminated side} \\ 0 ; & \text{shadow side} \end{cases}$$

yield the physical optics approximation for the far field impulse response,[8]

$$r_o \vec{H}^s_{po}(\vec{r}, t_f) = \frac{1}{2\pi} \frac{\partial^2 S(t_f)}{\partial t^2} \hat{a}_{H^i} \tag{57}$$

where

$S(t_f)$ = the silhouette area of the scatterer as delineated by the incident impulse assumed to be moving over the scatterer at one-half the free space velocity

$\hat{a}_{H^i}$ = the unit vector in the direction of $\vec{H}^i$

Equation (57) is simply the physical optics approximation to the impulse response, and since it is only a function of the projected area, then as noted earlier, it is polarization independent.

The first order correction to the physical optics approximation is obtained by applying the more general result of Appendix 8.3, which gives an expression for the effect of local currents on the observer. The validity of the consideration here is restricted to the leading edge portion of the impulse response.

The expression for the first order correction to the physical optics far field is

$$r_o \vec{H}^s_{pol} = \frac{1}{4\pi} \int_S \left\{ \frac{\partial \vec{J}_{pol}(\vec{r}', \tau)}{\partial \tau} \right\}_{\tau = t-r} \times a_r \, dS' \tag{58}$$

where

$$\vec{J}_{pol} = \frac{1}{2\pi} \int_S \hat{a}_n \times \left\{ \left[\frac{1}{R^2} + \frac{1}{R} \frac{\partial}{\partial \tau} \right] \vec{J}_{po}(\vec{r}', \tau) \times \hat{a}_R \right\}_{\tau = t-R} dS'$$

$$\vec{J}_{po} = 2\hat{a}_n \times \vec{H}^{inc}$$

It is worth noting that this forms the second term in an iteration scheme for the solution of the space-time integral equation that iterates over the interactions between currents rather than simply along in time. Stepping on in time is a far more efficient numerical solution procedure for the space-time integral equation, but this first interaction will give an analytic expression for the first order correction to the physical optics approximate impulse response which includes the polarization dependence.

Since consideration is restricted here to leading edge effects, only the currents in the vicinity of the observation point need be accounted for, and thus the general expression for the self-term correction as derived in Appendix 8.3 may be used to represent $\vec{J}_{pol}$. This is given by

$$\vec{J}_{pol} = \hat{a}_u \left(\frac{\kappa_u - \kappa_v}{4\pi} \right) \left[\pi \rho_o \, J_{pou} + \left(\frac{\pi \rho_o^2}{2} \right) \frac{\partial J_{pou}}{\partial \tau} \right]$$

$$+ \hat{a}_v \left(\frac{\kappa_v - \kappa_u}{4\pi} \right) \left[\pi \rho_o J_{pov} + \left(\frac{\pi \rho_o^2}{2} \right) \frac{\partial J_{pov}}{\partial \tau} \right] \tag{59}$$

where

$$J_{pou} = -2H_v^i$$

$$J_{pov} = 2H_u^i$$

ρ_o = the radius of a circular integration patch about the observer, and will be estimated from the mean area illuminated as a function of time.

Substituting the expressions for $\vec{J}_{po}$ into Eq. (59) yields

$$\vec{J}_{pol} = 2\left(\frac{\kappa_u - \kappa_v}{4\pi}\right)\left[\pi\rho_o + \left(\frac{\pi\rho_o^2}{2}\right)\frac{\partial}{\partial t}\right]\hat{a}_n \times \hat{a}_u H_u^i$$

$$+ 2\left(\frac{\kappa_v - \kappa_u}{4\pi}\right)\left[\pi\rho_o + \left(\frac{\pi\rho_o^2}{2}\right)\frac{\partial}{\partial t}\right]\hat{a}_n \times \hat{a}_v H_v^i \quad . \tag{60}$$

The relation for the first-order correction to the physical optics far field is obtained by replacing $\vec{J}_{pol}$ in Eq. (58) with the expression given in Eq. (60), which yields

$$r_o \vec{H}^s_{pol} = \frac{1}{2\pi}\frac{\partial}{\partial t}\left\{\hat{a}_{uo}\int_S \left(\frac{\kappa_u - \kappa_v}{4\pi}\right)\left[\pi\rho_o + \left(\frac{\pi\rho_o^2}{2}\right)\frac{\partial}{\partial \tau}\right] H_u^i \; dS_{proj}\right.$$

$$\tau = t - R$$

$$\left. + a_{vo}\int_S \left(\frac{\kappa_v - \kappa_u}{4\pi}\right)\left[\pi\rho_o + \left(\frac{\pi\rho_o^2}{2}\right)\frac{\partial}{\partial \tau}\right] H_v^i \; dS_{proj}\right\} . \tag{61}$$

$$\tau = t - R$$

As a first approximation for ρ_o, the surface at the specular point is assumed to be spherical with curvature κ, which gives

$$\rho_o = (t + z) - \frac{\kappa}{2}(t + z)^2 \tag{62}$$

where the coordinate surface is oriented so that the incident wave is propagating in the negative z direction and the specular point is located on the

z axis at the origin. The effect of the second term in Eq. (62) is second order, and thus for this consideration will be neglected.

Substitution of Eq. (62) (with $\kappa = 0$) into Eq. (61), letting the incident field be an impulse, and carrying out the integration yields, for the first order correction,

$$\vec{r_o H}_{pol} = \frac{1}{2\pi} \frac{\partial S(t_s)}{\partial t} \left[\hat{a}_u \left(\frac{\kappa_u - \kappa_v}{2} \right) + \hat{a}_v \left(\frac{\kappa_v - \kappa_u}{2} \right) \right] \tag{63}$$

where

$S(t_s)$ = the projected area given in Eq. (57)

κ_u = the curvature in tne u direction

κ_v = the curvature in the v direction.

Thus, from Eq. (63) it is noted that the first order correction to the physical optics approximation is proportional to the difference between the principal curvatures at the specular point. Moreover, this correction has the functional form of the first derivative of the projected area, versus the second derivative as given in Eq. (57) for the physical optics approximation itself. This means that for the case of smooth convex targets, such as the prolate spheroid off-axis, the step function in the physical optics approximation will be corrected, and this sign of correction will depend upon the polarization of the incident wave. For example, the amplitude of the negative step will increase (become more negative) for the case of TE polarization, whereas the amplitude of the negative step will decrease for TM polarization. In addition, this first order correction indicates that a ramp function is also present at the leading edge of the prolate spheroid response which has a positive sign in the TE case and a negative sign in the TM case.

It should be noted that the goodness of this analytical expression as a total correction for the physical optics approximation for the far field is a function of the goodness of the approximation used in deriving it. The crucial area is in the use of Eq. (59) and the subsequent approximation for ρ_o as a function of time. In addition, the assumption that the difference in principal curvatures remains the same in the vicinity of the specular point may also be questioned, although to a first approximation this assumption is certainly valid. Finally, the assumption that ρ_o is given by assuming its time variation is due to a plane tangent at the specular point may introduce errors, although this is again valid to a first approximation.

In summary, it is felt that the derivation given in this section is valid to the extent of giving the functional form of the correction terms, the polarization dependence they introduce, and their relationship to the difference of principal curvatures at the specular point. The exact value of the coefficients in these correction terms should, however, be obtained directly

from the computed smoothed impulse responses rather than from the expression given in Eq. (63). This is the technique used in the following two sections to obtain the augmentation functions with polarization dependence.

2.7 SCATTERING BY A PROLATE SPHEROID — NONAXIAL INCIDENCE

2.7.1 Impulse Response Augmentation Technique for Prolate Spheroid

Scattering by a prolate spheroid with a two-to-one axial ratio for axial incidence was considered in Sec. 2.4. This section deals with the case of nonaxial incidence in general and the cases of 30^{o}, 60^{o}, and 90^{o} angles of incidence in particular. As noted in Sec. 2.6.2, the augmentation function of the prolate spheroid will be taken as

$$f_a(t) = P_z\delta(t/a-T_z) + (S_z + S_{z2})u(t/a-T_z) + R_{z2}r_p(t/a-T_z) \qquad (64)$$

where

P_z = the impulse coefficient given by the physical optics approximation

S_z = the step coefficient given by the physical optics approximation

S_{z2} = the step coefficient due to the polarization dependence

R_{z2} = the ramp coefficient due to the polarization dependence

T_z = the time at which the leading edge of the impulse response starts.

The expressions for the physical optics impulse response coefficients for a prolate spheroid with semiminor axis a and semimajor axis b which are centered at the origin are derived in Appendix 8.4. The incident wave is assumed to make an angle α with the major axis. The resulting expressions are

$$T_z = -2\frac{B^{1/2}}{a}$$

$$P_z = \frac{1}{2}\frac{ab}{B} \qquad (65)$$

$$S_z = -\frac{1}{4}\frac{a^2b}{B^{3/2}}$$

$$B = a^2\sin^2\alpha + b^2\cos^2\alpha$$

In this work the values of S_{z2} and R_{z2} were computed from the smoothed impulse response $r(t)$ initially in time by assuming that the total value of $r(t)$ is due to the convolution of $f_a(t)$ given in Eq. (64) with the excitation $e(t)$. The values of S_{z2} and R_{z2} were then determined by equating f_a e with $r(t)$ at the initial time points in the smoothed impulse response and solving the resulting set of linear algebraic equations. Confidence in this approach was further strengthed by noting that the values of S_{z2} and R_{z2} were relatively independent of the particular time points used for their solution.

Table I displays both the physical optics parameters and the polarization dependent physical optics correction parameters for the prolate spheroid with an axial ratio of two-to-one. In Table I the polarization dependent physical optics correction parameters can represent a substantial contribution to the leading edge of the impulse response. It should also be noted that the sign of S_{z2} is negative for the TE case and positive for the TM case, as predicted in Sec. 2.6.2; however, the magnitude differs for the two polarizations. A similar effect is observed for the R_{z2} coefficient.

After obtaining the augmented frequency response, the procedure followed is the same as that described in Sec. 2.4 for the case of axial incidence. The exponential estimate of the high frequency variation is applied to the augmented frequency response to obtain an estimate of the total augmented frequency response,

$$H_a(\omega) = \begin{cases} H_a(\omega) & ; \ \omega < \omega_c \\ A_1 \exp\left[-B_1\omega^{1/3}\right] \exp\left[j\omega m_1 + jb_1\right] & ; \ \omega \geq \omega_c \end{cases} \qquad (66)$$

where b_1 was taken to be zero in all cases. The parameters that result from this procedure are summarized in Table II. Since this high frequency estimate represents the creeping wave, the m_1 parameter represents the time of arrival of the creeping wave. Note in Table II that the damping (which is represented by the B_1 parameter) increases with angle of incidence up through 60^0 and then decreases slightly at 90^0.

In the next two sections the responses obtained for a prolate spheroid with a 2:1 axial ratio are given. In all cases, the smoothed impulse response was calculated by numerical solution of the space-time integral equation with the improved self-term correction feature. The smoothed impulse response, the frequency response obtained by direct transformation, the total frequency response, and the impulse response are displayed for each aspect angle and polarization.

TABLE I

SUMMARY OF AUGMENTATION FUNCTION PARAMETERS
FOR THE PROLATE SPHEROID

Incident Angle	Polarization	T_z	P_z	S_z	S_{z2}	R_{z2}
0	N/A	-4.00	0.25	-0.0625	0.0	0.0
30	TE	-3.6055	0.3077	-0.0853	-0.016	0.012
30	TM	-3.6055	0.3077	-0.0853	0.032	-0.020
60	TE	-2.6458	0.5714	-0.216	-0.132	0.130
60	TM	-2.6458	0.5714	-0.216	0.144	-0.072
90	TE	-2.00	1.00	-0.50	-0.317	0.315
90	TM	-2.00	1.00	-0.50	0.328	-0.190

TABLE II

SUMMARY OF HIGH FREQUENCY ESTIMATION PARAMETERS
FOR AUGMENTED FREQUENCY RESPONSE OF PROLATE SPHEROID

Incident Angle	Polarization	ω_c	ω_2	A_1	B_1	m_1
0	N/A	2.15	3.80	2.185	1.778	-4.878
30	TE	1.50	2.50	2.447	1.942	-4.594
30	TM	2.05	3.20	15.378	3.177	-5.008
60	TE	2.50	3.50	10.656	3.237	-3.841
60	TM	1.40	2.60	13.584	3.244	-4.925
90	TE	2.00	3.00	7.778	3.064	-3.435
90	TM	1.50	2.40	4.674	2.688	-4.852

2.7.2 Prolate Spheroid — TE Polarization

The smoothed impulse response for a 30^{o} angle of incidence is displayed in Fig. 52, and the frequency response obtained by direct transformation of the smooth impulse response is displayed in Fig. 53. Figure 54 displays the impulse response and Fig. 55 displays the frequency response that results by applying the impulse response augmentation technique. In Fig. 54 the initial impulse and negative step due to the specular point is seen at $t/a = -3.6$ and is followed by a positive ramp. Later, at $t/a = 4.6$, a positive return due to the creeping wave may be noted. The frequency response in Fig. 55 displays a resonant character that may be attributed to the interference between the specular return and the creeping wave return.

The smoothed impulse response and the frequency response by direct transformation are shown in Figs. 56 and 57, respectively, for a 60^{o} angle of incidence. The positive ramp type variation predicted by the first order correction to the physical optics response is clearly obvious in the smoothed impulse response shown in Fig. 56. The impulse response and frequency response obtained using the augmentation technique are displayed in Figs. 58 and 59, respectively. It is interesting to note that the negative initial ramp response is larger than one would expect by examining only the smoothed impulse response. Moreover, the transition region from the obvious ramp variation to a different function variation at approxiately $t/a = -1.6$ coincides approximately with the time the incident wave first reaches the shadow region. The effect seems to be present for both polarizations.

In Figs. 60 and 61 appear the smoothed impulse response and direct frequency response, respectively, for a 90^{o} angle of incidence. The impulse response and frequency response for this aspect angle are drawn in Figs. 62 and 63, respectively. Note that both the amplitude of the negative step and the positive ramp have increased but that the creeping wave is less "sharp". Again the transition between the initial ramp occurs at approximately $t/a = 0$ or the time the incident wave first reaches the shadow boundary. In the frequency response displayed in Fig. 63 a resonance is still noted between the specular return and the creeping wave return; however, it possesses a longer period (in frequency) and is weaker than observed in the 30^{o} and 60^{o} cases.

2.7.3 Prolate Spheroid — TM Polarization

For a 30^{o} angle of incidence the smoothed impulse response and the directly transformed frequency response are shown in Figs. 64 and 65, respectively. The impulse response augmentation technique yields the impulse response given in Fig. 66 and the frequency response given in Fig. 67. The strong resonance noted in the frequency response is due to the interference between the specular return at $t/a = -3.6$ and the creeping wave return at $t/a = 5.0$, as seen in Fig. 66.

Figures 68 and 69 display the smoothed impulse response and the directly transformed frequency response, respectively, for a 60^{o} angle of incidence. Comparison of the smoothed impulse response shown in Fig. 68 for TM polarization with the response shown in Fig. 56 for TE polarization clearly illustrates the polarization dependence in the smoothed response

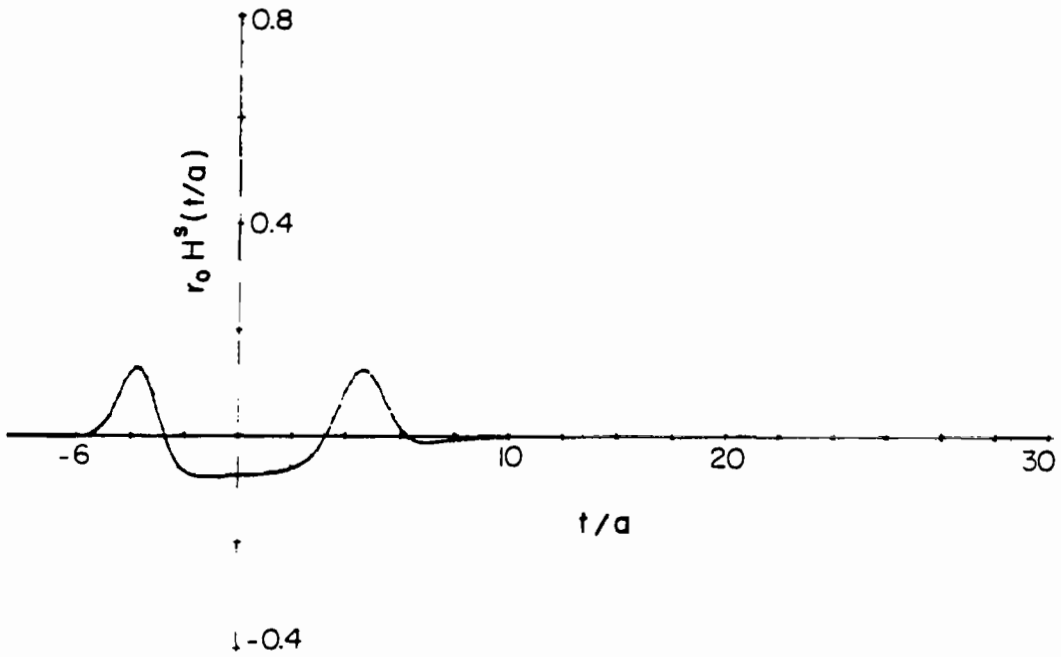

FIG. 52 Smoothed impulse response of prolate spheroid with radius a, axial ratio 2:1, TE polarization and 30^o angle of incidence.

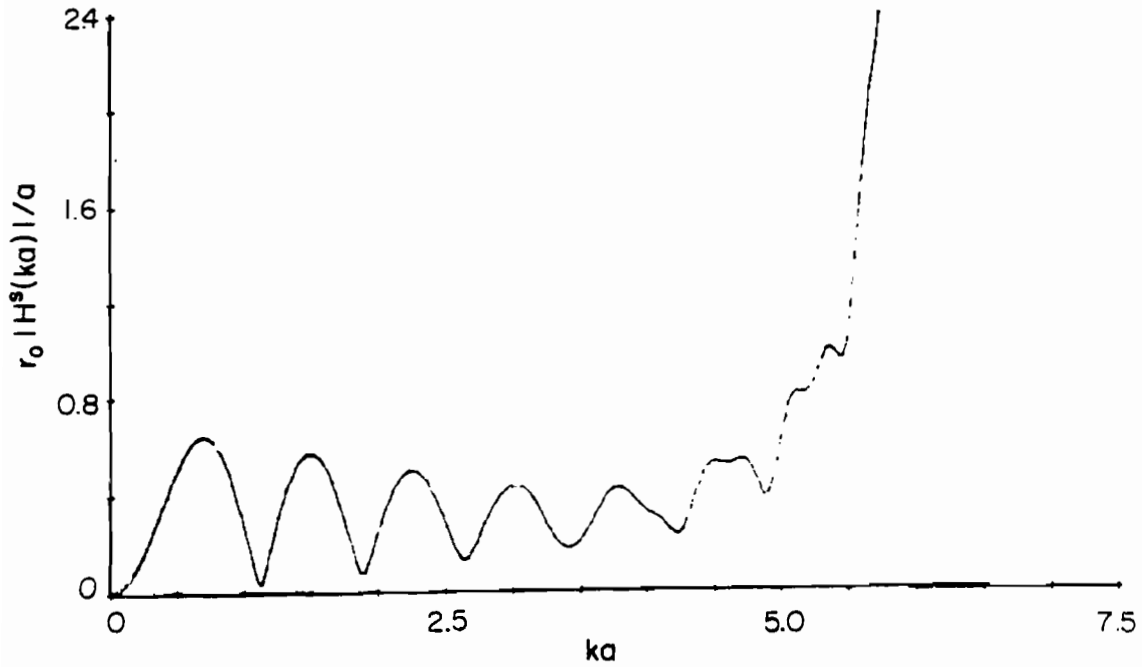

FIG. 53 Magnitude of frequency response of prolate spheroid obtained by direct transformation for TE polarization and 30^o angle of incidence.

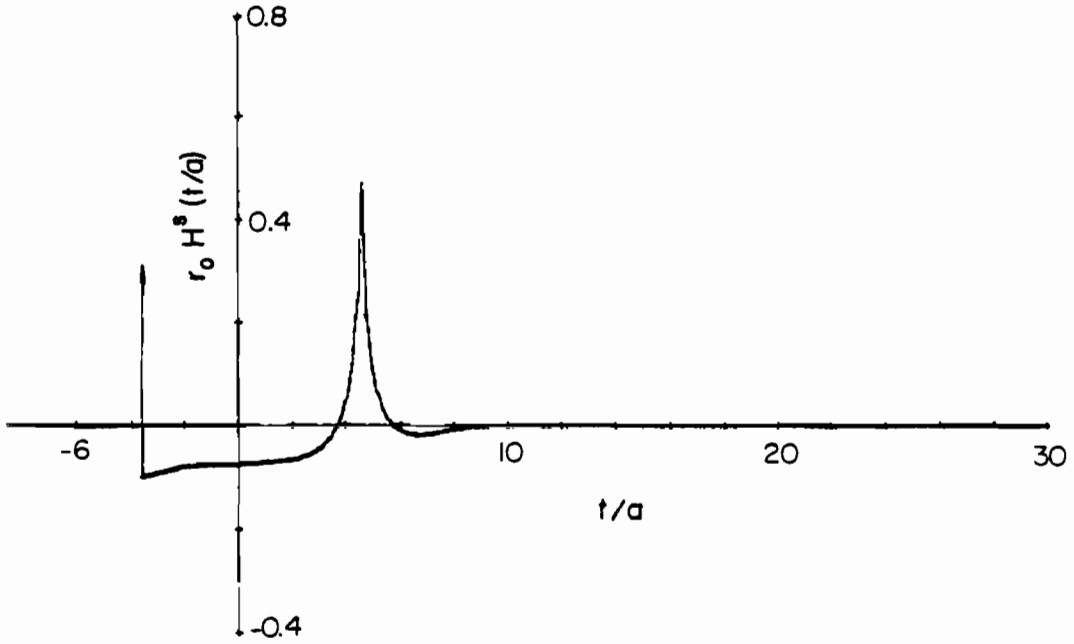

FIG. 54 Impulse response of prolate spheroid with radius a, axial ratio 2:1, TE polarization and 30° angle of incidence.

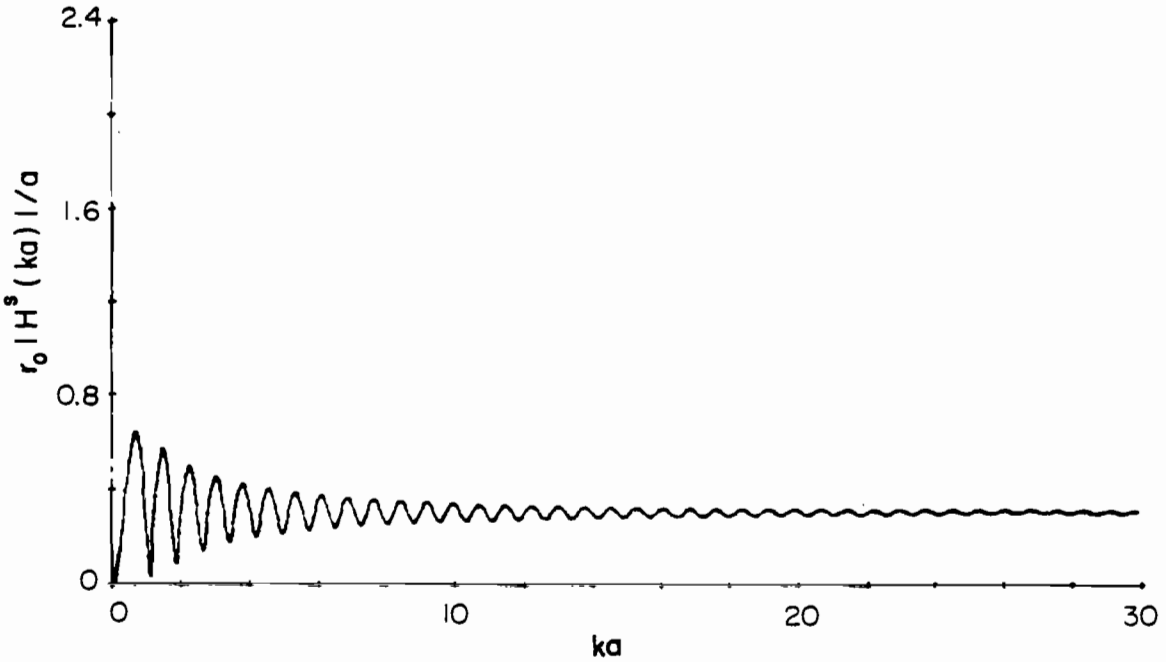

FIG. 55 Magnitude of frequency response of prolate spheroid with radius a, axial ratio 2:1, TE polarization and 30° angle of incidence.

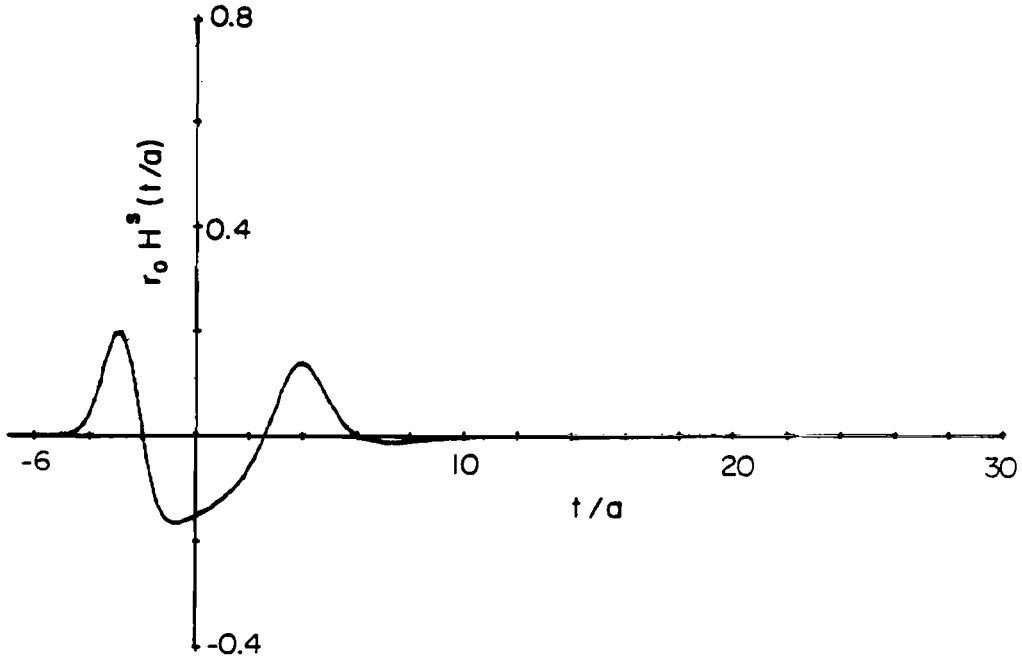

FIG. 56 Smoothed impulse response of prolate spheroid with radius a, axial ratio 2:1, TE polarization and 60^0 angle of incidence.

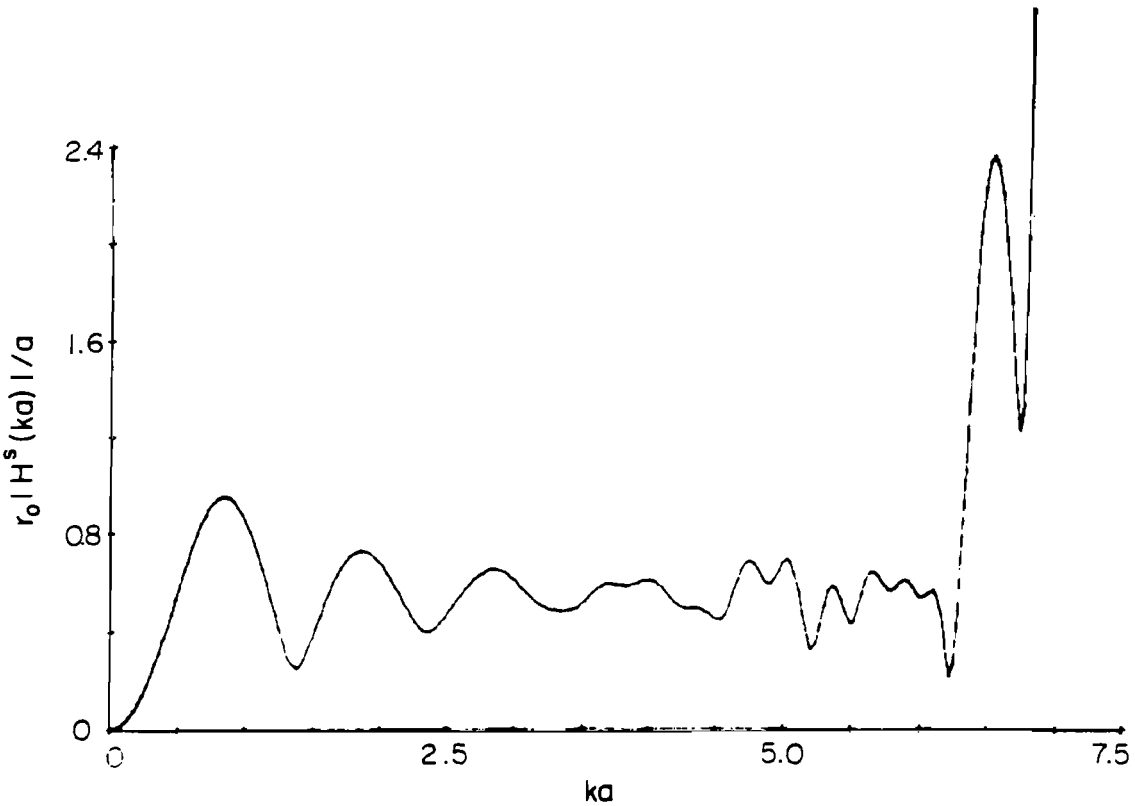

FIG. 57 Magnitude of frequency response of prolate spheroid obtained by direct transformation for TE polarization and 60^0 angle of incidence.

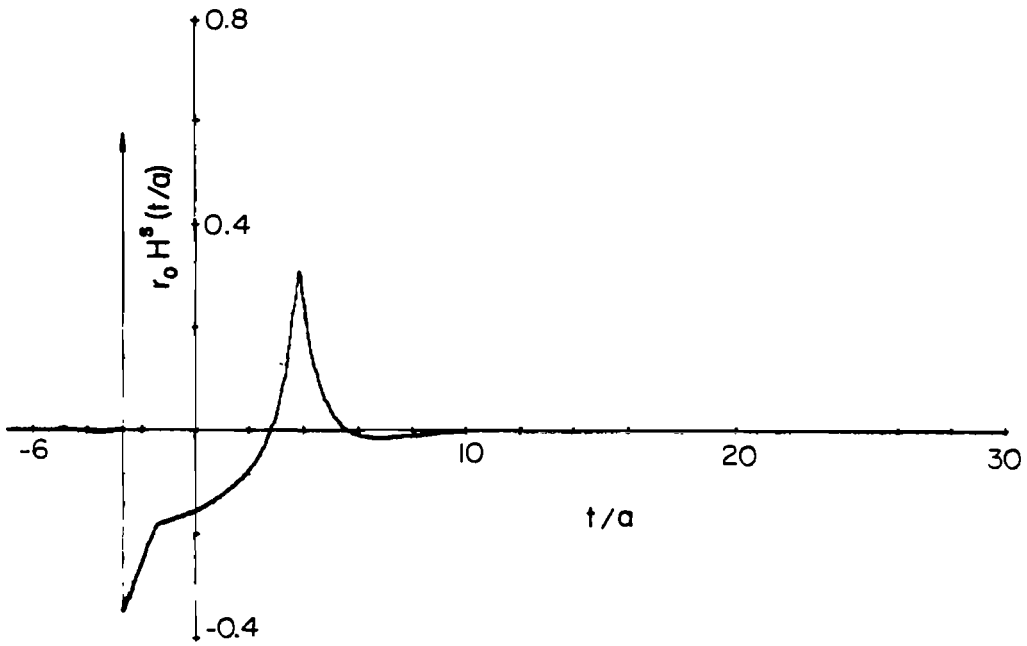

FIG. 58 Impulse response of prolate spheroid with radius a, axial ratio 2:1, TE polarization and 60^o angle of incidence.

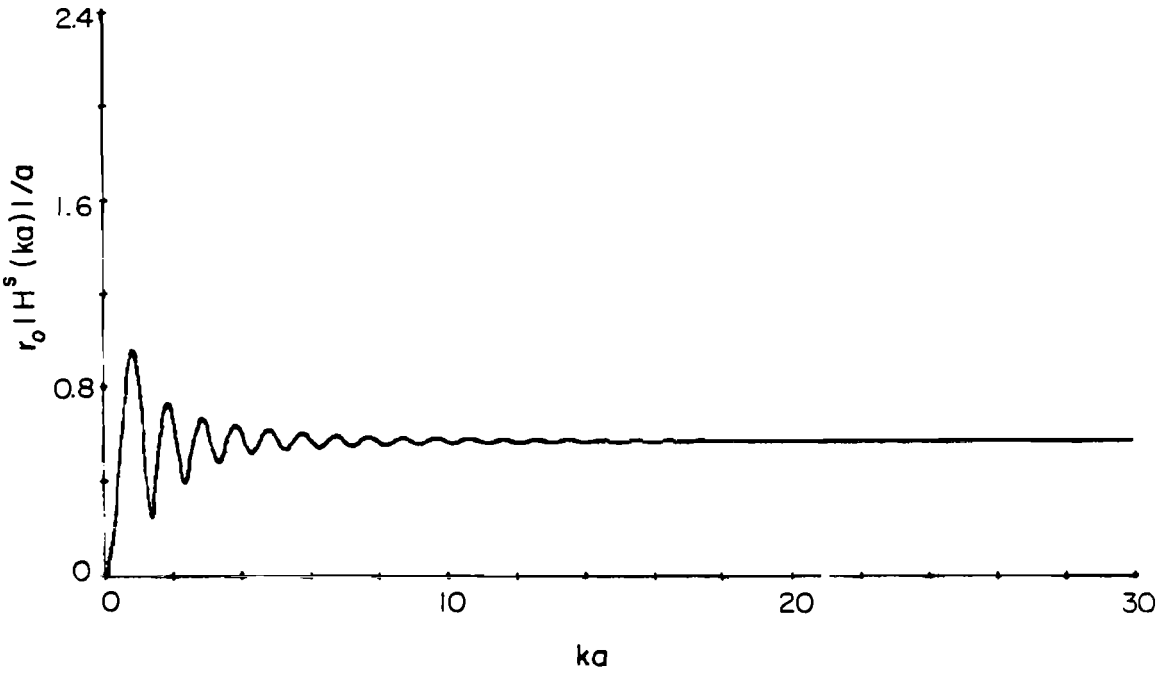

FIG. 59 Magnitude of frequency response of prolate spheroid with radius a, axial ratio 2:1, TE polarization and 60^o angle of incidence.

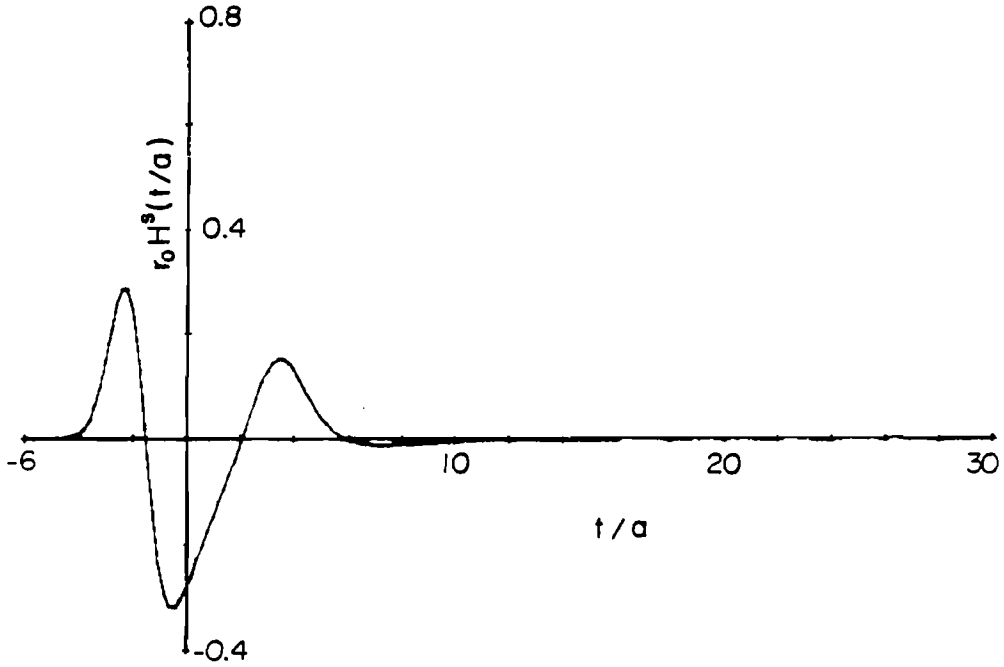

FIG. 60 Smoothed impulse response of prolate spheroid with radius a, axial ratio 2:1, TE polarization and 90^0 angle of incidence.

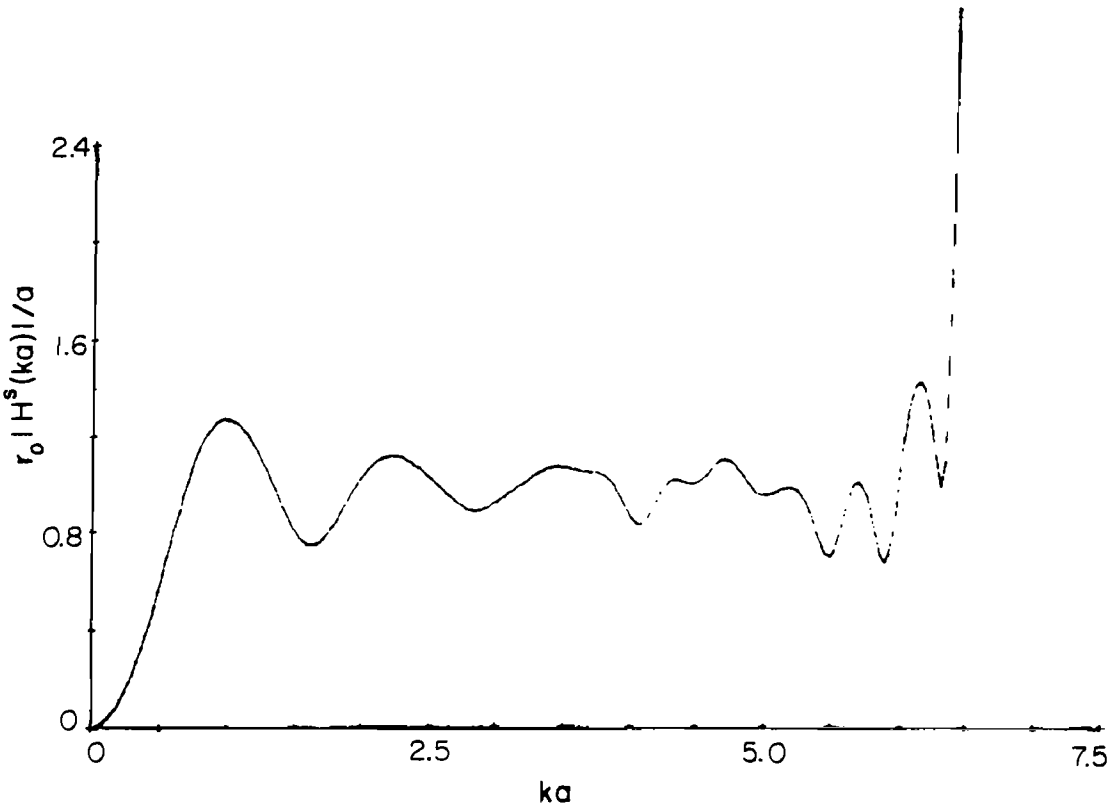

FIG. 61 Magnitude of frequency response of prolate spheroid obtained by direct transformation for TE polarization and 90^0 angle of incidence.

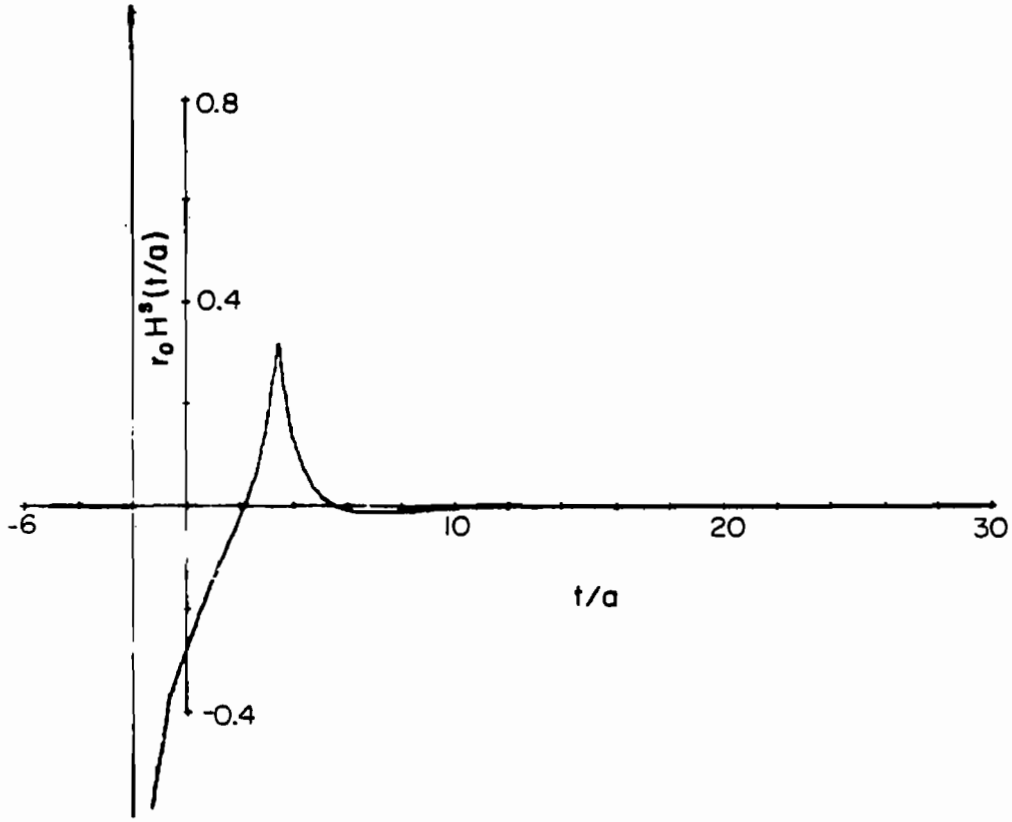

FIG. 62 Impulse response of prolate spheroid with radius a, axial ratio 2:1, TE polarization and 90^0 angle of incidence.

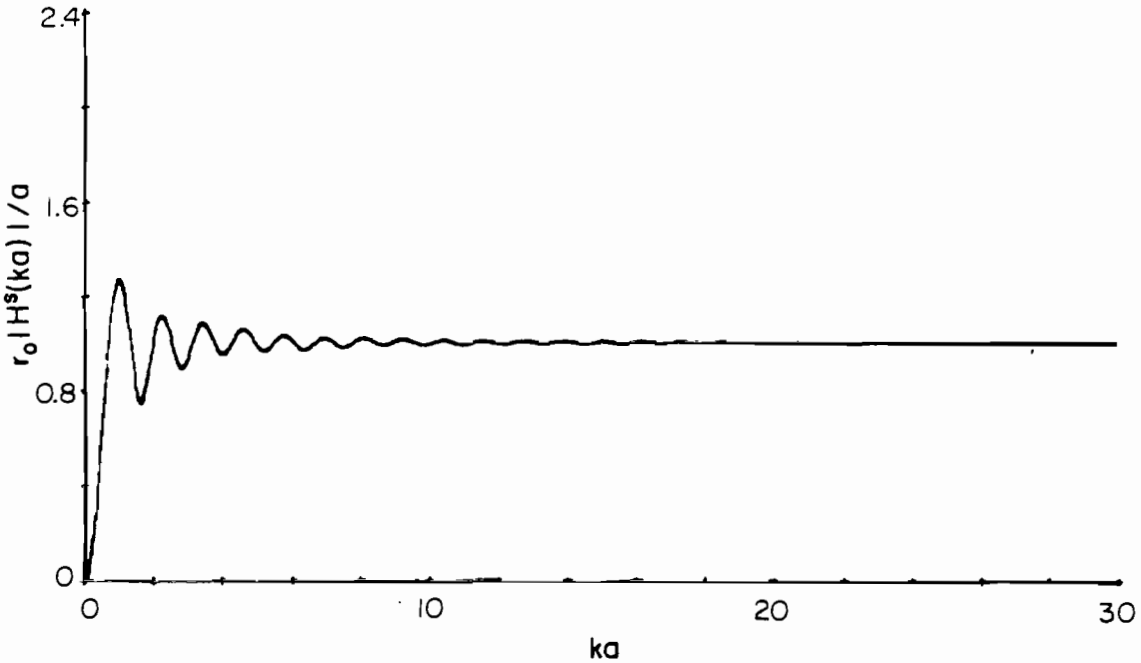

FIG. 63 Magnitude of frequency response of prolate spheroid with radius a, axial ratio 2:1, TE polarization and 90^0 angle of incidence.

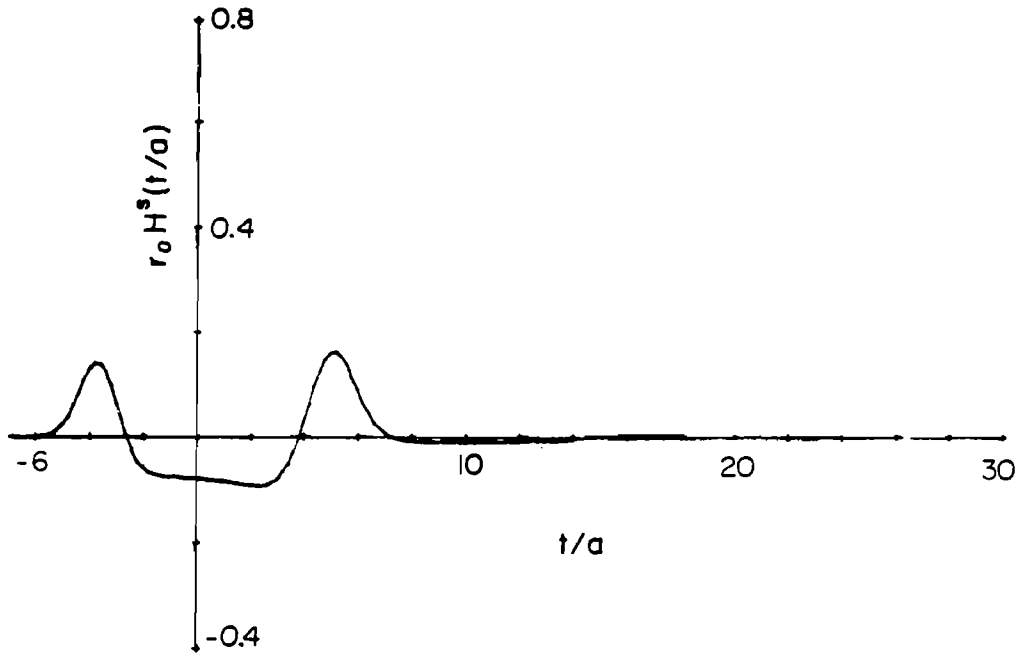

FIG. 64 Smoothed impulse response of prolate spheroid with radius a, axial ratio 2:1, TM polarization and 30^0 angle of incidence.

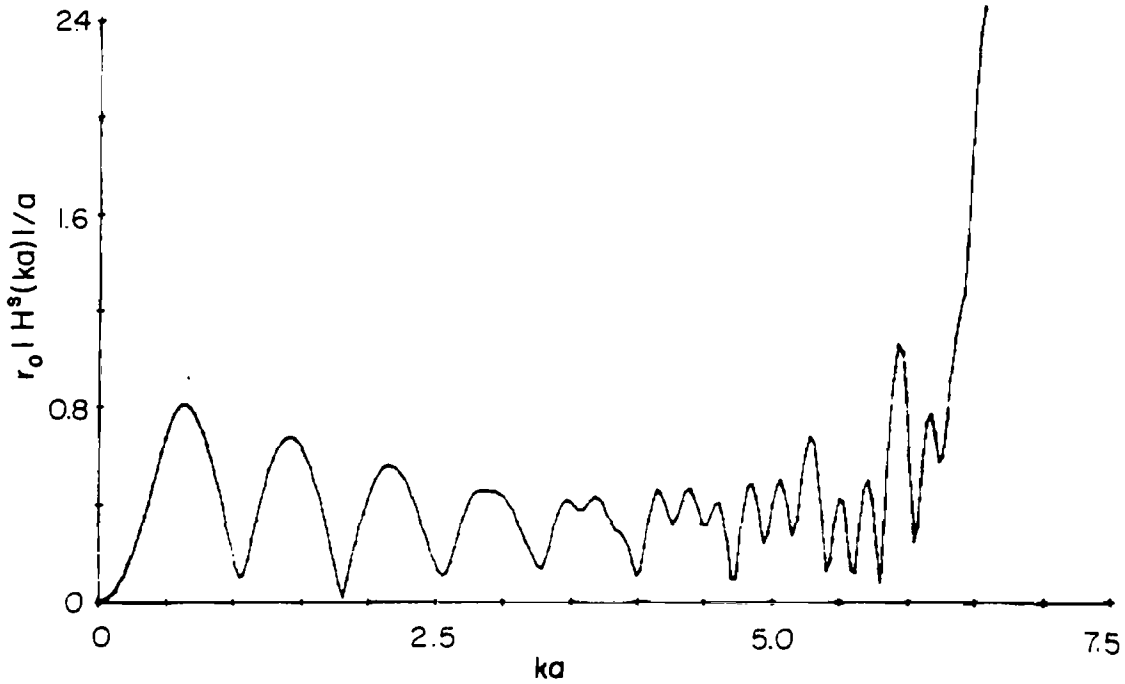

FIG. 65 Magnitude of frequency response of prolate spheroid obtained by direct transformation for TM polarization and 30^0 angle of incidence.

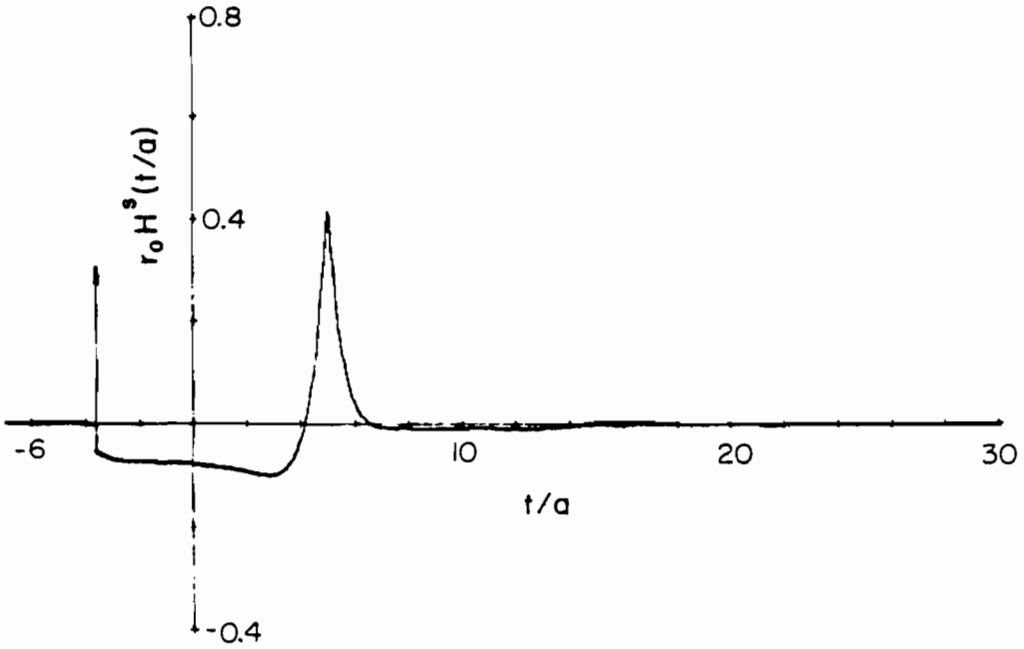

FIG. 66 Impulse response of prolate spheroid with radius a, axial ratio 2:1, TM polarization and 30^0 angle of incidence.

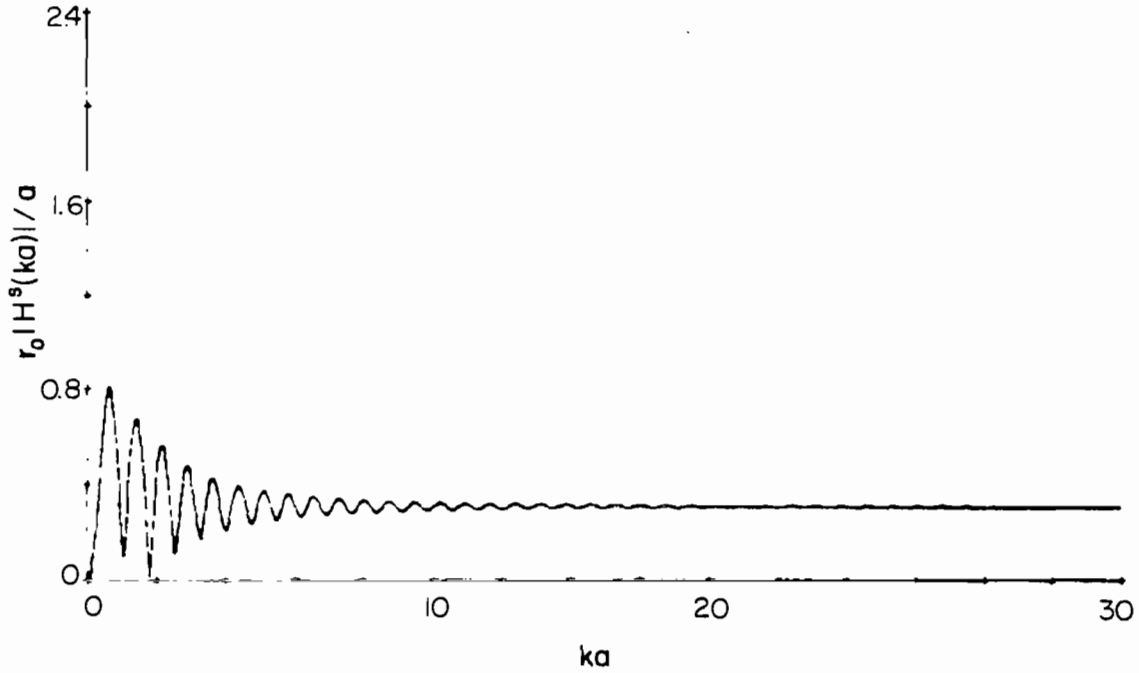

FIG. 67 Magnitude of frequency response of prolate spheroid with radius a, axial ratio 2:1, TM polarization and 30^0 angle of incidence.

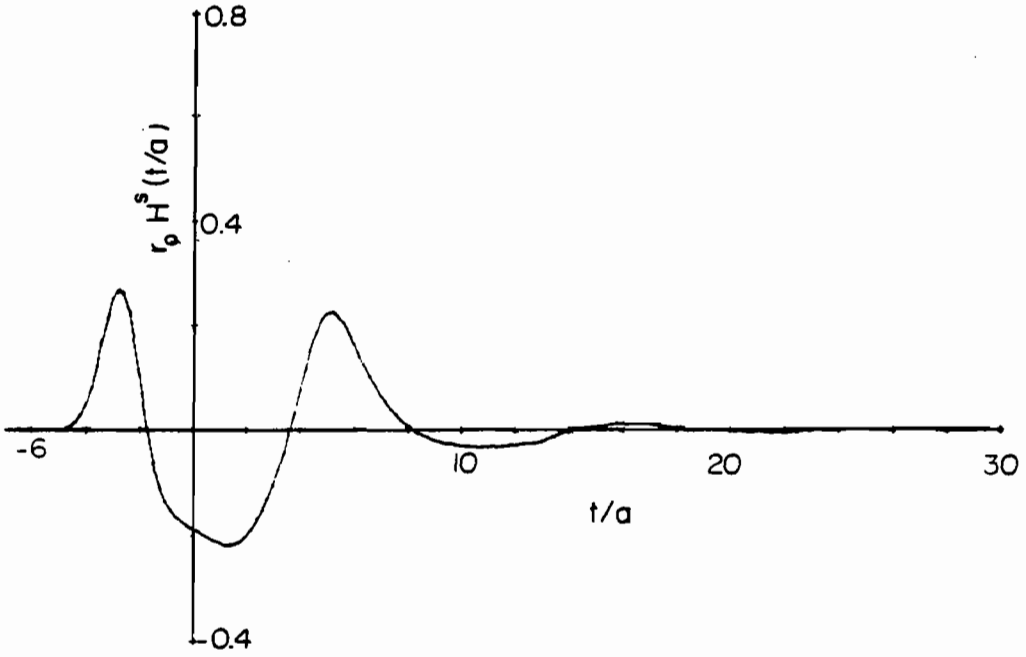

FIG. 68 Smoothed impulse response of prolate spheroid with radius a, axial ratio 2:1, TM polarization and 60^0 angle of incidence.

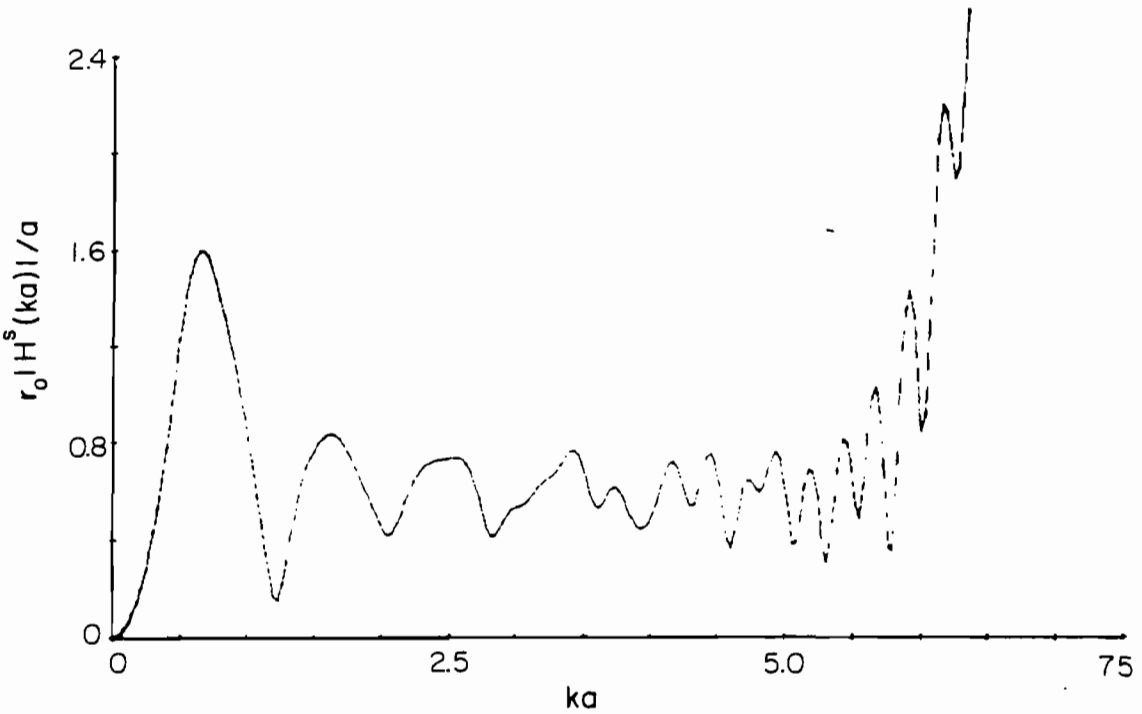

FIG. 69 Magnitude of frequency response of prolate spheroid obtained by direct transformation for TM polarization and 60^0 angle of incidence.

after the specular return. The impulse response and the frequency response for this case are shown in Figs. 70 and 71, respectively. As in the TE case, Fig. 70 also indicates that a transition from the initial ramp response occurs in the vicinity of the time the incident wave first reaches the shadow region.

The final example for the prolate spheroid is given for a 90^{o} angle of incidence. The smoothed impulse response is displayed in Fig. 72 and the frequency response obtained by direct transformation is shown in Fig. 73. It appears in Fig. 72 that a damped oscillation is set up after the creeping wave in the smoothed impulse, which would be expected for the TM polarization. The impulse response and frequency response computed using the impulse response augmentation technique are shown in Figs. 74 and 75, respectively. Note that the value of the initial step in Fig. 74 is less than that for the TE case in Fig. 62, and again the transition from the initial ramp appears at approximately the time the incident wave reaches the shadow region.

2.8 SCATTERING BY SPHERE-CAPPED CYLINDER — NONAXIAL INCIDENCE

2.8.1 Impulse Response Augmentation Technique for Sphere-Capped Cylinder

Scattering by a sphere-capped cylinder with a 3:1 length-to-diameter ratio for axial incidence was considered in Sec. 2.5. For that case, distinct returns were noted from the nose, from both the front and rear sphere-capped cylinder joins, and from the creeping wave. This section considers the case of nonaxial incidence in general and the incident angles of 30^{o}, 60^{o} and 90^{o} in particular for both TE and TM polarizations.

The augmentation function used for the leading edge of the impulse response of the sphere-capped cylinder was taken as

$$f_{a1}(t) = P_z\delta(t/a-T_z) + S_z u(t/a-T_z) + G_z(t/a-T_z)^{-3/2}\, u(t/a-T_z) + S_{z2}u(t/a-T_z) + H_z(t/a-T_z)^{-1/2}\, u(t/a-T_z) \qquad (67)$$

where $T_z = -2$

$P_z = 1/2$

$S_z = -1/4$

$$G_z = \begin{cases} 0 & ; \quad 0 \leq \alpha < 90 \\ -\frac{1}{\pi} & ; \quad \alpha = 90^{o} \end{cases}$$

S_{z2} = the polarization dependent correction to the step function from the physical optics approximation

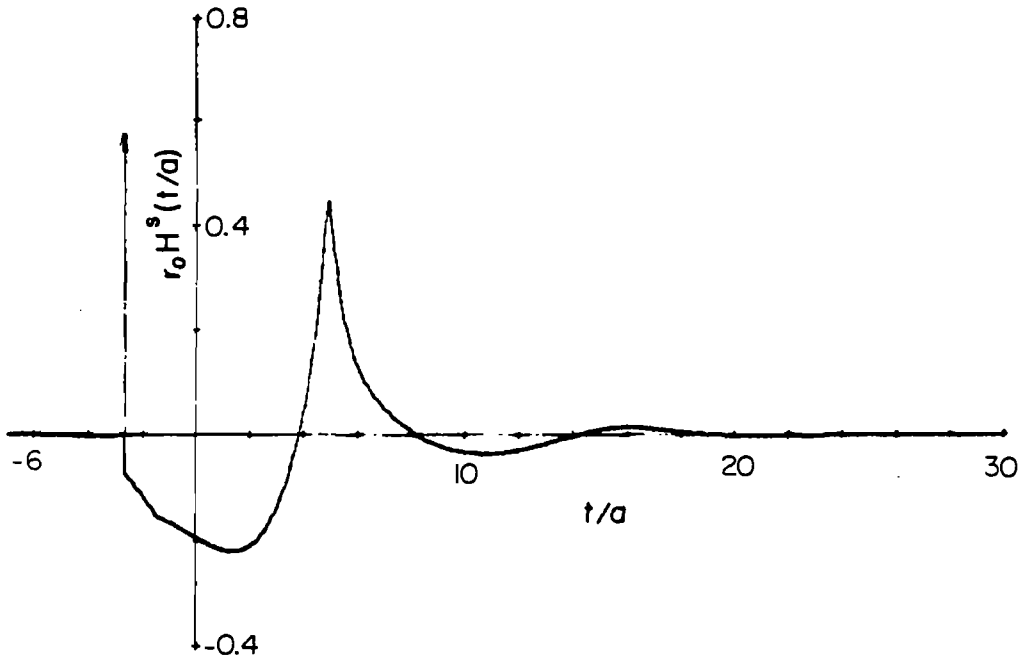

FIG. 70 Impulse response of prolate spheroid with radius a, axial ratio 2:1, TM polarization and 60^0 angle of incidence.

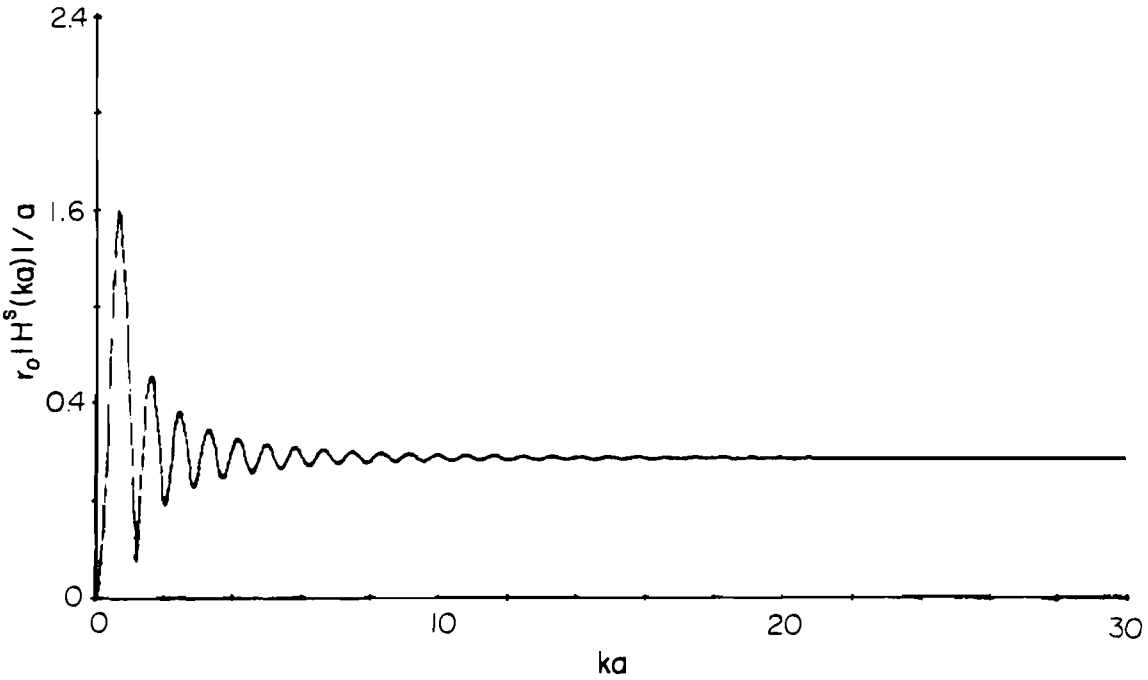

FIG. 71 Magnitude of frequency response of prolate spheroid with radius a, axial ratio 2:1, TM polarization and 60^0 angle of incidence.

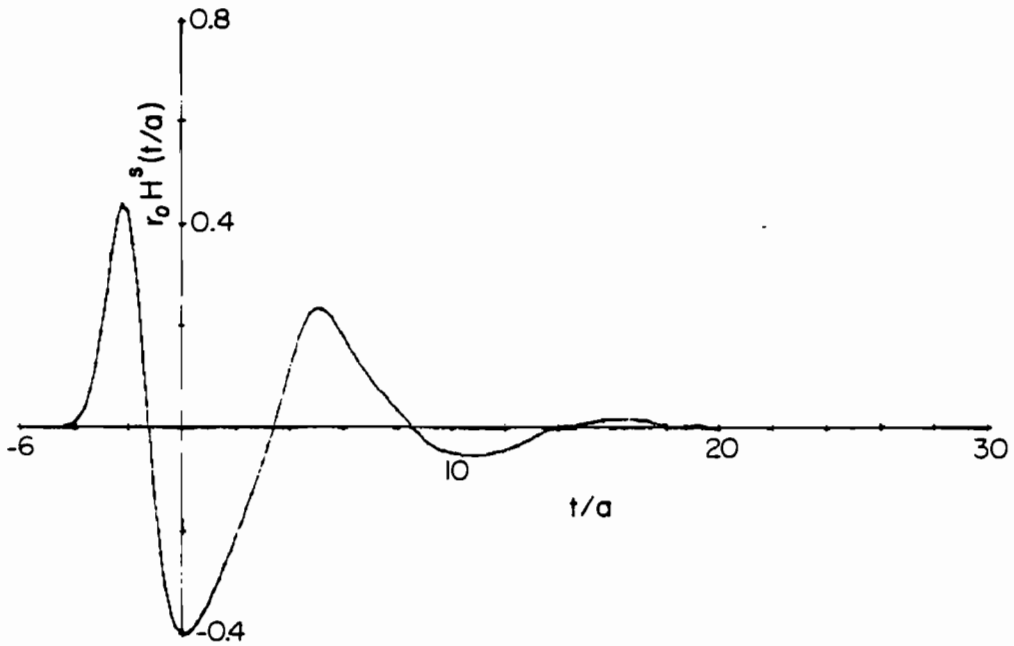

FIG. 72 Smoothed impulse response of prolate spheroid with radius a, axial ratio 2:1, TM polarization and 90^0 angle of incidence.

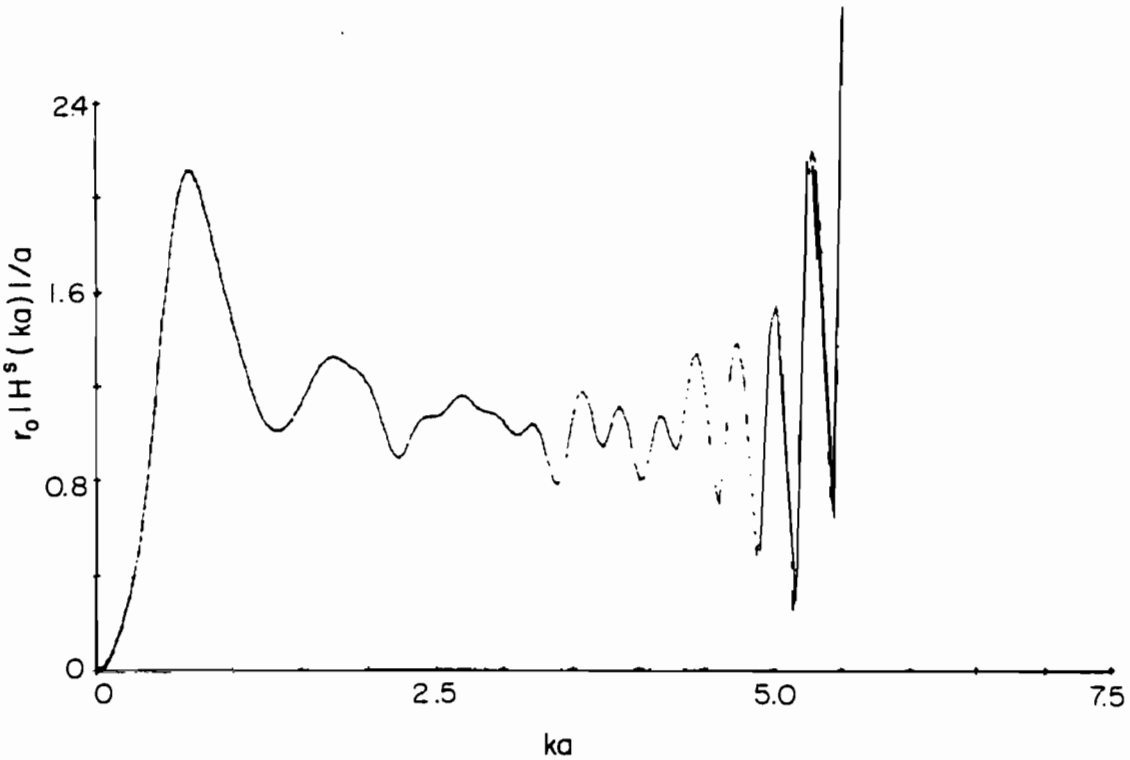

FIG. 73 Magnitude of frequency response of prolate spheroid obtained by direct transformation for TM polarization and 90^0 angle of incidence.

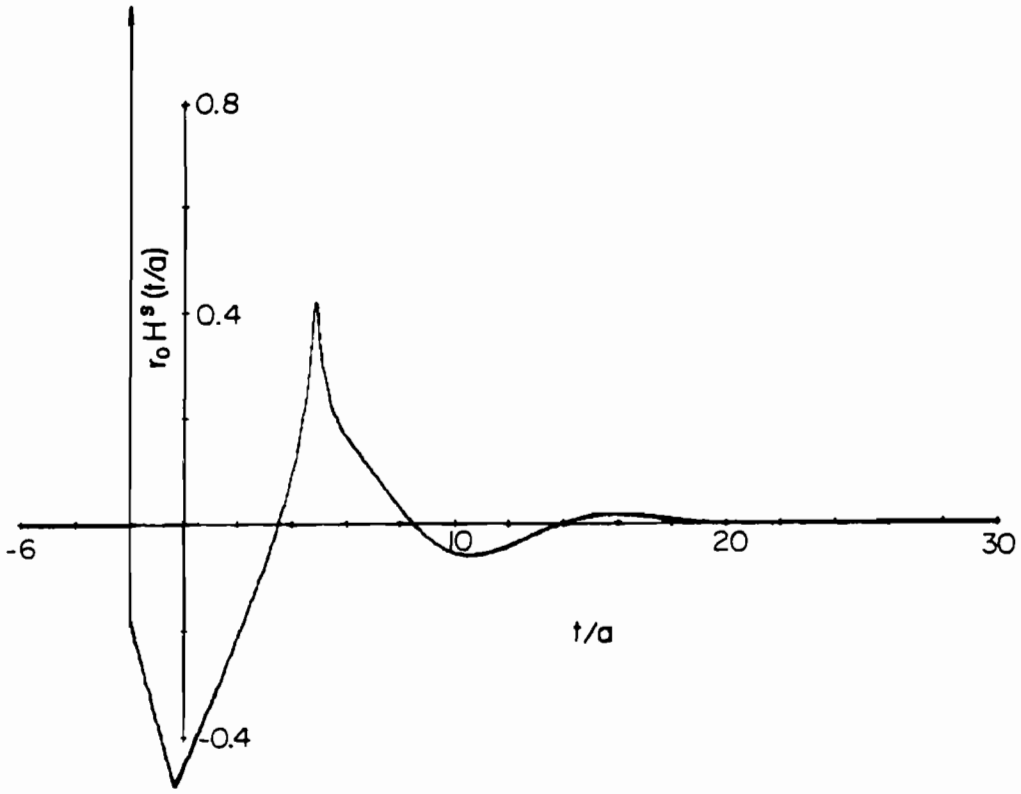

FIG. 74 Impulse response of prolate spheroid with radius a, axial ratio 2:1, TM polarization and 90^0 angle of incidence.

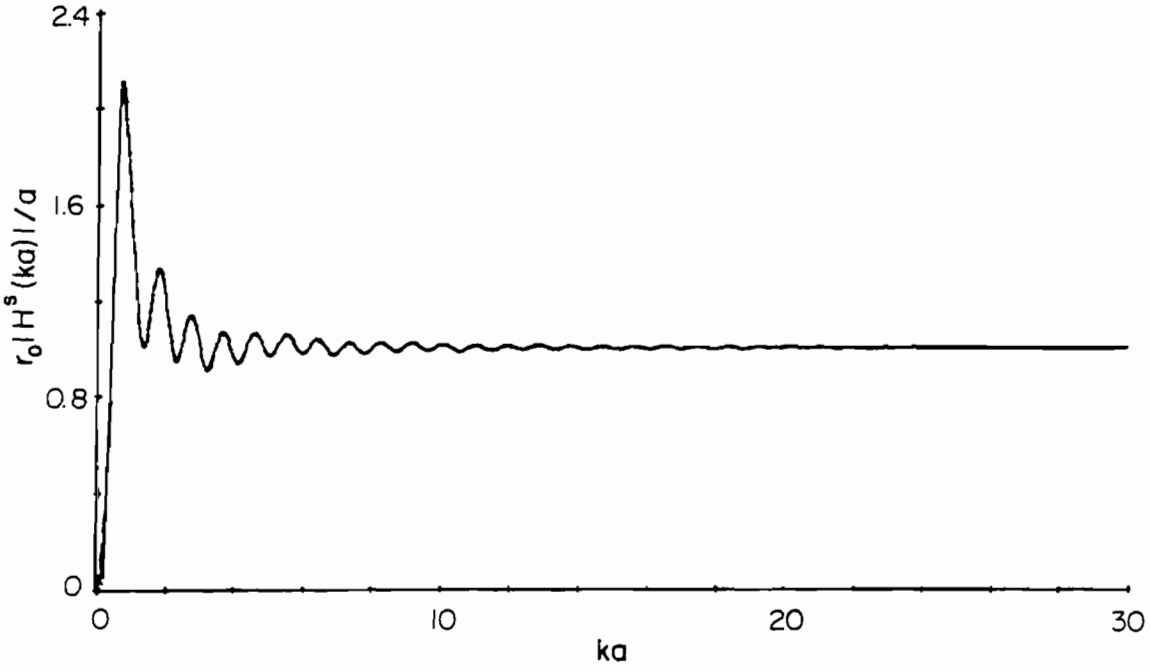

FIG. 75 Magnitude of frequency response of prolate spheroid with radius a, axial ratio 2:1, TM polarization and 90^0 angle of incidence.

H_z = the polarization dependent parameter from the first order correction to the physical optics approximation.

The expression for the first three terms and their coefficients in Eq. (67) is derived in Appendix 8.5 and is simply the leading edge of the impulse response obtained by the physical optics approximation. The fourth and fifth terms are the most significant part of the first derivative of the projected area and, as discussed in Sec. 2.6.2, are the polarization dependent first order corrections to the physical optics results. The parameters S_{z2} and H_z were obtained by equating $f_{a1}(t) * e(t)$ to $r(t)$ initially in time and had reasonable stability of value over the initial time points. The values of these parameters for the leading edge augmentation function of the sphere-capped cylinder are presented in Table III. It should be noted that the leading edge response is identical to that of a sphere except at an angle of 90^0, where the effect of the specular return from the cylinder is noted and the polarization dependent correction in the step function and in H_z due to the non-equal principal curvatures along the cylinder appears.

The augmentation function used to represent the return from the first sphere-capped cylinder join is given by

$$f_{a2} = A_{v2}(t/a-T_{J1})^{-1/2}\, u(t/a-T_{J1}) + A_{v3}(t/a-T_{J1})^{1/2}\, u(t/a-T_{J1}) \quad . \quad (68)$$

In Appendix 8.6 this functional form is derived based on the physical optics approximation for the surface currents. The value of T_{J1} was taken to be the initial time of the first join return, and the values of A_{v2} and A_{v3} were computed numerically by equating $f_{a2} * e$ with r_{a1}. Again, a reasonable degree of stability in the resulting coefficient values was obtained. The coefficients for the first join return are displayed in Table IV. Note that in all cases A_{v3} is greater than A_{v2} and in most cases A_{v3} is much greater than A_{v2}. This may lead one to suspect that perhaps A_{v2} should be zero, even though it is predicted by physical optics.

By applying the augmentation functions f_{a1} and f_{a2} and transforming, the augmented frequency response $H_a(\omega)$ is obtained. The high-frequency estimate of its variation is made assuming that the two contributors to it are the second join return and the creeping wave return. Thus, the estimate for the total augmented frequency response is written as

$$\hat{H}_a(\omega) = \begin{cases} H_a(\omega) \; ; \; \omega \le \omega_2 \\ A_1 \exp(-B_1\omega^{1/3})\exp(j\omega m_1 + jb_1) + \dfrac{A_2}{\omega^{3/2}} \exp(j\omega m_2 + jb_2); \; \omega > \omega_2 \end{cases} \quad . \quad (69)$$

The second join return is assumed here to have a $\omega^{3/2}$ variation, which in the time domain represents a $t^{1/2}$ variation. It is also assumed that the phase offset b_1 of the creeping wave is zero. The damping factor B_1 of

TABLE III

SUMMARY OF LEADING EDGE AUGMENTATION FUNCTION PARAMETERS FOR THE SPHERE-CAPPED CYLINDER

Incident Angle	Polarization	T_z	P_z	S_z	S_{z2}	G_z	H_z
0	N/A	-2.0	0.5	-0.25	0	0	0
30	TE	-2.0	0.5	-0.25	0	0	0
30	TM	-2.0	0.5	-0.25	0	0	0
60	TE	-2.0	0.5	-0.25	0	0	0
60	TM	-2.0	0.5	-0.25	0	0	0
90	TE	-2.0	0.5	-0.25	0.377	-0.3183	-0.458
90	TM	-2.0	0.5	-0.25	-0.154	-0.3183	0.195

TABLE IV

SUMMARY OF FIRST JOIN AUGMENTATION FUNCTION PARAMETERS FOR SPHERE-CAPPED CYLINDER

Incident Angle	Polarization	T_{J1}	A_{v2}	A_{v3}
0	N/A	0.	0.	0.
30	TE	-1.0	-0.008	0.150
30	TM	-1.0	0.028	0.138
60	TE	-1.732	0.029	0.083
60	TM	-1.732	0.035	0.270
90	TE	-2.0	0.	0.
90	TM	-2.0	0.	0.

the creeping wave is assumed to be the same as that of the sphere for all aspect angles and polarizations. This is based on the fact that the creeping wave will always travel around the back of the sphere-cap; however, it is suspected that the damping factor will vary with aspect angle, since the length of creeping wave travel will vary. The value of m_2 is chosen to correspond to the time location of the second join return. The remaining coefficients A_1, A_2, m_1, and b_2 are computed in the same manner as was used for the case of axial incidence, described in Sec. 2.5. The values of the parameters used in the computation are given in Table V and the resulting coefficients are given in Table VI.

In the following two sections, results are presented for 30^o, 60^o, and 90^o angles of incidence and both polarizations. The smoothed impulse response, which is the basis of all computations, was obtained by numerical solution of the space-time integral equation with the self-term correction feature incorporated into the solution procedure.

2.8.2 Sphere-Capped Cylinder — TE Polarization

The smoothed impulse response of the sphere-capped cylinder at a 30^o angle of incidence is shown in Fig. 76, and the companion frequency response obtained by direct transformation is given in Fig. 77. The smoothed impulse response in Fig. 76 appears to be very similar to the result obtained for axial incidence, which is displayed in Fig. 37. In application of the impulse response augmentation technique for all off-axis cases, the smoothed impulse response was considered as one function because it was not possible in general to divide it into two functions as was done for the case of axial incidence in Sec. 2.5. The resulting impulse response and frequency response are shown in Figs. 78 and 79, respectively. The initial portion of the impulse response contains an impulse and a negative step, and until the first join at $t/a = -1.00$ the response should be identical to that of the sphere. Next, at $t/a = -1$ the effect of the first join should appear. It is interesting to note that in this case the contribution due to the second join was found to be negligible since the A_2 coefficient is zero in Table VI. Finally, the creeping wave return is observed at $t/a = 10.19$ rather than at 10.07, which would be expected for a wave traveling at the speed of light.

Figures 80 and 81 display the smoothed impulse response and the directly transformed frequency response for a 60^o angle of incidence. Even in the smoothed impulse response the effect of the second join return is apparent at $t/a \simeq 2.3$ in Fig. 80. The impulse response and the frequency response computed with the impulse response augmentation technique are displayed in Figs. 82 and 83, respectively. Note in the impulse response that the initial portion of the return is identical to that of a sphere, but at $t/a = -1.73$ the effect of the first join return appears as a sharp positive increase in the response. Then there is a smooth region until the effect of the second join appears as a sharp negative swing at $t/a = 2.27$. Finally, the creeping wave appears as a positive pulse at $t/a = 7.50$ rather than at 7.14, where a wave moving at the speed of light would appear. The effects of the join returns are evident in the lower portion of the frequency response as irregularities in the resonant character of this response. However, as in most other cases, the source of the dominant response is the interference

TABLE V

PARAMETERS USED IN COMPUTATION OF HIGH FREQUENCY ESTIMATE OF AUGMENTED FREQUENCY RESPONSE FOR SPHERE-CAPPED CYLINDER

Incident Angle	Polarization	B_1	b_2	ω_2	ω_3	$H_a(\omega_3)$
0	N/A	2.05085	0	2.486	3.470	0.2095
30	TE	2.05085	0	2.976	-	-
30	TM	2.05085	0	1.690	2.348	0.280
60	TE	2.05085	0	1.610	2.211	0.1836
60	TM	2.05085	0	1.108	1.559	0.338
90	TE	2.05085	0	2.00	-	-
90	TM	2.05085	0	1.00	-	-

TABLE VI

SUMMARY OF HIGH FREQUENCY ESTIMATION PARAMETERS FOR AUGMENTED FREQUENCY RESPONSE OF SPHERE-CAPPED CYLINDER

Incident Angle	Polarization	M_1	M_2	b_2	A_1	A_2
0	N/A	-11.192	-8.00	-4.795	3.676	0.289
30	TE	-10.19	-5.93	-	2.741	0.0
30	TM	-10.706	-5.93	-4.930	2.987	0.303
60	TE	- 7.498	-2.27	-5.275	2.101	0.126
60	TM	- 9.242	-2.27	-4.583	2.698	0.171
90	TE	- 3.427	-2.00	-	4.401	-
90	TM	- 6.860	-2.00	-	1.699	-

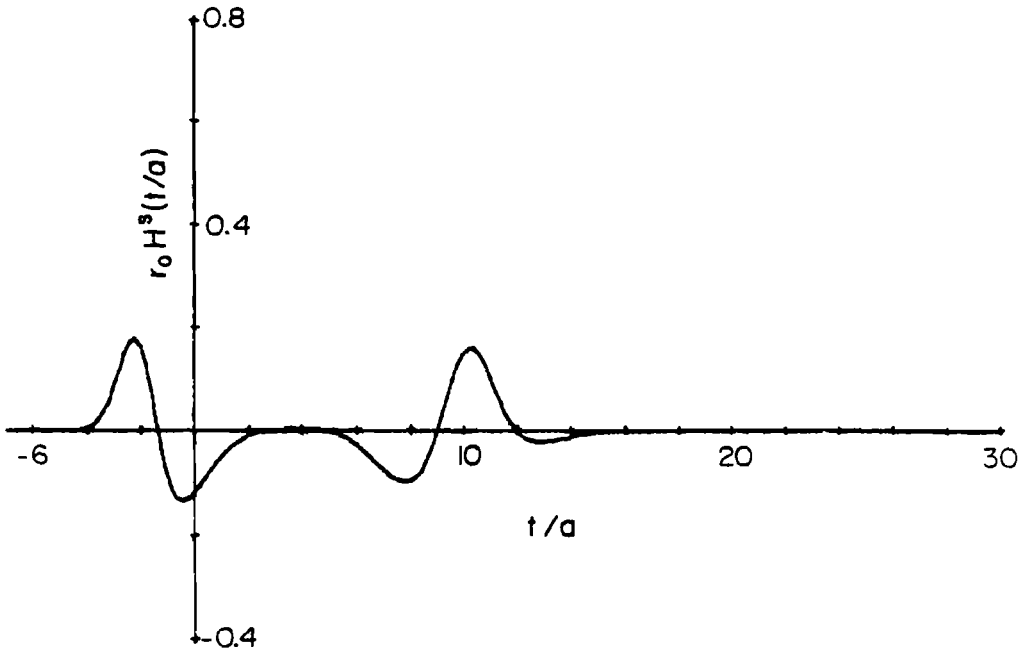

FIG. 76 Smoothed impulse response of sphere capped cylinder with radius a, length-to-diameter ratio 3:1, TE polarization and 30° angle of incidence.

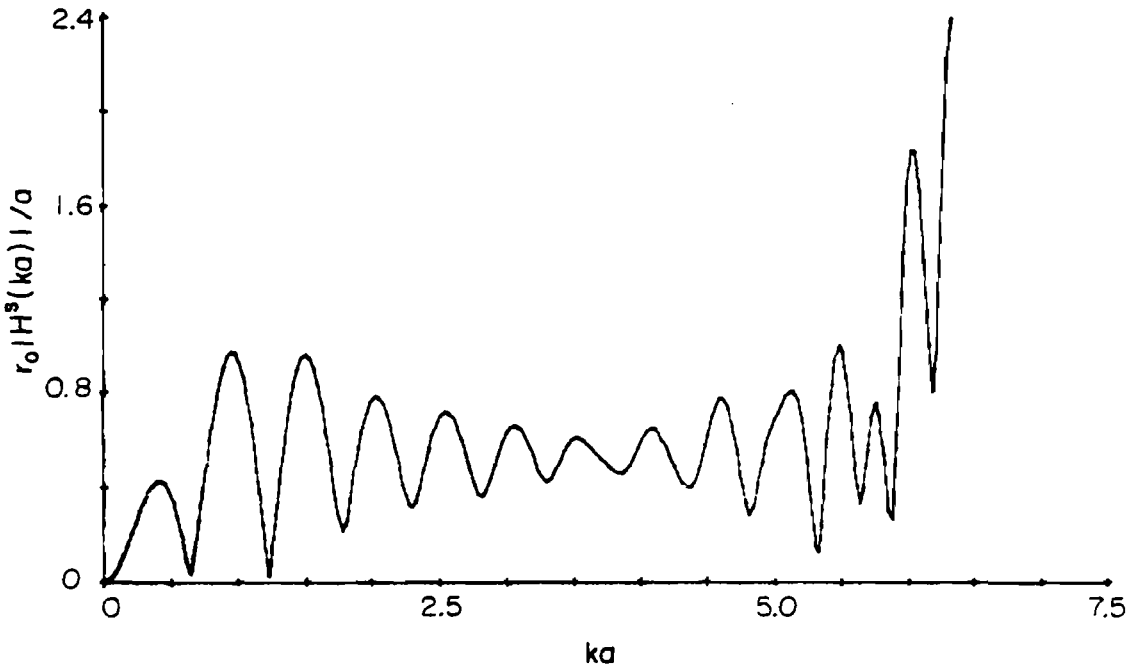

FIG. 77 Magnitude of frequency response of sphere capped cylinder obtained by direct transformation for TE polarization and 30° angle of incidence.

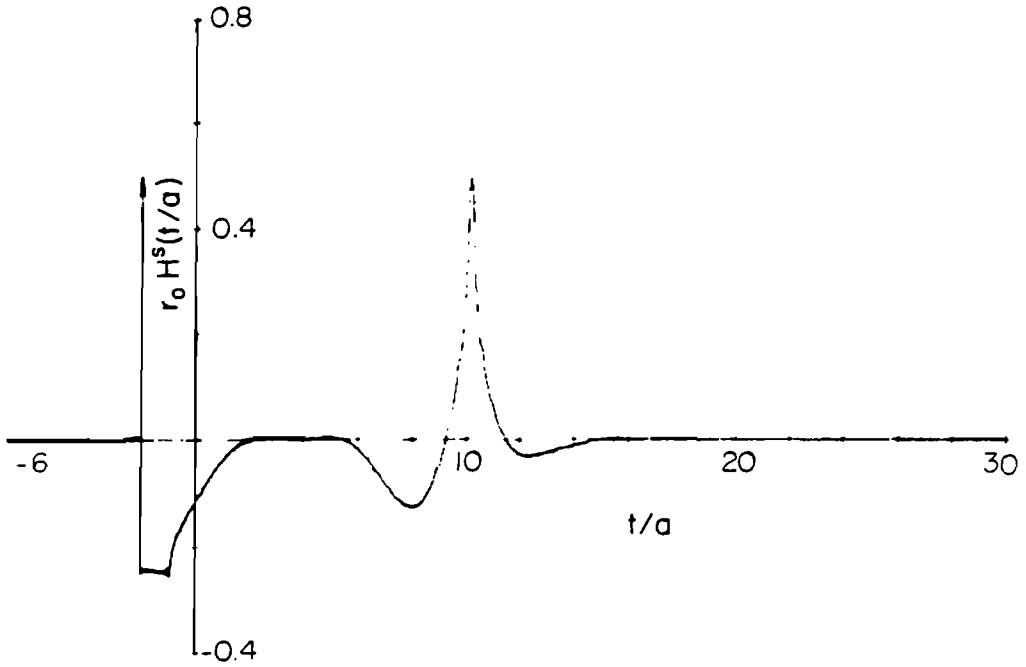

FIG. 78 Impulse response of sphere capped cylinder with radius a, length-to-diameter ratio 3:1, TE polarization and 30^o angle of incidence.

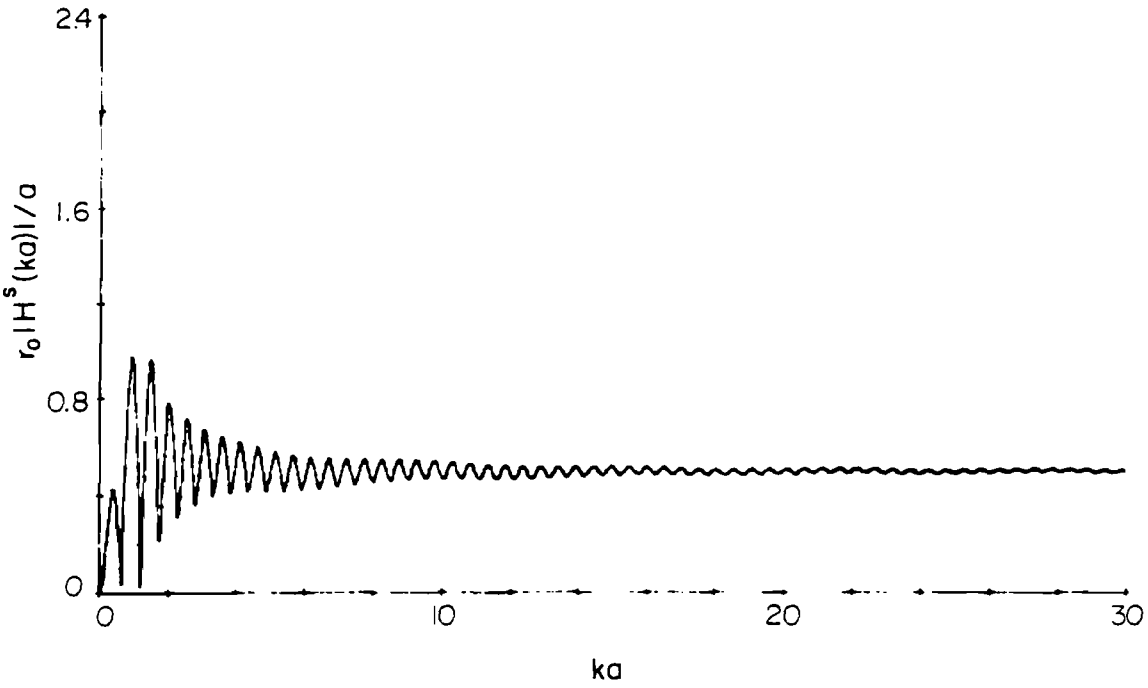

FIG. 79 Magnitude of frequency response of sphere capped cylinder with radius a, length-to-diameter ratio 3:1, TE polarization and 30^o angle of incidence.

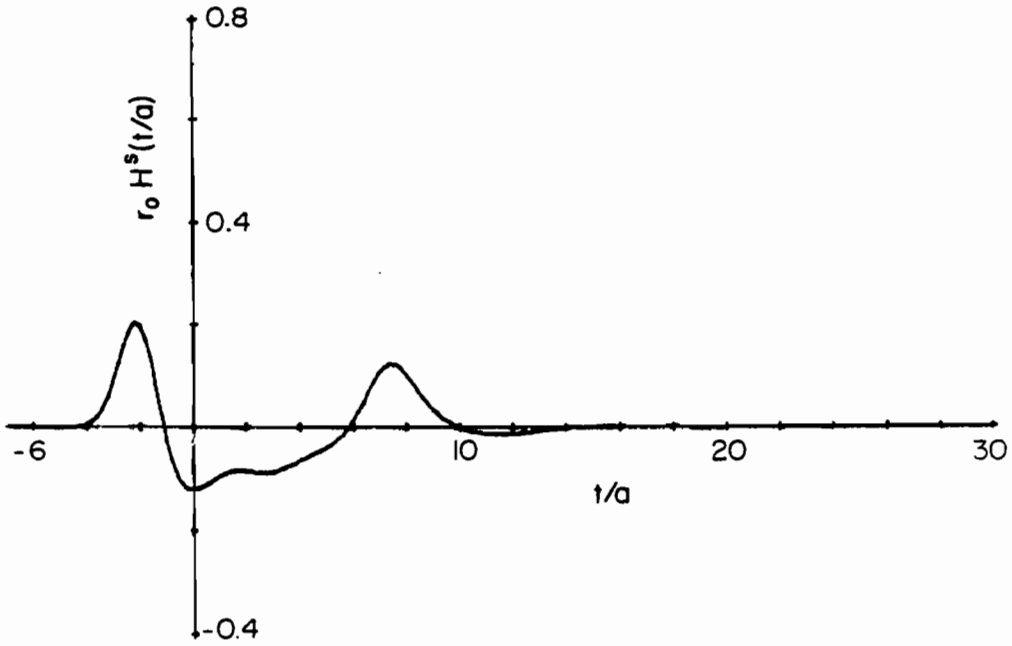

FIG. 80 Smoothed impulse response of sphere capped cylinder with radius a, length-to-diameter ratio 3:1, TE polarization and 60^o angle of incidence.

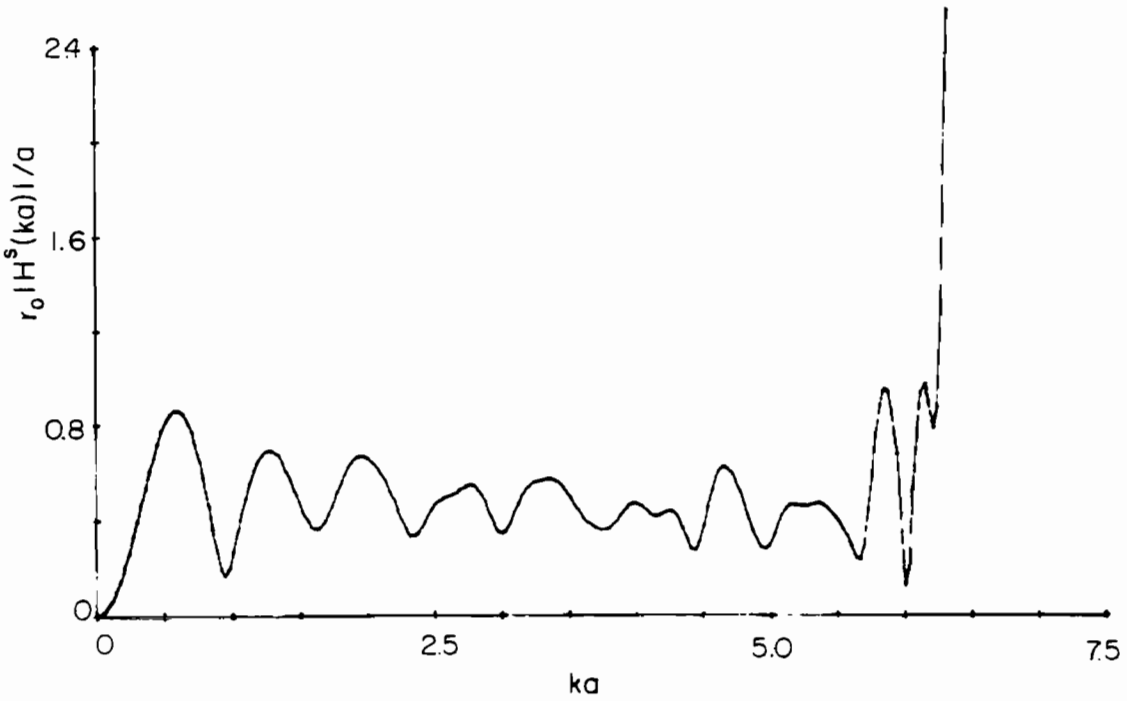

FIG. 81 Magnitude of frequency response of sphere capped cylinder obtained by direct transformation for TE polarization and 60^o angle of incidence.

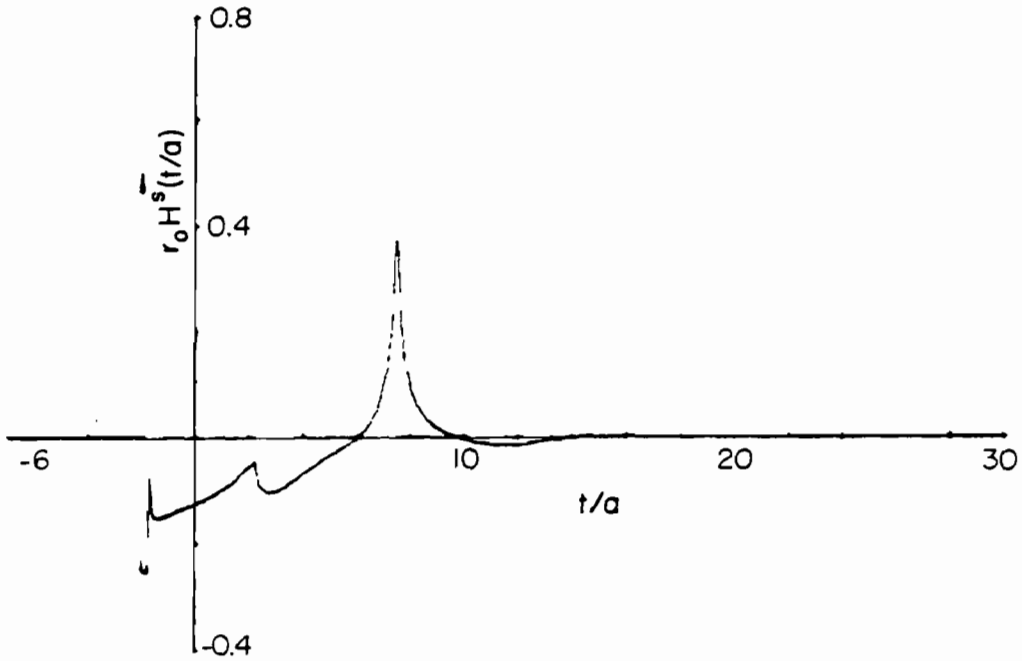

FIG. 82 Impulse response of sphere capped cylinder with radius a, length-to-diameter ratio 3:1, TE polarization and 60^0 angle of incidence.

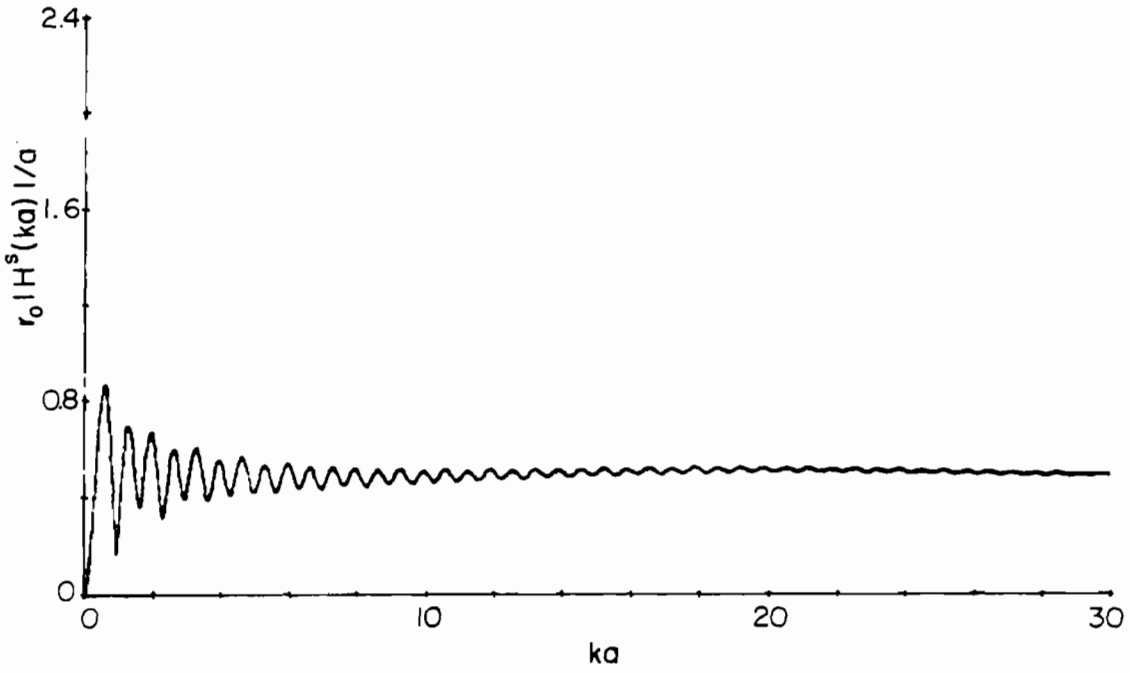

FIG. 83 Magnitude of frequency response of sphere capped cylinder with radius a, length-to-diameter ratio 3:1, TE polarization and 60^0 angle of incidence.

between the impulse in the specular return and the creeping wave return.

The smoothed impulse response and the directly transformed frequency response are plotted in Figs. 84 and 85, respectively, for the 90^{o} angle of incidence. The frequency response increase as $\omega^{1/2}$ is due to the cylinder being illuminated at broadside incidence in Fig. 85. The impulse response and the companion frequency response obtained with the augmentation technique are shown in Figs. 86 and 87, respectively. The leading edge of the impulse response contains an impulse, a step, a $(t)^{-3/2}$ functional and a $(t)^{-1/2}$ functional. The creeping wave return appears at $t/a = 3.43$ rather than at 3.14, as would be the case for a wave moving at the speed of light. Finally, in the frequency response the $\omega^{1/2}$ variation that results from the $(t)^{-3/2}$ variation in the impulse response is clearly evident.

2.8.3 Sphere-Capped Cylinder — TM Polarization

The smoothed impulse response and the frequency response obtained by direct transformation are shown in Figs. 88 and 89, respectively, for a 30^{o} angle of incidence. In this smoothed impulse response, as well as for the cases of 60^{o} and 90^{o} incidence, a damped sine wave oscillation was noted after the creeping wave return, as was expected since this structure is simply a very fat linear antenna. Rather than perform the numerical solution of the space-time integral until the response dies out, the solution was extrapolated beyond the first zero crossing after the creeping wave return with an exponentially damped sine wave. As was done in the TE case, the creeping wave damping coefficient B_1 was assumed to be the same as that of a sphere; however, it should be clear that this wave must travel a greater distance (along the cylinder body) in the TM case, and thus this assumption is probably the weakest. The impulse response and companion frequency response for this aspect angle and polarization are displayed in Figs. 90 and 91, respectively. In Fig. 90 the initial return coincides with that of a sphere, and then at $t/a = -1.00$ is followed by a sharp positive swing from the join, which then, interestingly enough, decays to zero at $t/a \simeq 2$ in an apparently linear fashion. Next, a sharp negative swing appears at $t/a = 5.9$, corresponding to the second join return, and is followed at $t/a = 10.71$ by the creeping wave return. Again, this is slightly later than the time $t/a = 10.61$ that would be expected for a wave traveling at the speed of light. The frequency response in Fig. 91 shows an irregular resonant character that may be attributed to interference between the specular return, the creeping wave return, the first join return, and the second join return.

Figures 92 and 93 show the smoothed impulse response and the frequency response obtained by direct transformation, respectively, for the case of a 60^{o} angle of incidence. The impulse response in Fig. 94 for this case is initially identical in time to that of a sphere, as expected. At $t/a = -1.73$ a sharp positive swing occurs due to the return from the first join, followed at $t/a = 2.27$ by a sharp negative swing due to the second join return. The creeping wave return appears at $t/a = -9.24$ rather than at -9.14, where a wave traveling at the speed of light would appear. The companion frequency response is shown in Fig. 95.

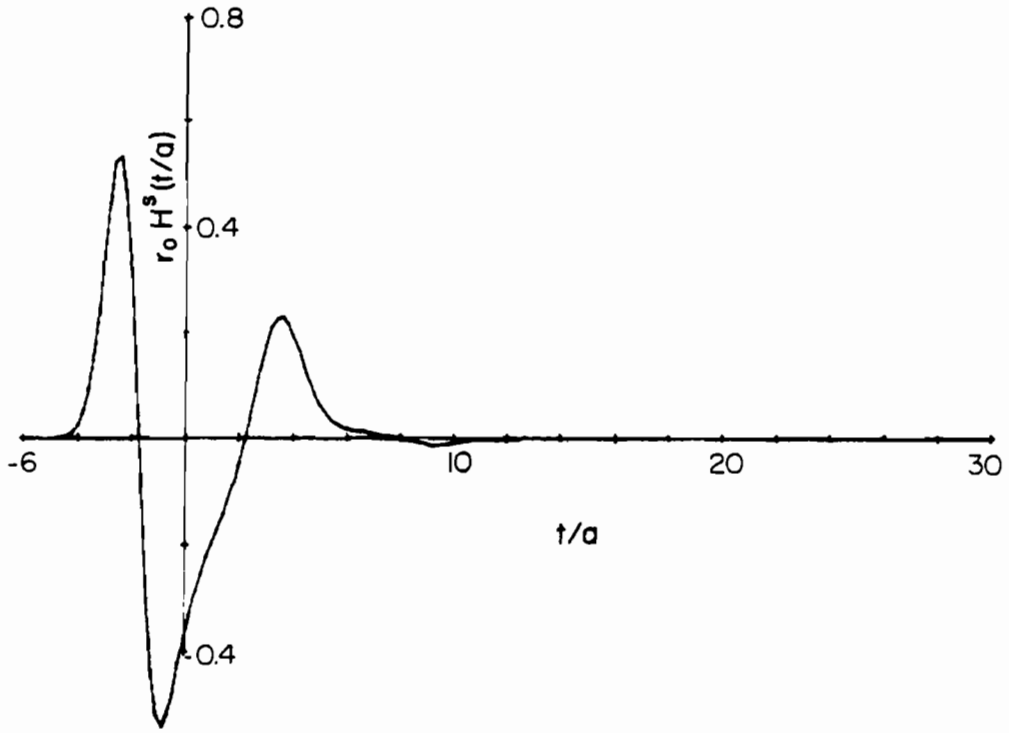

FIG. 84 Smoothed impulse response of sphere capped cylinder with radius a, length-to-diameter ratio 3:1, TE polarization and 90^0 angle of incidence.

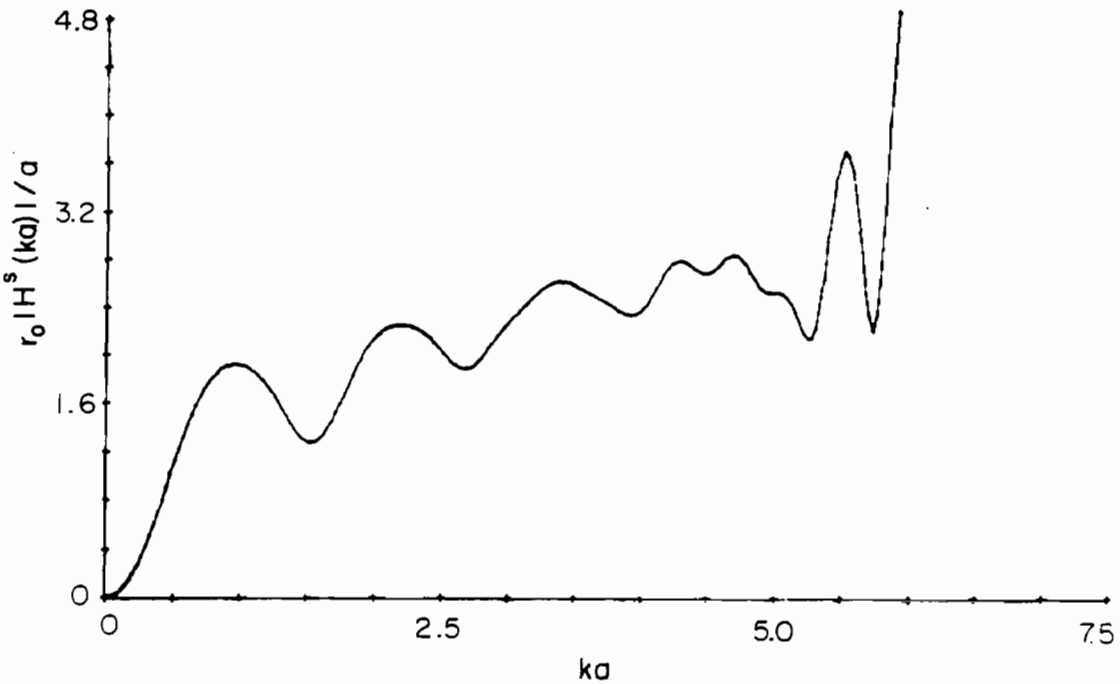

FIG. 85 Magnitude of frequency response of sphere capped cylinder obtained by direct transformation for TE polarization and 90^0 angle of incidence.

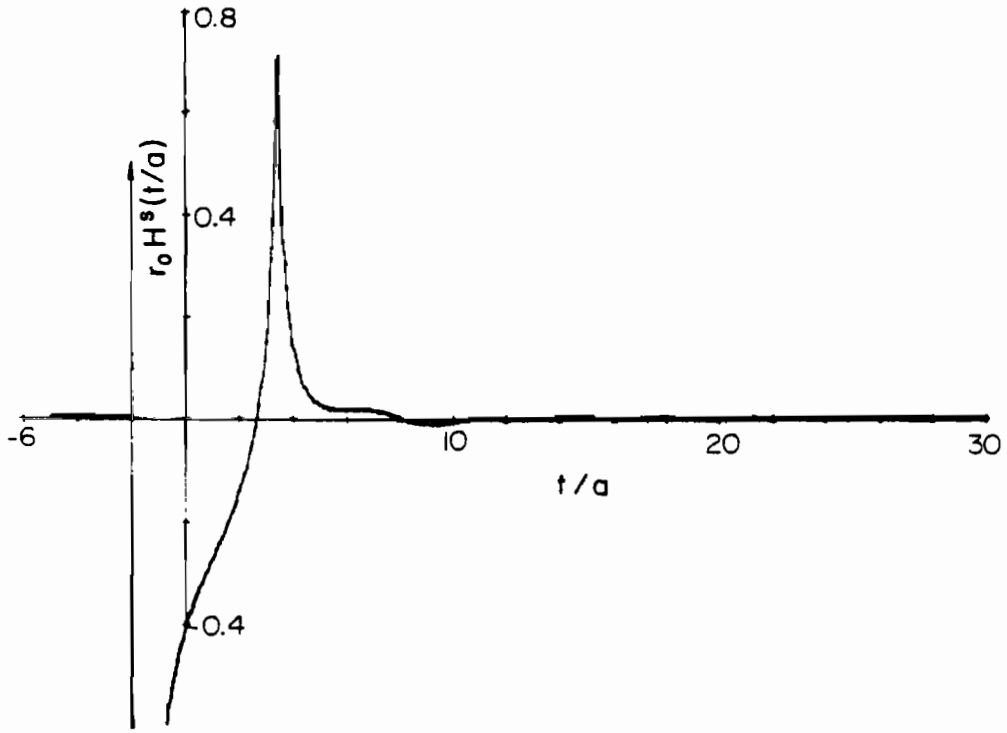

FIG. 86 Impulse response of sphere capped cylinder with radius a, length-to-diameter ratio 3:1, TE polarization and 90° angle of incidence.

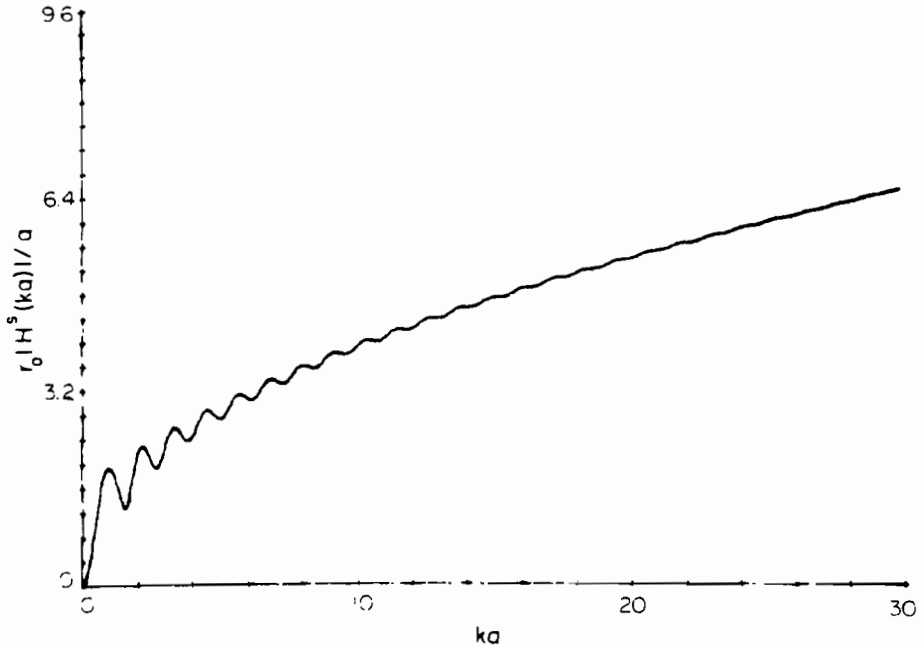

FIG. 87 Magnitude of frequency response of sphere capped cylinder with radius a, length-to-diameter ratio 3:1, TE polarization and 90° angle of incidence.

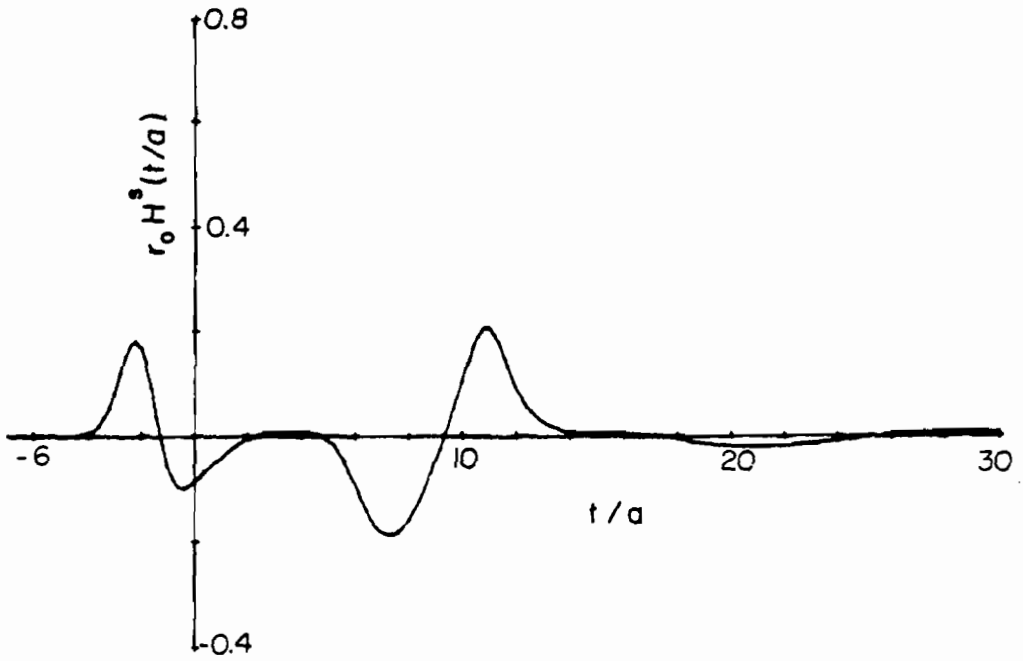

FIG. 88 Smoothed impulse response of sphere capped cylinder with radius a, length-to-diameter ratio 3:1, TM polarization and 30^0 angle of incidence.

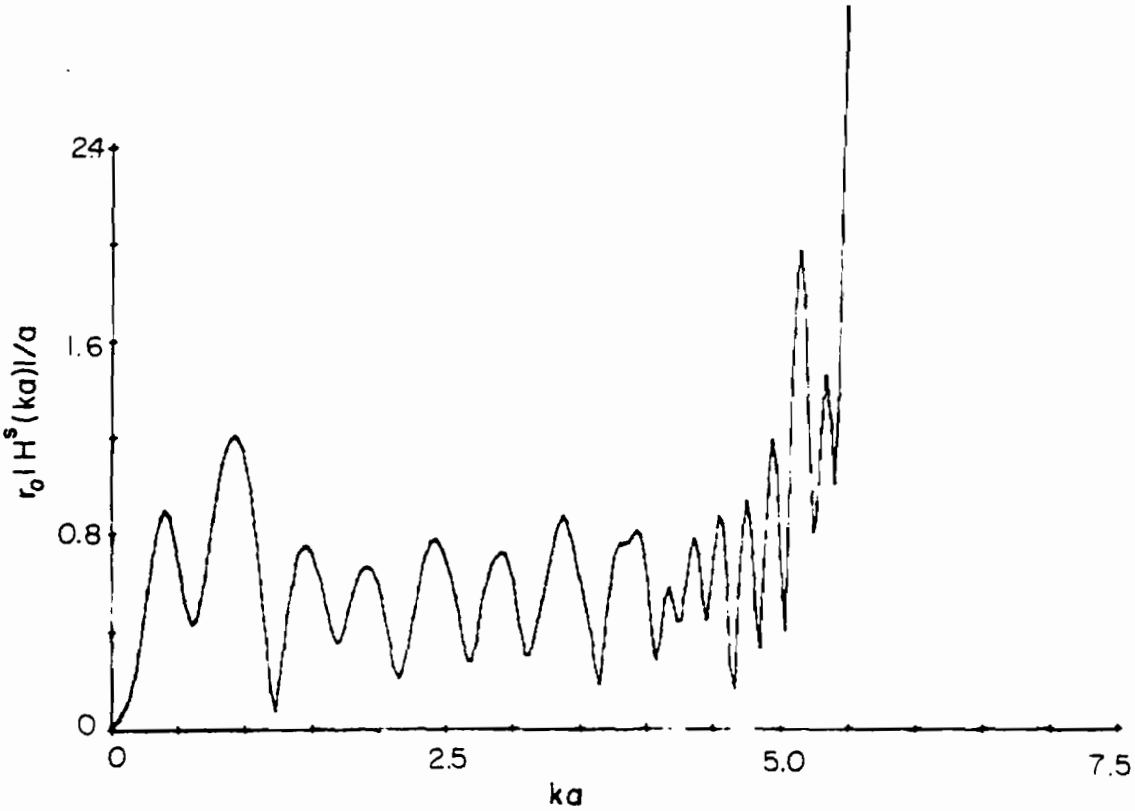

FIG. 89 Magnitude of frequency response of sphere capped cylinder obtained by direct transformation for TM polarization and 30^0 angle of incidence.

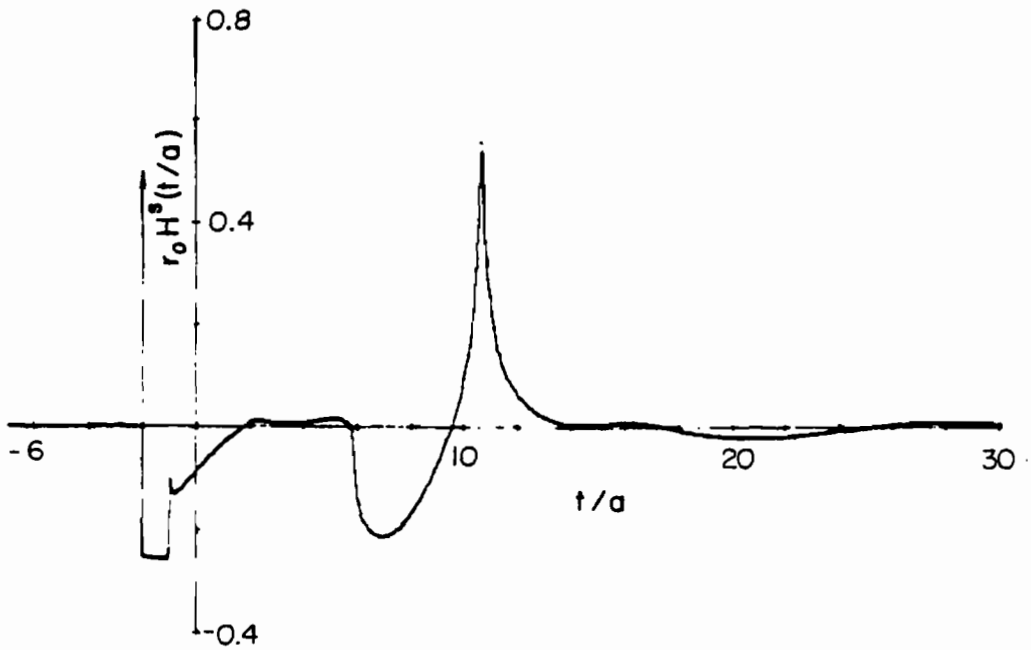

FIG. 90 Impulse response of sphere capped cylinder with radius a, length-to-diameter ratio 3:1, TM polarization and 30^0 angle of incidence.

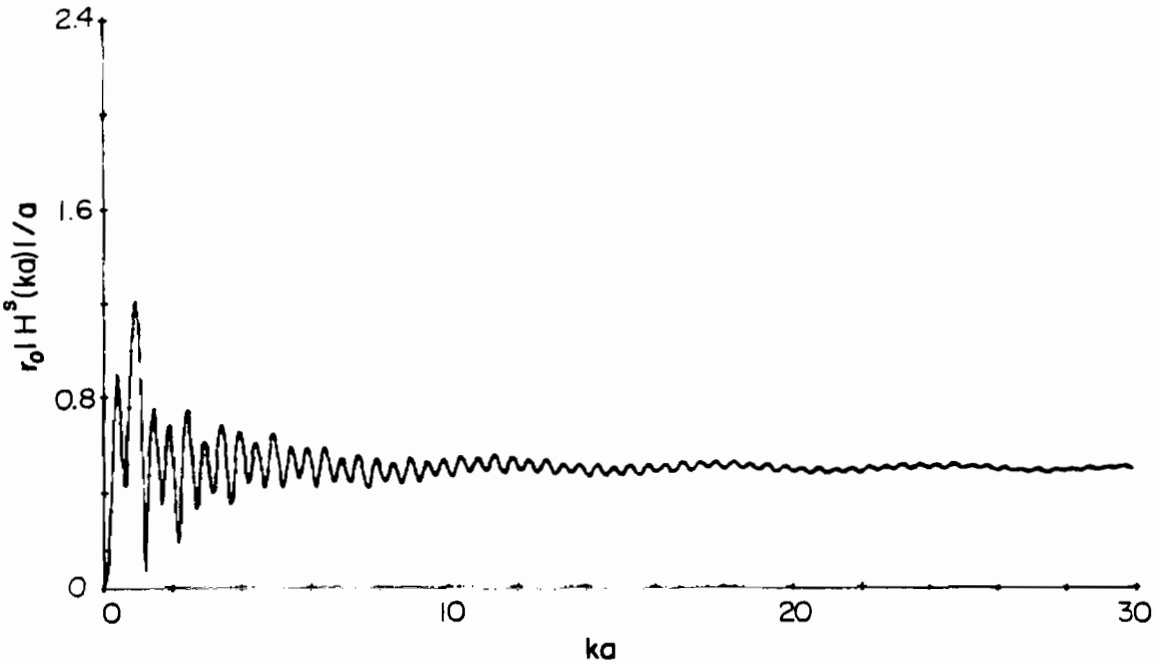

FIG. 91 Magnitude of frequency response of sphere capped cylinder with radius a, length-to-diameter ratio 3:1, TM polarization and 30^0 angle of incidence.

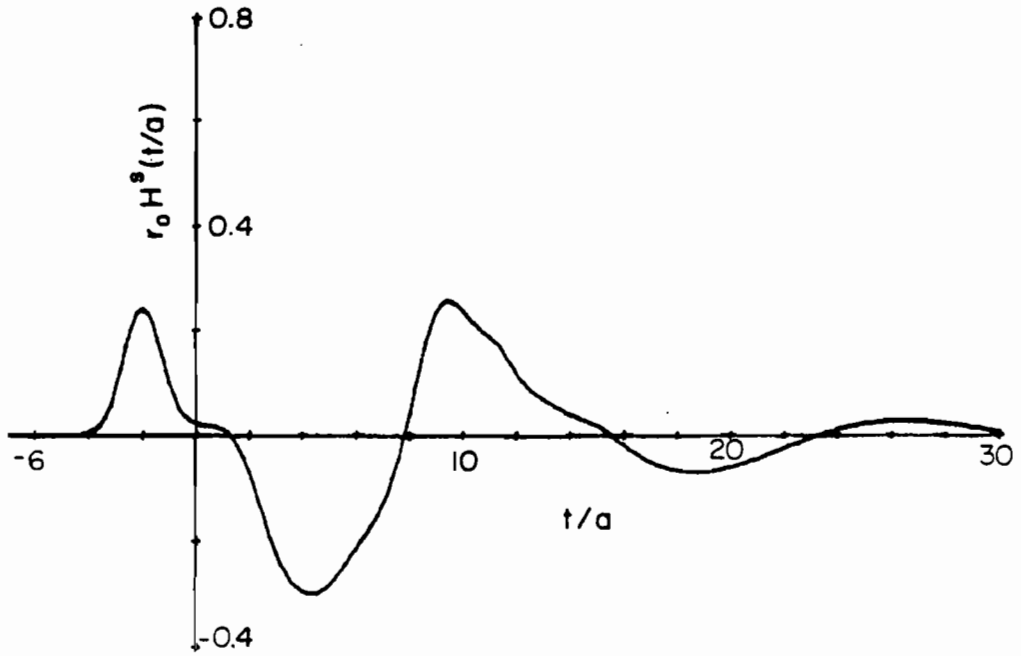

FIG. 92 Smoothed impulse response of sphere capped cylinder with radius a, length-to-diameter ratio 3:1, TM polarization and 60^o angle of incidence.

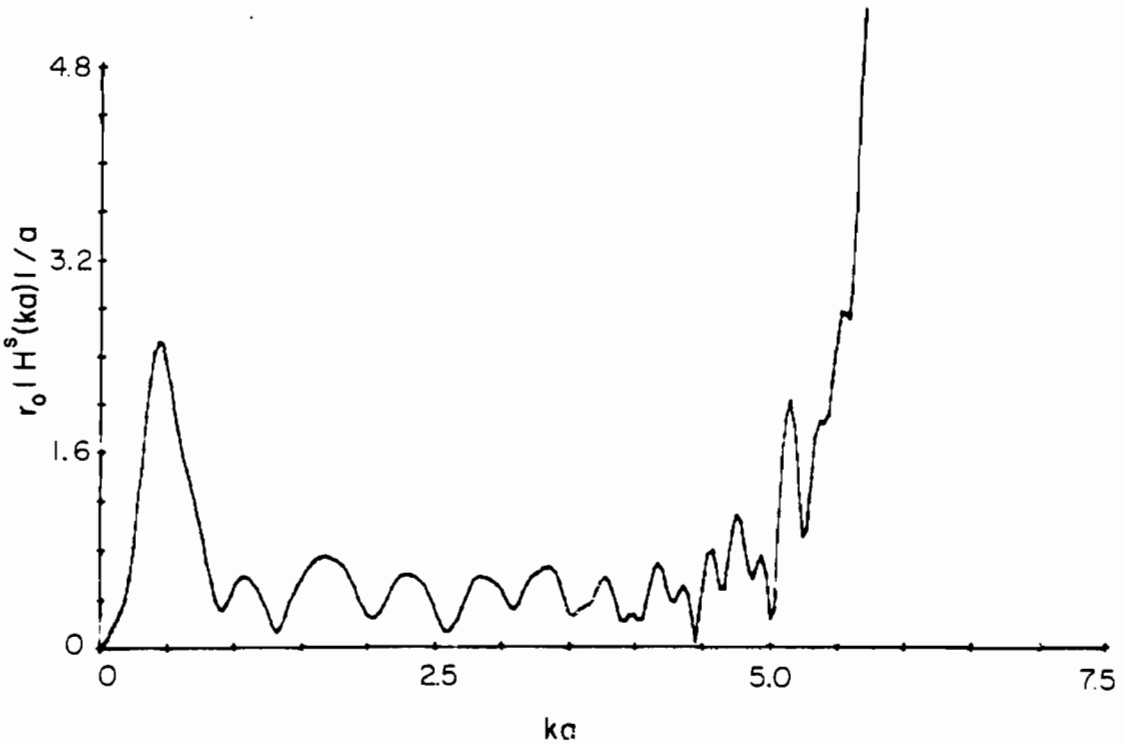

FIG. 93 Magnitude of frequency response of sphere capped cylinder obtained by direct transformation for TM polarization and 60^o angle of incidence.

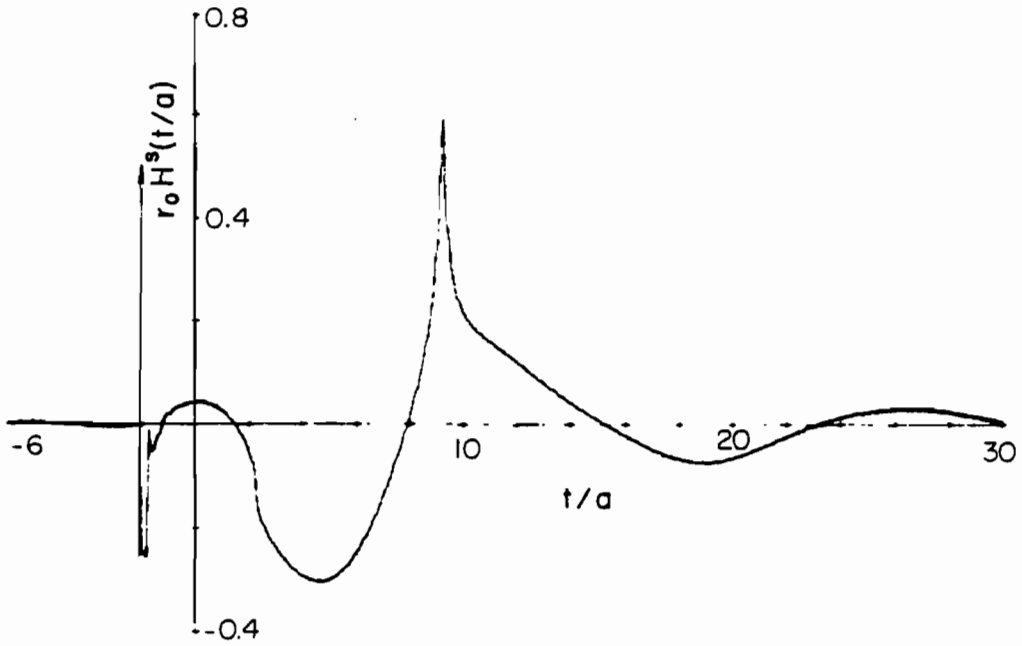

FIG. 94 Impulse response of sphere capped cylinder with radius a, length-to-diameter ratio 3:1, TM polarization and 60^0 angle of incidence.

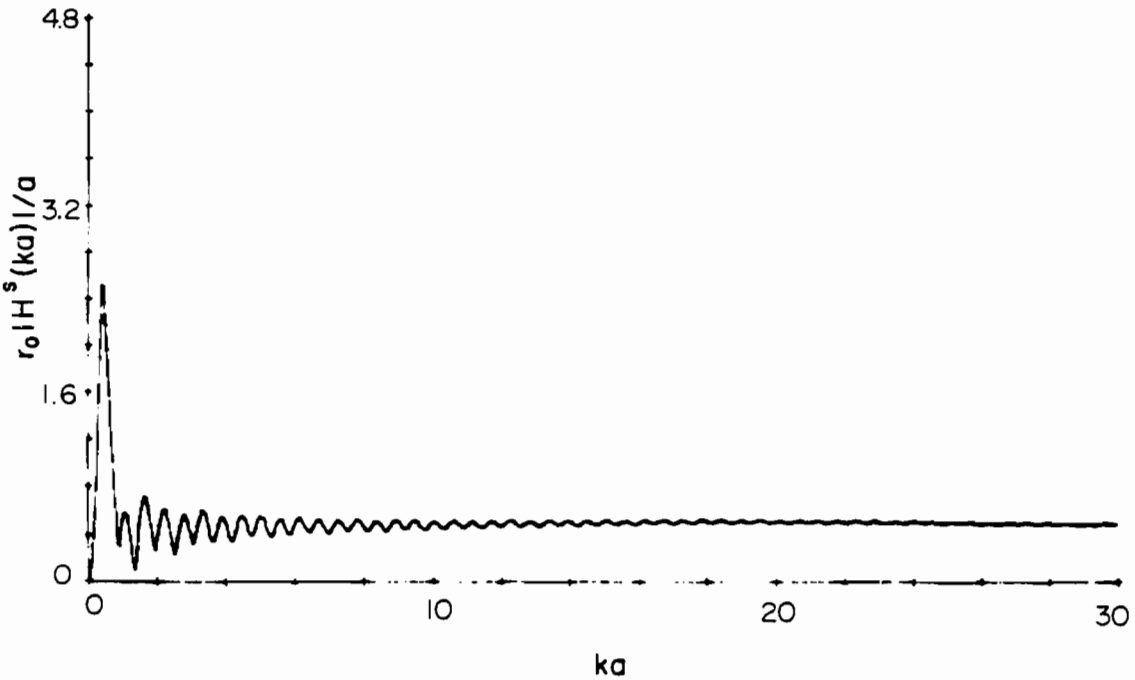

FIG. 95 Magnitude of frequency response of sphere capped cylinder with radius a, length-to-diameter ratio 3:1, TM polarization and 60^0 angle of incidence.

Finally, the results for the case of a 90^{o} angle of incidence are displayed in Figs. 96-99. The smoothed impulse response in Fig. 96 contains a substantial oscillation beyond the creeping wave return at $t/a \simeq 7$. The frequency response obtained by direct transformation in Fig. 97 clearly shows the effect of the specular return from the cylinder with the $\omega^{1/2}$ increase with frequency. At its leading edge the impulse response in Fig. 98 contains an impulse, a step, a $t^{-3/2}$ functional, and a $t^{-1/2}$ functional. The creeping wave still is apparent in the response at $t/a = 9.24$ and is followed by a slowly damped oscillation. The frequency response in Fig. 99 has a large initial resonant peak at $ka \simeq 0.5$ and following that exhibits a $\omega^{1/2}$ increase with frequency.

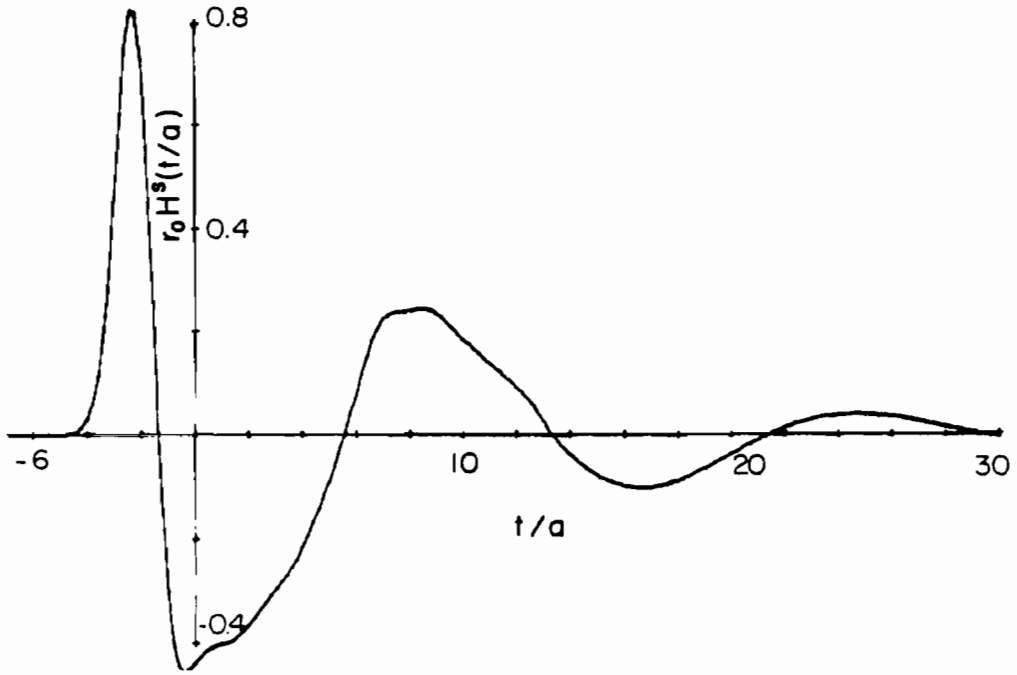

FIG. 96 Smoothed impulse response of sphere capped cylinder with radius a, length-to-diameter ratio 3:1, TM polarization and 90^0 angle of incidence.

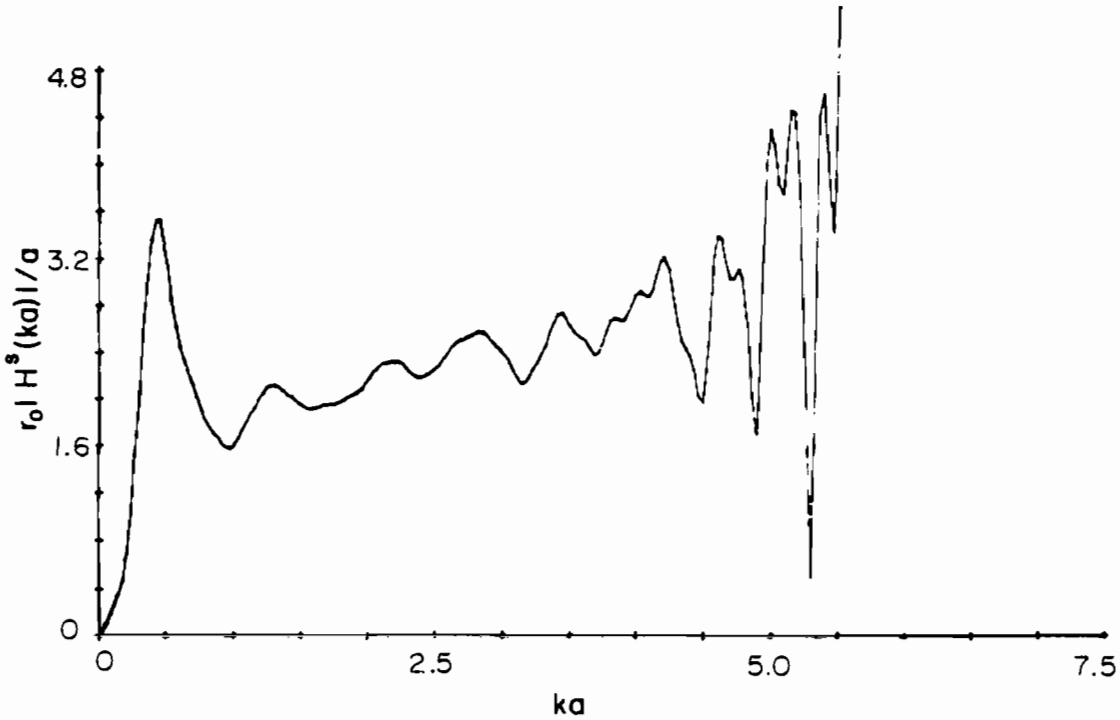

FIG. 97 Magnitude of frequency response of sphere capped cylinder obtained by direct transformation for TM polarization and 90^0 angle of incidence.

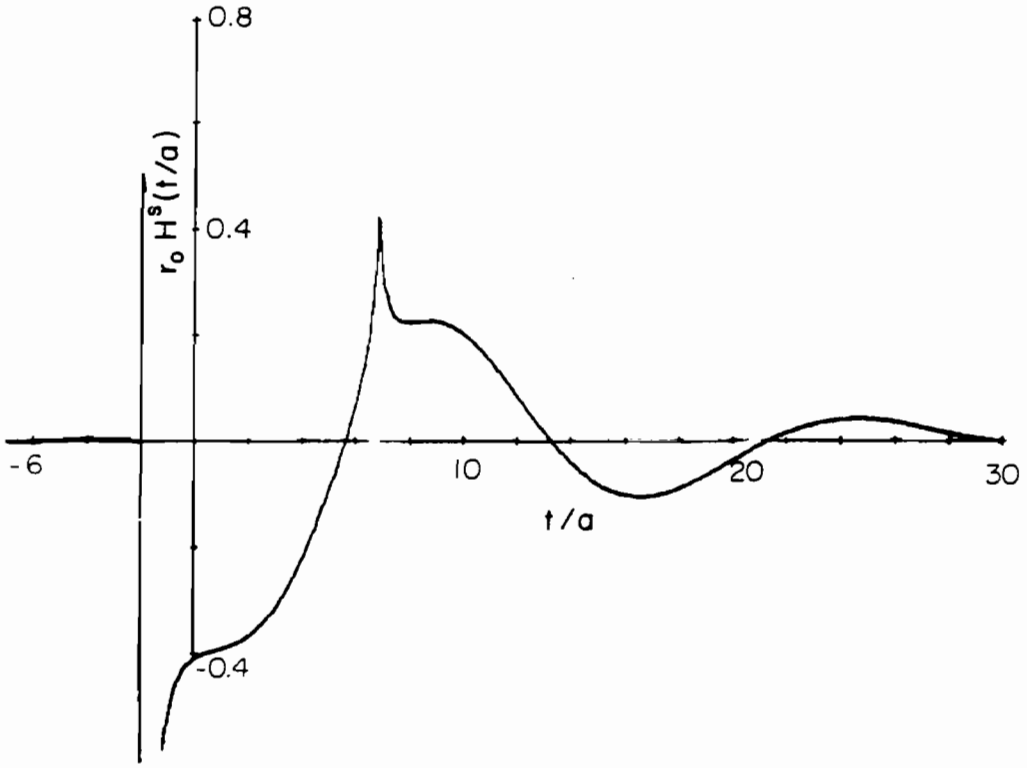

FIG. 98 Impulse response of sphere capped cylinder with radius a, length-to-diameter ratio 3:1, TM polarization and 90° angle of incidence.

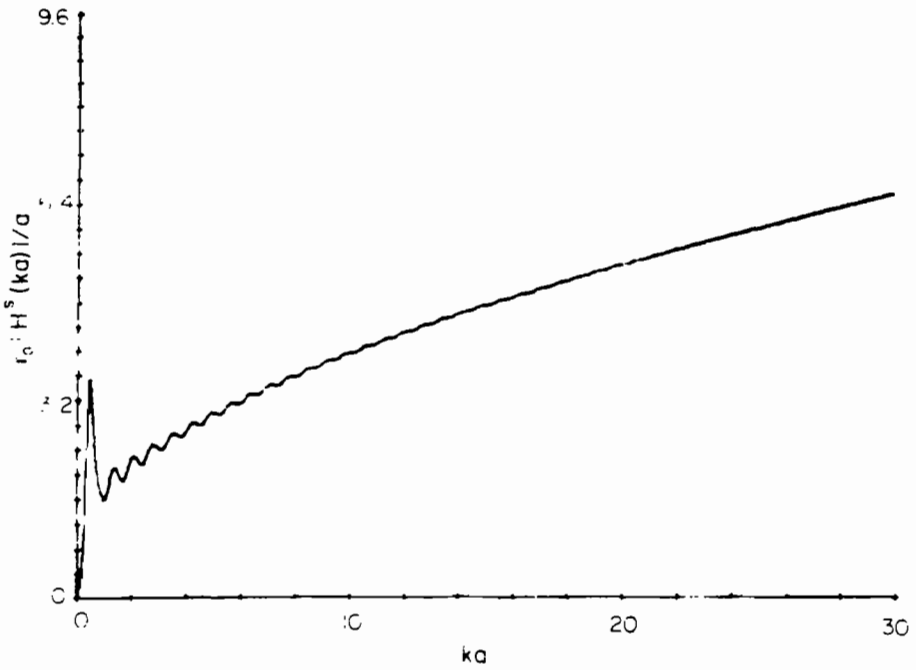

FIG. 99 Magnitude of frequency response of sphere capped cylinder with radius a, length-to-diameter ratio 3:1, TM polarization and 90° angle of incidence.

SECTION 3

RELATION BETWEEN ANGLE SAMPLING AND TIME SAMPLING IN TIME DOMAIN CALCULATIONS AND MEASUREMENTS

During the performance of Contract No. F30602-69-C-0357, a theoretical investigation into the problem of identifying targets from noisy impulse radar returns was carried out and an optimum digital identifier processor was developed. An integral part of the processor consists of a bank of matched filters, one for each expected waveform. Hence, for any target that is not spherically symmetric we must know how many waveforms must be stored in the matched filter band in order to cover all angles of incidence. In this section we shall develop a relationship between the angular sampling rate of a scatterer and the bandwidth of the pulse incident on the scatterer. The basic concept will be similar to the idea which forms the time sampling theorem; i.e., it is known that a time waveform must be sampled at twice the highest frequency present in order that the waveform be completely specified by its time samples.

3.1 SAMPLING THEOREM

Let us review the time sampling theorem. It states that if a signal is bandlimited and is sampled at a rate which is greater than twice the highest frequency present, then the entire waveform can be found from its sampled values: namely

$$f(t) = \sum_{n=-\infty}^{\infty} f(n\Delta t)\, \frac{\sin\omega_0(t-n\Delta t)}{\omega_0(t-n\Delta t)}$$

where $\omega_0 = \pi/\Delta t$ Nyquist frequency as long as $\omega_0 > \omega_c$, the bandwidth of the signal.

The proof of this theorem can be extended to multi-dimensional functions. For example, if the Fourier transform of a two dimensional function is bandlimited in both variables, i.e.,

$$F(\omega,k) = \int_{-\infty}^{\infty}\int_{-\infty}^{\infty} f(t,\theta)\, e^{-j(\omega t+k\theta)}\, dt\, d\theta$$

and

$$F(\omega,k) = 0 \qquad |\omega| > \omega_c,\ |k| > k_c$$

then the function is determined completely by its sampled values:

$$f(t,\theta) = \sum_{n=-\infty}^{\infty} \sum_{m=-\infty}^{\infty} f(n\Delta t,\ m\Delta\theta)\ \frac{\sin\omega_0(t-n\Delta t)}{\omega_0(t-n\Delta t)}\ \frac{\sin\ k_0(\theta-m\Delta\theta)}{k_0(\theta-m\Delta\theta)} \tag{70}$$

provided

$$\omega_0 = \frac{\pi}{\Delta t} \geq \omega_c$$

and

$$k_0 = \frac{\pi}{\Delta\theta} \geq k_c \tag{71}$$

The proof of this theorem is the same as the proof of the one dimensional theorem as proven, for example, in Papoulis.[14,15]

In general, we shall find the scattered responses will not be exactly bandlimited in both variables. Hence, Eq. (70) will be satisfied with some error. The analysis of these errors has been carried out in several reports.[15,16] In general, these errors depend upon the values of the transform for $|\omega| > \omega_0$ and $|k| > k_0$. In our analysis we shall assume that the bandwidth, ω_c and k_c, is determined when the Fourier transform is less than ϵ of the peak value: i.e.,

$$F(\omega,k) \leq \epsilon \max\left\{F(\omega,k)\right\} \text{ for } |\omega| > \omega_c$$
$$|k| > k_c$$

In the scattering problem the function $f(t,\theta)$ is periodic in θ with period 2π. Hence, it can be expressed as a Fourier series in θ:

$$f(t,\theta) = \sum_{n=-\infty}^{\infty} f_n(t)\ e^{+jn\theta}$$

where

$$f_n(t) = \frac{1}{2\pi} \int_0^{2\pi} f(t,\theta)\ e^{-jn\theta}\ d\theta\ .$$

Thus the two dimension Fourier transform will be

$$F(\omega,k) = \int_{-\infty}^{\infty}\int_{-\infty}^{\infty} f_n \sum_{n=-\infty}^{\infty} f_n(t)e^{+jn\theta}e^{-j(\omega t+k\theta)}\, dt\, d\theta$$

$$= \int_{-\infty}^{\infty}\int_{-\infty}^{\infty} 2\pi f_n(t)\delta(k-n)e^{-j\omega t}\, dt\ .$$

From Eq. (72) this becomes

$$F(\omega,k) = \sum_{n=-\infty}^{\infty} F(\omega,n)\delta(k-n) \tag{73}$$

where

$$F(\omega,n) = \int_{0}^{2\pi}\int_{-\infty}^{\infty} f(t,\theta)e^{-j(\omega t+n\theta)}\, dt\, d\theta\ . \tag{74}$$

From Eq. (73) it follows that it is sufficient to consider $F(\omega,n)$.

If the bandwidth in k is equal to k_c, then the number of samples in the angle 2π is equal to

$$N = \frac{2\pi}{\Delta\theta}\ .$$

From Eq.(71) the number of samples becomes

$$N = 2\left(\frac{\pi}{\Delta\theta}\right) \geq 2\ k_c\ . \tag{75}$$

Hence, the minimum number of samples necessary to represent the waveform is $2\ k_c$.

3.2 THEORETICAL STUDY WITH ROTATIONALLY SYMMETRIC SCATTERING MODEL

In this section we find the relationship between the bandwidth of the incident pulse and the angular sample rate of a rotationally symmetric scatterer.

In order to obtain a simple approximate relation between the bandwidth of the incident pulse and the angular dependence, we consider a target model which consists of pairs of ideal point scatterers spaced apart by a fixed distance d, but free to rotate in a plane about the center of a line which connects them. The normalized impulse response of this ideal configuration when the excitation field is incident along the line joining them is simply $h(t) = \delta(t) + \delta(t-2d/c)$, which is a pair of impulses spaced apart by the time $2d/c$. Clearly, if the range resolving capability of the pulse is such that we cannot resolve the separation $2d/c$ (for example, the incident pulse width $\tau = 1/t$, where t is the bandwidth of the incident pulse, is much greater than $2d/c$, the two returns are unresolvable at their maximum point of separation. Hence, as they rotate they remain unresolved, and therefore only one angular sampling point is required. On the other hand, if the range resolving capability of the pulse is such that we can resolve the separation $2d/c$, then we must use two dimensional Fourier transform technique on the response which is of the form

$$r(t,\theta) = e(t+d\cos\theta) + e(t-d\cos\theta) \tag{76}$$

where e(t) is the incident pulse.

It will be noted that this response has the property that the two pulses coincide at two angles of incidence, namely $\theta = \pi/2$ and $3\pi/2$. Most bodies have responses which can be approximated by two pulses whose separation is a function of the angle of incidence, as in Eq. (76), but whose minimum separation is nonzero. In order to retain the main features of Eq.(76) and yet allow a minimum separation of the pulses, we shall assume that the scattered impulse response is of the form:

$$h(t,\theta) = \delta\left(t + \frac{a+b}{2c} + \frac{1}{2c}(a-b)\cos 2\theta\right) + \delta\left(t - \frac{a+b}{2c} - \frac{1}{2c}(a-b)\cos 2\theta\right) \tag{77}$$

where $b < a$. This response is independent of ϕ (rotationally symmetric). The response is composed of two impulses separated by maximum time of za/c at $\theta = 0$ and decreases smoothly as a function of angle to a minimum time of $2b/c$ at $\theta = \pi/2$, where it increases again to $2a/c$ at $\theta = \pi$ and repeats itself with a period of π (see Fig. 100). This pair of impulses is a simple model of the impulse response of a rotationally symmetric scatterer, which is composed of an impulsive specular return and a creeping wave return. Since the creeping wave return travels around the surface of the body along a geodesic of the surface, the distances "a" and "b" must be measured along geodesics and they represent the maximum and minimum dimensions measured along these geodesics. For example, in the case of a sphere of radius r the maximum distance "a" is equal to πr, not $2r$. Put another way, 2a is the maximum distance the creeping wave travels and 2b is the minimum distance the creeping wave travels.

The two dimensional Fourier transform of Eq. (77), from Eqs. (73) and (74) is,

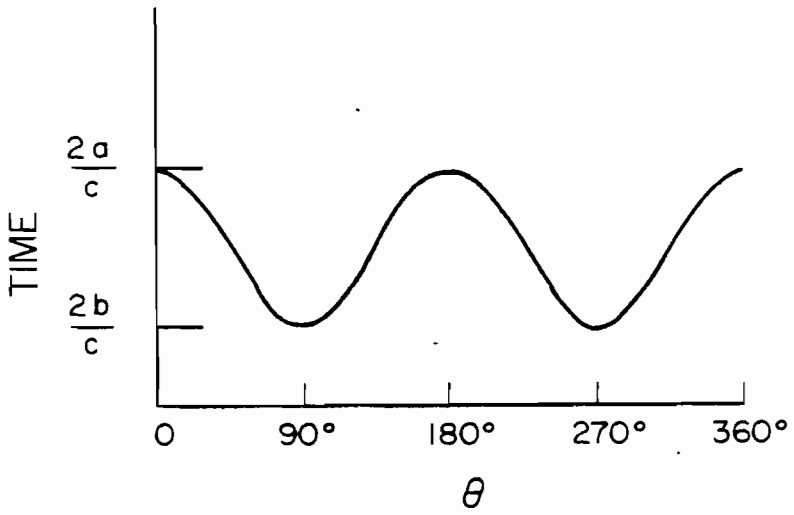

FIG. 100 Time separation of impulse as a function of the angle of incidence.

$$H(\omega,k) = \sum_{n=-\infty}^{\infty} H(\omega,n)\delta(k-n)$$

where

$$H(\omega,n) = \int_0^{2\pi} \int_{-\infty}^{\infty} h(t,\theta)e^{-j(\omega t+n\theta)}\, dt\, d\theta \qquad (78)$$

n is a dummy index, and k is the second argument of H. Now since $h(t,\theta)$ is periodic with period π Eq. (78) becomes

$$H(\omega,2n) = 2\int_0^{\pi} \int_{-\infty}^{\infty} h(t,\theta)e^{-j(\omega t+2n\theta)}\, dt\, d\theta$$

$$H(\omega,2n+1) = 0$$

where the dummy index n has been redefined as $n \rightarrow 2n$.

Let

$$H_1(\omega,2n) = 2\int_0^{\pi} \int_{-\infty}^{\infty} \delta(t+\frac{1}{2c}(a+b) + \frac{1}{2c}(a-b)\cos 2\theta)e^{-j(\omega t+2n\theta)}\, dt\, d\theta$$

$$H_2(\omega,2n) = 2\int_0^{\pi} \int_{-\infty}^{\infty} \delta(t-\frac{1}{2c}(a+b) - \frac{1}{2c}(a-b)\cos 2\theta)e^{-j(\omega t+2n\theta)}\, dt\, d\theta$$

Then

$$H(\omega,2n) = H_1(\omega,2n) + H_2(\omega,2n) .$$

Integrating with respect to t, we obtain

$$H_1(\omega,2n) = 2\int_0^{\pi} e^{+j\omega\left(\frac{1}{2c}(a+b) + (a-b)\cos 2\theta\right)} e^{-j2n\theta}\, d\theta$$

$$H_2(\omega,2n) = 2\int_0^{\pi} e^{-j\omega\left(\frac{1}{2c}(a+b) + \frac{(a-b)}{2c}\cos 2\theta\right)} e^{-j2n\theta}\, d\theta\ .$$

Making a change in variable, the integrals become

$$H_1(\omega,2n) = e^{+j\frac{\omega(a+b)}{2c}}\, e^{+j\frac{n\pi}{2}} \int_{\pi/2}^{2\pi+\pi/2} e^{+j\left[\frac{\omega}{2c}(a-b)\sin\theta - n\theta\right]}\, d\theta$$

$$H_2(\omega,2n) = e^{-j\frac{\omega(a+b)}{2c}}\, e^{+j\frac{n\pi}{2}} \int_{\pi/2}^{2\pi+\pi/2} e^{-j\left[\frac{\omega}{2c}(a-b)\sin\theta + n\theta\right]}\, d\theta .$$

These integrals can be recognized as Bessel functions; hence we get

$$H_1(\omega,2n) = 2\pi e^{+j\frac{\omega(a+b)}{2c}}\, (j)^n\, J_n\left(\frac{\omega}{2c}(a-b)\right)$$

$$H_2(\omega,2n) = 2\pi e^{-j\frac{\omega(a+b)}{2c}}\, (j)^n\, J_n\left(\frac{\omega}{2c}(a-b)\right) \qquad (79)$$

From a well known property of Bessel functions, Eq. (79) becomes

$$H_2(\omega,2n) - 2\pi e^{-j\frac{\omega(a+b)}{2c}}\, (j)^n\, J_n\left(\frac{\omega}{2c}(a-b)\right)\ .$$

Hence the total transform is

$$H(\omega,4n) = 4\pi(-1)^n \cos\frac{\omega(a+b)}{2c}\, J_{2n}\left(\frac{\omega}{2c}(a-b)\right) \qquad (80)$$

$$H(\omega,4n+2) = 4\pi(-1)^{n+1} \sin\frac{\omega(a+b)}{2c}\, J_{2n}\left(\frac{\omega}{2c}(a-b)\right) \qquad (81)$$

$$H(\omega,2n+1) = 0\ . \qquad (82)$$

Let us assume that the target is illuminated by a bandlimited pulse with a flat passband whose spectrum is

$$E(\omega) = 1 \qquad |\omega| \le \omega_c$$
$$= 0 \qquad |\omega| > \omega_c \ . \tag{83}$$

Then the resulting two dimensional Fourier transform of the scattered waveform will be

$$R(\omega,n) = E(\omega)H(\omega,n) \ . \tag{84}$$

From Eqs. (80)-(84) this becomes

$$R(\omega,4n) = 4\pi(-1)^n \cos\frac{\omega(a+b)}{2c}\, J_{2n}\left(\frac{\omega}{2c}(a-b)\right) \qquad |\omega| \le \omega_c \tag{85}$$

$$R(\omega,4n+2) = 4\pi(-1)^{n+1} \sin\frac{\omega(a+b)}{2c}\, J_{2n+1}\left(\frac{\omega}{2c}(a-b)\right) \qquad |\omega| \le \omega_c \tag{86}$$

$$R(\omega,n) = 0 \qquad \text{elsewhere} \ . \tag{87}$$

From Eqs. (85)-(87) we see that the two dimensional Fourier transform is not bandlimited in the k direction, since the Bessel function does not vanish identically for any value of n. However, the Bessel function for large n may be approximated by

$$J_n(x) \sim \frac{1}{\sqrt{2\pi n}} \left(\frac{ex}{2n}\right)^n \tag{88}$$

where e is the natural logarithm base, 2.718.

From Eq. (88) we see that response approaches zero rapidly as n gets large. It follows that the Fourier transform is approximately bandlimited in the k direction. Hence, the scattered response can be represented by a finite number of samples in angle.

It can be shown that the error in using a finite number of samples is a function of the transform at the Nyquist rate ($\pi/\Delta t$ or $\pi/\Delta\theta$). Let us assume that if the amplitude of the transform outside of the band is less than ϵ times the peak amplitude of the transform then the error is acceptable.

From Eqs. (85)-(87) the ratio of the amplitude of the transform to the peak amplitude is of the form

$$\left|\frac{R(\omega,2n)}{R(0,0)}\right| \leq \left|J_n\left(\frac{\omega}{2c}(a-b)\right)\right| \qquad |\omega| \leq \omega_c \tag{89}$$

$$= 0 \quad \text{elsewhere.}$$

Hence, for the amplitude outside of the band to be ϵ or less times the peak amplitude, the Nyquist rate, k_c, must staisfy

$$\epsilon \geq \left|J_{\frac{kc}{2}}\left(\frac{\omega}{2c}(a-b)\right)\right| \qquad |\omega| \leq \omega_c \tag{90}$$

From Eq. (75) the minimum number of samples M must satisfy

$$\epsilon \geq \left|J_{N/4}\left(\frac{\omega}{2c}(a-b)\right)\right| \qquad |\omega| \leq \omega_c \tag{91}$$

A plot of $|J_n(x)|$ is shown in Fig.101. It is clear from Fig.101 that $|J_n(x)|$ for a particular value of n has its absolute maximum at its first peak. From this we can conclude that either Eq. (91) is satisfied for all ω or that

$$\max \left|J_{N/4}\left[\frac{\omega_c}{2c}(a-b)\right]\right| > \epsilon \tag{92}$$

and that there is a value of ω_c which satisfies

$$\epsilon = J_{N/4}\left(\frac{\omega_c}{2c}(a-b)\right) . \tag{93}$$

Furthermore, the smallest such value of ω_c will guarantee that Eq. (93) is satisfied. Otherwise

$$J_{N/4}\left(\frac{\omega}{2c}(a-b)\right) < \epsilon \quad \text{for all } \omega .$$

A plot of Eq. (93) is given in Fig.102 for various values of ϵ, where $\lambda = 2\pi c/\omega_c$, the wavelength of the cutoff frequency. For values of N from 40 to 400 the following equations are least mean squares fits to Eq. (93).

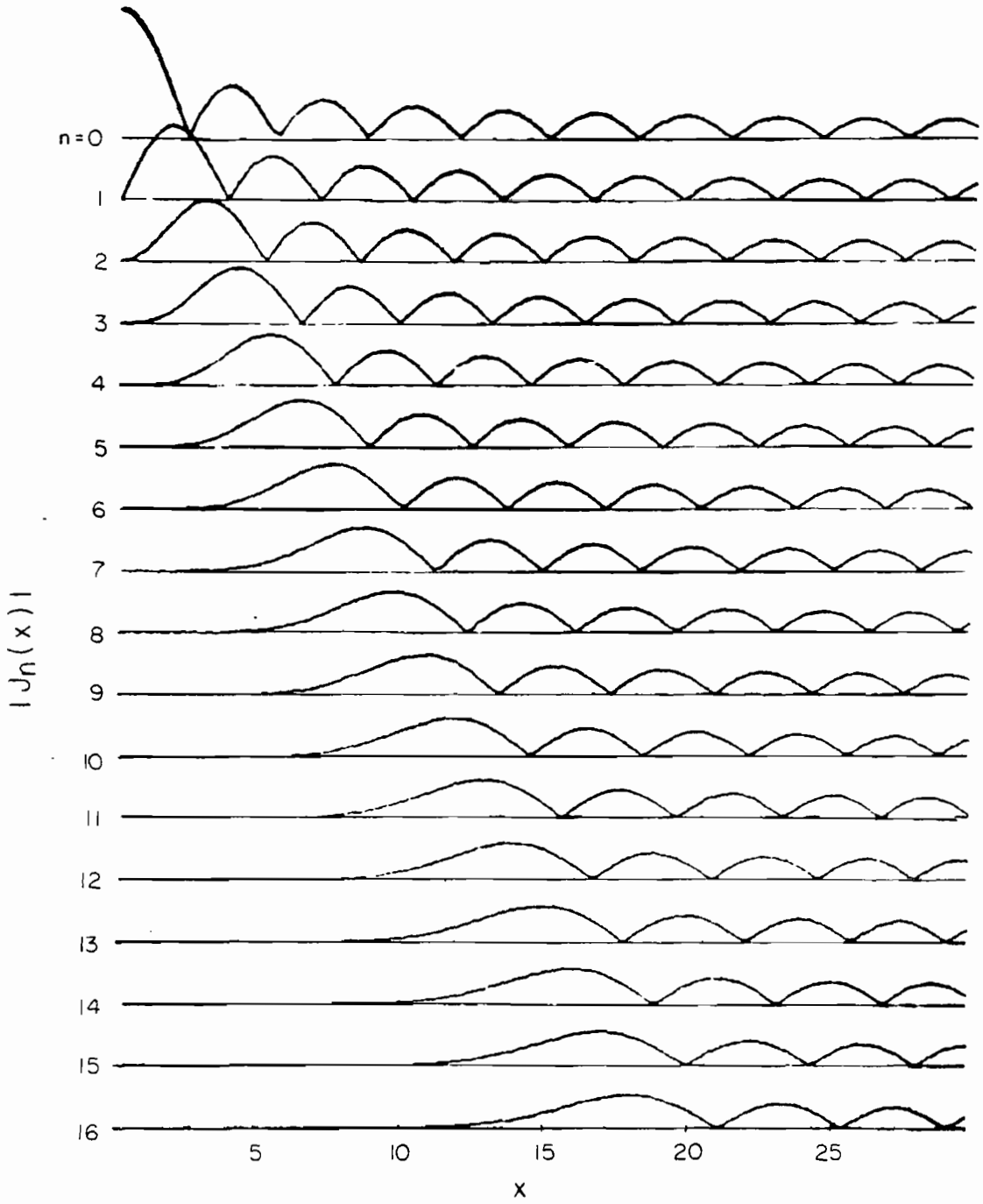

FIG. 101 Magnitude of the Bessel function of the first kind for integer orders.

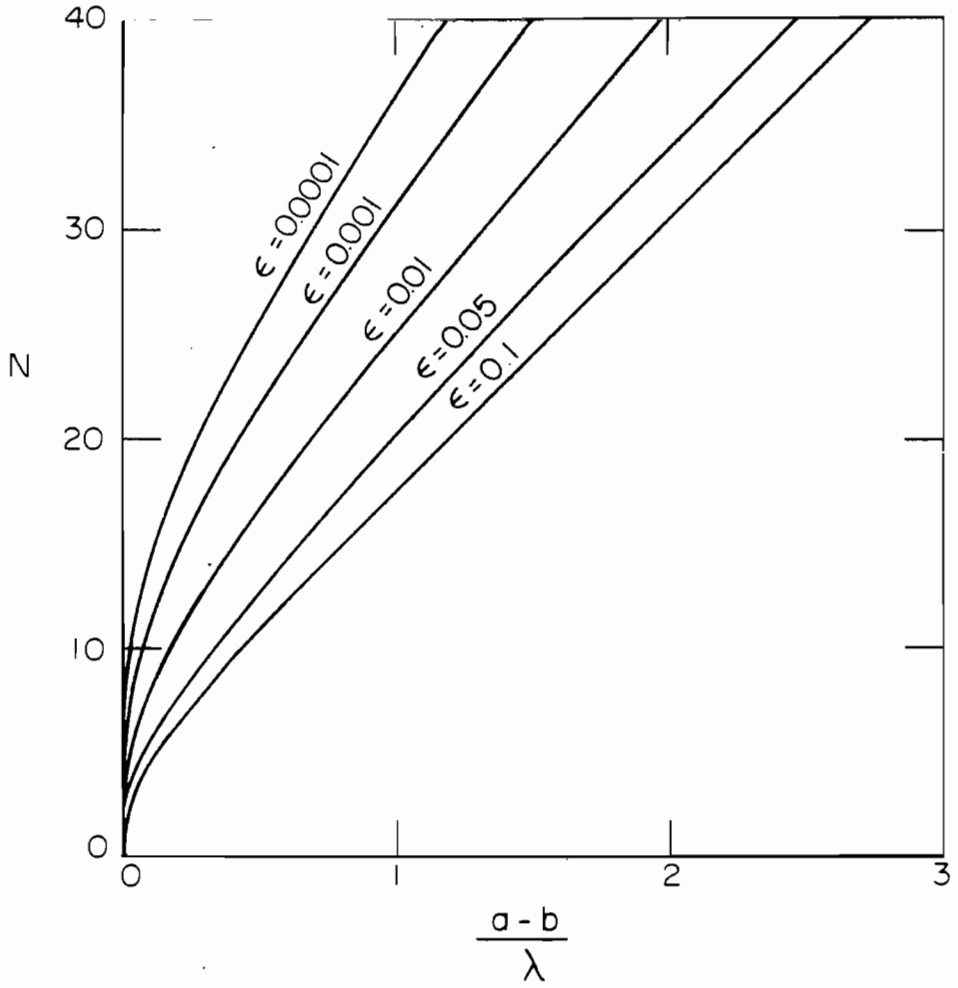

FIG.102 Plot of the minimum number of samples as a function of $(a-b)/\lambda$ for N less than or equal to 40.

$$\epsilon = .1 \qquad N = 12.34\left(\frac{a-b}{\lambda}\right) \qquad \frac{a-b}{\lambda} \geq 1.0 \qquad (94)$$

$$\epsilon = .05 \qquad N = 12.60\left(\frac{a-b}{\lambda}\right) \qquad \frac{a-b}{\lambda} \geq 1.0 \qquad (95)$$

$$\epsilon = .01 \qquad N = 13.01\left(\frac{a-b}{\lambda}\right) \qquad \frac{a-b}{\lambda} \geq 1.0 \qquad (96)$$

$$\epsilon = .001 \qquad N = 13.46\left(\frac{a-b}{\lambda}\right) \qquad \frac{a-b}{\lambda} \geq 1.0 \qquad (97)$$

$$\epsilon = .0001 \qquad N = 14.36\left(\frac{a-b}{\lambda}\right) \qquad \frac{a-b}{\lambda} \geq 1.0 \qquad (98)$$

These equation are reasonable fits for cases in which the value of the first peak is greater than ϵ. For other cases, a more precise analysis of the errors is required. However, these equations appear to cover the most useful ranges.

To summarize, the above equations and Fig. 102 give the minimum number of sample points, N, as a function of the incident bandwidth ($\lambda = 1/f_c$) and the dimensions of the body. The representation is not exact, but is accompanied by some error. The parameter ϵ is the relative magnitude of the two dimensional spectrum at the Myquist rate and is a function of the allowable error. f_c is the ϵ bandwidth (the frequency at which the incident spectrum falls to ϵ times the peak magnitude of the spectrum). "a" and "b" are, respectively, the maximum and minimum dimensions of the body (as measured along its surface).

In order to use these equations on practical data, first select ϵ (a practical lower limit would be the signal-to-noise ratio). Then measure the dimensions of the body along the surface. Next find the ϵ bandwidth of the incident pulse. Finally, compute N, the minimum number of samples to be taken in 360^0 of rotation of the body. In the next section we apply this technique to smoothed impulse response of a sphere-capped cylinder.

3.3 EXPERIMENTAL VERIFICATION WITH SPHERE-CAPPED CYLINDER

Measurements of the smoothed impulse response of a sphere-capped cylinder was made in order to compare the results of the previous analysis to analysis of a real scatterer.

Figure 103 shows the geometry of the target. The smoothed impulse response was measured in the SRRC time domain metrology laboratory. The response was measured for angles of incidence from 0^0 to 90^0 at an interval of $5\text{-}5/8^0$. This gave effectively 64 angular samples over 360^0 of rotation. Figure 104 shows these measured smoothed impulse responses. These responses are an even function of θ about the angle $\theta = 90^0$, and from 180^0 to 360^0 are a

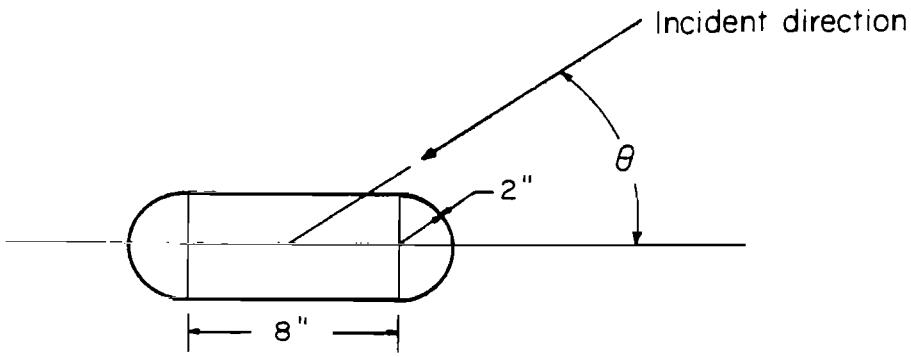

FIG. 103 Geometry of sphere-capped cylinder.

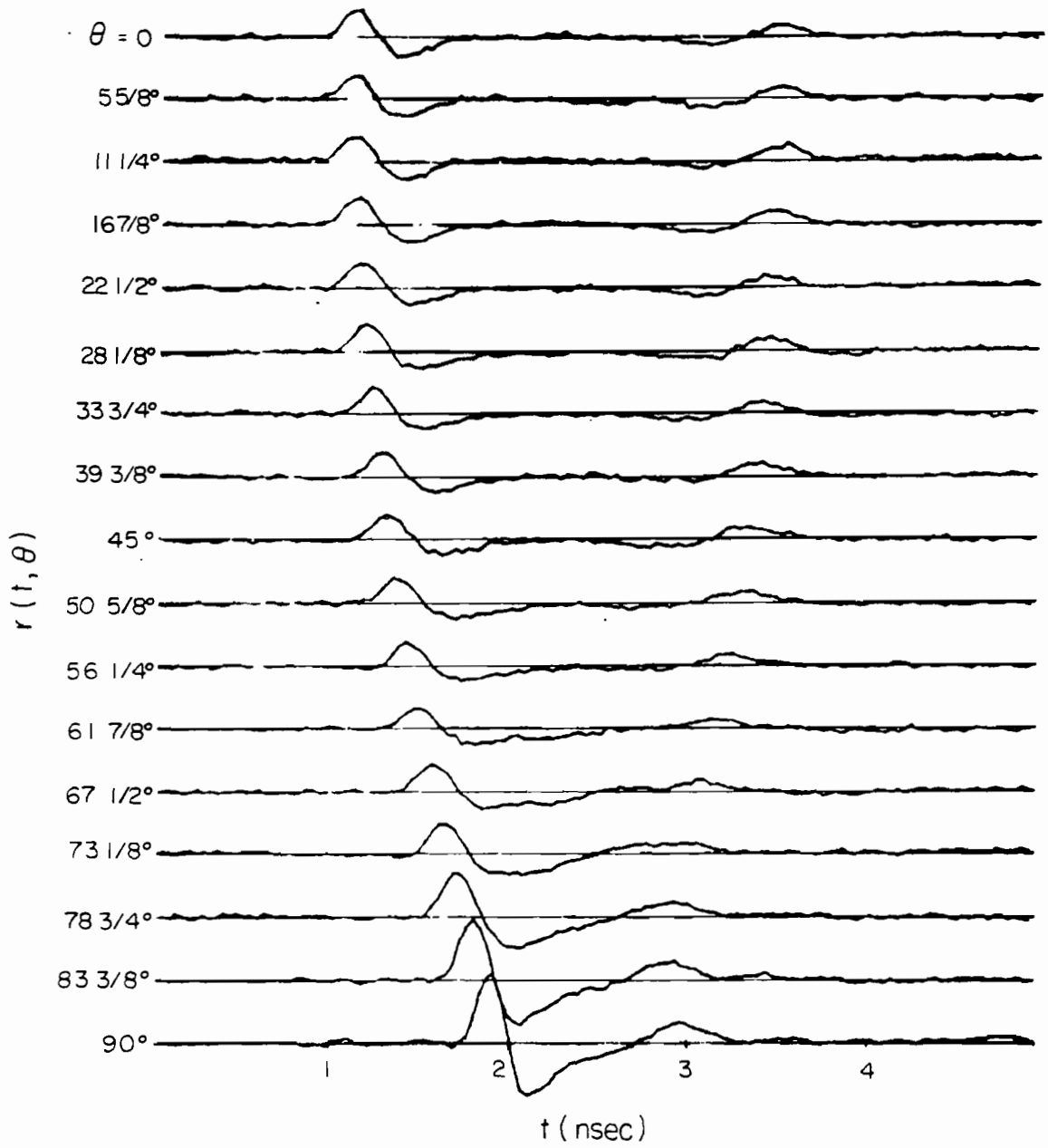

FIG.104 Smoothed impulse response of sphere-capped cylinder as a function of time and angle.

periodic replication of the responses in the interval from 0^o to 180^o. In Fig.104 there are two pulses whose separation decreases from a maximum at $\theta = 0^o$ to a minimum at $\theta = 90^o$, which is the behavior that is basically being represented in our simple model. The maximum and minimum separation of the pearks is in good agreement with the geodesic calculations given below. From Fig.103 we find that the maximum and minimum dimensions along the geodesics of the body are

$$a = 8" + \frac{1}{2}\pi\ 2" + \frac{1}{2}\pi\ 2" \tag{99}$$

$$a = 8" + \pi\ 2"$$

$$b = \pi\ 2" \tag{100}$$

Therefore

$$a-b = 8"$$

The two-dimensional Fourier transforms of the time waveforms were computed and the amplitude is presented in Fig. 105. We note that the transform decreased to the noise level in both the k and ω directions. In order to make a comparison to the theoretical results, let us assume that we will allow the amplitude to be less than or equal to .1 of the peak amplitude at the Nyquist rate in both the ω and k directions.

The amplitude of the spectrum of the incident pulse falls to .1 of its peak at 3.8 GHz. We shall use this number as the bandwidth of the incident pulse. Using a f_c of 3.8 GHz, we find that

$$\frac{a-b}{\lambda} = \frac{f_c(a-b)}{c}$$

$$= 2.53$$

From Fig.105 we find that amplitude of the two-dimensional Fourier transform falls to .1 of the peak at k = 20. This gives the number of samples in angle to be 40, as compared to the theoretical result of 38 samples.

In addition, the data was bandlimited to various different bandwidths in order to obtain a variety of points for comparison. The bandlimiting was accomplished by multiplying the transforms by Gaussian pulses of various widths. The resulting bandwidths were .5, 1, 1.5, 2, 3, and 3.8 GHz. In

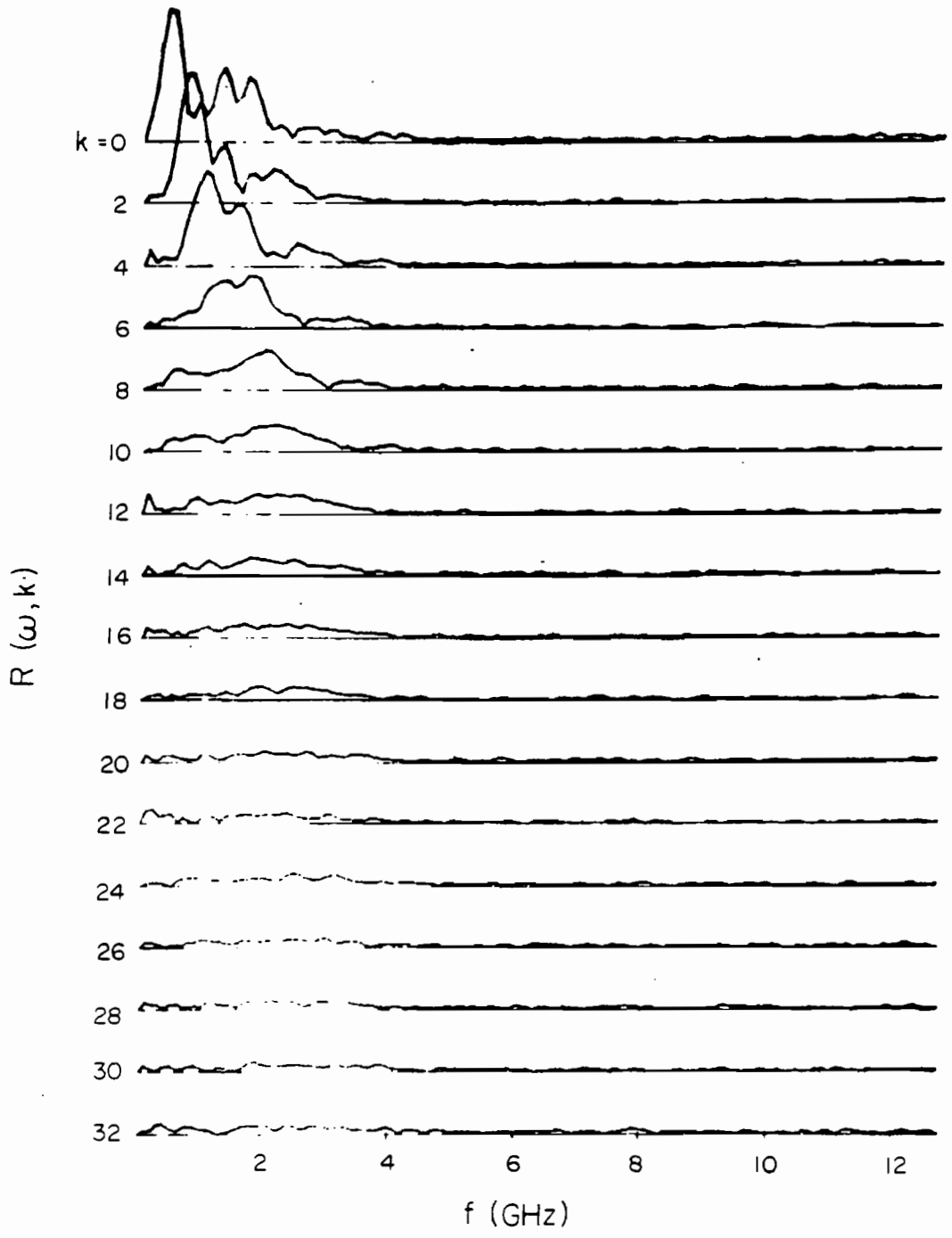

FIG. 105 Two-dimensional spectrum of smoothed impulse response of sphere-capped cylinder as a function of ω and k.

Fig.106, we show the results of bandlimiting the data so that the incident pulse had a 20 dB bandwidth of 3 GHz. As compared with Fig. 105, the spectrum falls off more rapidly in both the ω and k directions, as would be expected. The spectrum falls to .1 times the peak at k = 16. This gives the resulting minimum number of samples to be 32, as compared to the theoretical result of 31 samples. A further reduction in bandwidth to 2 GHz yields the spectrum in Fig. 107. We note that the spectrum falls off even more rapidly than in the previous cases. In this case the spectrum falls to .1 times the peak at k = 10, which gives the resulting number of samples to be 20 as compared to a theoretical result of 22. The results from the bandlimiting study are presented in Fig. 108, together with the results from the theoretical analysis. Figure 108 shows that the experimental results agree quite well with the theoretical results and hence this theoretical expression yields a very good estimate of the number of samples needed on any rotationally symmetric body.

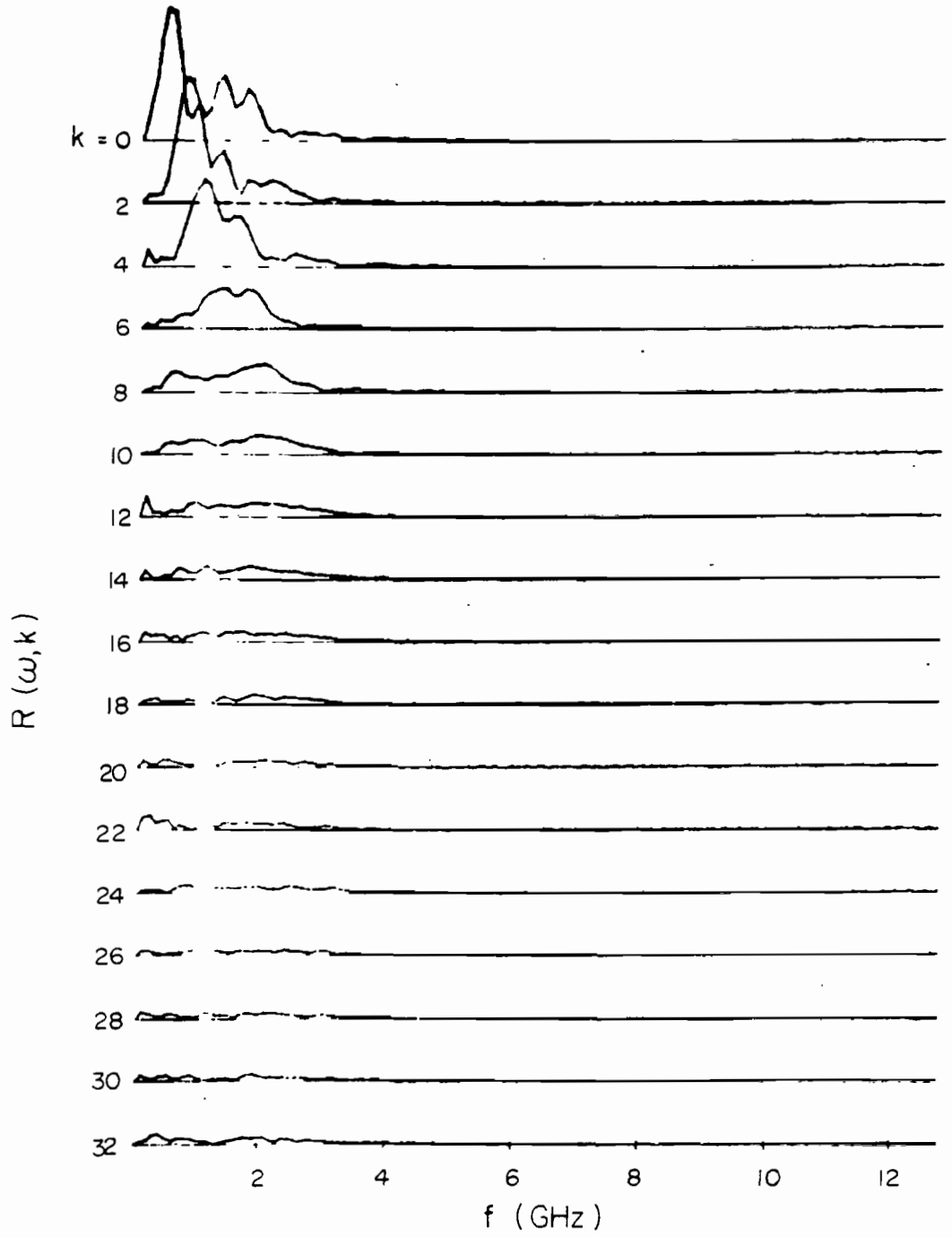

FIG. 106 Two-dimensional spectrum of smoothed impulse response bandlimited to 3 GHz.

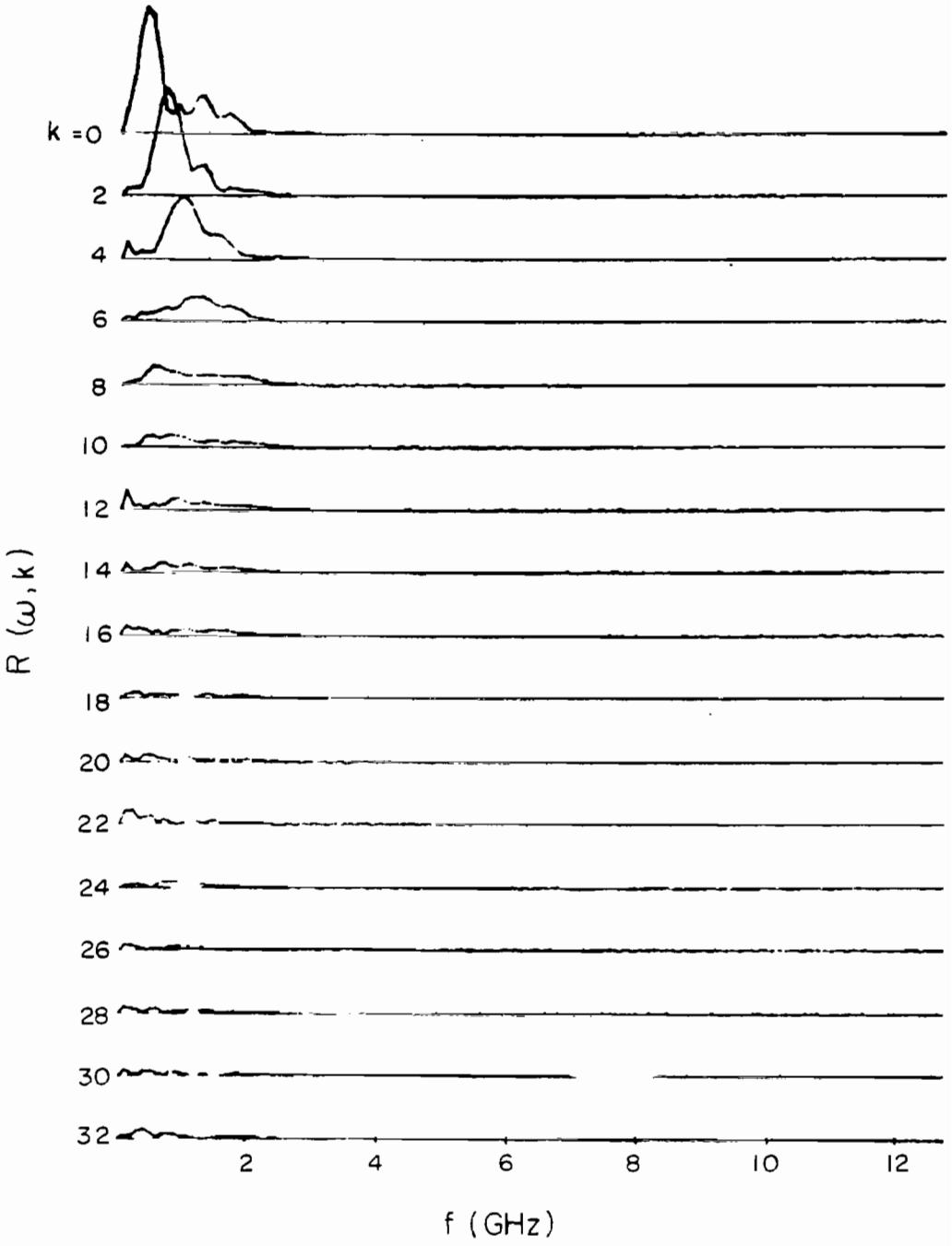

FIG. 107 Two-dimensional spectrum of smoothed impulse response bandlimited to 2 GHz.

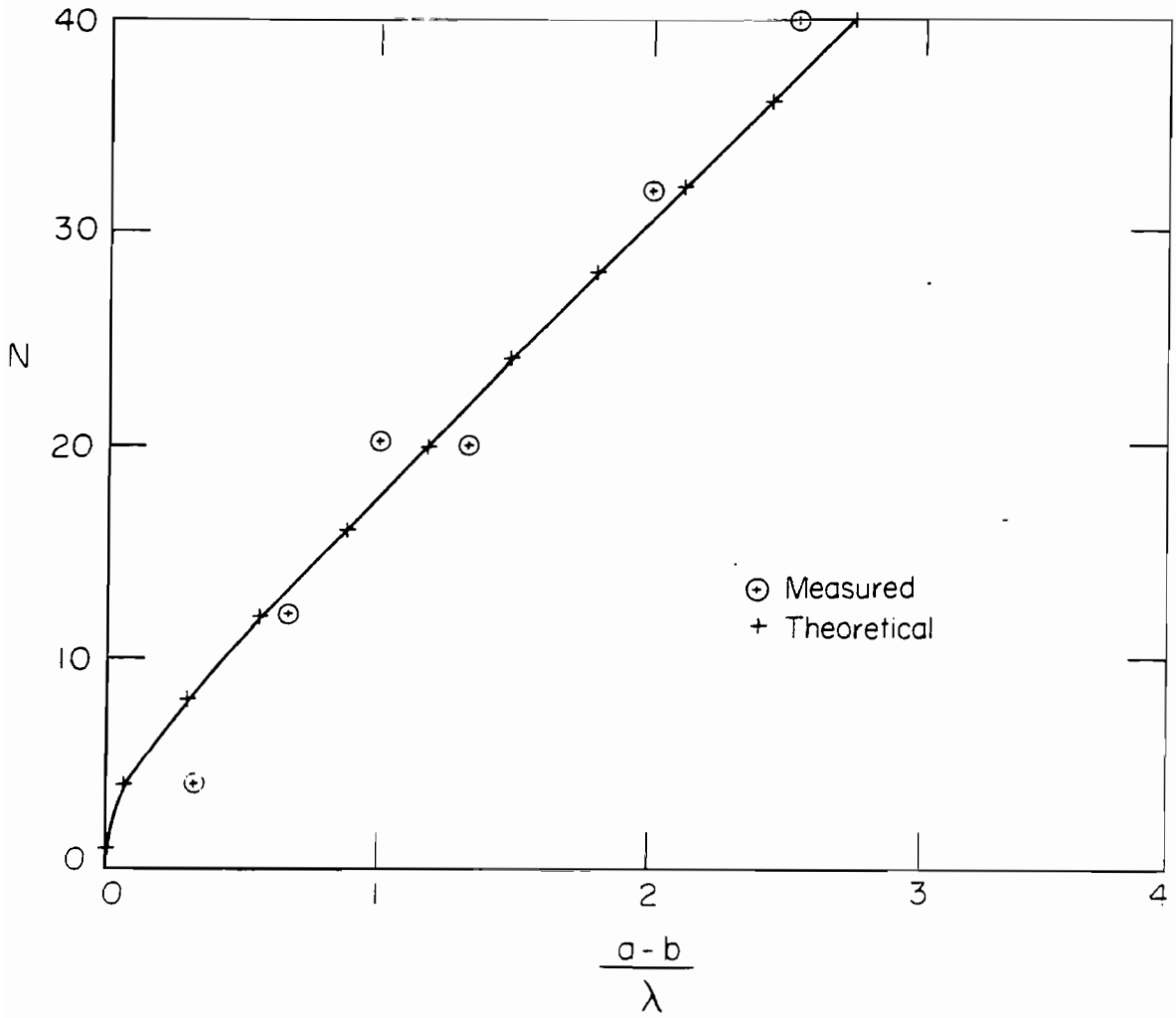

FIG. 108 Measured and theoretical results of minimum number of samples as a function of $(a-b)/\lambda$.

SECTION 4

TIME DOMAIN SCATTERING MEASUREMENTS

4.1 DESCRIPTION OF MEASUREMENTS

The functional block diagram of the scattering range is shown in Fig. 109. The system signal source is a high-voltage switch which generates a 300 V step function with a risetime less than 100 psec. The signal is radiated, virtually undistorted, from a wire transmitting antenna protruding through a circular ground plane 20 feet in diameter. This wave is then reflected by a target and the scattered waveform is received on a coaxial horn antenna, which essentially smooths and differentiates the signal and thus provides the smoothed impulse response of the target. The received waveform is sampled by a 12 GHz oscilloscope that has been triggered by the initial pulse and whose sampling gate deflection is under the control of a small instrumentation computer. Unprocessed data are displayed on the oscilloscope CRT while the sampled-and-held waveform is passed through a loq-pass filter, digitized, read into the computer, and stored on magnetic tape automatically. This system has been designed to correct for long-term timing drift, and/or amplifier drift. In addition, the waveforms are stored in such a way that they are ready for the subsequent operations of averaging (to remove short-term noise) and baseline processing. The effects of a time varying baseline are subtracted from measured waveforms to improve system accuracy.

The salient characteristics of the range are the speed and simplicity with which multi-octave frequency-domain data can be obtained. These advantages accrue because the time-domain scattering range yields an "uncontaminated" interval of time between the arrival of the direct wave and the arrival of unwanted reflections. This is most easily explained by considering the sketch in Fig. 110 which shows the relative location of the elements on the ground plane, and the photographs in Fig. 111 which show the range response as it appears at the oscilloscope (no data processing has been used at this point). The transmitted signal travels outward from the base of the wire antenna and is received at R at time $t_0 = d/c$ (where c is the speed of light). This time is marked by the pulse at the left end of the trace in Fig. 111. The outgoing wave reaches the target at $t = r/c$, is reflected, and arrives at the receiver at $t_1 = (2r+d)/c = t_0 + (2r/c)$. The targets are usually located anywhere from 2 to 5 feet from the transmitting antenna; therefore, target returns lie in the region marked by the doublets at t_1 and t_2 in the lower photographs. The erratic response at the right edge of the trace which occurs after t_3 marks the arrival of the pulse reflected by the table edge and the effects of the pulse radiated from the tip of the transmitting antenna. It should be noted that a "clear window" exists between the second doublet and the table edge. This is required because many of the targets are highly dispersive and their response will extend far beyond the specular reflection (e.g., see Fig. 115). The entire region between the direct transmission and the table edge response forms a convenient time "window" to view the target response and allows one to "gate out" (in time) unwanted reflections. Thus, undistorted transient target responses can be viewed without resorting to elaborate and expensive anechoic chambers. In addition, a single time-domain measurement obviates the requirement for tedious measurement of the amplitude and phase responses at

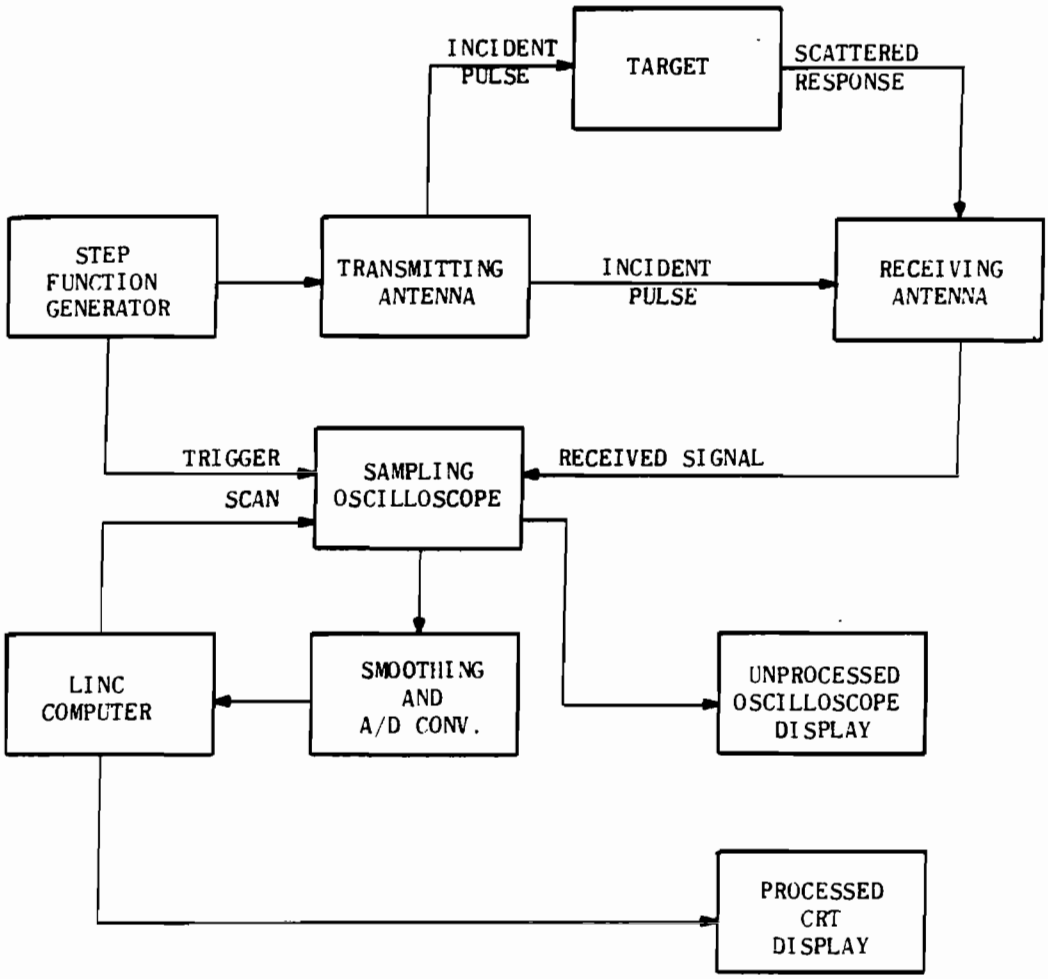

FIG. 109 Functional block diagram of video time-domain scattering range.

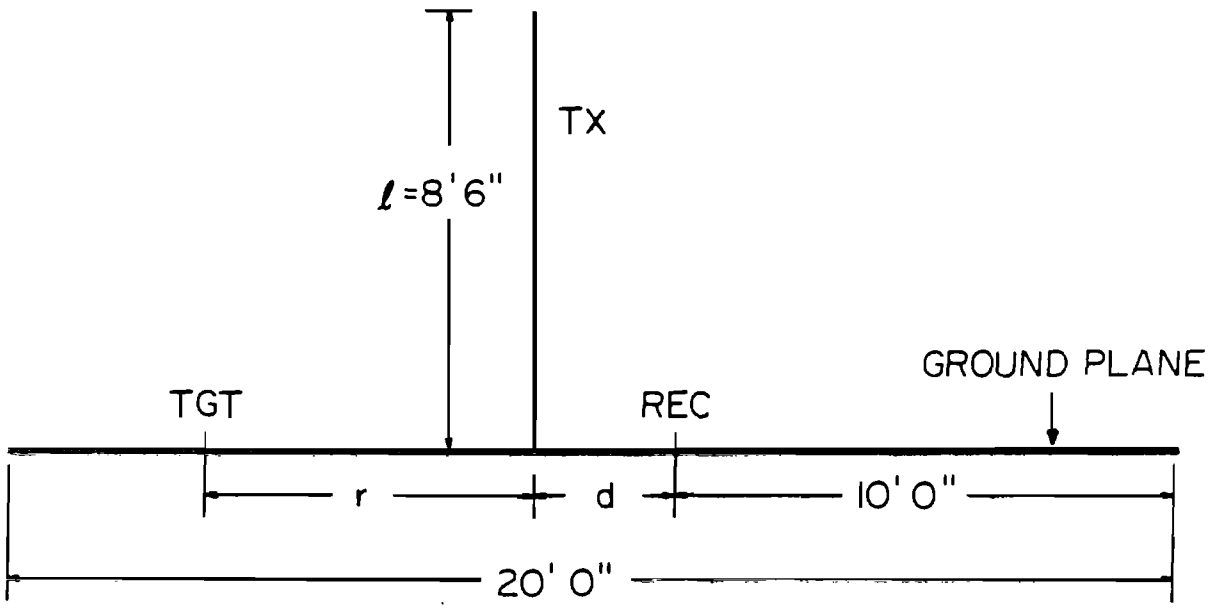

FIG. 110 Geometrical configuration of video time-domain scattering range.

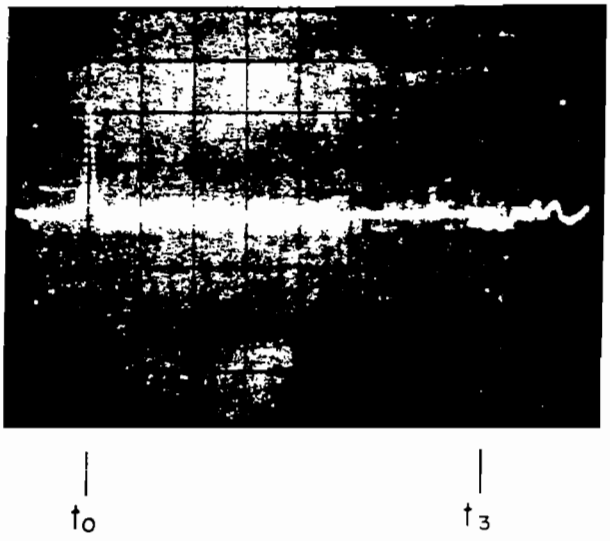

Incident pulse with clear range

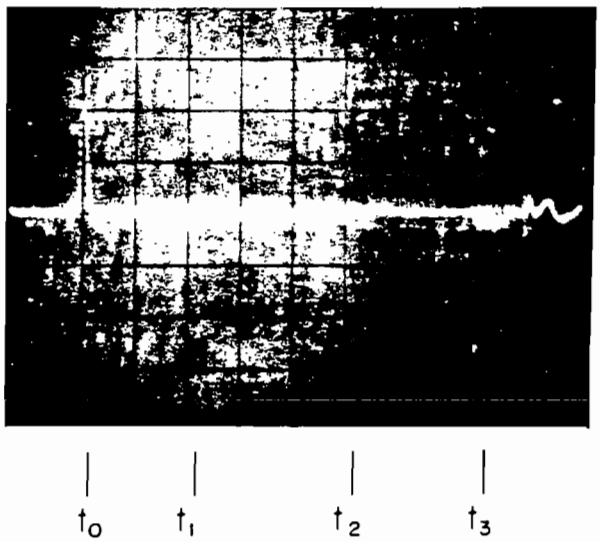

Incident pulse with markers at 2 ft. (t_1) and at 5 ft. (t_2) from transmitting antenna.

FIG. 111 Response of video time-domain scattering range showing incident pulse and time window (horizontal scale: 2 nsec/div.; vertical scale: 200 mV/div.).

many frequencies.

The accuracy of the measurement system can be estimated by realizing that the situation that prevails is essentially the same as the elementary statistical problem of estimating the mean V_m of a random variable V when given N independent sample values V_i. In our case, the signal voltage is V_m, the signal plus noise is the random variable, V, and the expected value of the noise voltage is zero. We therefore use the sample mean

$$\bar{V} = \frac{\sum_{i=1}^{N} V_i}{N}$$

as an estimator for V_m (the signal value at a particular point t on the sampled waveform) since it is consistent and unbiased. We take as an error estimate the standard deviation of $\bar{V}$,

$$\sigma_{\bar{V}} \approx \frac{S}{\sqrt{N}}$$

which is computed using the sample variance

$$S^2 = \frac{\sum_{i=1}^{N} (V_i - \bar{V})^2}{N}$$

as an estimate for the population variance.

The peak of the incident pulse, as measured on the sampling oscilloscope, is approximately 500 mV, and a typical target response has a peak value in the vicinity of 10 mV. When using the 10 mV scale on the sampling oscilloscope, we estimate the standard deviation of $\bar{V}$, as described in the preceding paragraph, to be

$$\sigma_{\bar{V}} = 0.059 \text{ mV}$$

if N = 64 scans are averaged. Thus, the estimated standard deviation of $\bar{V}$ is in the vicinity of 0.6% of the peak value of the target response.

4.2 RESULTS

In a previous study[17] the smoothed impulse response was measured for 23 target aspect angles. Under the present contract, the responses for an additional 35 target aspect angles were measured. The resulting 58 waveforms were used on OLPARS as a basis for design of an identification processor. The OLPARS portion of this work is described in Sec. 5. These 58 waveforms result from measurements on nine target geometries at various aspect angles and polarizations and are summarized in Table VII. The sphere geometry and the four cylinder geometries are displayed in Fig. 112. In Fig. 113, the cube, sphere-cone-sphere, UES satellite model, and SSS satellite model geometries are shown.

In Fig. 114 the smoothed impulse response (in the backscatter direction) of an 8 inch cube is shown for three angles of incidence. In this case, the image plane is normal to the four cube faces. For 0^0 incidence the return from the front face takes the form of a smoothed doublet, as expected. Next, the response becomes small, indicating little return from the sides of the cube, and approximately 1.4 nsec after the smoothed doublet there appears a negative pulse whose timing can be attributed to the back edge of the cube. For 45^0 incidence the first part of the response is a positive pulse that may be attributed to the front vertical edge of the cube. This is followed approximately 0.9 nsec later by a return that may be attributed to the two middle vertical edges. The return due to a wave traveling around the rear of the cube at the speed of light would be expected 2.5 nsec after the return from the front edge, and indeed the measured response does show a pulse approximately 2.7 nsec after the initial pulse.

In Fig. 115 the smoothed impulse response of the 8-inch cube is shown for the case where the image plane passes through the diagonals on two opposite faces. This is the case when the target on one side of the image plane looks like a roof. For 0^0 incidence the return appears to be nearly the same as for the case of 0^0 incidence with a normal image plane as shown in Fig. 114. There does appear to be slight difference immediately following the initial smoothed doublet. The response varies continuously as the angle of incidence increases. At 90^0 there is an initial positive pulse due to scattering from the edge region, followed by negligible return and then a negative pulse approximately 1.1 nsec later that can be attributed to the top edge of the cube. Next, there is again negligible return followed by a second positive pulse approximately 1.4 nsec. after the negative pulse. This can be attributed to either a "reflection" from the rear edge or a wave traveling around the rear of the cube.

In Fig. 116 the smoothed impulse response of a right square cylinder with a normal image plane that was 12 inches long and 4 inches square is shown for various angles of incidence. For 0^0 incidence the first portion of the return approximates a doublet and is followed by a negligible return from the sides of the cylinder. The return from the rear edge of the cylinder appears approximately 2.1 nsec later and is followed by the return due to the wave traveling around the rear (a positive pulse at 2.5 nsec). These two

TABLE VII

SUMMARY OF MEASURED WAVEFORMS

Object Shape Class	Image Plane	Polarization	Aspect Angles	No. Waveforms
Sphere D = 8"				1
Circular Cylinder with Sphere Caps D = 4", L = 12"	Coincident with axis	TE	0^o, 30^o, 60^o, 90^o	4
	Normal to axis	TM		1
Right Circular Cylinder D = 4", L = 12"	Coincident with axis	TE	0^o, 30^o, 40^o, 60^o, 90^o	5
	Normal to axis	TM		1
Right Circular Cylinder D = 4", L = 8"	Coincident with axis	TE	0^o, 30^o, 45^o, 60^o, 90^o	5
	Normal to axis	TM		1
Right Square Cylinder D = 4", L = 12"	Coincident with axis and normal to faces	TE	0^o, 30^o, 60^o, 90^o	4
	Coincident with axis and diagonal to faces	TE	0^o, 30^o, 45^o, 60^o 90^o	5
	Normal to axis	TM	0^o, 30^o, 45^o	3
Cube D = 8"	Normal to faces		0^o, 15^o, 30^o, 45^o	4
	Diagonal to faces		0^o, 30^o, 45^o, 60^o, 90^o	5
Sphere-Cone-Sphere $\theta = 15^o$, $D_1 = 2"$, $D_2 = 8"$	Coincident with axis	TE	0^o, 30^o, 60^o, 90^o, 120^o, 150^o, 180^o	7
UES Satellite Model $D_1 = 2"$, $L_1 = 2"$ $D_2 = 6"$, $L_2 = 8"$ $D_3 = 2"$, $L_3 = 2"$	Coincident with axis	TE	0^o, 30^o, 45^o, 60^o, 90^o	5
	Normal to axis	TM		1
SSS Satellite Model D = 4" L/Dw = 32, L = 4"	Normal to wire axis			1
	Diagonal to wire axis		0^o, 30^o, 45^o, 60^o, 90^o	5

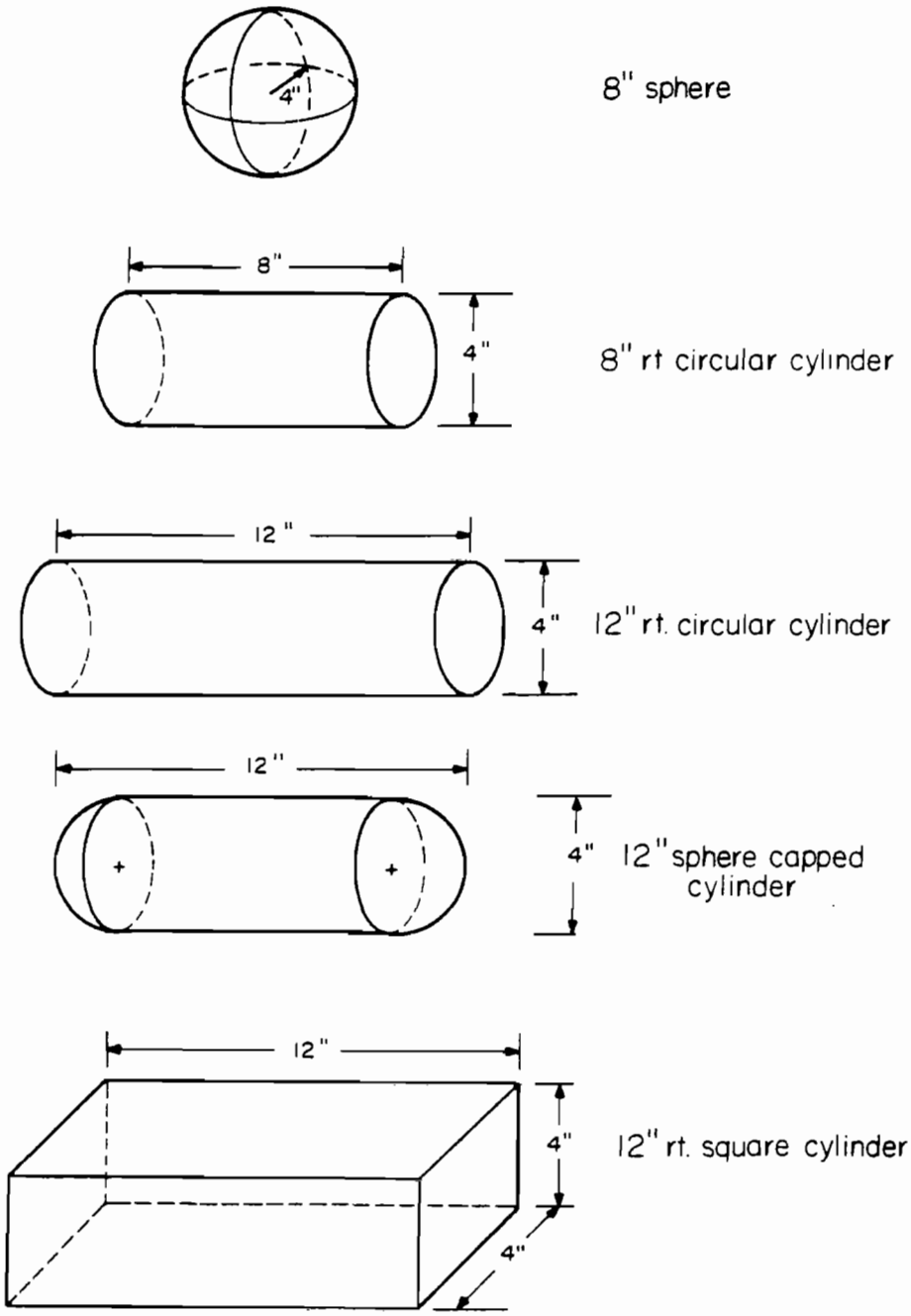

FIG. 112 Target geometries used for scattering range measurements.

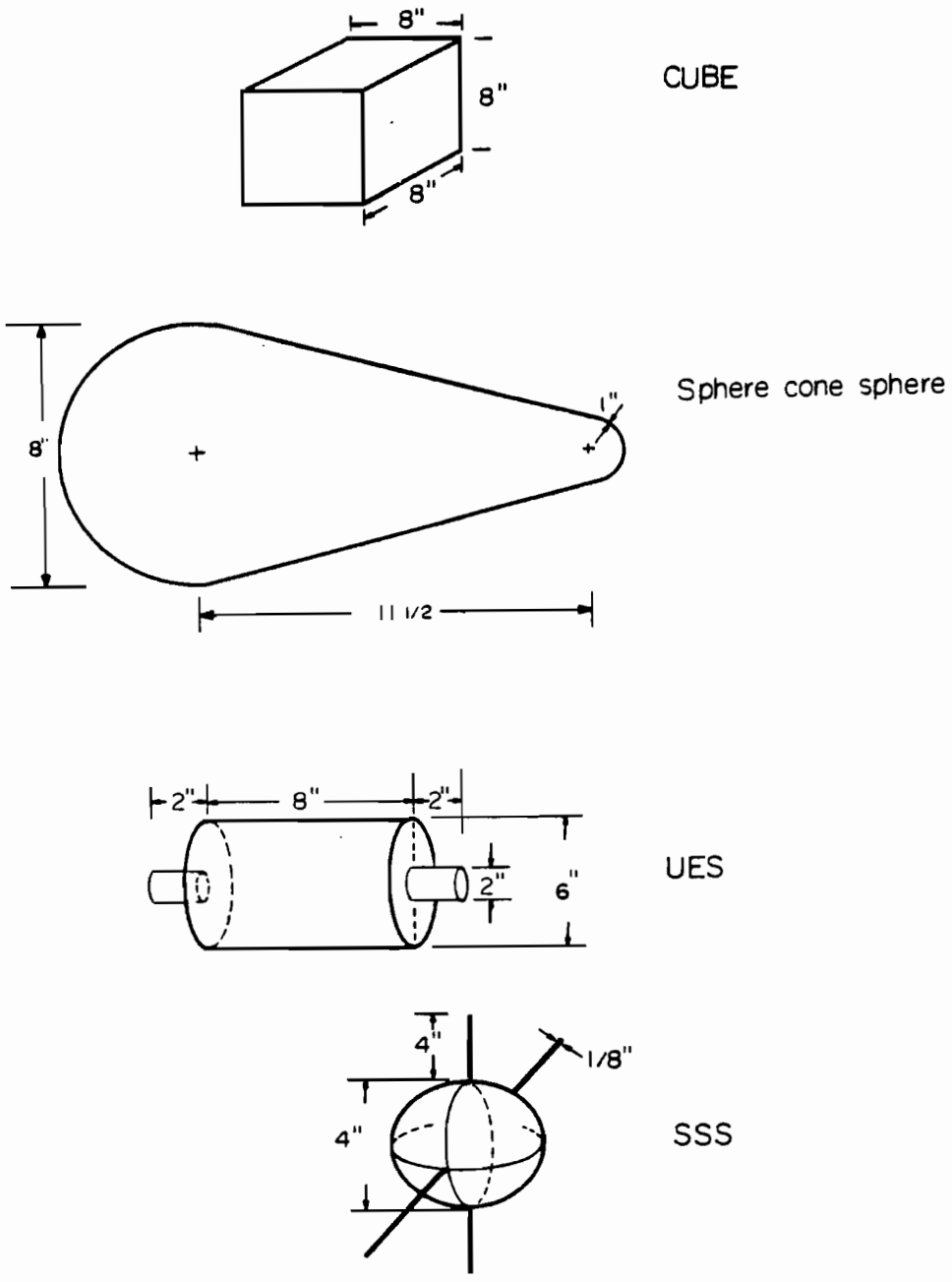

FIG. 113 Target geometries used for scattering range measurements.

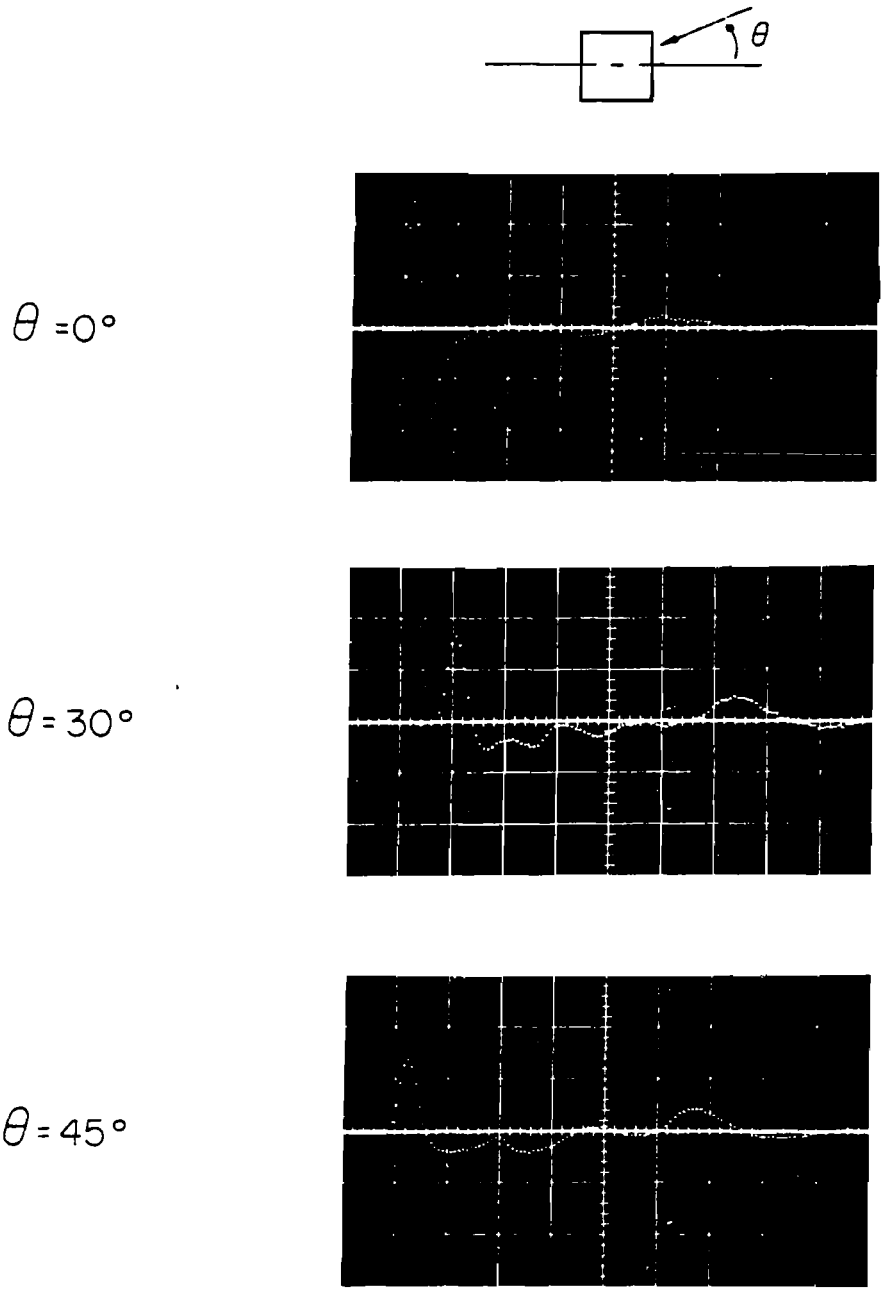

FIG. 114 Smoothed impulse response of 8 inch cube with image plane normal to faces. Horizontal scale: 0.5 nsec/div., vertical scale: 10 mV/div.)

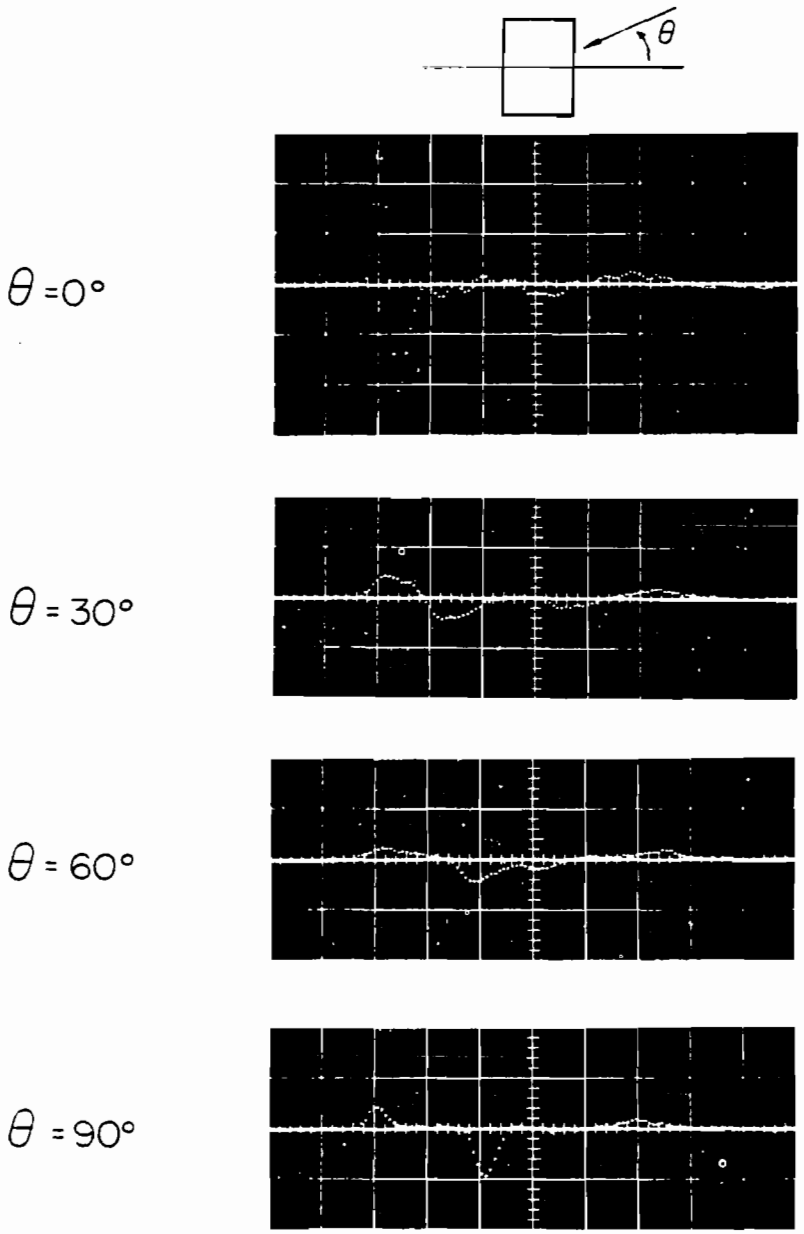

FIG. 115 Smoothed impulse response of 8 inch cube with diagonal image plane (horizontal scale: 0.5 nsec/div., vertical scale: 10 mV/div.).

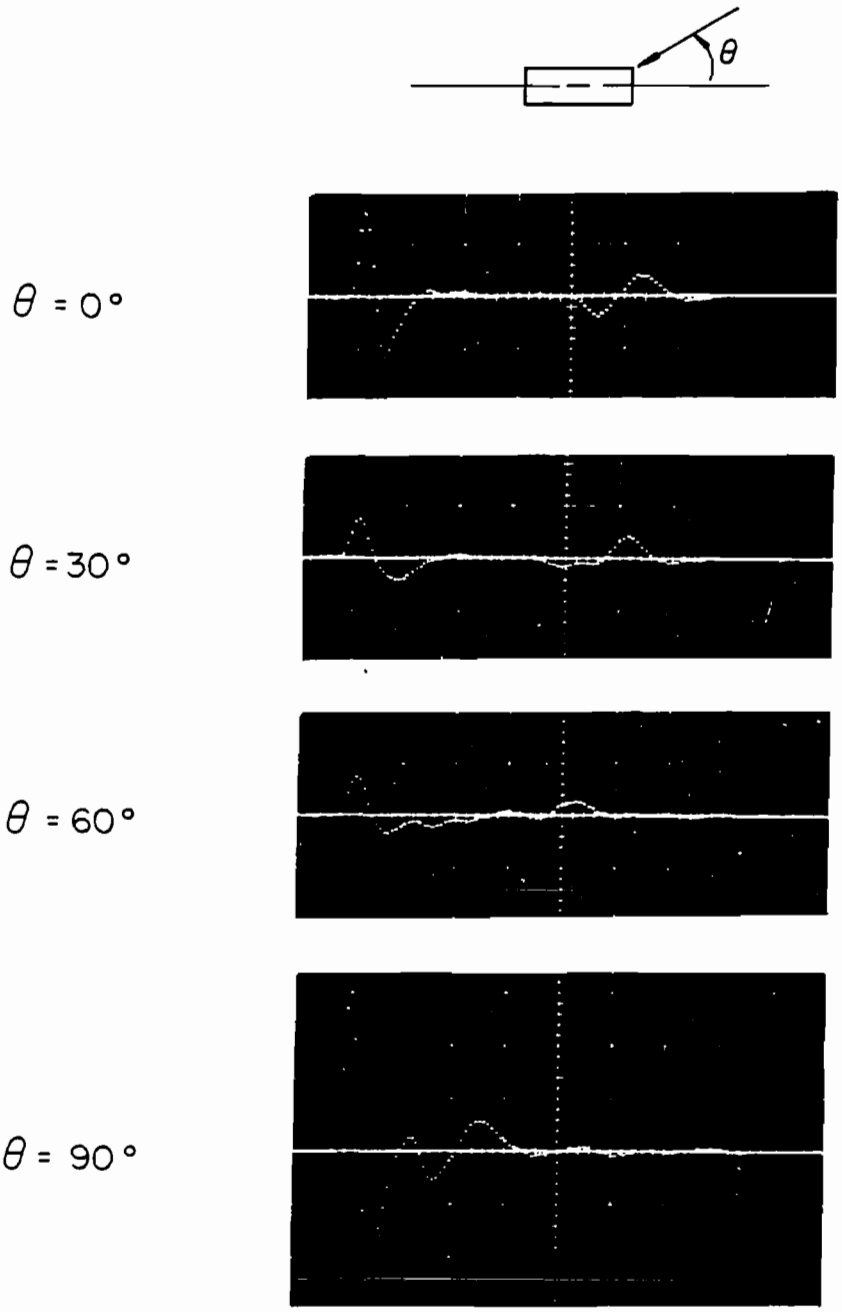

FIG. 116 Smoothed impulse response of a right square cylinder with normal image plane and TE polarization (horizontal scale: 0.5 nsec/div.; vertical scale: 5 mV/div.).

returns, when combined, are "doublet-like" in shape, but are of opposite polarity from the return from the front face. This change of polarity would produce a 180^0 phase shift if convolved with a sinusoidal waveform. At 30^0 and 60^0 incidence the doublet character of the initial return and the back return disappears, but the waveform features can again be attributed to various geometric features of the target. Finally, at 90^0 incidence the large doublet return from the side face of the square cylinder appears and is followed by returns due to the back side (a negative pulse at 0.65 nsec) and a wave traveling around the rear (a positive pulse at 1.1 nsec).

In Fig. 117 the smoothed impulse response of the right square cylinder with a diagonal image plane is displayed for various angles of incidence. The response for 0^0 incidence appears the same as for the case of a normal image plane. The response shape varies continuously as the angle of incidence increases. At 90^0 the return from the leading edge of the square cylinder is in the form of a positive pulse. This is followed approximately 0.5 nsec later by a negative pulse which can be attributed to the top and bottom edges. Finally, 0.75 nsec after this negative pulse, a positive pulse appears which can be attributed to either a "reflection" from the rear edge or to a wave traveling around the rear of the square cylinder.

The smoothed impulse response of a right circular cylinder that was 12 inches long and 4 inches in diameter is displayed in Fig. 118 for several angles of incidence. For 0^0 incidence the response is nearly the same as that measured for the right square cylinder. The main difference is that the amplitude of the initial doublet is slightly smaller for the circular cylinder, as expected because the cross-sectional area of the circular cylinder is smaller. At 30^0 and 60^0 incidence, slight differences in the responses from the two cases appear, but the gross features again may be related to the actual geometry. At 90^0 incidence, however, the return from the right circular cylinder is markedly different from the right square cylinder. The initial part of the circular cylinder return at 90^0 incidence approximates an impulse and is followed by a negative swing, as predicted by physical optics. The second positive pulse that appears approximately 2.0 nsec after the first pulse may be attributed to a wave traveling around the rear of the cylinder. Comparison of this measured response with the smoothed impulse response from an infinitely-long circular cylinder with TE polarization[18] shows remarkable similarity, and indicates that the effect of the ends on a finite cylinder for this polarization of the incident wave is small. This effect has been rigorously discussed by DeLorenzo.[19]

The smoothed impulse response of a right circular cylinder (TE polarization) that was 8 inches long and 4 inches in diameter is shown in Fig. 119 for several angles of incidence. The responses for this target are very similar to those obtained for the 12 inch circular cylinder and displayed in Fig. 118. For 0^0 incidence the return from the nose is the same in the two cases and the return from the far end appears quite similar in shape and amplitude. However, this return for the 8 inch cylinder appears approximately 0.7 nsec earlier, than the corresponding return for the 12 inch cylinder, as expected. For 90^0 incidence, both returns appear to have the same shape; however, the 12 inch cylinder has a slightly larger amplitude.

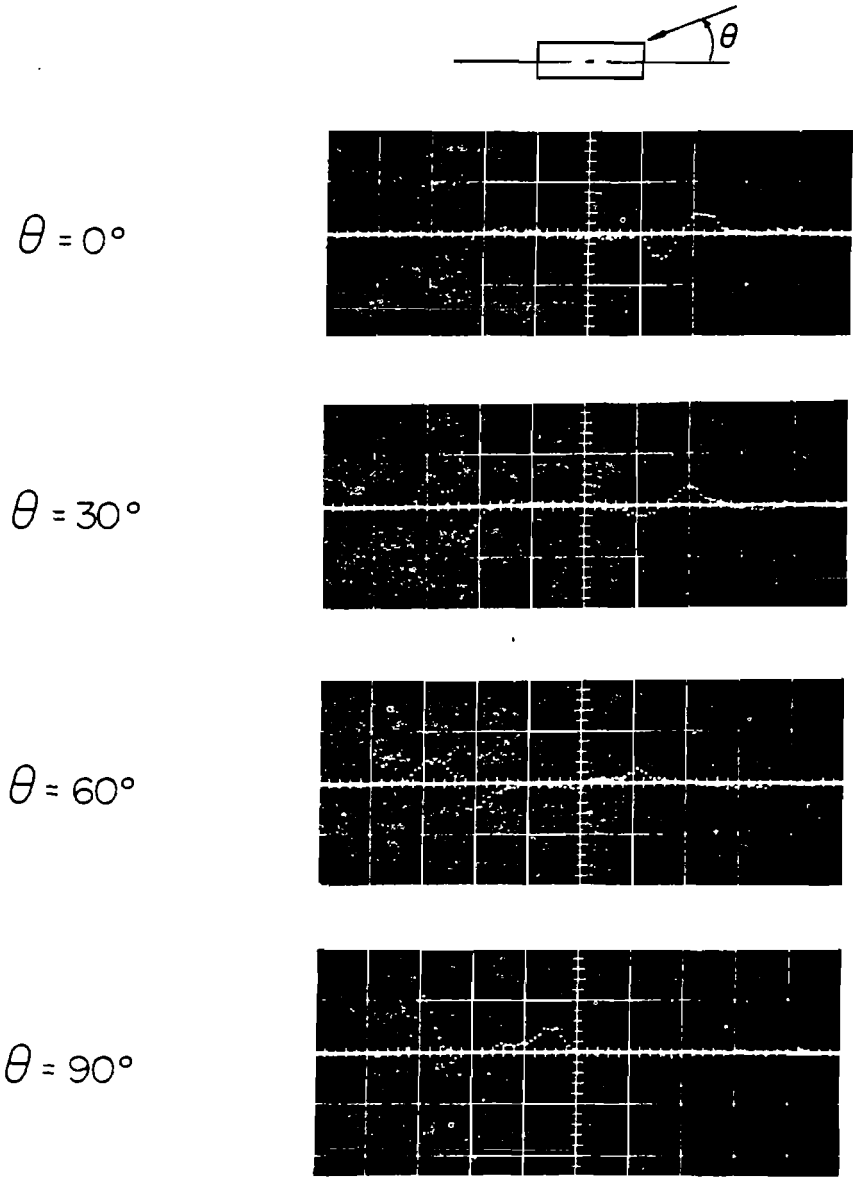

FIG. 117 Smoothed impulse response of right square cylinder with diagonal image plane and TE polarization (horizontal scale: 0.5 nsec/div.; vertical scale: 5mV/div.).

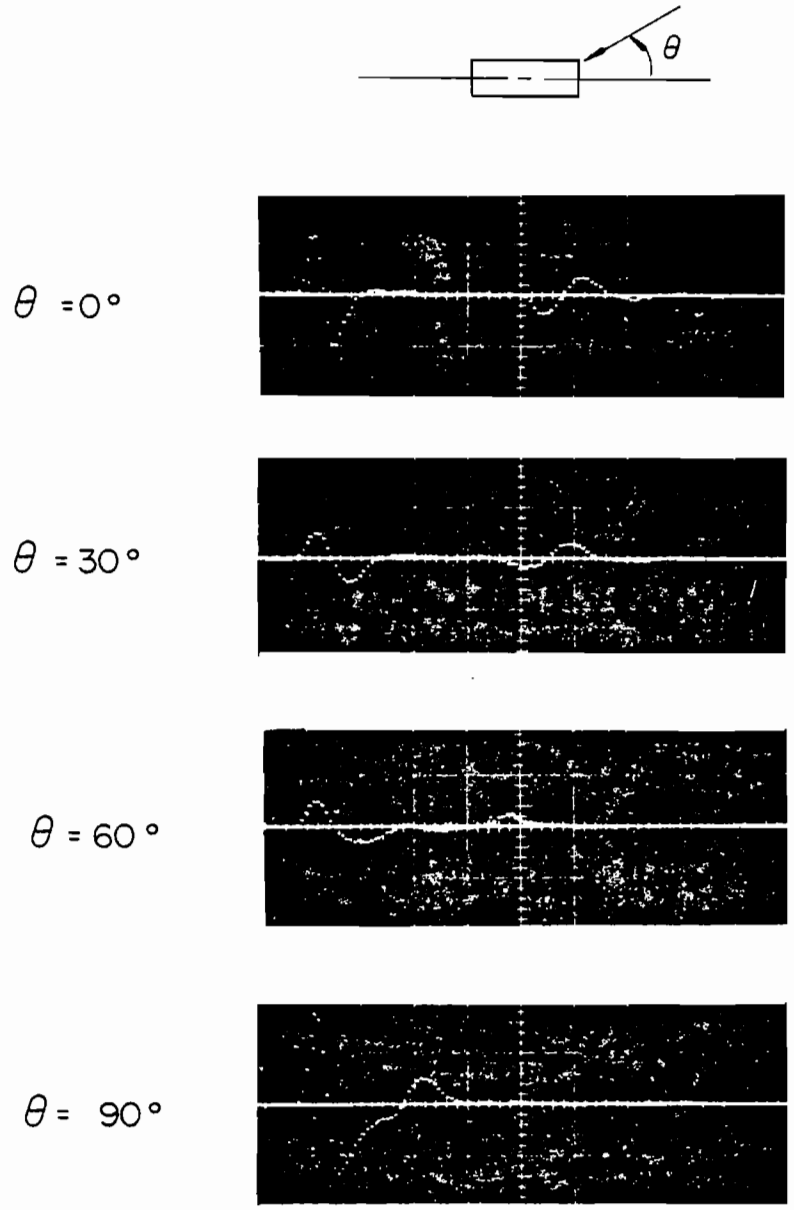

FIG. 118 Smoothed impulse response of a right circular cylinder for TE polarization (horizontal scale: 0.5 nsec/div.; vertical scale: 5 mV/div.).

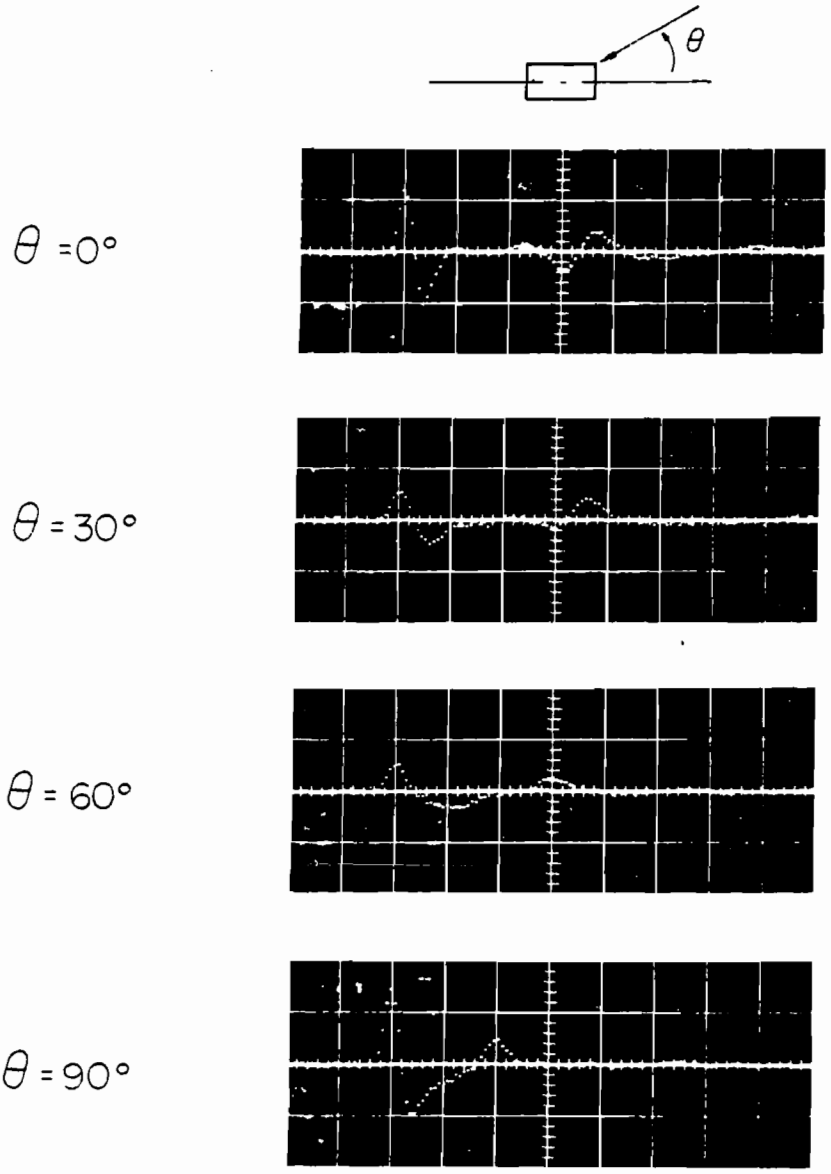

FIG. 119 Smoothed impulse response of right circular cylinder for TE polarization (horizontal scale: 0.5 nsec/div.; vertical scale: 5 mV/div.).

In Fig. 120 the smoothed impulse responses of a 4 inch diameter sphere and an 8 inch diameter sphere are shown. These will be used for comparison with the responses of the sphere-capped cylinder and sphere-cone-sphere.

The smoothed impulse response of a sphere-capped cylinder with a length of 12 inches and a diameter of 4 inches is shown in Fig. 121 for various angles of incidence. For 0° incidence the initial part of the return is, as expected, identical to the return from the 4 inch diameter sphere shown in Fig. 72(a). This is followed by a near zero signal, indicating that there is little return from the sides of the cylinder. Finally, the return from the joint between the cylinder and the sphere cap appears, along with the return due to the wave traveling around the rear of the cylinder. At 30° and 60° incidence the gradual modification from the 0° case to the 90° incidence case can be noted. At 90° incidence the shape of the response is virtually the same as it was for the right circular cylinder at 90° incidence. This is as expected, since the effect of the cylinder ends appears to be negligible for this polarization and angle of incidence, as pointed out earlier.

The smoothed impulse response of a sphere-cone-sphere (with a half angle of 15°, a large sphere diameter of 8 inches, and a small sphere diameter of 2 inches) is displayed in Fig. 122. For the case with axial incidence on the small sphere tip (0° incidence), Fig. 122 shows the small return from the tip, followed by a negligible return from the conical part of the structure. Next, a negative return, apparently from the joint between the large sphere and the cone, appears. This is followed by the return that can be attributed to a wave traveling around the rear spherical surface of the structure. By viewing Figs. 122 and 123, the gradual change in character of the response from the case of 0° incidence to the case of 180° incidence can be observed. For the case of axial incidence on the large sphere base (180° incidence), the initial part of the return is the same as that for the 8 inch diameter sphere shown in Fig. 120(b), as expected. This is followed by a near zero return from the conical surface, which by the way is in the geometric light shadow. Finally, the return from the tip region of the structure may be observed approximately 3.2 nsec after the initial pulse. It is also interesting to note that the initial portion of the returns for 180°, 150°, 120° and 90° incidence all possess the same shape as the initial return for the 8 inch diameter sphere shown in Fig. 120(b).

Figure 124 displays the smoothed impulse response of the University Explorer Satellite (UES) model with TE polarization for various angles of incidence. At $\theta = 0^{\circ}$ the return from the small cylinder face is followed in approximately 0.4 nsec by the return from the large cylinder face. Both of these approximate a smoothed doublet, as would be predicted by physical optics. The complicated interaction between the two cylinders and the various edges present in this target follow. At 90° the return from the large cylinder now appears first. Close examination of the response approximately 0.4 nsec later in time reveals a perturbation which can be attributed to a return from the small cylinder.

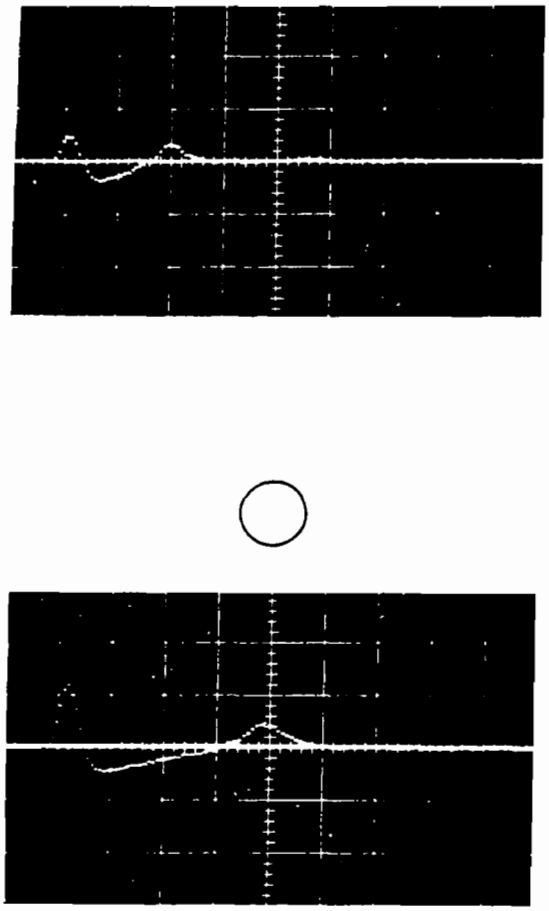

FIG. 120 Smoothed impulse response of spheres (horizontal scale: 0.5 nsec/div.; vertical scale: 5 mV/div.).

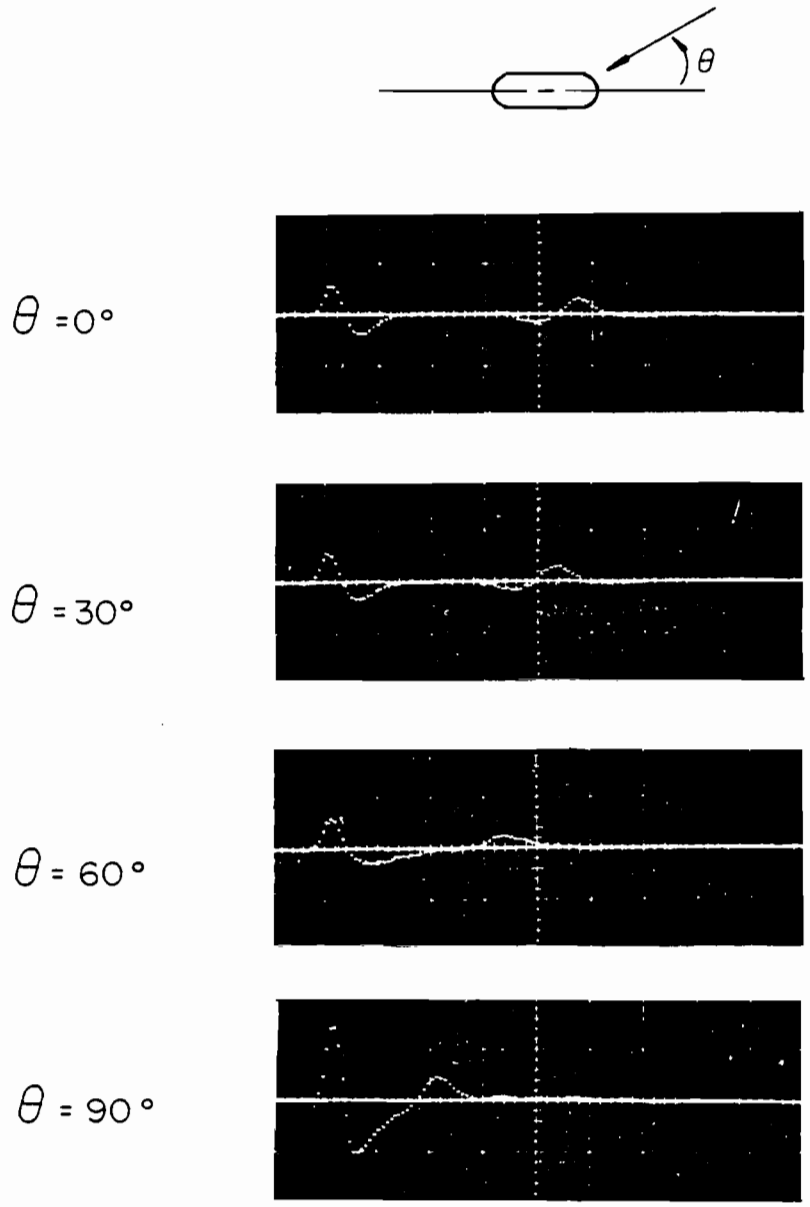

FIG. 121 Smoothed impulse response of sphere-capped cylinder for TE polarization (horizontal scale: 0.5 nsec/div.; vertical scale: 5 mV/div.).

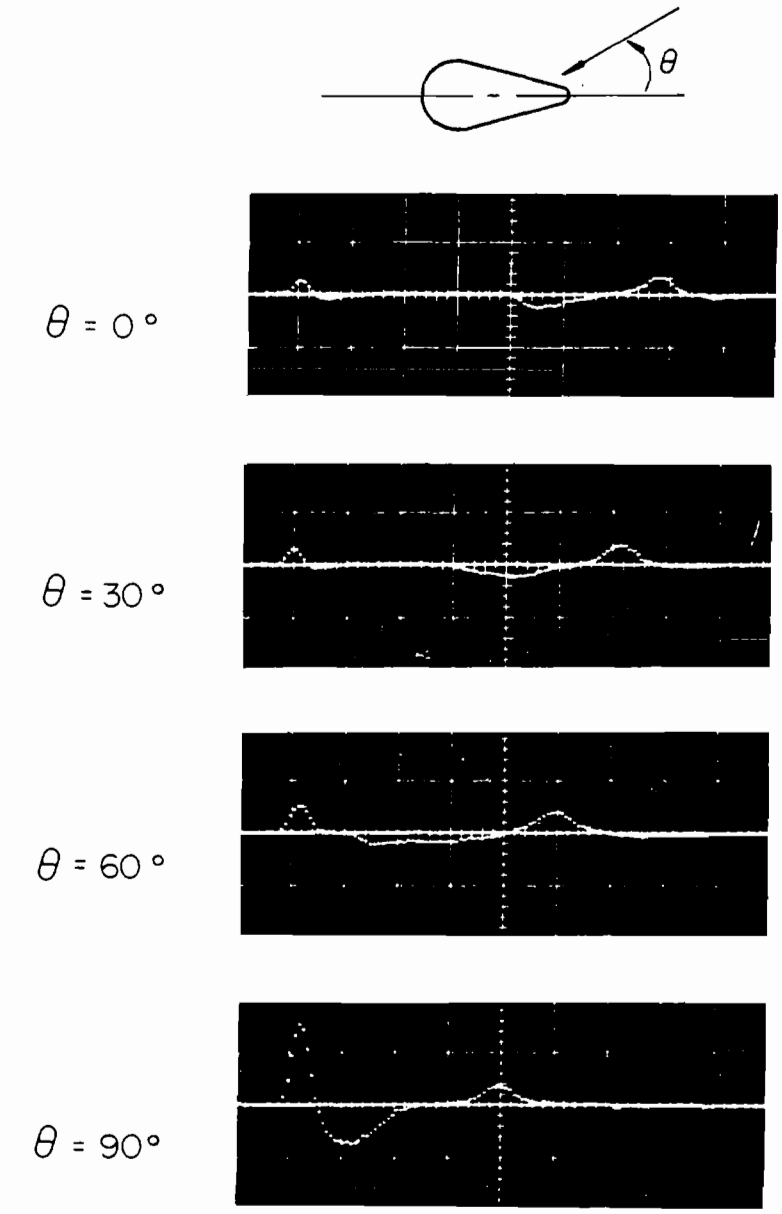

FIG. 122 Smoothed impulse response of sphere-cone-sphere for TE polarization (horizontal scale: 0.5 nsec/div.; vertical scale: 5 mV/div.).

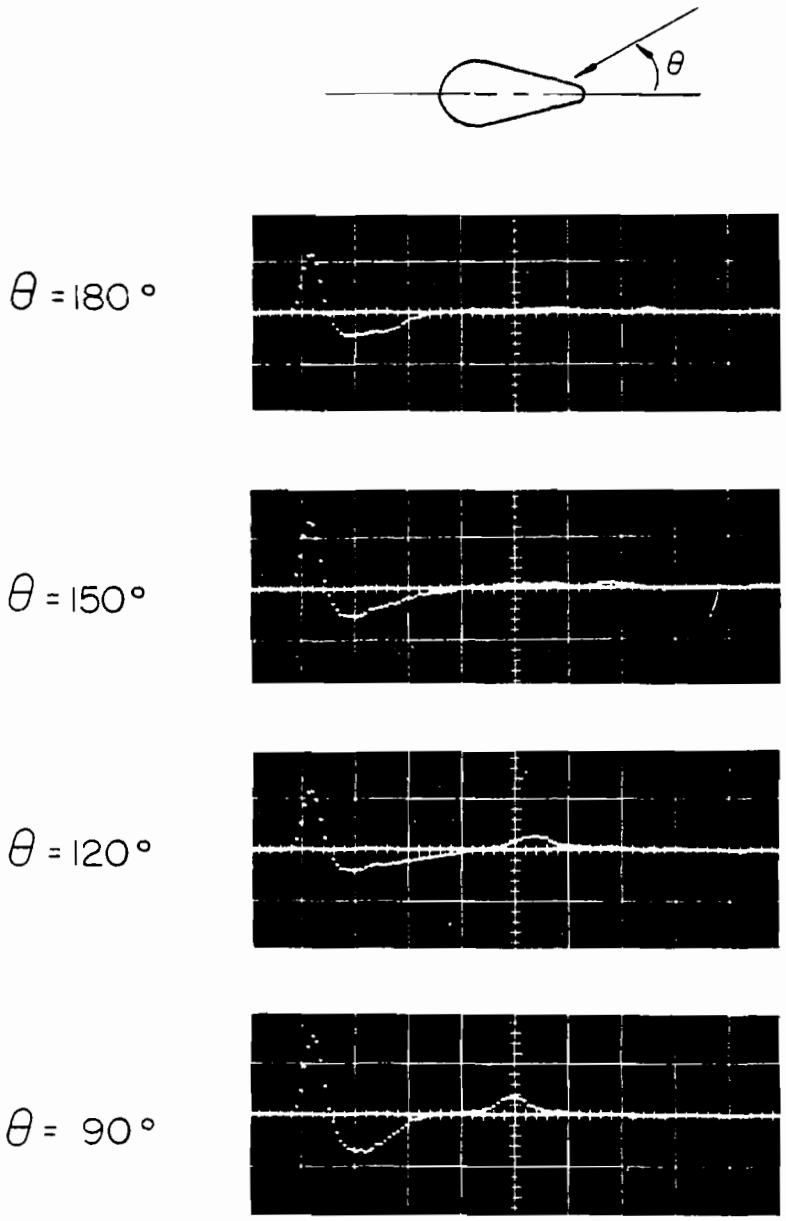

FIG. 123 Smoothed impulse response of sphere-cone-sphere for TE polarization (horizontal scale: 0.5 nsec/div.; vertical scale: 5 mV/div.).

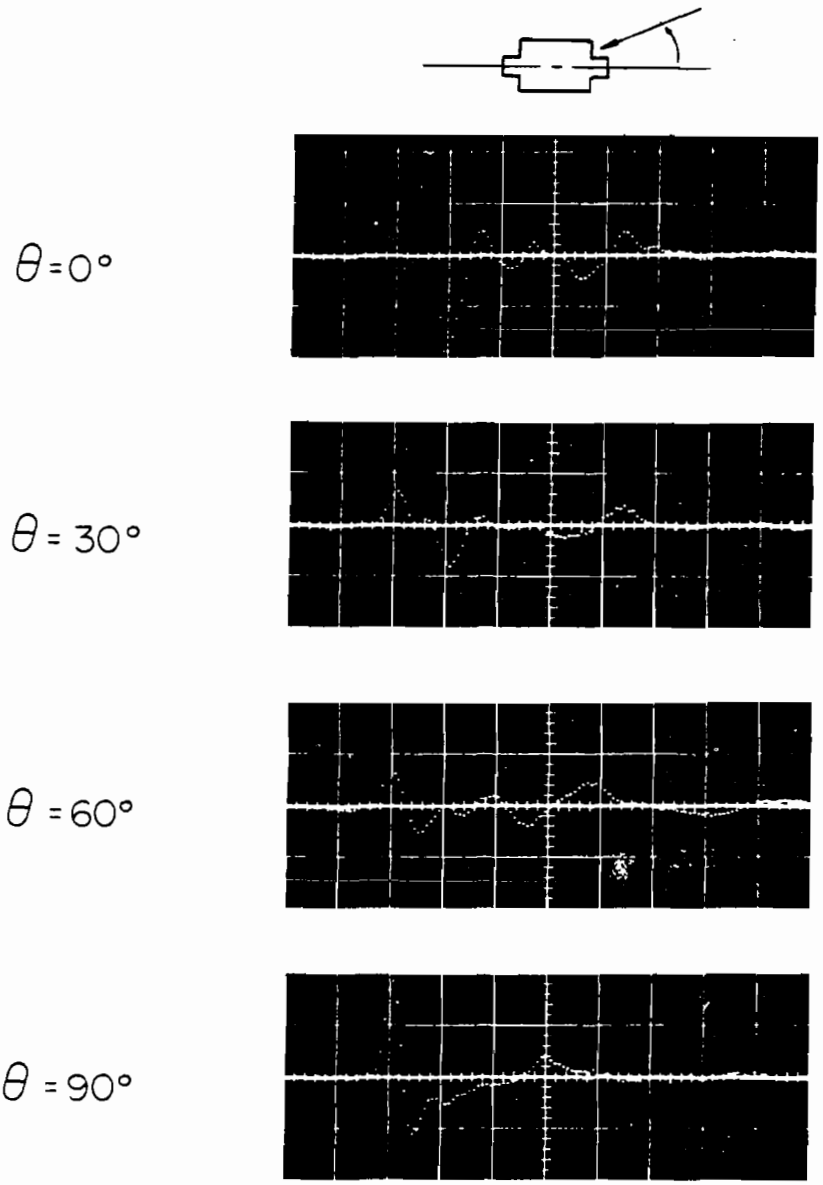

FIG. 124 Smoothed impulse response of university explorer satellite model for TE polarization (horizontal scale: 0.5 nsec/div,; vertical scale: 5 mV/div.).

In Fig. 125 the smoothed impulse response of the small scientific satellite model is shown for the case of a diagonal image plane with respect to the axis of the four attached wires. At $\theta = 0^0$ the response from the nose of the sphere appears first, followed by the response due to the wires attached, which appear to dominate the response from then on. At other angles of incidence the effect of the wires is also clearly evident, and comparison with Fig. 120(a) demonstrates the marked change in response that is obtained by simply attaching some wire struts.

The smoothed impulse response of the three circular cylinders measured is displayed in Fig. 126 for the case of TM polarization and normal incidence. The shapes of these three responses are similar. However, note that the initial pulse is approximately 15 mV for the 12 inch right circular cylinder, approximately 10 mV for the 8 inch right circular cylinder, and approximately 12 mV for the 12 inch sphere-capped circular cylinder. These amplitudes are consistent with the "size" of the specular region in the three cases. Note also that the period of the damped oscillation is least for the 8 inch cylinder and most for the 12 inch flat-end cylinder, again as expected.

Figure 127 displays the smoothed impulse response of the right square cylinder for TM polarization and normal incidence with three aspect angles. At $\theta = 0^0$ the smoothed doublet due to the specular return from the front face is evident. This is followed approximately 0.8 nsec later by a negative perturbation in the response which can be attributed to the "reflection" from the back edge. The subsequent positive swing in the response is due to a wave traveling along the length of the cylinder. It is interesting to note that this oscillation is damped by a negative perturbation in the response which can be attributed to the "reflection" from the back edge. The subsequent positive swing in the response is due to a wave traveling along the length of the cylinder. It is interesting to note that this oscillation damps out less rapidly as the angle of incidence θ increases.

The smoothed impulse responses of the UES and SSS satellite models for TM polarization and normal incidence are shown in Fig. 128.

Finally, the waveforms which were used as the six unknown target aspect angles for testing OLPARS are displayed in Figs. 129 and 130. These six smoothed impulse responses correspond to the following target measurements.

No. 1 Right circular cylinder, L = 8 inches, TE polarization, $\theta = 45^0$

No. 2 Right square cylinder with diagonal image plane, TE polarization, $\theta = 45^0$

No. 3 Cube with noraml image plane, $\theta = 15^0$

No. 4 Cube with diagonal image plane, $\theta = 45^0$

No. 5 UES satellite model, TE polarization, $\theta = 45^0$

No. 6 SSS satellite model with diagonal image plane, $\theta = 45^0$.

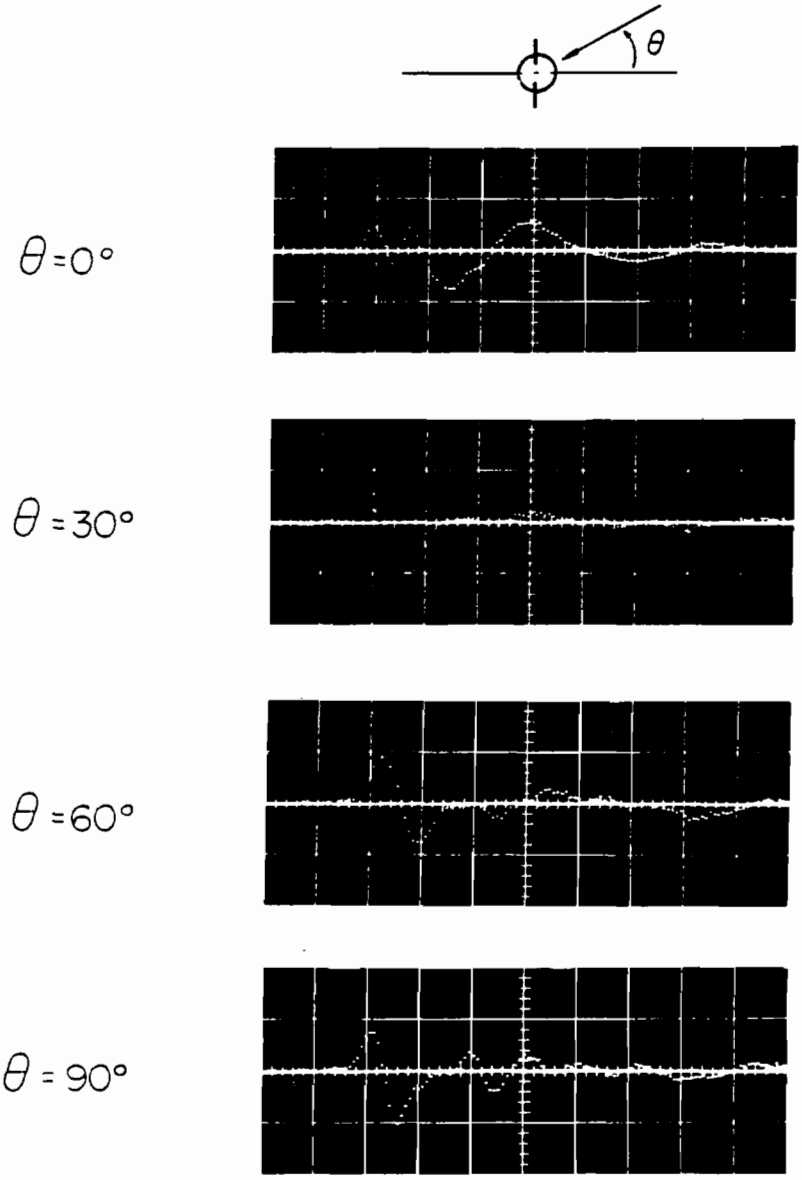

FIG. 125 Smoothed impulse response of small scientific satellite model with a diagonal image plane (horizontal scale: 0.5 nsec/div.; vertical scale: 5 mV/div.).

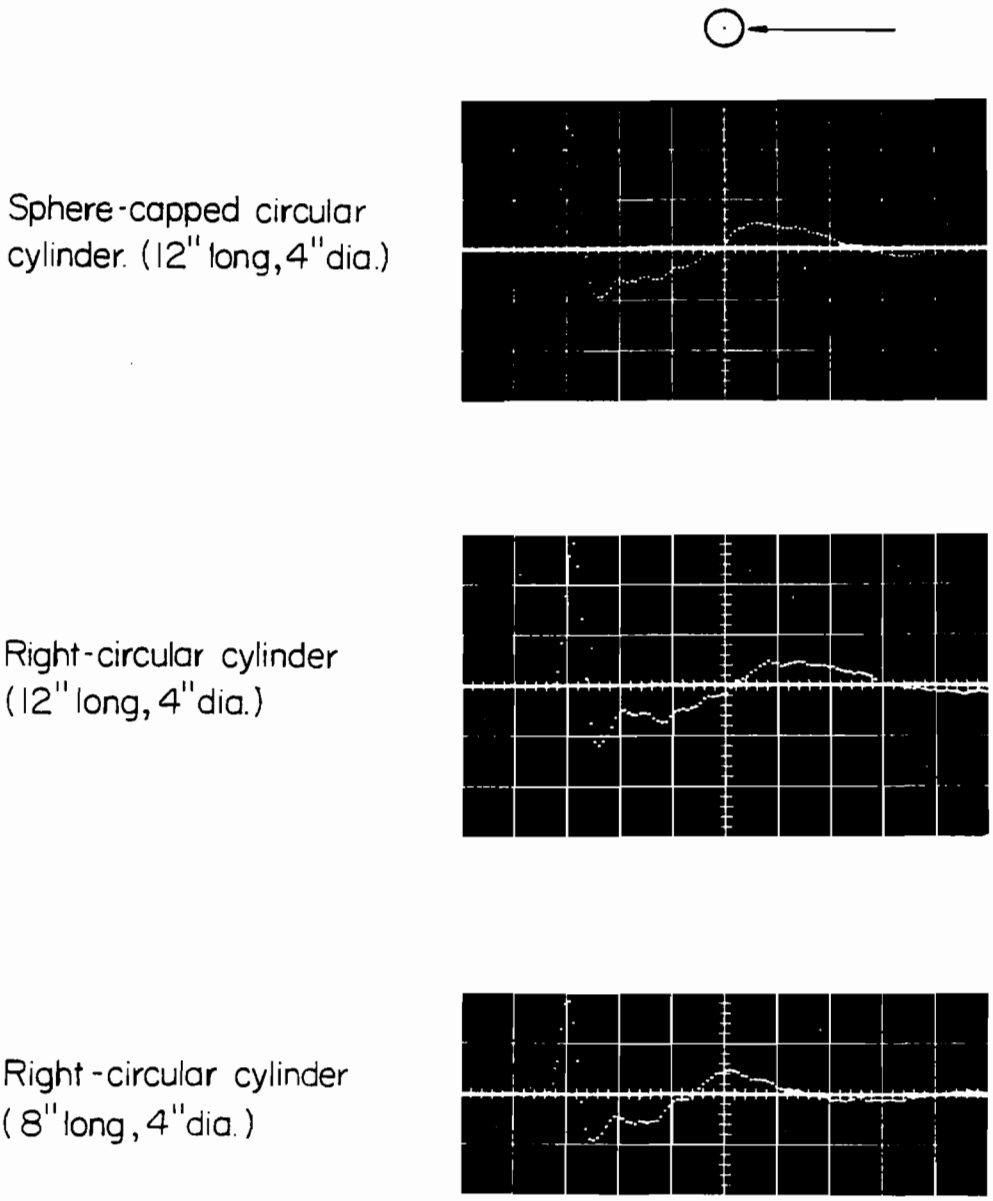

FIG. 126 Smoothed impulse response of circular cylinders for TM polarization and normal incidence (horizontal scale: 0.5 nsec/div.; vertical scale: 5 mV/div.).

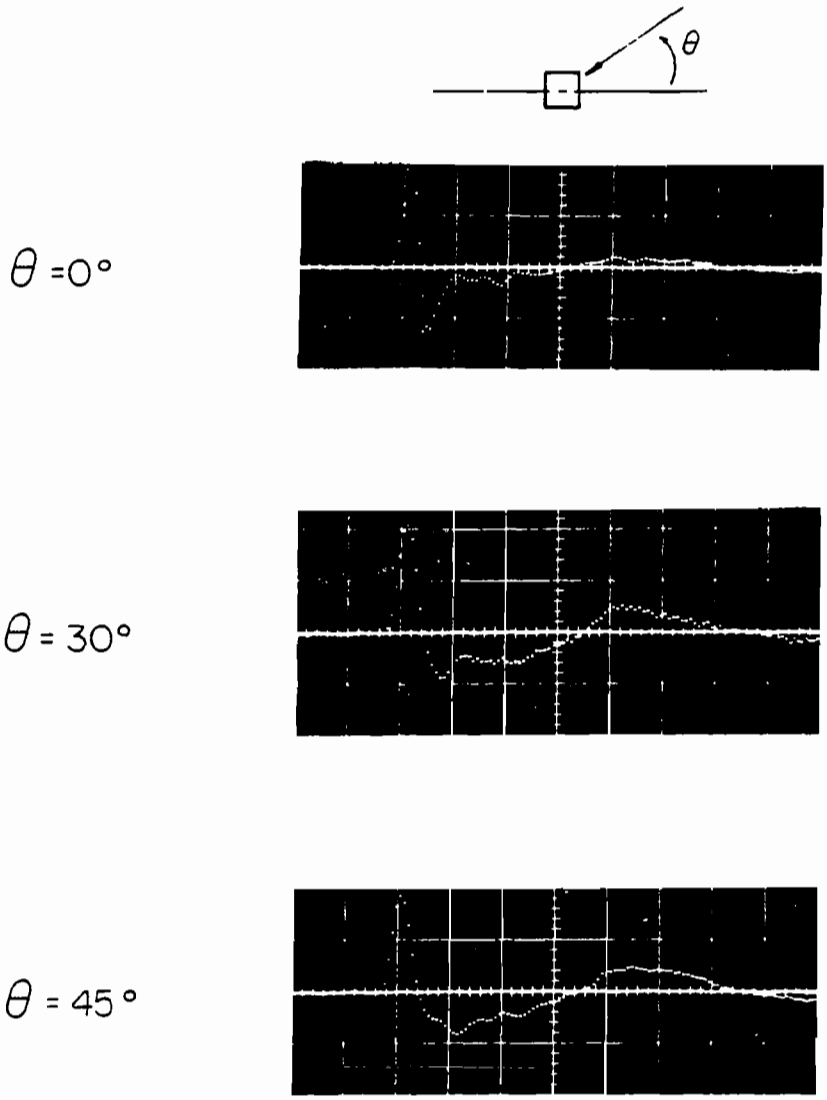

FIG. 127 Smoothed impulse response of right square cylinder for TM polarization and normal incidence (horizontal scale: 0.5 nsec/div.; vertical scale: 5 mV/div.).

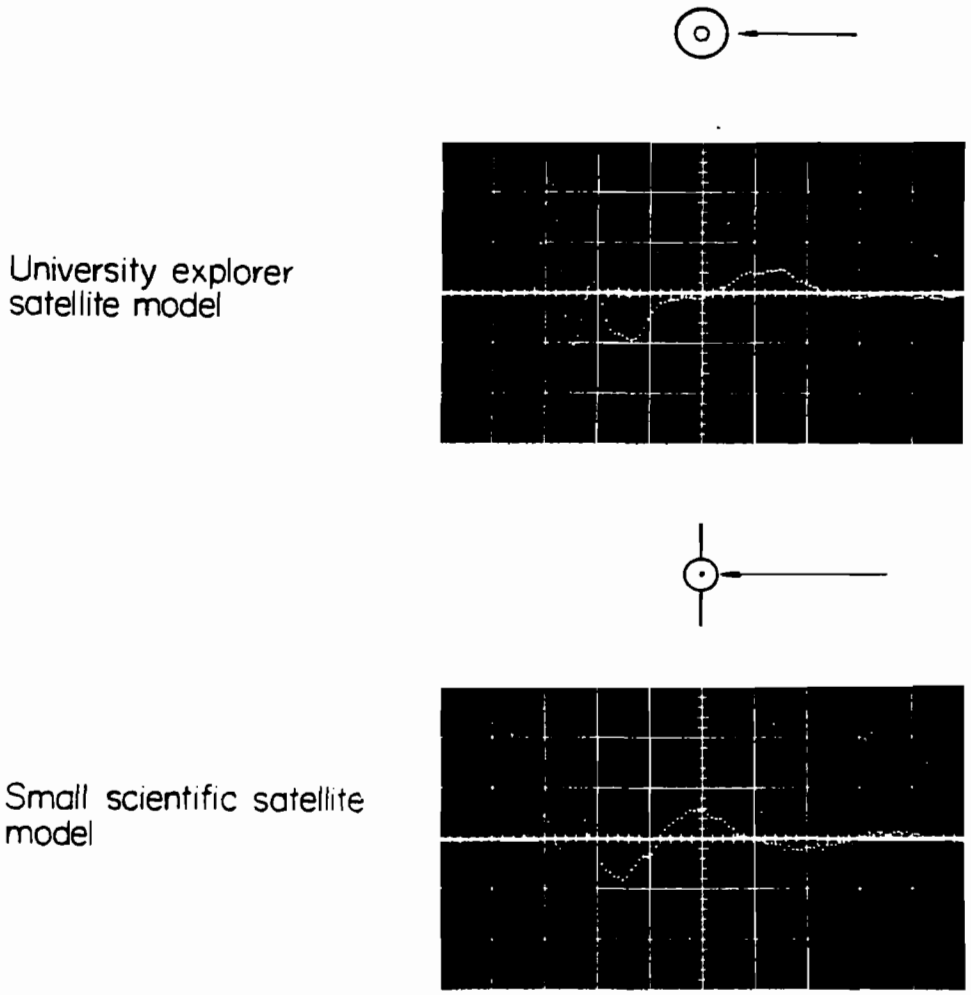

FIG. 128 Smoothed impulse response of two satellite models for TM polarization with normal incidence (horizontal scale: 0.5 nsec/div.; vertical scale: 5 mV/div.).

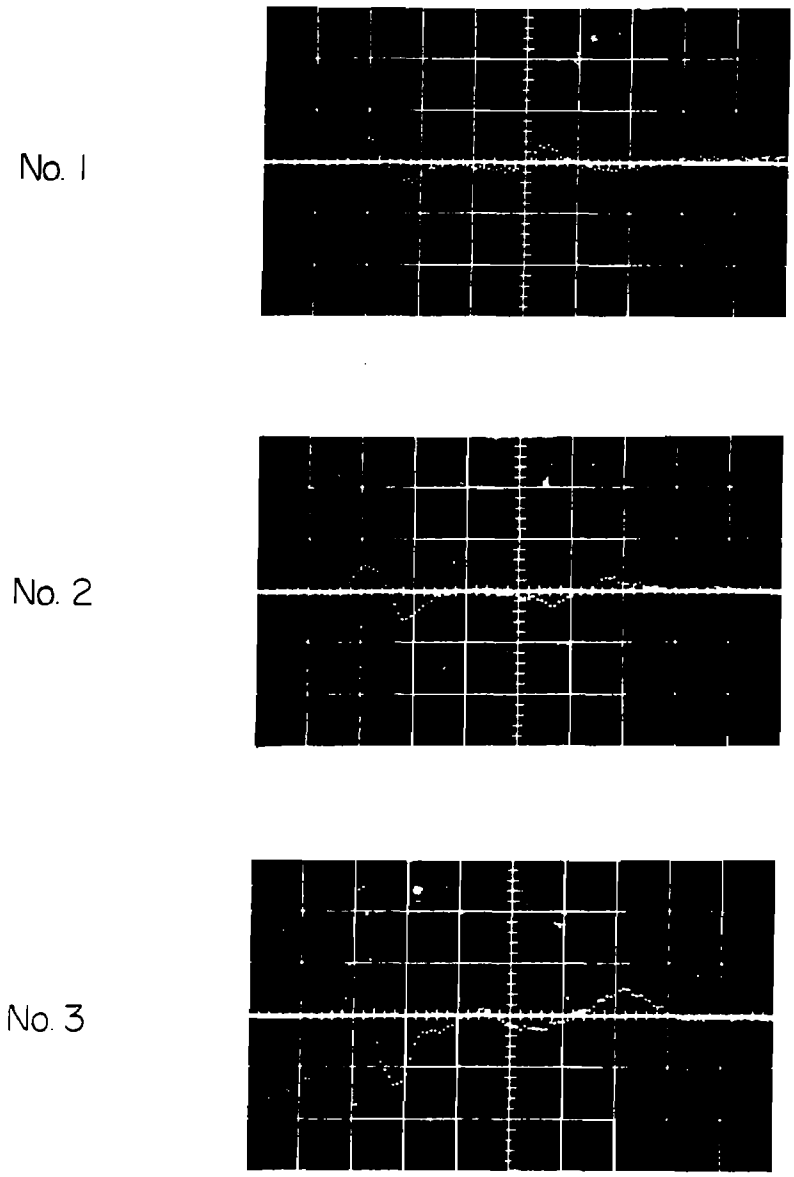

FIG. 129 Smoothed impulse responses of unknown targets for testing OLPARS (horizontal scale: 0.5 nsec/div.; vertical scale: 5 mV/div.).

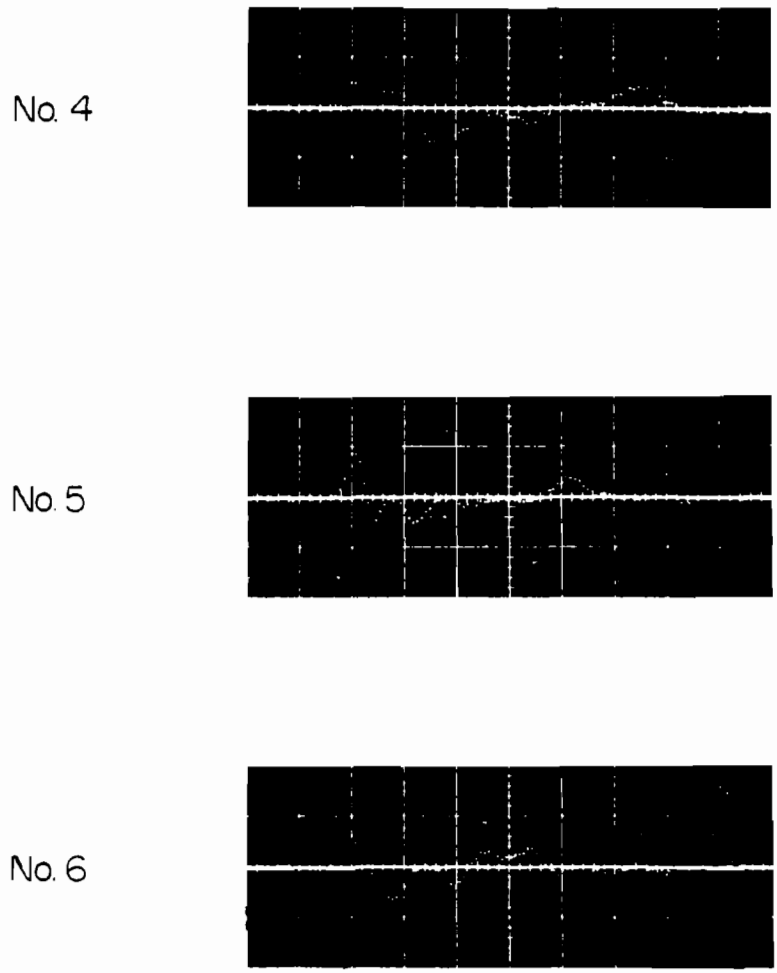

FIG. 130 Smoothed impulse responses of unknown targets for testing OLPARS (horizontal scale: 0.5 nsec/div.; vertical scale: 5 mV/div.).

SECTION 5

TARGET IDENTICATION USING OLPARS AND MEASURED SMOOTHED IMPULSE RESPONSES

This report describes the initial phase of a pattern recognition research project conducted by Pattern Analysis and Recognition Corp. (PAR) to determine the feasibility of automatic classification of object shapes using the detected radar waveform returns. The specific objective accomplished during this initial phase was the determination of the effects of orientation, polarization, additive noise, epoch uncertainty, and the classification logic type on classification accuracy. This objective was accomplished largely through the use of the On-Line Pattern Analysis and Recognition System - OLPARS[20, 21, 22] located at the Rome Air Development Center. The results of a variety of classification studies conducted using OLPARS are reported here.

Basically, four types of classification logic were designed and tested. These logics ranged in complexity from a simple matched filter type to a complex piecewise linear discriminant type. Each type of logic was evaluated by testing it in a "blind study" fashion. The individual logics were designed using known representative sample waveforms derived from the object shape classes. Each resultant logic was then tested by using it to classify a set of unknown waveforms.* The accuracy of classification on the unknown set was then used as a direct measure of the utility of that type of logic.

5.1 DATA DESCRIPTION

The data base utilized during this research was supplied to PAR by Sperry Rand Research Center and consisted of 57 digitized waveforms. These waveforms were collected using the radar returns from the eight different object shape classes listed below;

---

* - The unknown set of waveforms represent an independent test set which was not used for logic design. The true object shape class identification was supplied to PAR by Sperry Rand upon completion of the design and testing experiments.

	Object Class	Symbol
A	Sphere Cone Sphere	SCS
B	Sphere Capped Cylinder	SCC
C	Flat End Cylinder - 12" diameter	FEC - 12"
D	Flat End Cylinder - 8" diameter	FEC - 8"
E	Rectangular Cylinder	REC
F	Cube	CUB
G	University Explorer Satellite	UES
H	Small Scientific Satellite	SSS

One additional class of objects was set aside for testing purposes. This latter set was comprised of 6 waveforms whose shape identity was initially unknown to PAR. Note that the alphabetic labels A through H and UN are used to designate the eight object classes and the unknown class respectively throughout this report.

Within each of the eight basic shape classes, waveform samples were collected for varying aspect angles and polarizations. Each waveform was digitized and represented by a string of 128 numbers. The first operation performed by PAR was the conversion of the 128 dimensional waveforms to 43 dimensional waveforms, since the OLPARS system requires dimensionalities of 45 or less. The dimensionality reduction was accomplished by averaging adjacent sets of 3 numbers together; the 43rd component being the average of the last two numbers representing the waveform. This operation simply smooths the original waveform.

The 57 waveforms were distributed within the nine object classes (the ninth class being designated as the Unknown class - UN) as shown below;

Design Subset:

Class A	SCS	7 vectors
	TE Polarization	
Class B	SCC	5 vectors
	TE Polarization 0^{o}, 30^{o}, 60^{o}, 90^{o} TM Polarization	
Class C	FEC - 12"	6 vectors
	TE Polarization 0^{o}, 30^{o}, 40^{o}, 60^{o}, 90^{o} TM Polarization	

Class D	FEC - 8"	5 Vectors
	TE Polarization 0^o, 30^o, 60^o, 90^o TM Polarization	
Class E	REC	11 Vectors
	TE Polarization Perpendicular Incidence - 0^o, 30^o, 60^o, 90^o Diagonal Incidence - 0^o, 30^o, 60^o, 90^o TM Polarization 0^o, 30^o, 45^o	
Class F	CUB	7 Vectors
	Perpendicular Incidence 0^o, 30^o, 45^o Diagonal Incidence 0^o, 30^o, 60^o, 90^o	
Class G	UES	5 Vectors
	TE Polarization 0^o, 30^o, 60^o, 90^o TM Polarization	
Class H	SSS	5 Vectors
	TE Polarization Diagonal Polarization 0^o, 30^o, 60^o, 90^o	

Independent Test Subset

Class U	Unknowns	6 Vectors
	No. 1 - FEC - 8"	TE Polarization 45^o
	No. 2 - REC	TE Polarization-Diagonal Incidence 45^o
	No. 3 - CUB	Perpendicular Incidence 15^o
	No. 4 - CUB	Diagonal Incidence 45^o
	No. 5 - UES	TE Polarization 45^o
	No. 6 - SSS	Diagonal Polarization 45^o

It is important to realize that this data was not normalized for a common time origin. The basic 57 waveform data base (non-time origin normalized) is referenced to as Data Set 1.

Data Set 1 was used to create several other data bases which in turn were utilized in our experiments. Specifically, Data Set 2 was generated by time normalizing Data Set 1. The normalization was accomplished by scanning each waveform (from left to right) to detect the point at which the amplitude first exceeded 100_8. The waveform was then shifted such

that this point occupies the 32_8 position along the normalized waveform. Leading and trailing zeros were inserted for a right and left shift respectively.

Data Sets 3 and 4 were generated by adding randomly distributed vectors (i.e., 43 dimensional random vectors) to the original vectors contained in the Design Subset of Data Set 1. The random vectors were generated in accord with a multivariate Gaussian distribution with a covariance matrix $\sum = \sigma^2 I$ (this is equivalent to corrupting the original waveforms with additive white Gaussian noise). Specifically, two data sets were generated (for two values of σ) by adding 30 random vectors to each of the original 51 data vectors of Data Set 1 in classes A - H. Data Set 3 was obtained using a variance of 100 (i.e., $\sigma^2 = 100$), whereas Data Set 4 was generated using a variance of 1 (i.e., $\sigma^2 = 1$). Each of the original data vectors, in conjunction with the random vector program, produces 31 data vectors (30 by adding noise, plus the original).

Data Sets 5 and 6 were generated in exactly the same manner as were 3 and 4 with the exception that the time normalized 51 vector set (i.e., Data Set 2) was used in lieu of Data Set 1. Data Set 5 corresponds to the large noise sample (i.e., $\sigma^2 = 100$) and Data Set 6 to the low noise sample (i.e., $\sigma^2 = 1$). The number of 43 dimensional vectors in Data Sets 3, 4, 5, and 6 were as follows;

Class A = Sphere Cone Sphere	=	217
Class B = Sphere Capped Cylinder	=	155
Class C = Flat End Cylinder - 12"	=	186
Class D = Flat End Cylinder - 8"	=	155
Class E = Rectangular Cylinder	=	341
Class F = Cube	=	217
Class G = University Explorer Satellite	=	155
Class H = Small Scientific Satellite	=	155

Data Set 7 was obtained by removing certain TM polarized waveforms from the time origin normalized Data Set 2 and incorporating these waveforms into the independent test set associated with Data Set 7, as listed below;

Design Subset

Class A	SCS	7 Vectors
	TE Polarization	
Class B	SCC	4 Vectors
	TE Polarization 0^{o}, 30^{o}, 60^{o}, 90^{o}	
Class C	FEC - 12"	5 Vectors
	TE Polarization 0^{o}, 30^{o}, 40^{o}, 60^{o}, 90^{o}	
Class D	FEC - 8"	4 Vectors
	TE Polarization 0^{o}, 30^{o}, 60^{o}, 90^{o}	
Class E	REC	8 Vectors
	TE Polarization Perpendicular Incidence - 0^{o}, 30^{o}, 60^{o}, 90^{o} Diagonal Incidence - 0^{o}, 30^{o}, 60^{o}, 90^{o}	
Class F	CUB	7 Vectors
	Perpendicular Incidence 0^{o}, 30^{o}, 45^{o} Diagonal Incidence 0^{o}, 30^{o}, 60^{o}, 90^{o}	
Class G	UES	4 Vectors
	TE Polarization 0^{o}, 30^{o}, 60^{o}, 90^{o}	
Class H	SSS	1 Vector
	TE Polarization	

Independent Test Subset

Class U	UNK1 - UNK6		6 Vectors
	SCC	TM Polarization	1 Vector
	FEC-12"	TM Polarization	1 Vector
	FEC-8"	TM Polarization	1 Vector

REC	TM Polarization 0^o, 30^o, 45^o	3 Vectors
UES	TM Polarization	1 Vector
SSS	Diagonal Polarization 0^o, 30^o, 60^o, 90^o	4 Vectors

Data Set 8 was generated by adding randomly distributed vectors to the design subset of Data Set 7. The random vectors were generated from a multivariate Gaussian distribution with a covariance matrix $\sum = 100\ I$ (i.e., $\sigma^2 = 100$). Forty (40) random vectors were added to the original 40 vectors in the design subset. Each of the original data vectors, in conjunction with the random vector program, produces 41 data vectors (40 by adding noise, plus the original).

5.2 SUMMARY OF EXPERIMENTS

Although a large number of analysis procedures were conducted during the research period covered by this report, it is possible to describe the basic experiments in three groups. The principle distinction between these three groups was related to the Data Sets utilized to design and independently test various classification schemes. Group 1 experiments utilized Data Sets 1, 3, and 4. These sets are typified by the fact that radar polarization, object orientation and time origin alignment are not utilized by the classification logic. The object classes are only defined upon the shape of the objects and not by the specific orientation of the object or the polarization utilized. In addition, the data within sets 1, 3, and 4 were not epoch normalized. A second common factor to the experiments of Group 1 was related to the logic testing procedure. Specifically, all testing was conducted using the six unknown waveforms designated UN1 through UN6.

Group 2 experiments utilized Data Sets 2, 5, and 6. These sets are typified by the fact that radar polarization and object orientation are not utilized by the classification logic; however, this data was time origin normalized. The independent testing procedure common to all experiments of this group utilized the six unknown waveforms (time origin normalized) designated UN1 through UN6.

Finally, Group 3 experiments utilized Data Sets 7 and 8. These sets are distinguished by the fact that the orientation of the objects within their respective shape classes is not utilized by the classification logic. The TM polarization waveforms were not contained in the design set, however they were incorporated into the test set as described in Section 2. Since sets 7 and 8 were originally derived from the time normalized Data Set 2, these experimental results reflect a time origin normalization.

The individual experiments comprising the three groups consisted of the design and independent testing of four basic types of logic. The first type used was the Nearest Mean Vector Logic where only the mean vectors of the object shape classes (the class mean vectors were estimated using the design set) were used in the decision process. The unknown vectors were classified in accord with the class associated with the nearest mean vector. This logic is analogous to using a single matched filter per class where the Euclidean metric replaces the correlation metric. The second logic type used was the Nearest Neighbor Logic. This type of logic utilizes every vector in the design set in order to compute a decision. An unknown vector is classified in accord with the class associated with the nearest vector (in the Euclidean sense) contained in the design set. That is, the distance between the unknown vector and each of the vectors in the design set is computed and stored. The class associated with the closest vector is then used as the decision class. This type of logic is quite similar to multiple matched filters where several filters are used to represent templates for each class and the Euclidean metric replaces the correlation metric. The third logic type used was a Piecewise Linear Logic. This logic is composed of $K * (K-1)/2$ Fisher Linear Discriminants which are functionally combined as shown below. A detailed description of this type of logic is contained in (1), (2), and (3).

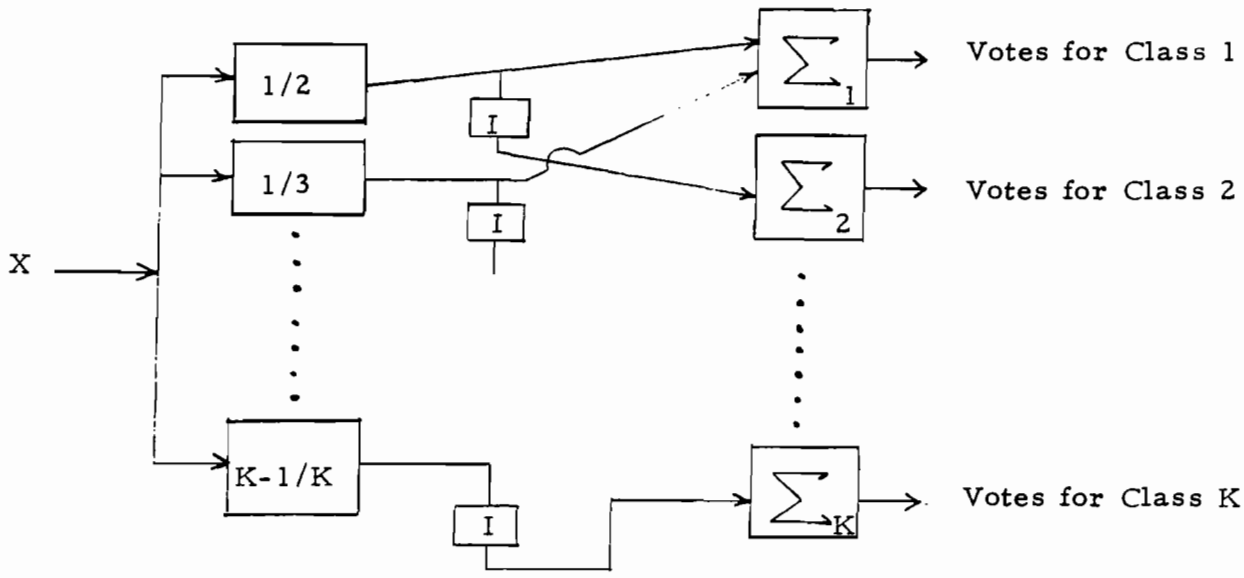

Piecewise Linear Logic

The vector X is the 43-dimensional waveform vector which is to be classified. The [I/J] box represents the Fisher linear discriminant which discriminates between class I and class J. The output from the [I/J] box is a binary variable. A "one" out is interpreted as a vote for class I and a "zero" out as a vote for class J. The [I] is an inverter. The [$\sum_J$] box symbolically represents a vote summer for class J. Notice that the maximum number of votes achievable by any class is K - 1, where K is the number of classes. A positive class decision is rendered for class J if and only if J receives K - 1 votes.

The last logic type utilized in our experimentation involved the use of piecewise linear logic, however, the data structure of the design set was first analyzed to determine the modal properties of inter-class data. Any class which exhibited multi-modal structure (that is, the data resides in disjoint parts of the 43-dimensional vector space) was partitioned into subclasses. The partition function was accomplished via visual cluster analysis conducted at the OLPARS CRT to subdivide those classes which appeared to be widely separated (i.e., multi-modal). The pairwise decision logic described above was then used to discriminate all classes and subclasses.

5.3 EXPERIMENTAL RESULTS

This section presents a capsulation of the most important experimental results obtained to date. The results are discussed in accord with the grouping described in the previous section and are presented in tabular summary form at the end of this section.

It was mentioned above that the criterion for evaluating a classification logic was its performance in correctly classifying the unknown waveforms contained in the independent test set. For this reason we shall list here the true identification of these unknown waveforms as presented to us by Sperry. It should be noted, however, that this information was not available to PAR at the time of conducting the majority of the experiments described below. Furthermore, the true identification of the unknown waveforms was never utilized when designing any classification logic including those experiments conducted after this information was given to PAR. This procedure insures a fair and unbiased evaluation consistent with the concept of a blind study. The true identification of the six unknowns are as follows;

UN1	Class D	Flat End Cylinder - 8" diameter
UN2	Class E	Rectangular Cylinder
UN3	Class F	Cube
UN4	Class F	Cube
UN5	Class G	University Explorer Satellite
UN6	Class H	Small Scientific Satellite

True Class Identification of Unknowns

Group 1 Experiments

The initial experiment of this group involved the design and test of the Nearest Mean Vector Logic using Data Set 1. The OLPARS system was used to compute the mean vectors of classes A - H. The six unknown vectors, UN1 - UN6, of Data Set 1 were classified in accord with the class associated with the nearest mean vector. This classification procedure, although appealing due to its inherent simplicity, has been found to be unreliable in all but the simplest of problems and therefore it is not surprising that its performance is inadequate. The independent classification results are listed below:

Unknown Vectors	Decision Class
UN1	D = FEC - 8"
UN2	F = CUB
UN3	H = SSS
UN4	F = CUB
UN5	C = FEC - 12"
UN6	H = SSS

Nearest Mean Vector Test Results - Data Set 1

Notice that three of six were correctly classified while the remaining three were misclassified.

The next experiment within this group involved the testing of the Nearest Neighbor Classification Logic using Data Set 1. The independent classification results are listed below:

Unknown Vector	Decision Class
UN1	C = FEC - 12"
UN2	B = SSS
UN3	C = FEC - 12"
UN4	F = CUB
UN5	E = REC
UN6	E = REC

Nearest Neighbor Test Results - Data Set 1

Notice that only one unknown was classified correctly utilizing this method.

The third experiment within Group 1 experiments involved the design and test of the Fisher Pairwise Discriminant Logic using the noisy data of Data Set 3. The design subset of Data Set 3 was used to design the Piecewise Linear Logic as described in Section 3. This logic was next used to classify the vectors contained in the design subset. The resultant confusion matrix is given below. The columns represent the true class and the rows the decision class. The I, J element is set equal to ten times the number of vectors from class J which were misclassified as class I. For example, the twelve A's were called E. A geometric understanding of these errors can be obtained by viewing the "optimal discriminant plane" shown in Figure 83. This plot shows the orthogonal projection of the 43-dimensional vectors from classes A and E onto a discriminant plane. The X axis of this plane is the Fisher direction between A and E. The plot it a cluster plot in that the symbol A corresponds to the projection of one or more vectors from class A. Overprints of A's and E's are represented by the symbol ↓. The decision boundary is a vertical line bisecting the X axis.

Confusion Matrix for Tree Design Set Fisher 01

	A	B	C	D	E	F	G	H
A	0	0	0	0	0	0	0	0
B	0	0	30	0	0	0	0	0
C	0	0	0	0	20	0	0	0
D	0	0	0	0	0	0	0	0
E	120	10	30	0	0	0	0	0
F	0	0	0	0	0	0	0	0
G	0	0	0	0	0	0	0	0
H	0	0	0	0	0	0	0	0

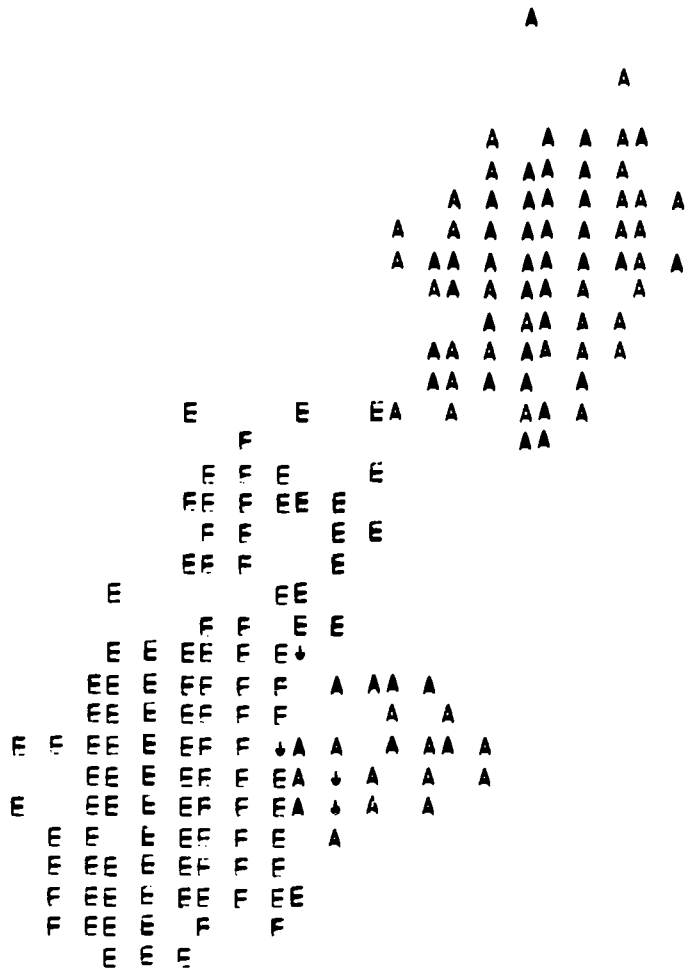

**********CC**********

SCALE= 1.55103 A /E CLUSTER
X PLOT CENTER= -.12901 Y PLOT CENTER= -.38341

MULTIPLE POINT DISTRIBUTIONS

FIG. 131 Discriminant plane projection - class A vs class E.

This logic was next used to classify the six unknown vectors. The results are listed below.

Vector	Classification	Votes
UN1	Class D	7
UN2	Class E tied Class A	6 each
UN3	Class F	7
UN4	Class F	7
UN5	Class G	7
UN6	Class H tied Class B	6 each

Maximum No. Votes Possible = 7

Fisher Piecewise Linear Discriminant Logic Test - Data Set 3 (σ = 10)

These results were quite encouraging since no errors were made; four unknowns were correctly classified and the other two unknowns were tied.

The exact same procedure outlined in the preceeding experiment was repeated for Data Set 4. The pairwise logic was tested using the design data, and perfect classification resulted.

Next, the logic was used to classify the six unknown vectors. The results of this classification were as follows:

Vector	Classification	Votes
UN1	Class C	7
UN2	Class E tied Class A	6 each
UN3	Class F	7
UN4	Class F	7
UN5	Class G tied Class A	6 each
UN6	Class H tied Class B tied Class G	6 each

Maximum No. Votes Possible = 7

Fisher Piecewise Linear Discriminant Logic Test - Data Set 4 (σ = 1)

Notice that two unknowns were correctly classified; one incorrectly classified and the remaining three tied.

The final experiment in this group involved the design and test of Piecewise Linear Discriminant Logic With Mode Analysis. The analysis was conducted by orthogonally projecting the eight classes A - H of the design subset of Data Set 3 onto the plane described by the two eigenvectors corresponding to the two largest eigenvalues of the lumped data covariance matrix. A visual cluster analysis was conducted at the OLPARS CRT to subdivide those classes which appeared to be widely separated. The results of this analysis are depicted by the "data tree" below;

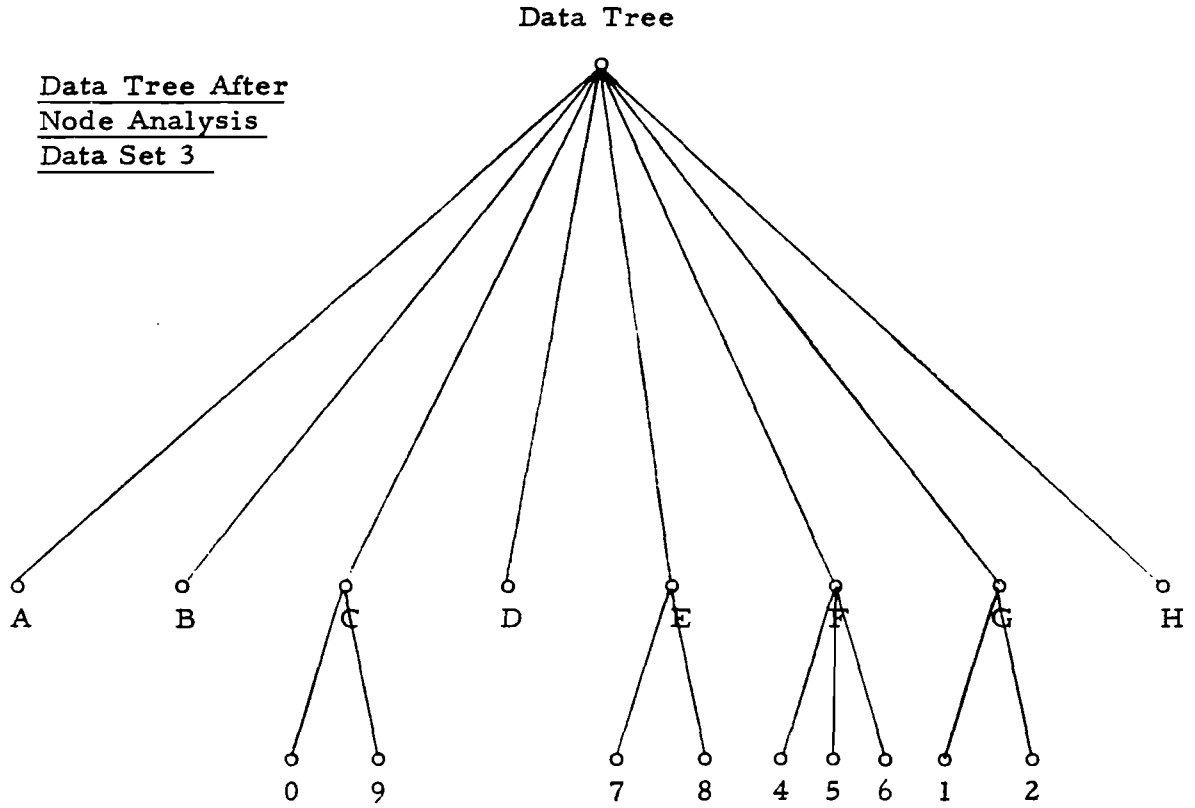

Notice that classes C, E, F and G were subdivided into disjoint subclasses.

A typical eigenvector display of classes G and H is shown in Figure 84.

The pairwise decision logic described above was designed to discriminate the 13 classes resulting from the clustering analysis. This logic was next used to classify the six unknown vectors. The results were as follows:

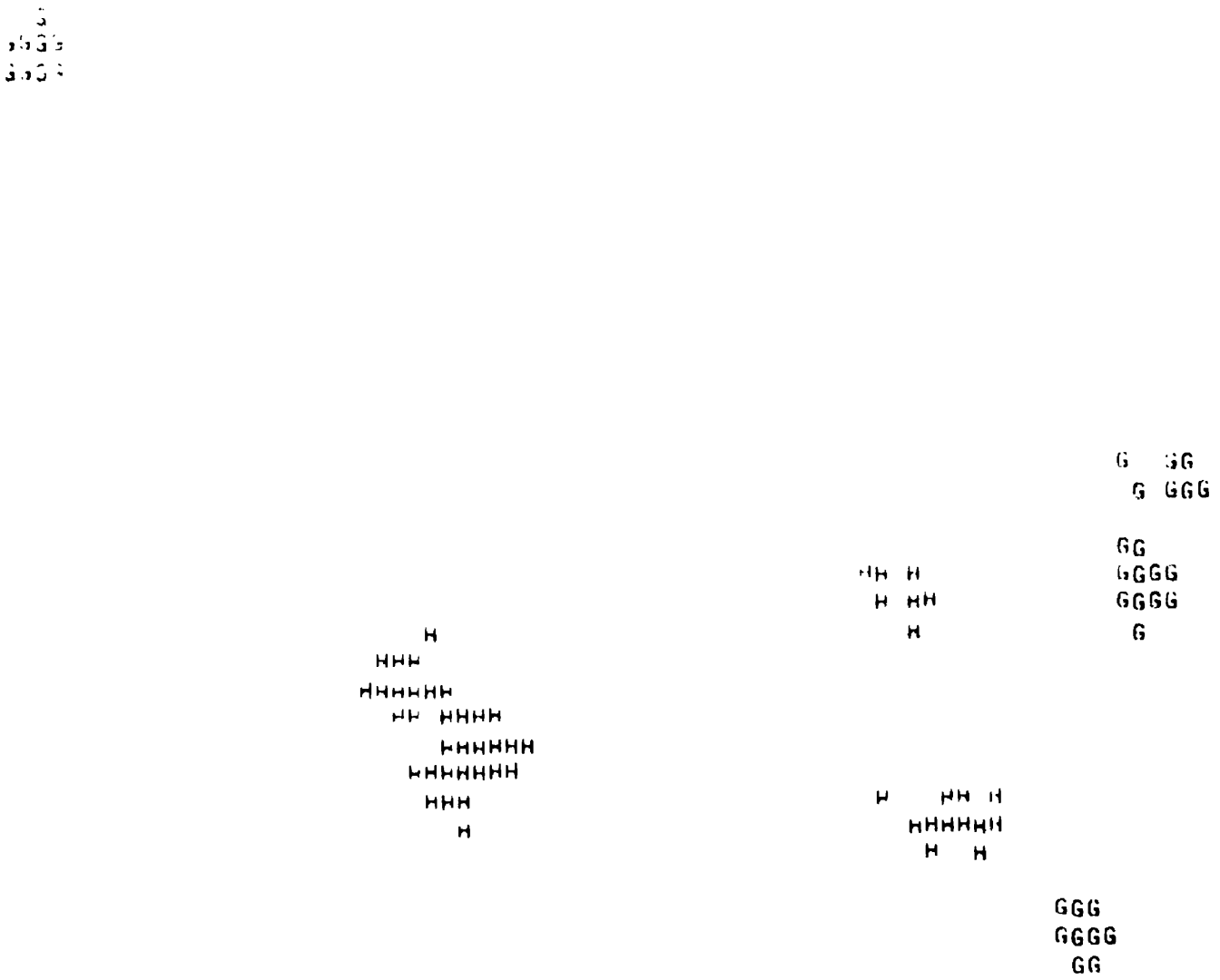

FIG. 132 Eigenvector plane $\underline{E}_1$ vs $\underline{E}_2$ - class H and G.

Vector	Classification	Votes
UN1	Class 9 ; Class C	12
UN2	Class A	11
UN3	Class 8 tied Class 0 ; Class E tied Class C	11 each
UN4	Class 6 ; Class F	12
UN5	Class 7 ; Class E	12
UN6	Class H	12

Maximum Number of Votes = 12

Fisher Piecewise Linear Discriminant Logic With Mode Analysis
Test Results - Data Set 3 (σ = 10)

These results were considered poor since only two unknowns were correctly identified.

It is observed that excellent results were achieved using the Piecewise Linear Logic designed using the highly corrupted data of Data Set 3 (σ = 10). The results for all other experiments were considerably degraded. One would ordinarily expect that the classification accuracy would improve directly with an increase in the logic complexity. However, this thought was not demonstrated when one compares the Nearest Neighbor result to the Nearest Mean result nor when one compares the Piecewise Linear Logic result with and without mode analysis. This phenomena can partially be explained by the fact that the data used in the Group 1 experiments was not time origin normalized. Therefore, the more complex logic may tend to "over compensate" by fitting too closely to the design data.

Group 2 Experiments

The first experiment within this group involved the design and independent testing of the Nearest Neighbor Classification Logic using the time normalized Data Set 2. The independent classification results are listed below:

Unknown Vector	Decision Class
UN1	B - SCC
UN2	C - FEC - 12"
UN3	F - CUB
UN4	F - CUB
UN5	E - REC
UN6	B - SCC

Nearest Neighbor Test Results - Data Set 2

Notice that only two of the unknowns were correctly classified while the remaining four were misclassified. These results indicate a slight improvement over the corresponding results on the unnormalized data reported above under Group 1 experiments (1 correct, 5 incorrect); however, the performance is still considered poor.

The second experiment within Group 2 experiments involved the design and test of the Fisher Pairwise Discriminant Logic using the time normalized noisy data of Data Set 5 (σ = 10). The design subset of Data Set 5 was used to design the Piecewise Linear Logic as described in Section 3. The resulting logic was next tested using the test subset of that data. The classification results are listed below;

Vector	Classification	Votes
UN1	Class C	7
UN2	Class E	7
UN3	Class E	7
UN4	Class F	7
UN5	Class G	7
UN6	Class H	7

Maximum No. Votes Possible = 7

Fisher Piecewise Linear Discriminant Logic Test - Data Set 5 (σ = 10)

Two errors were committed (i.e., UN1 and UN3) using this logic, which represents some degradation from the corresponding results obtained on the unnormalized data reported above under Group 1 experiments. A detailed examination of the votes indicated that the second best choices for UN1 and UN3 were the correct classes D and F respectively.

The exact same procedures outlined in the preceeding experiment were repeated for Data Set 6 (σ = 1). The pairwise logic was tested using the six unknown waveforms of the test subset of Data Set 6. The results of this classification were as follows:

Vector	Classification	Votes	
UN1	Class C	7	
UN2	Class E	7	Max. No.
UN3	Class F	7	Votes
UN4	Class F	7	Possible
UN5	Class G	7	= 7
UN6	Class B	6	

Fisher Piecewise Linear Discriminant Logic Test - Data Set 6 (σ = 1)

This result indicates an improvement over the corresponding results obtained on the unnormalized data previously reported since four unknowns were correctly classified, one misclassified and the remaining unknown received less than the maximum number of votes.

The fourth experiment of Group 2 involved the design and test of Piecewise Linear Discriminant Logic with Mode Analysis. The analysis procedure was conducted using the design subset of Data Set 5 (σ = 10) and the multitude of analysis tools contained in OLPARS. The results of this analysis were reflected by a decision to subdivide classes F and C into two nodes each as shown below.

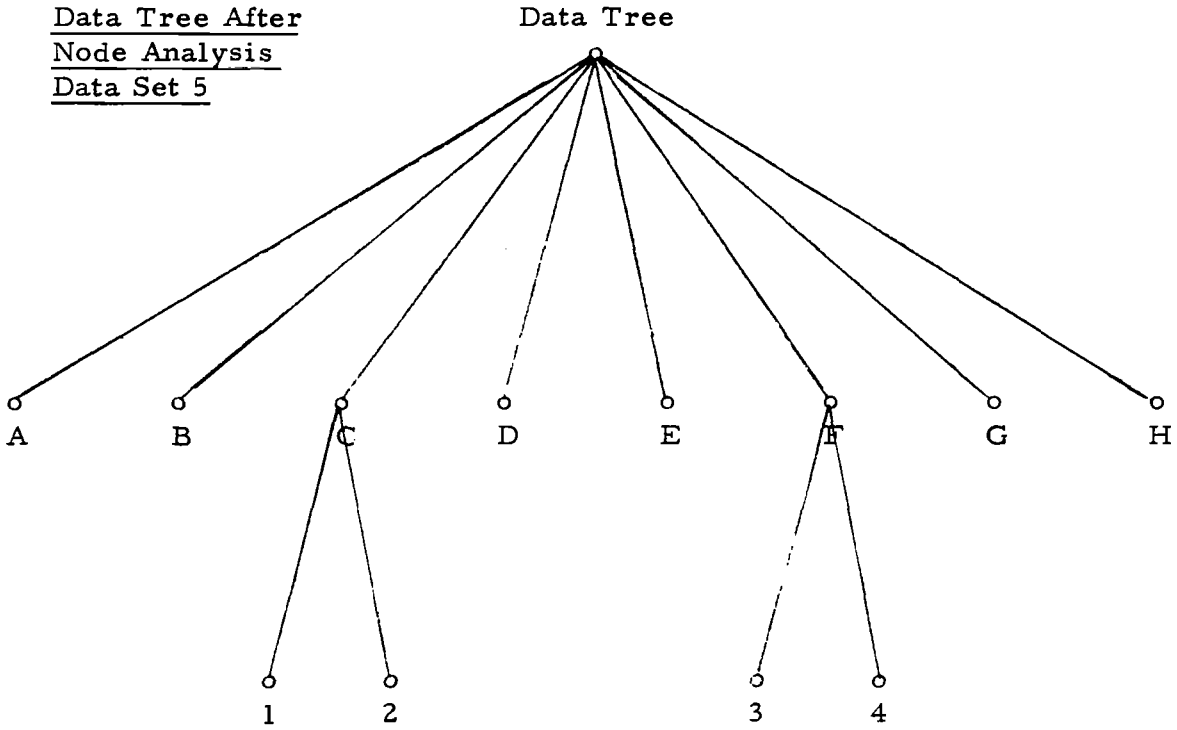

The pairwise logic described in Section 3 was designed to discriminate the 10 classes resulting from the mode (or clustering) analysis. This logic was next used to classify the independent subset of Data Set 5. The results were as follows:

Vector	Classification	Votes
UN1	Class D	8
UN2	Class E	9
UN3	Class E	9
UN4	Class 4 = F	9
UN5	Class G	9
UN6	Class H	9

Maximum No. Votes Possible = 9

Fisher Piecewise Linear Discriminant Logic with Node Analysis

Data Set 5 (σ =10)

This result may be interpreted as the best result achieved to date since five of six unknowns were correctly classified (UN1 was classified correctly as Class D with 8 votes since all other classes received less votes).

The final experiment within Group 2 involved a human visual classification of the six unknown waveforms. This was achieved by comparing (by eye) the photographs of the unknown waveforms with the photographs of the 52 original waveforms. Since these photographs represented time normalized data, this experiment has been included under Group 2. It should be appreciated that this experiment is of fundamental importance since we normally cannot expect a machine to outperform a human. Thus, we might view the results below as the optimal performance achieveable.

Vector	Subjective Classification
UN1	Class D
UN2	Class E
UN3	Class C
UN4	Class F
UN5	Class G
UN6	Class H tied with Class D

It is interesing to note that our best performance (i.e., the previous experiment) closely parallels these results, even to the extent that UN3 was the only waveform in error for both experiments.

Group 3 Experiments

These experiments were conducted, at the request of Sperry Rand, to determine how a classifier would perform if polarization samples were not included in the design set but were included in the independent test set. To this end, Data Set 7 was constructed and used to design and test the Nearest Mean Classification Logic, the Nearest Neighbor Classification Logic ; Data Set 8 was constructed from 7 and used to design and test the Fisher Piecewise Linear Discriminant Logic. The independent test set contained 17 vectors as described in Section 2. The results of these experiments are listed below:

	Data Set 7		Data Set 8
True Class	Nearest Mean	Nearest Neighbor	Fisher Pcws. Linear Discrim.
UN1 = D	E	B	(D)
UN2 = E	G	C	A
UN3 = F	D	(F)	(F)
UN4 = F	G	(F)	(F)
UN5 = G	C	E	(G)
UN6 = H	A	B	B
TM SCC = B	D	A	A
TM FEC-12" = C	D	A	F
TM FEC-8" = D	(D)	G	G
TM REC-0° = E	D	F	F
TM REC-30° = E	D	F	F
TM REC-45° = E	D	F	F
TM VES = G	D	A	A
DIA SSS-0° = H	D	(H)	(H)
DIA SSS-30° = H	(H)	E	C
DIA SSS-60° = H	B	E	E
DIA SSS-90° = H	A	E	G
Number Correct	2	3	5

These results clearly indicate the need to include polarization data in the design set if that data will appear in the future test sets.

Tabular Summary of Groups 1 and 2 Experiments

	Group 1 Experimental Results					Group 2 Experimental Results				
True Class	Nearest Mean	Nearest Neighbor	Fisher P.W.L. $\sigma = 10$	Fisher P.W.L. $\sigma = 1$	Fisher PWL w/ Mode Anal $\sigma = 10$	Nearest Neighbor	Fisher PWL $\sigma = 10$	Fisher PWL $\sigma = 1$	Fisher PWL w/ Mode Anal. $\sigma = 10$	Human Visual
UN1 = FEC - 8" = D	D	C	D	C	C	B	C	C	D	D
UN2 = REC = E	F	B	E/A	E/A	A	C	E	E	E	E
UN3 = CUBE = F	H	C	F	F	E/C	F	E	F	E	C
UN4 = CUBE = F	F	F	F	F	F	F	F	F	F	F
UN5 = UES = G	C	E	G	G/A	E	E	G	G	G	G
UN6 = SSS = H	H	E	H/B	H/B/G	H	B	H	B	H	H/D
# Correct	3	1	4	2	2	2	4	4	5	4
# Incorrect	3	5	0	1	3	4	2	2	1	1
# Tied	0	0	2	3	1	0	0	0	0	1

5.4 CONCLUSIONS AND RECOMMENDATIONS

The results obtained during this research period are regarded as significant since it appears that automatic shape classification based upon the Sperry radar return is feasible. It is concluded that the best possibilities for accurate classification lie in the use of piecewise linear discriminant logic. Based upon our experiments with Nearest Mean Logic and Nearest Neighbor Logic, it would appear that methods such as template matching or matched filtering will not provide adequate performance. It is also clear from the results of the Group 3 experiments that polarized returns cannot be accurately classified if such samples are not included in the design set.

The best result was obtained using Fisher Piecewise Linear Logic with Mode Analysis under the condition that the waveform return is time normalized. The result obtained is considered at least as good as that achieved by human visual classification. This fact is regarded as highly significant since human classification performance is viewed as the basic standard to be achieved. The classification accuracy obtained using this method is further regarded as relatively insensitive for the following reasons;

- The waveform was smoothed by averaging three adjacent amplitudes along the wave. The effect of this operation is to smooth the wave and thereby reduce the information content in the resulting waveform.

- No distinction was made within a basic shape class; that is, orientation and polarization information were neglected. The implication is that an object's shape can be accurately predicted independent of its orientation or the polarization of the return.

- Excellent results were obtained when a large amount of Gaussian (white noise) noise was added. The implication is that the results are relatively insensitive to additive noise.

- Although there appears to be some sensitivity to the time origin of the waveform, the results from Group 1 experimentation indicate only a reasonable degradation. This sensitivity may not be a problem since the method used to achieve normalization is perhaps the simplest of all possible methods. The thought is that even this simple method results in good classification.

The results reported here must be considered encouraging, particularly in view of the difficulty of the classification problem. However, much work remains to be done if these achievements are to become of practical significance. The basic step towards the practical achievement will involve extensive testing of the Piecewise Linear Discriminant Logic under all conditions which would ordinarily arise in an operating environment. It is therefore recommended that more data in the form of digitized waveform returns be supplied to PAR for further testing. It cannot be overstressed that a practical solution is heavily dependent on a large representative data base.

In addition to a larger data base, it is recommended that more sophisticated features be extracted from the waveform returns for the purpose of automatic classification. The present results were obtained using the most simplistic feature set; namely, the averaged time samples along the wave. Features directly related to the "shape" of the waveform such as the number of peaks, the location and amplitudes of peaks, zero crossings, inflection points, etc., should be extracted and used to classify returns. It is recommended that Piecewise Linear Logic be designed, tested and compared to the results reported here using the new feature set.

SECTION 6

CONCLUSIONS

In this study the space-time integral equation approach has been extended to the solution of the large body problem. This has been accomplished by the development of the impulse response augmentation technique. This technique combines the smoothed impulse response, which is computed exactly with the space-time integral equation, and the specular return of the impulse response, which is know exactly from physical optics, to produce a total impulse response and a frequency response over the entire spectrum.

The validity of the impulse response augmentation technique has been demonstrated on three smooth convex targets with axial incidence. For the case of a sphere (the only target for which there exists a theoretical check of both the impulse response and the frequency response), the results are in good agreement with the theory. For the case of a prolate spheroid with an axial ratio of 2:1 and with axial incidence, the results agree well with the Moffatt-Kennaugh exponential sum approximation over the higher frequency portion of the spectrum. The impulse response augmentation technique was also demonstrated for a sphere-capped cylinder with a length-to-diameter ratio of 3:1 and yielded results which had not been previously obtained.

In addition, the polarization dependent effects for nonaxial incidence on smooth convex bodies have been considered and found to modify the step and ramp singularity terms at the leading edge of the impulse response. These effects have been incorporated into the impulse response augmentation technique and demonstrated for the case of the prolate spheroid with nonaxial incidence. The technique was also demonstrated for the sphere-capped cylinder with nonaxial incidence, where the returns from both the front and rear joins were accounted for.

The results of this study are extremely encouraging, since a technique has been both developed and demonstrated for obtaining the impulse response and/or frequency response of the entire spectrum for smooth, convex targets with arbitrary incidence. These results should be extended to more complicated targets.

An expression was developed for the minimum number of orientations at which the smoothed impulse response of a target must be measured or calculated for a given time sample rate or, equivalently, a given bandwidth of the incident pulse. This expression yielded results which were in good agreement with measurements performed on the time domain scattering range. This treatment, however, was limited to target orientations about a fixed axis, and thus should be extended to the case of arbitrary target orientations.

Smoothed impulse response measurements were made on an additional 35 target aspect angles and polarizations. These 35 waveforms, together with the 22 waveforms previously measured, were used by PAR, Inc. as the basis for the design of various identification processors with OLPARS. The results of this preliminary work encourage further study to examine the performance of the identification processors for signals corrupted with realistic noise.

SECTION 7

REFERENCES

1. M. G. Andreasen, "Scattering from Rotationally Symmetric Metallic Bodies," DDC-610-607, April 1964.

2. F. K. Oshiro, F. P. Torres and H. C. Heath, "A Source Distribution Technique for the Solution of General Electromagnetic Scattering Problems," DDC-624-586, October 1965.

3. C. L. Bennett, W. L. Weeks, "A Technique for Computing Approximate Electromagnetic Impulse Response of Conducting Bodies," Interaction Note 222, June 1968.

4. C.L. Bennett, J.D. DeLorenzo and A.M. Auckenthaler, "Integral Equation Approach to Wideband Inverse Scattering," Volume I: Development of Procedures for Numerical Solution and Volume II: Computer Program Descriptions and Listings, Interaction Notes 226 and 227, June 1970.

5. J. R. Mentzer, Scattering and Diffraction of Radio Waves (New York, The MacMillan Company), pp. 27-34, 1955.

6. R. G. Kouyoumjian, "Asymptotic High-Frequency Methods," Proc. IEEE, Vol. 53, No. 8, pp. 864-876, August 1965.

7. J. B. Keller, "The Geometric Theory of Diffraction," J. Opt. Soc. Amer., Vol. 52, pp. 116-130, February 1962.

8. E. M. Kennaugh and R. L. Cosgriff, "The Use of Impulse Response in Electromagnetic Scattering Problems," 1958 IRE Nat'l Conv. Rec., pt. 1, pp. 72-77.

9. G. Mie,"Beiträge zur Optik trüber Medien, speziell kolloidalev Metallösungen," Ann. d. Physik, Vol. 25, pp. 377-442, 1908.

10. T. B. A. Senior and R. F. Goodrich, "Scattering by a Sphere," Proc. IEEE, Vol. 111, No. 5, pp. 907-916, May 1964.

11. D. L. Moffatt and E. M. Kennaugh, "The Axial Echo Area of a Perfectly Conducting Prolate Spheroid," IEEE Trans. Antennas and Propagation, Vol. AP-13, pp. 401-409, May 1965.

12. A. M. Nicolson, et al, IEEE Trans. Microwave Theory and Techniques, Vol. MTT-20, No. 1, pp. 3-9, January 1972.

13. R. Smith, "Discrete Deconvolution, " Sperry Rand Research Center, Sudbury, Mass., Addendum to Final Report on Contract F30602-68-C-0176.

14. A Papoulis, The Fourier Integral and its Application (McGraw-Hill, New York, 1962).

15. A. Papoulis, "Error Analysis in Sampling Theory," Proc. IEEE, Vol 54, No. 7, pp. 947-955, July 1966.

16. G. Ross, A. M. Nicolson, R. Smith, et al., "Transient Behavior of Microwave Networks," RADC-TR-68-92, April 1968.

17. R. S. Smith, J. D. DeLorenzo and C. L. Bennett, "Wideband Surface Current Analysis," Sperry Rand Research Center, Sudbury, Mass., Final Report on Contract No. F30602-69-C-0357, July 1970.

18. C. L. Bennett and W. L. Weeks, "Transient Scattering from Conducting Cylinders," IEEE Trans. Antennas and Propagation, Vol. AP-18, No. 5, September 1970.

19. J. D. DeLorenzo, "Electromagnetic Transient Studies in Space-Time," Ph.D. Dissertation, Boston University, April 1970.

20. J. W. Sammon, D. B. Connell, et al, "Programs for On-Line Pattern Analysis," Final Report to Contract F30602-70-C-0223, RADC-TR-71-177.

21. J. W. Sammon, "Interactive Pattern Analysis and Classification," IEEE Trans. on Computers, Vol. C-19, No. 7, pp. 594-616, July 1970.

22. J. W. Sammon, "An Optimal Discriminant Plane," IEEE Trans. on Computers, Vol. C-19, No. 9, pp. 826-829, September 1970.

23. R.E.A.C. Paley and N. Weiner, "Fourier Transforms in the Complex Domain," Am. Math. Soc. Colloquium Publication, Vol. 19, New York, 1934.

24. M. J. Lighthill, Fourier Analysis and Generalized Functions, (Cambridge University Press, 1964) p. 30.

SECTION 8

APPENDIX

8.1 SCALING

It is the goal of any study such as this to display the results in the form of universal curves so they may be applied to a maximum number of problems with a minimum amount of effort. The thrust of this section is to document for easy reference the parameters which may be used as coordinates such that the resultant curves are invariant with body size changes.

First consider the frequency domain. This discussion will be limited to the magnetic field intensity, although the results are equally applicable to the electric field intensity. The far scattered magnetic field, $H^s(ka)$, is weighted by the incident field, the distance from the target r_o, and the linear dimension of the target a, and plotted as a function of ka, where k is the wave number ($k = 2\pi/T$; T = period of one cycle of sine wave in light meters). Thus,

$$\frac{r_o H^s(ka)}{a H^i(ka)} \text{ vs } ka$$

yields a curve which is invariant with body size changes.

The other important parameter in the frequency domain is radar cross section σ, which is defined as

$$\sigma = \lim_{r_o \to \infty} 4\pi r_o^2 \frac{|H^s(ka)|^2}{|H^i(ka)|^2} \quad .$$

Both the effect of the incident field and the distance from the target have been normalized by the definition. The size may be accounted for by weighting the radar cross section σ with its value in the geometric optics limit, $\sigma_{g.o.}$. Thus,

$$\frac{\sigma}{\sigma_{g.o.}} \text{ vs } ka$$

yields a curve which is invariant with body size changed.

Next consider the time domain. The far scattered magnetic field $H^s(t/a)$ is weighted by the distance from the target and plotted as a function of t/a, where t is measured in light meters. This is for the case of an

incident pulse excitation of the form

$$e(t/a) = \frac{n}{\sqrt{\pi}} e^{-(na)^2(t/a)^2}$$

where n is chosen such that (na) is a constant. This specification on n merely makes the incident pulse width constant relative to the body dimensions and assures that the smoothed impulse response yields an invariant curve. Thus,

$$r_o H^s(t/a) \text{ vs } t/a$$

yields a curve which is invariant with body size changes. It should be noted that singularity functions are a special case, and in particular the function a $\delta(t)$ when plotted vs t/a yields $\delta(t/a)$ which is "invariant" under body size changes. That is,

$$\delta(t/a) = a\ \delta(t)$$

by standard definition in the theory of distributions.

Finally, it is of interest to document the relationships between these two domains when the curves are normalized. Define these normalized variables as follows:

$$t' = t/a$$

$$\omega' = ka$$

$$H(\omega') = \frac{r_o H^s(ka)}{a H^i(ka)}$$

$$h(t') = r_o H^s(t/a)$$

Thus,

$$H(\omega') \text{ vs } \omega'$$

$$h(t') \text{ vs } t'$$

yield curves invariant under size changes.

Moreover

$$H(\omega') = F\{h(t')\} = \int_{-\infty}^{\infty} h(t')e^{-j\omega' t'}\, dt'$$

$$h(t') = F^{-1}\{H(\omega')\} = \frac{1}{2\pi}\int_{-\infty}^{\infty} H(\omega')e^{j\omega' t'}\, d\omega'$$

8.2 CAUSALITY

Both the impulse response and the augmented impulse response of a target are known to be causal functions. The smoothed impulse response which is computed by numerical solution of the space-time integral equation is also a causal function. As noted in Sec. 2.3.3, the augmented frequency response which is obtained from the transform of the computed smoothed impulse response yields valid results over the lower portion of the frequency range. However, the noise grows exponentially at the higher frequencies, and since it is known that the augmented frequency response goes to zero as the frequency goes to infinity, an estimate of this high frequency portion of the augmented frequency response is made. Both a phase estimate and an amplitude estimate must be considered. Since the augmented impulse response is causal, it is desirable that the amplitude estimate and the phase estimate be consistent with the causality condition. In this Appendix several techniques are described. for imposing the causality condition.

Ideally, one would like to estimate the amplitude response and obtain a phase response which is consistent with causality (or vice versa). However, it is not possible to do this, since obtaining unique phase from amplitude information (or vice versa) requires that the response be minimum phase in addition to being causal. Physically, there is no reason to expect the impulse response to be minimum phase. However, it is known that causality implies that the real part of the frequency response can be obtained from the imaginary part (and vice versa). The plan then is to use the real part of the frequency response to obtain an imaginary part which is consistent with causality, and use the imaginary part to obtain a real part which is consistent with causality. This technique will be applied directly to the estimate of the augmented impulse response because the augmentation function is already causal.

Let us assume that augmented impulse response has been shifted in time so that the impulse arrives at t = 0. Then the condition of causality is

$$h_a(t) = 0 \qquad t < 0$$

$$= f(t) \qquad t \geq 0 \tag{102}$$

To examine what relationship Eq. (102) implies between the real and imaginary parts of $H_a(\omega)$, it is convenient to express $h_a(t)$ as the sum of an even function $f_e(t)$ and an odd function $f_o(t)$:

$$h_a(t) = f_e(t) + f_o(t) \tag{103}$$

where

$$f_e(t) = f_e(-t)$$

$$f_o(t) = -f_o(-t) \ .$$

Using the causality condition Eq. (102) it is easily shown that

$$f_e(t) = \frac{1}{2} h_a(t) \qquad t > 0 \tag{104}$$

$$f_o(t) = \frac{1}{2} h_a(t) \qquad t > 0 \ . \tag{105}$$

Taking Fourier transforms of Eq. (103), we obtain

$$H_a(\omega) = R(\omega) + jX(\omega) \tag{106}$$

where

$$R(\omega) \leftrightarrow f_e(t) \tag{107}$$

$$X(\omega) \leftrightarrow f_o(t) \tag{108}$$

Hence we can construct a causal time function from the real part of the spectrum by taking the Fourier transform of the real part $R(\omega)$, which yields the even part of the time function $f_e(t)$. Then by Eq. (104) we get the causal time function $h_{a_2}(t)$:

$$h_{a_2}(t) = \begin{cases} 0 & t < 0 \\ f_e(t) & t = 0 \\ 2f_e(t) & t > 0 \end{cases} \tag{109}$$

From Eq. (104) we can obtain the entire spectrum, $H_{a_2}(\omega)$, for the causal time function $h_{a2}(t)$ by the Fourier transformation:

$$H_{a_2}(\omega) \leftrightarrow h_{a_2}(t) \ . \tag{110}$$

Similarly, we can obtain a causal time function from the imaginary part $X(\omega)$ by Eqs. (108) and (105), which yield

$$\begin{aligned} h_{a_1}(t) &= 2f_o(t) \qquad t > 0 \\ &= 0 \qquad\quad t \leq 0 \ . \end{aligned} \tag{111}$$

The spectrum of causal time is then simply

$$H_{a_1}(\omega) \leftrightarrow h_{a_1}(t) \ .$$

There is an alternative way of producing these two causal responses from the original noncausal response. For example, let us consider the problem of constructing the causal response $h_{a2}(t)$ from the real part. Let us define the following odd function of time:

$$h_o(t) = \begin{cases} h_a(t) & t < 0 \\ 0 & t = 0 \\ -h_a(-t) & t > 0 \ . \end{cases} \tag{112}$$

Now we can form $h_{a2}(t)$ by subtracting $h_o(t)$ from $h_a(t)$:

$$h_{a_2}(t) = h_a(t) - h_o(t) \tag{113}$$

or

$$h_{a_2}(t) = \begin{cases} 0 & t < 0 \\ h_a(t) & t = 0 \\ h_a(t) + h_a(-t) & t > 0 \ . \end{cases} \tag{114}$$

The above expression follows because the Fourier transform of $h_o(t)$ is imaginary and hence the operation in Eq. (113) does not affect the real part of the transform of $h_a(t)$. Since both the functions in Eq. (113) and the function obtained from the real part (Eq. (104)) are causal and have the same real part, they must be identified by the uniqueness of Fourier transforms.

In a similar fashion the causal function $h_{a_2}(t)$ determined by the imaginary part can be obtained by

$$h_{a_1}(t) = \begin{cases} 0 & t \leq 0 \\ h_a(t) - h_a(-t) & t > 0 \, . \end{cases} \tag{115}$$

A third causal function can be obtained by simply setting the function to 0 for $t < 0$, i.e.,

$$h_{a_3}(t) = \begin{cases} 0 & t < 0 \\ h_a(t) & t \geq 0 \, . \end{cases} \tag{116}$$

During the course of this investigation we found that it was possible to obtain a causal augmented impulse response without resorting to the above described procedures. It may be worth noting that the amplitude functions used augmented frequency response all satisfied the Piley-Wiener condition,[23] and thus it was assured that a phase function existed that would produce a causal inverse. In particular, it can shown that

$$A(\omega) = e^{-\omega\alpha}$$

satisfies the Paley-Weiner condition for

$$0 < \alpha < 1 \, .$$

The exponential estimate used for the creeping wave was with $\alpha = 1/3$.

8.3 SPACE-TIME INTEGRAL EQUATION SELF-TERM CORRECTION

The purpose of this section is to derive an analytic expression for the contribution due to the self term in the numerical solution of the space-time integral equation. This self-term contribution is the contribution to the total current due to the currents flowing in the patch on which the observer is sitting. The expression for this contribution is given by

$$\vec{J}_\epsilon(\vec{r},t) = \frac{1}{2\pi}\int_{S_\epsilon} \hat{a} \times \left\{ L\,[\vec{J}(\vec{r}',\tau] \times \hat{a}_R \right\} dS' \qquad (117)$$

$$\tau = t - R$$

where

$\vec{r}$ = the position vector to the observation point

$\vec{r}'$ = the position vector to the integration point

S_ϵ = the patch on which the observer is sitting

t = the time in light meters

$R = |\vec{r} - \vec{r}'|$

$\hat{a}_R = (\vec{r} - \vec{r}')/R$

$L = \left(\frac{1}{R^2} + \frac{1}{R}\frac{\partial}{\partial t}\right)$

$\hat{a}_n$ = the unit normal vector at $\vec{r}$.

It is also useful at this point to express the surface S_ϵ in a Taylor series expansion about the point $\vec{r}$: i.e.,

$$\vec{r}' - \vec{r} = u\vec{r}_{uo} + v\vec{r}_{vo} + \frac{1}{2}u^2\vec{r}_{uuo} + uv\,\vec{r}_{uvo} + \frac{1}{2}v^2\vec{r}_{vvo} \qquad (118)$$

where

$$\vec{r}_{uo} = \left(\frac{\partial \vec{r}'}{\partial u}\right)_{\vec{r}'=\vec{r}}$$

$$\vec{r}_{vo} = \left(\frac{\partial \vec{r}'}{\partial v}\right)_{\vec{r}'=\vec{r}}$$

$$\vec{r}_{uuo} = \left(\frac{\partial^2 \vec{r}'}{\partial u^2}\right)_{\vec{r}'=\vec{r}}$$

$$\vec{r}_{uvo} = \left(\frac{\partial^2 \vec{r}'}{\partial u \partial v}\right)_{\vec{r}'=\vec{r}}$$

$$r_{vvo} = \left(\frac{\partial^2 \vec{r}'}{\partial v^2} \right)_{\vec{r}' = \vec{r}} .$$

Let the u,v curves be lines of curvature so that

$$\hat{a}_n \cdot \vec{r}_{uuo} = K_u = \text{curvature in } u \text{ direction}$$

$$\hat{a}_n \cdot \vec{r}_{uvo} = 0$$

$$\hat{a}_n \cdot \vec{r}_{vvo} = K_v = \text{curvature in } v \text{ direction}$$

and K_u and K_v are the principal curvatures at $\vec{r}$. Writing the surface current in terms of its components gives

$$\vec{J} = J_u \hat{a}_u + J_v \hat{a}_v \tag{119}$$

where

$$\hat{a}_u = \vec{r}_u / |\vec{r}_u|$$

$$\hat{a}_v = \vec{r}_v / |\vec{r}_v| \quad .$$

Expansion of the triple cross product in Eq. (117) yields

$$\vec{J}_\epsilon(\vec{r},t) = \frac{1}{2\pi} \int_{S_\epsilon} \left\{ \hat{a}_n \cdot \hat{a}_R \, L(\vec{J}) - L(a_n \cdot \vec{J}) \, \hat{a}_R \right\} dS' \tag{120}$$

$$\tau = t - R$$

Applying Eqs. (118) and (119) to the dot product terms in Eq. (120) gives

$$\hat{a}_n \cdot \hat{a}_R = -\frac{1}{2} \frac{1}{R} (K_u u^2 + K_v v^2)$$

$$\hat{a}_n \cdot \vec{J} = J_u(K_u u) + J_v(K_v v) \quad . \tag{121}$$

Next, the terms given in Eq. (121) are combined in Eq. (120) to yield the expression for the self term as

$$\vec{J}_\varepsilon(\vec{r},t) = \frac{1}{2\pi}\int_{S_\varepsilon} L\left\{\hat{a}_{uo}J_u\,\frac{1}{2}\,(K_u u^2 - K_v v^2) + \hat{a}_{vo}J_v\,\frac{1}{2}\,(K_v v^2 - K_u u^2)\right\}\frac{1}{R}\,dS' \quad (122)$$

where it was noted that odd functions of u or v yield zero on integration over S_ε

Only the first terms in the space expansion of the surface current and its time derivative are retained, and since they are constant they may be taken outside the integral along with the unit vectors, giving

$$\vec{J}_\varepsilon(\vec{r},t) = \hat{a}_u\,\frac{1}{2\pi}\left\{J_u\int_{S_\varepsilon}\frac{K_u u^2 - K_v v^2}{R^3}\,dS' + \frac{\partial J_u}{\partial t}\int_{S_\varepsilon}\frac{K_u u^2 - K_v v^2}{R^2}\,dS'\right\}$$

$$+ \hat{a}_v\,\frac{1}{2\pi}\left\{J_v\int_{S_\varepsilon}\frac{K_v v^2 - K_u u^2}{R^3}\,dS' + \frac{\partial J_v}{\partial t}\int_{S_\varepsilon}\frac{K_v v^2 - K_u u^2}{R^2}\,dS'\right\} . \quad (123)$$

A circularly shaped patch for S_ε with radius ρ_o is assumed, and to facilitate the integration the following change of variables is introduced:

$$u = \rho\cos\theta$$

$$v = \rho\sin\theta$$

$$R = \rho = \sqrt{u^2 + v^2}$$

$$dS = dudv = \rho d\theta d\rho$$

The integration is then carried out to yield

$$\vec{J}_\varepsilon(\vec{r},t) = \hat{a}_u\left(\frac{K_u - K_v}{4\pi}\right)\left[\pi\rho_o J_u + \left(\frac{\pi\rho_o^2}{2}\right)\frac{\partial J_u}{\partial t}\right]$$

$$+ \hat{a}_v\left(\frac{K_v - K_u}{4\pi}\right)\left[\pi\rho_o J_v + \left(\frac{\pi\rho_o^2}{2}\right)\frac{\partial J_v}{\partial t}\right] \quad (124)$$

This may be further written in terms of the patch area ΔS as

$$\vec{J}_\epsilon(\vec{r},t) = \hat{a}_u \frac{1}{4}\sqrt{\frac{\Delta S}{\pi}}\,(\kappa_u-\kappa_v)\left(J_u + \frac{1}{2}\sqrt{\frac{\Delta S}{\pi}}\,\frac{\partial J_u}{\partial t}\right)$$

$$+ \hat{a}_v \frac{1}{4}\sqrt{\frac{\Delta S}{\pi}}\,(\kappa_v - \kappa_u)\left(J_v + \frac{1}{2}\sqrt{\frac{\Delta S}{\pi}}\,\frac{\partial J_v}{\partial t}\right) \qquad (125)$$

It is of interest to note that if the patch is taken to be square rather than circular, then the expression for $\vec{J}_\epsilon$ becomes

$$\vec{J}_\epsilon(\vec{r},t) = \hat{a}_u \frac{1}{4}\sqrt{\frac{\Delta S}{\pi}}\,(\kappa_u - \kappa_v)\left(1.083\,J_u + \frac{1}{2}\sqrt{\frac{\Delta S}{\pi}}\,\frac{\partial J_u}{\partial t}\right)$$

$$+ \hat{a}_v \frac{1}{4}\sqrt{\frac{\Delta S}{\pi}}\,(\kappa_v - \kappa_u)\left(1.083\,J_v + \frac{1}{2}\sqrt{\frac{\Delta S}{\pi}}\,\frac{\partial J_v}{\partial t}\right) \qquad (126)$$

where

$$1.083 = 2\,\ell n\left(\frac{\sqrt{5}+1}{\sqrt{5}-1}\right)$$

The only difference is that the coefficient of the J_u and J_v terms is 8.3% higher; otherwise the expression remains the same. In the work that was performed in this report, Eqs. (124) and (125) were used for the numerical computation.

8.4 PROLATE SPHEROID PHYSICAL OPTICS IMPULSE RESPONSE COEFFICIENTS

The purpose of this section is to derive a general expression for the initial time portion of the prolate spheroid impulse response. This will yield both the impulse and step singularity values which are obtained by assuming physical optics currents on the scattering surface. The Kennaugh-Cosgriff formula will be utilized to facilitate this derivation.[8]

Consider a prolate spheroid with semi-minor axis a and semi-major axis b which are centered at the origin and whose major axis coincides with the z axis as shown in Fig. 133. The equation for this prolate spheroid is

$$\frac{x^2 + y^2}{a^2} + \frac{z^2}{b^2} = 1 \qquad (127)$$

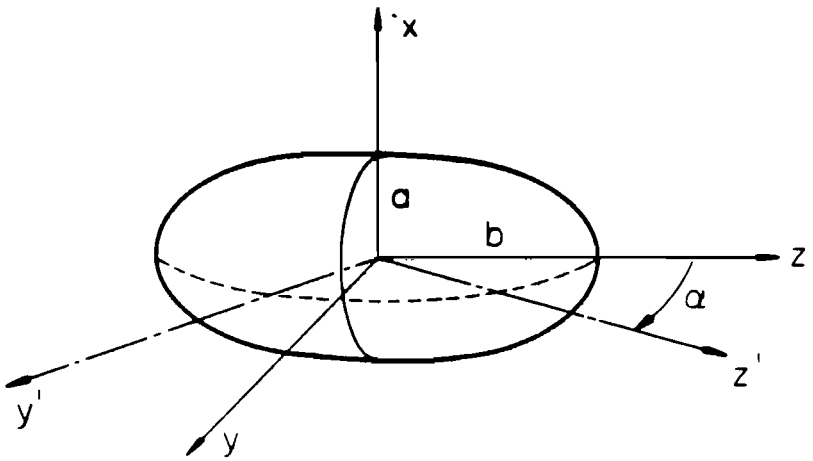

FIG. 133 Geometry of prolate spheroid.

To treat the case of a wave incident on the target at an angle α with respect to the z axis, it is convenient to consider the (x, y', z') coordinate system which results when the y-z axis is rotated by an angle α. This transformation is given by

$$z = -y' \sin \alpha + z' \cos \alpha$$

$$y = y' \cos \alpha + z' \sin \alpha \tag{128}$$

By substituting Eq. (128) into (127), the equation for the prolate spheroid becomes

$$\frac{x^2}{r_x^2} + \frac{(y' + f)^2}{r_y^2} = 1 \tag{129}$$

where

$$f = \frac{C(\alpha)}{B(\alpha)} z'$$

$$r_x^2 = \frac{B(\alpha)}{b^2} r_y^2$$

$$r_y^2 = \frac{a^2 b^2}{B(\alpha)} + z'^2 \left[\frac{C^2(\alpha)}{B^2(\alpha)} - \frac{D(\alpha)}{B(\alpha)} \right]$$

$$B(\alpha) = b^2 \cos^2 \alpha + a^2 \sin^2 \alpha$$

$$C(\alpha) = (b^2 - a^2) \sin \alpha \cos \alpha$$

$$D(\alpha) = b^2 \sin^2 \alpha + \alpha^2 \cos^2 \alpha \tag{130}$$

Thus, by Eq. (129) it is demonstrated that a plane wave incident on the target from the α direction (i.e., along the negative z' axis) will yield an elliptical silhouette area with principal radii r_x and r_y

The impulse response that results when physical optics currents are assumed to be set up on the surface is given by

$$r_o H^s_{po} = \frac{1}{2\pi} \frac{\partial^2 S(t)}{\partial t^2} \tag{131}$$

where $S(t)$ is the projected area of the scatterer as delineated by the incident impulse as it moves across the scatterer at one-half the free space

velocity.

Thus, for this case $S(t_s)$ is simply the area of the ellipse given in Eq. (129), i.e.

$$S(z') = \pi r_x r_y \tag{132}$$

which may be written in the form

$$S(z') = \frac{\pi a^2 b}{\Gamma^2(\alpha) B^{1/2}_{(\alpha)}} \left[\Gamma^2(\alpha) - z'^2\right] u[\Gamma(\alpha) - z'] \tag{133}$$

where

$$\Gamma(\alpha) = \frac{ab}{\sqrt{D(\alpha) - \frac{C^2(\alpha)}{B(\alpha)}}} = B^{1/2}_{(\alpha)} \tag{134}$$

In this case

$$z' = -t/2$$

which, on substitution into Eq. (133), yields the expression

$$\frac{1}{2\pi} S(t) = \frac{a^2 b}{8\Gamma^2(\alpha) B^{1/2}(\alpha)} \left[4\Gamma^2(\alpha) - t^2\right] u\left[t + 2\Gamma(\alpha)\right] . \tag{135}$$

Taking the first derivative gives

$$\frac{1}{2\pi} \frac{\partial S(t)}{\partial t} = - t \frac{a^2 b}{4\Gamma^2(\alpha) B^{1/2}_{(\alpha)}} u\left[t + 2\Gamma(\alpha)\right] . \tag{136}$$

Differentiating Eq. (136) again yields

$$r_o H^s_{po} = \frac{a^2 b}{2\Gamma(\alpha) B^{1/2}_{(\alpha)}} \delta[t + 2\Gamma(\alpha)] - \frac{a^2 b}{4\Gamma^2(\alpha) B^{1/2}_{(\alpha)}} u[t + 2\Gamma(\alpha)] .$$

So, in summary, if we represent the leading edge of the impulse response as

$$r_o H^s_{po} = P_z \delta(t/a - T_z) + S_z u(t/a - T_z) \tag{137}$$

then

$$T_z = -2 \frac{B^{1/2}(\alpha)}{a}$$

$$P_z = \frac{ab}{2B(\alpha)}$$

$$S_z = -\frac{a^2 b}{4 B^{3/2}(\alpha)}$$

$$B(\alpha) = b^2 \cos^2\alpha + a^2 \sin^2\alpha$$

8.5 SPHERE-CAPPED CYLINDER PHYSICAL OPTICS IMPULSE RESPONSE COEFFICIENTS

The purpose of this section is to derive a general expression for the initial time portion of the sphere-capped circular cylinder impulse response. This will yield the singularity functions which are obtained by assuming physical optics currents on the scattering surface. The area function technique will be used to facilitate this derivation.

Consider the case of a circular cylinder with spherical end caps as shown in Fig. 134. The length of the cylinder portion is taken to be L and the radius to be a. The axis of the cylinder coincides with the z axis and the ends of the target intersect the z axis at $z = -(L+a)$ and $z = a$ as displayed in Fig. 134. To treat the case of a wave incident on the target at at angle α with respect to the z axis, it is convenient to consider the (x, y', z') coordinate system which is obtained by rotating the y-z axis about the x axis by an angle α. This transformation is given by

$$z = -y' \sin\alpha + z' \cos\alpha$$

$$y = y' \cos\alpha + z' \sin\alpha \qquad (138)$$

Thus, a plane wave that is incident from the α direction travels in the negative z' direction and the projected area function initially in "time" is given by

$$S(z') = \begin{cases} \pi(a^2 - z'^2) & ; \ 0 \le \alpha < 90^0 \\ \pi(a^2 - z'^2) + 2L\sqrt{a^2 - z'^2} & ; \ \alpha = 90^0 \end{cases} \qquad (139)$$

The impulse response that results when physical optics currents are assumed to be set up on the surface is given by

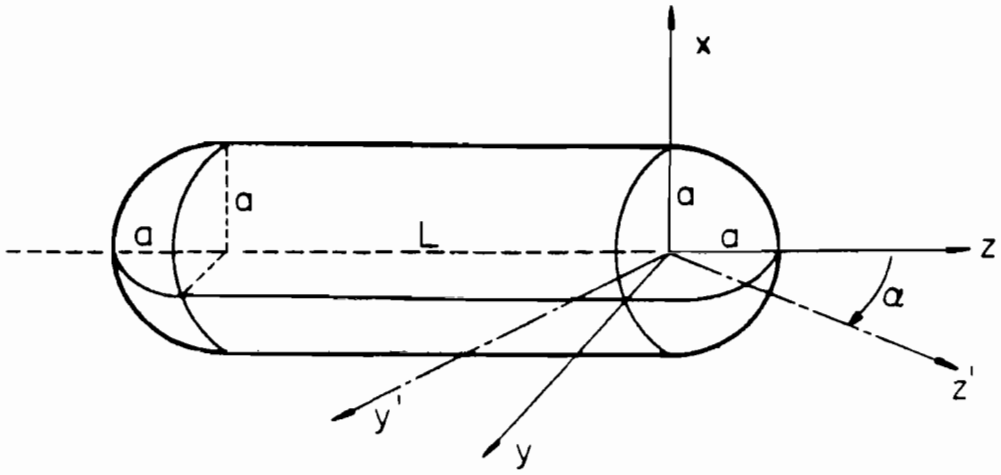

FIG. 134 Geometry of sphere-capped circular cylinder with length-to-diameter ratio of (L + 2a)/2a.

$$r_o H^s_{po} = \frac{1}{2\pi} \frac{\partial^2 S(t)}{\partial t^2} \tag{140}$$

where $S(t)$ is the projected area of the target on the plane of the incident wave front as it travels across the scatterer at one-half the free space velocity. In this case

$$z' = -t/2$$

and thus,

$$\frac{1}{2\pi} S(t) = \begin{cases} \frac{1}{8}(4a^2 - t^2) \; ; \; 0 \le \alpha < 90^o \\ \\ \frac{1}{8}(4a^2 - t^2) + \frac{L}{2\pi}(2a + t)^{1/2}(2a - t)^{1/2} \; ; \; \alpha = 90^o \end{cases} \tag{141}$$

This expression is going to be used only in the vicinity of the leading edge, and thus it may be approximated in this region by

$$\frac{1}{2\pi} S(t) = \begin{cases} \frac{1}{8}(4a^2 - t^2)u(t + 2a) \; ; \; 0 \le \alpha < 90^o \\ \\ \frac{1}{8}(4a^2 - t^2)u(t + 2a) + \frac{L\sqrt{a}}{\pi}(2a + t)^{-1/2}u(t + 2a) \; ; \\ \qquad \alpha = 90^o \; . \end{cases} \tag{142}$$

The first derivative is

$$\frac{1}{2\pi} \frac{\partial S(t)}{\partial t} = \begin{cases} -\frac{t}{4} u(t + 2a) \quad ; \quad 0 \le \alpha < 90^o \\ \\ -\frac{t}{4} u(t + 2a) + \frac{L\sqrt{a}}{2\pi}(2a + t)^{-1/2} u(t + 2a) \; ; \; \alpha = 90^o \end{cases} \tag{143}$$

The second derivative is

$$\frac{1}{2\pi}\frac{\partial^2 S(t)}{\partial_t{}^2} = \begin{cases} \frac{a}{2}\,\delta(t+2a) - \frac{1}{4}\,u(t+2a) & ;\ 0 \le \alpha < 90^o \\ \\ \frac{a}{2}\,\delta(t+2a) - \frac{1}{4}\,u(t+2a) - \frac{L\sqrt{a}}{4\pi}\,(2a+t)^{-3/2}\,u(t+2); & a=90^o. \end{cases} \tag{144}$$

Writing now in terms of the normalized time

$$t' = t/a$$

gives

$$\frac{1}{2\pi}\frac{\partial^2 S(t)}{\partial_t{}^2} = \begin{cases} \frac{1}{2}\,\delta(t'+2) - \frac{1}{4}\,u(t'+2) & ;\ 0 \le \alpha < 90^o \\ \\ \frac{1}{2}\,\delta(t'+2) - \frac{1}{4}\,u(t'+2) - \frac{L}{4\pi a}\,(t'+2)^{-3/2}\,u(t'+2); & \alpha = 90^o \end{cases} \tag{145}$$

where the generalized function $(t')^{-3/2}\,u(t')$ is defined as

$$\left\langle (t')^{-3/2}\,u(t'),\ \varphi(t') \right\rangle \equiv \int_o^\infty (t')^{-3/2}\,[\varphi(t') - \varphi(o)]\,dt' \tag{146}$$

and it should be noted that

$$\left\langle (t')^{-3/2}\,u(t'),\ \varphi(t') \right\rangle = -\frac{1}{2}\left\langle (t')^{-1/2}\,u(t'),\ \frac{d\varphi(t')}{dt'} \right\rangle$$

$$= -\frac{1}{4}\left\langle (t')^{1/2}\,u(t'),\ \frac{d^2\varphi(t')}{dt'^2} \right\rangle$$

as shown by Lighthill.[24]

In summary, the leading edge of the impulse response of the sphere-capped circular cylinder is

$$r_o H^s_{po} = P_z \delta(t/a - T_z) + S_z u(t/a - T_z) + G_z (t/a - T_z)^{-3/2} u(t/a - T_z) \quad (147)$$

where

$$T_z = -2$$

$$P_z = \frac{1}{2}$$

$$S_z = -\frac{1}{4}$$

$$G_z = \begin{cases} 0 & ; \ 0 \le \alpha < 90^o \\ \frac{-L}{4\pi a} & ; \ \alpha = 90^o \end{cases}$$

8.6 SPHERE-CAPPED CYLINDER FIRST JOIN RETURN

The purpose of this section is to derive a simple estimate for the type of initial response that can be expected from the sphere-cap cylinder join region of a sphere-capped cylinder. The approach is to use the physical optics approximation and then reduce the problem to the determination of the projected area function.

Figure 135 displays the top view of a sphere-capped cylinder with radius a and with a wave incident on it at an angle α with respect to the cylinder axis. The distance of the incident wave from the origin (the center of the first sphere cap in this problem) is taken to be r. The incident wave, when it completely intersects the cylinder, will generate an elliptical cross section with semi-minor axis a and semi-major axis b, given by

$$b = \frac{a}{\cos \alpha} \ .$$

The incident wave produces a circular area function up until it reaches the join region, at which time the projected area is the combination of a circle with an edge sliced off and an ellipse with an edge sliced off. The ellipse, as noted earlier, has a semi-major axis b and semi-minor axis a, and for the initial portion of time the projected area may be approximated by a circle with suitable radius p. Thus, for this approximation the projected area is given by

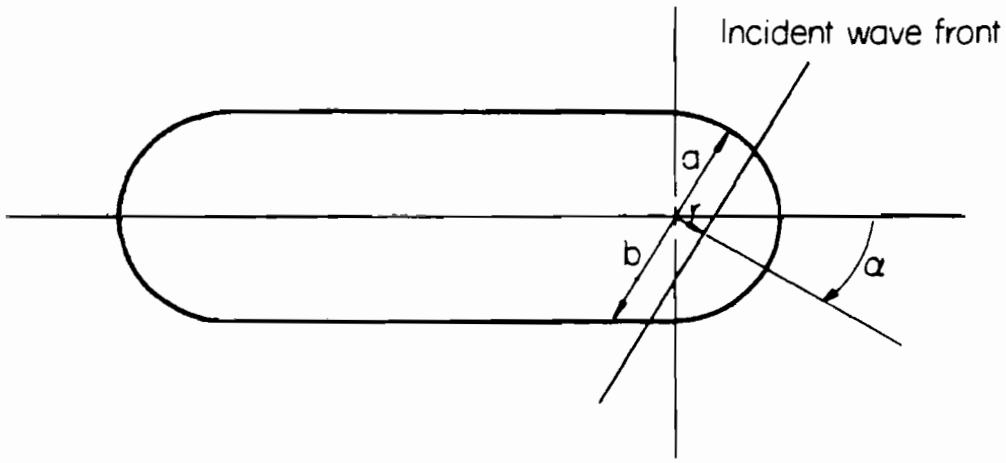

FIG. 135 Join region geometry of sphere-capped cylinder.

$$S(t) = p^2 \tan^{-1}\left(\frac{\sqrt{p^2 - t^2}}{t}\right) - t\sqrt{p^2 - t^2}$$

where now t has been suitably redefined.

The first derivative is

$$\frac{\partial S}{\partial t} = -2\sqrt{p^2 - t^2}$$

and the second derivative becomes

$$\frac{\partial^2 S}{\partial t^2} = 2\frac{t}{\sqrt{p^2 - t^2}}$$

Thus, from this expression, it is noted that at the leading edge the response has a $t^{-1/2}$ type variation.

8.7 USEFUL TRANSFORM PAIRS

In traveling from the impulse response in the time domain to the frequency response in the frequency domain, the Fourier transform must be used. In this work, this was accomplished by use of the finite Fourier transform, together with the analytic expressions for the singularity functions. It is the purpose of this section to document these analytic transform-pair expressions for easy future reference.

$$\delta(t - T_z) \leftrightarrow \exp(-j\omega T_z)$$

$$u(t - T_z) \leftrightarrow \frac{1}{j\omega}\exp(-j\omega T_z)$$

$$r_p(t - T_z) \leftrightarrow \frac{1}{(j\omega)^2}\exp(-j\omega T_z)$$

$$(t - T_z)^{-3/2}\, u(t - T_z) \leftrightarrow -2\sqrt{\pi}\sqrt{\omega}\exp(-j\omega T_z + j\pi/4)$$

$$(t - T_z)^{-1/2}\, u(t - T_z) \leftrightarrow \frac{\sqrt{\pi}}{\sqrt{\omega}}\exp(-j\omega T_z - j\pi/4)$$

$$(t - T_z)^{-1/2} u(t - T_z) \leftrightarrow \frac{\sqrt{\pi}}{\omega^{3/2}} \exp(-j\omega T_z - j3\pi/4)$$

$$e^{-\alpha(t-T_z)}(t - T_z)^{-1/2} u(t - T_z) \leftrightarrow \frac{\sqrt{\pi}}{\sqrt{\omega}} \frac{1}{\left(1 \pm \frac{\alpha^2}{\omega^2}\right)^{1/4}} \exp\left(-j\omega T_z - j\frac{1}{4}\tan^{-1}\left(\frac{\alpha}{\omega}\right)\right.$$

$$\left[1 + \cos \pi \left(\frac{t-T_z}{T_n-T_z}\right)\right]\left[u(t-T_z) - u(t-T_n)\right] \leftrightarrow$$

$$- \frac{1}{\omega(\omega_o^2-\omega^2)} \left\{\omega_o^2 (\sin \omega T_z - \sin \omega T_n) - 2\omega^2 \sin \omega T_z\right.$$

$$\left. + j\left[\omega_o^2(\cos \omega T_z - \cos \omega T_n) - 2\omega^2 \cos \omega T_z\right]\right\}$$

where

$$\omega_o = \left(\frac{\pi}{T_n - T_z}\right)$$

All of the above expressions are valid for ω greater than zero. For ω less than zero, the real time function feature may be used to develop the symmetry conditions about zero, and the result can then be derived from the above expressions.

☆U.S. GOVERNMENT PRINTING OFFICE: 1976—A-0298/(42) 35